

Ferrohydrodynamic Flows in Uniform and Non-uniform
Rotating Magnetic Fields

by

Xiaowei He

Submitted to the Department of Electrical Engineering and Computer Science

in partial fulfillment of the requirements for the degree of

Doctor of Philosophy

at the

MASSACHUSETTS INSTITUTE OF TECHNOLOGY

[September 2006]
August 2006

© Massachusetts Institute of Technology, MMVI. All rights reserved.

Author.....

Department of Electrical Engineering and Computer Science

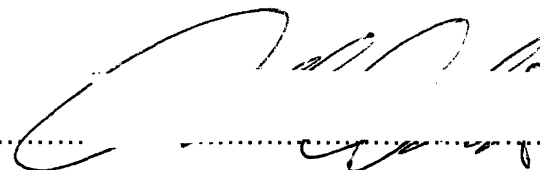
August 24, 2006

Certified by.....

Markus Zahn

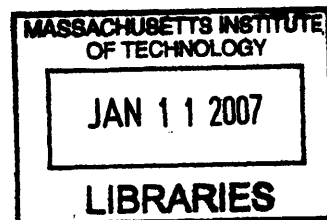
Professor

Thesis Supervisor

Accepted by.....

Arthur C. Smith

Chairman, Department Committee on Graduate Students



ARCHIVES

2011

10/10/11

10/10/11

Ferrohydrodynamic Flows in Uniform and Non-uniform Rotating Magnetic Fields

By

Xiaowei He

Submitted to the Department of Electrical Engineering and
Computer Science on August 15, 2006 in fulfillment of the requirements for
the degree of Doctor of Philosophy

Abstract

Ferrofluids are conventionally used in such DC magnetic field applications as rotary and exclusion seals, stepper motor dampers, and heat transfer fluids. Recent research demonstrates ferrofluid use in alternating and rotating magnetic fields for MEMS/NEMS application of microfluidic devices and bio-applications such as targeted drug delivery, enhanced Magnetic Resonance Imaging, and hyperthermia.

This thesis studies ferrofluid ferrohydrodynamics in uniform and non-uniform rotating magnetic fields through modeling and measurements of ferrofluid torque and spin-up flow profiles. To characterize the water-based and oil-based ferrofluids used in the experiments, measurements were made of the mass density, surface tension, viscosity, magnetization curve, nanoparticle size, and the speed of sound. Initial analysis for planar Couette and Poiseuille flows exploit DC magnetic field effects on flow and spin velocities with zero spin viscosity. Above critical values of magnetic field strength and flow velocity, multiple values of magnetic field, spin velocity, and effective magnetoviscosity result, indicating that zero spin viscosity may be non-physical. Torque and spin-up flow profile measurements show the effect of volume torque density and body force density in uniform and non-uniform rotating magnetic fields. Ferrofluid “negative viscosity” measurements in uniform and non-uniform rotating magnetic fields occur when magnetic field induced flow creates torque that exceeds the torque necessary to drive a viscometer spindle. Numerical simulations of torque and spin-up flow in uniform and non-uniform rotating magnetic fields, including contribution from the spin velocity and spin viscosity terms, are fitted to measurements to estimate the value ranges of relaxation time $\tau \approx 1.3\text{-}30 \mu\text{s}$ and spin viscosity $\eta' \approx 1\text{-}11.8 \times 10^{-9} \text{ N}\cdot\text{s}$ in waterbased ferrofluid. Based on the ferrohydrodynamic theory and models, theory of the complex magnetic susceptibility tensor is derived, which depends on spin velocity, that can be a key to external magnetic field control of ferrofluid biomedical applications. Preliminary impedance analysis and measurements investigate complex magnetic susceptibility change of ferrofluid in

oscillating and rotating uniform magnetic fields and allow calculation of the resulting dissipated power or mechanical work in pumping fluid.

Thesis Supervisor: Markus Zahn

Title: Professor

Acknowledgements

I would like to thank my thesis advisor, Dr. Markus Zahn, for being a superior mentor and generously sharing his knowledge, experience, and time. He has helped me become a better researcher and technical writer.

I also thank Mr. Thomas F. Peterson for his generous support of my ferrofluid research; and to the US National Science Foundation (Grant # CTS-0084070), and the Lemelson Foundation (Grant # 1575-03) for their support of my research. This research was also partially supported by a grant from the United States - Israel Binational Science Foundation (BSF), Jerusalem, Israel (Grant # 2004081).

I would like to thank Wayne Ryan, my best friend, who makes graduate student life easy in the N10 laboratory. All of the experiments described in Chapters 6-8 were in some way supported by his ideas, his labor, and his creations.

I would like to thank Shihab Elborai for standing together with me to fight against all the numerical simulation puzzles in our "War Room". With his help I have learned and understood more about ferrofluids and their modeling using Femlab.

I would like to thank Professor Carlos Rinaldi for his collaboration and help to understand the theory that models my experiments.

I would like to thank my colleagues Se-Hee Lee, Shahrooz Amin and Zachary Thomas for their helpful support.

Thanks to Prof. Caroline Ross of the Department of Chemical Engineering of MIT for allowing use of the Vibrating Sample Magnetometer for magnetization measurements; and to Dr. Anthony Garratt-Reed for helping me use the TEM

scanner; and to Stephen Samouhos for his help with viscometer measurements.

Thanks also to Ferrofluidics Corp. (now FerroTec Corp.) for supplying the ferrofluids that were used in my experiments and to Brookfield Corp. for donating a viscometer to the Zahn laboratory.

On a personal level, I thank my wife, Lei Jiang, the most important person in my life. Without her support my thesis would not be yet completed. I also thank my parents, Xusheng He and Zishu Xiao for opening my eyes to the world of science and engineering and supporting me all the time across the Pacific Ocean.

Contents

| | |
|--|-----------|
| Ferrohydrodynamic Flows in Uniform and Non-uniform Rotating Magnetic Fields | 3 |
| Contents..... | 7 |
| List of Figures | 11 |
| List of Tables | 23 |
| Chapter 1. Introduction to Ferrofluids | 25 |
| 1.1 Background and Research Motivations | 25 |
| 1.2 Scope of the Thesis | 28 |
| Chapter 2. Physical and Magnetic Properties of Ferrofluids | 31 |
| 2.1 Physical Properties | 31 |
| 2.1.1 Mass Density | 31 |
| 2.1.2 Surface Tension..... | 32 |
| 2.1.3 Viscosity | 32 |
| 2.2 Magnetization Characteristics..... | 33 |
| 2.3 Magnetic Particle Size..... | 39 |
| 2.4 Relaxation Times..... | 42 |
| 2.5 Transmission Electron Microscope Measurements..... | 44 |
| 2.6 Speed of Sound Measurements | 47 |
| Chapter 3. Theoretical Background and Governing Equations | 53 |
| 3.1 Maxwell's Equations | 53 |
| 3.2 Magnetization Relaxation Equation | 54 |
| 3.3 Fluid Dynamic Equations | 55 |
| 3.4 Boundary Conditions | 57 |

| | |
|--|-----------|
| 3.5 Turbulence in Planar Couette Flow and Taylor Instability in Taylor-Couette Flow | 59 |
| 3.6 Skin Depth | 62 |

Chapter 4. Effective Magnetoviscosity with Zero Spin

| | |
|--|-----------|
| Viscosity Coefficients ($\eta' = 0, \lambda' = 0$) | 65 |
|--|-----------|

| | |
|--|-----------|
| 4.1 Governing equations for Planar Couette Flow | 67 |
| 4.1.1 Magnetic Field and Magnetization | 67 |
| 4.1.2 Magnetic Force and Torque Density..... | 69 |
| 4.1.3 Planar Couette Flow | 70 |
| 4.1.4 Shear Stress..... | 71 |
| 4.2 Spin Velocity and Effective Viscosity Solutions for Planar Couette Flow | 72 |
| 4.2.1 The Solution for an Imposed External Magnetic Field H_x | 72 |
| 4.2.2 The Solution for an Imposed External Magnetic Flux Density B_x ... | 76 |
| 4.3 Effective Viscosity Solutions for Planar Poiseuille Flow | 79 |
| 4.3.1 Governing Equations and Boundary Conditions for Planar Poiseuille Flow..... | 79 |
| 4.3.2 Effective Viscosity Solutions for Planar Poiseuille Flow..... | 81 |

Chapter 5. Complex Magnetic Susceptibility Tensor

| | |
|-------------------------------|-----------|
| and Applications | 91 |
|-------------------------------|-----------|

| | |
|---|------------|
| 5.1 Brief Summary of Current Research. | 92 |
| 5.1.1 Magnetocytolysis | 92 |
| 5.1.2 Drug Delivery | 94 |
| 5.1.3 Separations | 95 |
| 5.1.4 Immunoassays | 96 |
| 5.1.5 Magnetic Resonance Imaging | 97 |
| 5.1.6 Bacterial Threads of Nanomagnets | 98 |
| 5.2 Complex Magnetic Susceptibility Tensor | 98 |
| 5.3 Power Dissipation | 101 |
| 5.4 Impedance Measurements | 106 |
| 5.4.1 Experiment Setup And Apparatus | 106 |
| 5.4.2 Complex Magnetic Susceptibility And Impedance | 108 |
| 5.4.3 Experimental Results | 114 |

| | |
|--|------------|
| Chapter 6. Viscometer Torque Measurements in | |
| Uniform Rotating Magnetic Fields | 121 |
| 6.1 Experimental Apparatus | 121 |
| 6.2 Viscometer Torque and Magnetoviscosity Relationship in a Couette | |
| Viscometer | 124 |
| 6.2.1 Viscous Shear Stress | 124 |
| 6.2.2 Magnetic Field Shear Stress..... | 128 |
| 6.2.3 Measurement Procedure | 129 |
| 6.3 Measurements of Viscometer Torque during Spin-Up Flow | 132 |
| 6.3.1 Effective Magnetoviscosity Measurements..... | 132 |
| 6.3.2 Stationary Spindle Torque Measurements..... | 134 |
| Chapter 7. Viscometer Torque Measurements in | |
| Non-uniform Rotating Magnetic Fields | 143 |
| 7.1 Non-uniform Magnetic Field..... | 143 |
| 7.2 Measurement Apparatus and Procedure | 146 |
| 7.3 Experimental Measurements in Non-uniform Rotating Magnetic Fields | |
| | 150 |
| Chapter 8. Spin-up Flow Velocity Measurements In A | |
| Non-uniform Rotating Magnetic Field | 155 |
| 8.1 Measurement Apparatus | 155 |
| 8.2 Measurement Setup and Procedure | 159 |
| 8.3 Measurement of The Spin-up Flow Velocity Profile | 163 |
| 8.4 Spin-up Velocity Profile Measurements | 165 |
| 8.4.1 MSG W11 Water-based Ferrofluid With Top Cover..... | 165 |
| 8.4.2 MSG W11 Water-based Ferrofluid Without Top Cover..... | 174 |
| Chapter 9. Numerical Simulations for Torque | |
| Measurements and Spin-up Flow Velocity | |
| Measurements | 181 |
| 9.1 Torque on a Cylindrical Boundary in a Rotating Magnetic Field | 182 |
| 9.1.1 Torque Evaluation in Cylindrical Geometry..... | 183 |

| | |
|---|------------|
| 9.1.2 Torque Evaluation in Cartesian Geometry..... | 185 |
| 9.2 Governing Equations for Numerical Simulation..... | 190 |
| 9.2.1 Assumption for Numerical Simulation..... | 190 |
| 9.2.2 Differential Equations for Numerical Simulation..... | 192 |
| 9.2.3 Boundary Conditions for Numerical Simulations..... | 197 |
| 9.3 Numerical Simulation Types | 198 |
| 9.4 Numerical Simulation Software and Algorithms | 201 |
| 9.5 Simulation Results | 205 |
| 9.5.1 One Regional Simulations | 205 |
| 9.5.1.1 Spin-up Velocity Profile Simulation in a Non-uniform Rotating Magnetic field | 205 |
| 9.5.1.2 Simulated Flow and Field Solutions | 212 |
| 9.5.1.3 Torque Simulation for Ferrofluid inside the Spindle in a Uniform Rotating Magnetic field..... | 219 |
| 9.5.1.4 Torque Simulation for Ferrofluid inside the Spindle in a Non-uniform Rotating Magnetic field | 222 |
| 9.5.2 Two Region Simulations | 225 |

Chapter 10. Thesis Summary and Suggestions for

| | |
|--|------------|
| Continuing Work | 229 |
| 10.1 Key Contributions | 229 |
| 10.2 Suggested Future Work..... | 230 |
| Bibliography | 233 |

List of Figures

Figure 2-1 Measured magnetization curve for EMG705 water-based ferrofluid 35

Figure 2-2 Measured magnetization curve for MSG W11 water-based ferrofluid 36

Figure 2-3 Measured magnetization curve for EFH1 oil-based ferrofluid 36

Figure 2-4 Measured magnetization linear region for EMG705 water-based ferrofluid, $\chi \approx 3.14$ 38

Figure 2-5 Measured magnetization linear region for MSG W11 water-based ferrofluid, $\chi \approx 0.56$ 38

Figure 2-6 Measured magnetization linear region for EFH1 oil-based ferrofluid, $\chi \approx 1.59$ 39

Figure 2-7 Transmission Electron Microscope image of EMG705 water-based ferrofluid (50,000 magnification). The magnetic nanoparticles have a mean diameter of 9.4 nm and a standard deviation of ± 3.4 nm. 45

Figure 2-8 Transmission Electron Microscope image of MSG W11 water-based ferrofluid (60,000 magnification). The magnetic nanoparticles have a mean diameter of 15.6 nm and a standard deviation of ± 5.3 nm. 46

Figure 2-9 Schematic cross-section showing the container used to measure the speed of sound in the sample fluids. 48

Figure 2-10 Echo intensity image of DI water, MSG W11 water-based ferrofluid and EFH1 oil-based ferrofluid. The speed of sound in the DOP 2000 was set as the speed of sound in water, $v_{s_nominal}$. By evaluating the echo correlation signals and the round-trip travel time of sound in the sample fluid, the effective distances were estimated. Using equation (2.14) the speeds of sound for all samples were calculated, where the actual distance was measured using the micrometer. Note the echoes close to 0 distance are the transducer echo, which is from the transducer impedance mismatching with the plastic container wall/ferrofluid interface. 50

Figure 4-1 (a) With a constant DC current source the DC magnetic field H is spatially constant in the ferrofluid, $H = NI_0 / s$ for planar Couette flow because the spin velocity is uniform and B will be a spatial constant that depends on the fluid spin velocity $\bar{\omega}$. For non-Couette flow $NI = \int_0^s H_x dx$

(b) With an impulse voltage source, $v = \Lambda_0 \delta(t)$, the DC magnetic flux Λ_0 is imposed and the DC magnetic flux density B is spatially uniform in the ferrofluid, $B = \Lambda_0 / A$, where H depends on the fluid spin velocity and is spatially constant only for Couette flow. 66

Figure 4-2 A planar ferrofluid layer between rigid walls, in planar Couette flow driven by the $x=d$ surface moving at velocity V , is magnetically stressed by

a uniform x directed DC magnetic field H_x or magnetic flux density B_x .

..... 67
 Figure 4-3 The solution for the change in magnetoviscosity for planar Couette

flow versus related magnetic field parameter $\left(P_H = \frac{\mu_0 \chi_0 H_x^2 \tau}{4\zeta} \right)$ and

magnetic flux density parameter $\left(P_B = \frac{\chi_0 B_x^2 \tau}{\mu_0 (1 + \chi_0)^2 4\zeta} \right)$ for various values

of $\frac{V\tau}{d}$. For imposed magnetic flux density B_x , $\chi_0 = 1.55$ for oil-based magnetic fluid Ferrotec EFH1 [40, 41]..... 74

Figure 4-4 The magnetic flux density parameter $\left(\frac{B_x}{B_0} \right)^2$ versus magnetic field

parameter $P_H = \frac{\mu_0 \chi_0 H_x^2 \tau}{4\zeta}$ for an imposed constant magnetic field H_x for

planar Couette flow for various $\frac{V\tau}{d}$, where $\chi_0 = 1.55$ for oil based ferrofluid Ferrotec EFH1..... 76

Figure 4-5 The relationship of related magnetic flux density parameter

$P_B = \frac{\chi_0 B_x^2 \tau}{\mu_0 (1 + \chi_0)^2 4\zeta}$ and magnetic field parameter $\left(\frac{H_x}{H_0} \right)^2$ for an imposed

magnetic flux density B_x for various values of $\frac{V\tau}{d}$, where $\chi_0 = 1.55$ for oil based ferrofluid Ferrotec EFH1. 78

Figure 4-6 A planar ferrofluid layer between rigid stationary walls, in planar Poiseuille flow driven by the constant pressure gradient, $\frac{\partial p}{\partial z}$, along the planar channel, is magnetically stressed by a uniform x directed DC magnetic flux density B_x 79

Figure 4-7 Calculated spin velocity profiles (solid lines) and flow velocity profiles (dashed lines) as a function of x for various magnetic flux density parameter values of $\left(P_p = \frac{\chi_0 B_x^2 \tau (\zeta + \eta)}{\mu_0 4\zeta \eta} \right)$ for $K = 1$, $\chi_0 = 1.55$ and

$\phi = 7.52\%$ for EFH1 oil-based ferrofluid..... 83

Figure 4-8 Calculated spin velocity profiles (solid lines) and flow velocity profiles (dashed lines) as a function of x for various magnetic flux density

parameter values of $\left(P_p = \frac{\chi_0 B_x^2 \tau (\zeta + \eta)}{\mu_0 4 \zeta \eta} \right)$ for $K = 20$, $\chi_0 = 1.55$ and

$\phi = 7.52\%$ for EFH1 oil-based ferrofluid..... 84

Figure 4-9 Calculated spin velocity profiles (solid lines) and flow velocity profiles (dashed lines) as a function of x for various magnetic flux density

parameter values of $\left(P_p = \frac{\chi_0 B_x^2 \tau (\zeta + \eta)}{\mu_0 4 \zeta \eta} \right)$ for $K = 40$, $\chi_0 = 1.55$ and

$\phi = 7.52\%$ for EFH1 oil-based ferrofluid..... 85

Figure 4-10 The solution for magnetoviscosity versus related magnetic flux

density parameter $\left(P_p = \frac{\chi_0 B_x^2 \tau (\zeta + \eta)}{\mu_0 4 \zeta \eta} \right)$ for various pressure gradient

parameter values of $K = \frac{\tau d}{2\eta} \frac{\partial p}{\partial z}$. The linearized magnetoviscosity curve in

the small spin velocity limit [85] (* markers) overlaps with the

magnetoviscosity curve with $K = 1$, $\chi_0 = 1.55$ and $\phi = 7.52\%$ for EFH1

oil-based ferrofluid..... 88

Figure 5-1 Power dissipation density in an oscillating magnetic field versus

$\Omega \tau$ as a function of spin velocity $\omega_x \tau$ 105

Figure 5-2 Power dissipation density in a rotating magnetic field versus $\Omega \tau$

as a function of spin velocity $\alpha |\omega_x \tau|$, where $\alpha = 1$ when the spin velocity

co-rotates with the magnetic field, and $\alpha = -1$ when the spin velocity

counter-rotates with the magnetic field..... 106

Figure 5-3 Experiment setup of the impedance measurement. A 20 turn 18

gauge copper wire solenoidal coil was placed vertically or horizontally in

MSG W11 water-based ferrofluid in a VWR 400 ml plastic beaker. The

beaker was centered in a uniform rotating magnetic field generated by a 2

pole three phase AC motor stator winding. 108

Figure 5-4 Equivalent circuit for an N turn copper wire coil submerged into

ferrofluid with a complex magnetic susceptibility $\chi = \chi' - j\chi''$. R_w is the

resistance of the coil winding due to the copper wire, while L is the

complex inductance. 109

Figure 5-5 The calculated inductance of the solenoidal coil, placed vertically

and horizontally in a uniform rotating magnetic field, for various spin

velocities ω_x using the equilibrium magnetic susceptibility value of $\chi_0 =$

0.56 for MSG W11 water-based ferrofluid and an estimated value of relaxation time constant $\tau \approx 10 \mu\text{s}$. Note that L'_v is independent of spin velocity ω_x 112

Figure 5-6 The calculated resistance of the solenoidal coil, placed vertically and horizontally in a uniform rotating magnetic field, for various spin velocities ω_x using the equilibrium magnetic susceptibility value of $\chi_0 = 0.56$ for MSG W11 water-based ferrofluid and an estimated value of relaxation time constant $\tau \approx 10 \mu\text{s}$. Note that $R_{\text{eff-v}}$ is independent of spin velocity ω_x 113

Figure 5-7 The measured inductance change of a vertically oriented coil in a uniform rotating magnetic field in the horizontal plane at 100 Hz..... 115

Figure 5-8 The measured resistance change of a vertically oriented coil in a uniform rotating magnetic field in the horizontal plane at 100 Hz..... 115

Figure 5-9 The measured inductance change of a horizontally oriented coil in a uniform rotating magnetic field in the horizontal plane at 100 Hz..... 116

Figure 5-10 The measured resistance change of a horizontally oriented coil in a uniform rotating magnetic field in the horizontal plane at 100 Hz..... 116

Figure 5-11 The measured inductance change of a horizontally oriented coil in a uniform rotating magnetic field in the horizontal plane at 400 Hz, 76 Gauss for various vertical DC magnetic fields..... 118

Figure 5-12 The measured resistance change of a horizontally oriented coil in a uniform rotating magnetic field in the horizontal plane at 400 Hz, 76 Gauss for various vertical DC magnetic fields..... 118

Figure 5-13 The measured inductance change of a horizontally oriented coil in a uniform rotating magnetic field in the horizontal plane at 400 Hz, 114 Gauss for various vertical DC magnetic fields..... 119

Figure 5-14 The measured resistance change of a horizontally oriented coil in a uniform rotating magnetic field in the horizontal plane at 400 Hz, 114 Gauss for various vertical DC magnetic fields..... 119

Figure 6-1 The experimental setup to measure magnetic field induced torque on a rotating or stationary Lexan spindle using the 2-pole motor stator winding to impose a uniform magnetic field. The Lexan spindle is connected to the viscometer and is centered in the beaker of ferrofluid, which is itself centered within the motor stator winding..... 123

Figure 6-2 The experimental setup for spindle torque measurements with a stationary cylinder using the 2-pole motor stator winding to impose a uniform magnetic field. The 10 ml syringe, which is used as a test spindle with ferrofluid inside and/or outside, is connected to the viscometer and is

| | |
|---|-----|
| centered in the beaker of ferrofluid, which is itself centered within the motor stator winding. | 124 |
| Figure 6-3 The experimental setup of the Couette viscometer. The spindle with radius a rotates in the counter-clockwise direction with spin velocity ω , centered in the cylindrical ferrofluid container with radius b | 125 |
| Figure 6-4 Measured spindle torque at 100 rpm counter-clockwise with surrounding water-based ferrofluid as a function of magnetic field amplitude, frequency, and direction of rotation. CCW spindle rotation shows a torque increase for co-rotation of spindle and magnetic field and a torque decrease including zero and negative values with counter-rotation, corresponding to zero and negative viscosity [33, 34, 42]. | 133 |
| Figure 6-5 Viscometer torque required to restrain 20 ml stationary spindle syringe with water-based ferrofluid inside the spindle with 133 Gauss rms applied magnetic field as a function of volume of ferrofluid for various magnetic field frequencies. | 135 |
| Figure 6-6 Viscometer torque required to restrain the 10 ml stationary spindle syringe with 9.5 ml MSG W11 water-based ferrofluid as a function of uniform magnetic field amplitude and frequency with ferrofluid entirely inside, entirely outside, and both inside and outside the syringe. | 137 |
| Figure 6-7 Viscometer torque required to restrain the 20 ml stationary spindle syringe with 16.5 ml MSG W11 water-based ferrofluid as a function of uniform magnetic field amplitude and frequency with ferrofluid entirely inside, entirely outside, and both inside and outside the syringe. | 138 |
| Figure 6-8 Viscometer torque required to restrain the 10 ml stationary spindle syringe with 9.5 ml EFH1 oil-based ferrofluid as a function of uniform magnetic field amplitude and frequency with ferrofluid entirely inside, entirely outside, and both inside and outside the syringe. | 139 |
| Figure 6-9 Viscometer torque required to the restrain 20 ml stationary spindle syringe with 16.5 ml EFH1 oil-based ferrofluid as a function of uniform magnetic field amplitude and frequency with ferrofluid entirely inside, entirely outside, and both inside and outside the syringe. | 140 |
| Figure 7-1 Ideal non-uniform magnetic field in a 4-pole motor stator winding with current equal to 4 Ampere peak (2.83 Amperes rms) corresponding to ~167 Gauss peak (118 Gauss rms) magnetic field at radius of 50.8 mm, which is the closest approach to the outer wall of the stator winding due to the thickness of the gaussmeter probe. The magnetic field lines indicate the 4-pole structure of the stator winding. The color shows the rms strength of the magnetic flux density in Gauss and cylindrical symmetry of the non-uniform magnetic field. | 144 |
| Figure 7-2 The theoretical and measured rms magnitude of a 4-pole non-uniform magnetic field strength vs. radius from the center of a 4-pole motor stator winding with current equal to 4 Amperes peak (2.83 Amperes rms). | 145 |

Figure 7-3 The 4-pole motor stator winding to impose a non-uniform magnetic field showing the cylindrical vessel to hold ferrofluid and the grooved channels in the outer wall to hold ultrasound transducers to measure fluid flow profiles to be described in Chapter 8. 145

Figure 7-4 The Lexan hollow spindle. The upper section of diameter D_1 was solid and was connected to the viscometer while the lower section of diameter D_2 was hollow so that it could be filled with ferrofluid. The lower hollow section has an inside dimension with height of 73.2 mm and diameter of 86.7 mm. The dimensions shown in the figure are outside dimensions. 147

Figure 7-5 A floating force balance system used in torque measurements with a non-uniform magnetic field. For measurements with ferrofluid inside the spindle, the spindle filled with ferrofluid was submerged in a beaker filled with water to make the total weight attached to the viscometer less than 5 oz (142 g), the weight limit of the Brookfield viscometer. For measurements with ferrofluid outside the spindle, the spindle was filled with water and submerged in a beaker filled with ferrofluid to make the total weight attached to the viscometer less than 5oz. For measurements with ferrofluid both inside and outside the spindle, the spindle and the beaker were filled with ferrofluid to make the total weight attached to the viscometer less than 5 oz (142 g). The beaker used in measurements was a VWR 1000ml beaker Cat. No. 89000-212. 148

Figure 7-6 Torque measurements with 432 ml MSG W11 water based ferrofluid inside the stationary hollow spindle with clockwise rotating non-uniform magnetic field. 151

Figure 7-7 Torque measurements with 250 ml MSG W11 water based ferrofluid outside the stationary hollow spindle with counter-clockwise rotating non-uniform magnetic field. 152

Figure 7-8 Torque measurement with MSG W11 water based ferrofluid of 432 ml inside, 250 ml outside and both inside and outside the stationary hollow spindle in rotating non-uniform magnetic fields. 153

Figure 8-1 Cylindrical polycarbonate container for spin-up velocity profile measurements in a non-uniform rotating magnetic field. Right: slots in the container wall with angles of 0° , 5° , 10° , 15° , 20° , 25° with respect to normal and radius to measure v_r and v_ϕ components and a slot at the bottom center diameter of the container for measurement of v_z . Left: container cover prevents a free surface interface by covering and contacting a fully filled container. 158

Figure 8-2 Configuration of motor stator and cylindrical vessel for the spin-up flow profile measurement experiments. A three-phase, 4-pole motor stator winding was used to excite a rotating non-uniform magnetic field. The

| | |
|---|-----|
| ring-light and video camera record the surface velocity profile at the same time as the UVP velocity profile was taken..... | 159 |
| Figure 8-3 The placement of the ultrasound probes at different heights (values of z) in containers of ferrofluid with and without a top cover. The top cover of the left cylindrical container forces zero flow at $z = z_f$ and reduces surface shear stress effects, whereas in the right container the absence of the top cover allows the free top surface to develop surface shear stress driven flows. | 160 |
| Figure 8-4 Geometry for spin-up flow profile measurement experiments. The ultrasound probe measures the component of the fluid velocity v_m along the probe's axis. | 165 |
| Figure 8-5 The azimuthal component of spin-up flow profiles at $z = z_f/2$ for MSG W11 water-based ferrofluid excited by a non-uniform magnetic field rotating counter-clockwise at 300 Hz. Counter-clockwise velocities increase with increasing applied magnetic field (increasing current in A rms). In the central region the flow profiles resemble the linear profile of a fluid in rigid body co-rotation with the applied magnetic field. The velocity is zero at the $r = R = 46$ mm stationary wall. The cylindrical container was covered so that there were no free ferrofluid surfaces. | 167 |
| Figure 8-6 The azimuthal component of spin-up flow profiles at $z = z_f/2$ for MSG W11 water-based ferrofluid excited by a non-uniform magnetic field rotating counter-clockwise at 400 Hz. Counter-clockwise velocities increase with increasing applied magnetic field (increasing current in A rms). The cylindrical container was covered so that there were no free ferrofluid surfaces..... | 168 |
| Figure 8-7 The azimuthal component of spin-up flow profiles at $z = z_f/2$ for MSG W11 water-based ferrofluid excited by a non-uniform magnetic field rotating counter-clockwise at 500 Hz. Counter-clockwise velocities increase with increasing applied magnetic field (increasing current in A rms). The cylindrical container was covered so that there were no free ferrofluid surfaces..... | 169 |
| Figure 8-8 Relation between the bulk rotational rate in the central region of the MSG W11 ferrofluid, $\Omega = v_\phi/r$, and the frequency of the applied rotating magnetic field for various magnetic field strengths. The ultrasound probe was place at height $z = z_f/2$ in the outside wall of a cylindrical container with a top cover. | 170 |
| Figure 8-9 Relation between the bulk rotational rate in the central region of the MSG W11 ferrofluid, $\Omega = v_\phi/r$, and the applied currents for various magnetic field frequencies. The ultrasound probe was place at height $z = z_f/2$ in the outside wall of a cylindrical container with a top cover. The rate of rotation increases monotonically with applied field strength for the investigated range of magnetic field strength..... | 171 |

Figure 8-10 The azimuthal component of spin-up flow profiles at $z = z_f/2$, $z = 3z_f/4$ and $z = z_f/4$ for MSG W11 water-based ferrofluid excited by a non-uniform magnetic field rotating counter-clockwise at 500 Hz with balanced 3 phase currents of 5 A (rms). The cylindrical container was covered so that there were no free ferrofluid surfaces. 172

Figure 8-11 Relation between the bulk rotational rate in the central region of the MSG W11 ferrofluid, $\Omega = v_\phi/r$, and the applied rotating magnetic field frequency with current of 5 A (rms) at various heights. The ultrasound probes were placed at heights $z = z_f/4$, $z = z_f/2$ and $z = 3z_f/4$ with a top cover. 173

Figure 8-12 Relation between the bulk rotational rate in the central region of the MSG W11 ferrofluid, $\Omega = v_\phi/r$, and the applied current at applied rotating magnetic field frequency of 500 Hz for heights. The ultrasound probes were placed at heights $z = z_f/4$, $z = z_f/2$ and $z = 3z_f/4$ with a top cover. 174

Figure 8-13 The azimuthal component of spin-up flow profiles at $z = z_f/2$, for MSG W11 water-based ferrofluid excited by a non-uniform magnetic field rotating counter-clockwise at 500 Hz with balanced 3 phase currents of 5 A (rms). The cylindrical container with free and covered ferrofluid surfaces had similar velocity variations with radius at $z = z_f/2$ 175

Figure 8-14 Relation between the co-rotating bulk rotational rate in the central region of the MSG W11 ferrofluid, $\Omega = v_\phi/r$, and the applied CCW rotating magnetic field frequency for balanced 3 phase currents of 5 A (rms). The ultrasound probe was place at height $z = z_f/2$ 176

Figure 8-15 Relation between the co-rotating bulk rotational rate in the central region of the MSG W11 ferrofluid, $\Omega = v_\phi/r$, and the applied CCW rotating magnetic field frequency of 500 Hz for various magnetic field 3 phase balanced currents (rms). The ultrasound probe was place at height $z = z_f/2$ 177

Figure 8-16 The co-rotational rates visually observed on the free top surface of MSG W11 water-based ferrofluid as a function of the frequency of the applied CCW rotating non-uniform magnetic field. 178

Figure 8-17 Azimuthal flow profiles at $z=z_f/2$ for MSG W11 water-based ferrofluid excited by a magnetic field rotating counter-clockwise at 200Hz. This flow profile results when water-based ferrofluid in a container without a free surface was placed in a uniform rotating applied magnetic field [82]. 179

Figure 9-1 Ferrohydrodynamic induced torque on hollow spindle wall with ferrofluid inside spindle. Spindle has a radius R and Depth D..... 182

Figure 9-2 Experiment setup for velocity profile and torque measurements with ferrofluid inside the spindle with clockwise (\vec{H}_{CW}) or counter clockwise (\vec{H}_{CCW}) rotating magnetic fields. 198

Figure 9-3 Experiment setup for torque measurements with ferrofluid just outside the spindle in the annulus gap between the spindle and the container wall. 199

Figure 9-4 Experiment setup for torque measurements with ferrofluid simultaneously inside and outside the spindle. Ferrofluid was filled in the hollow spindle and the annulus gap between the spindle and the container, so that the simulation is a two region problem. 200

Figure 9-5 Schematic of algorithm to numerically solve the governing ferrohydrodynamic equations using Femlab. By guessing an initial functional form for the force and torque densities, the ferrohydrodynamic equations are decoupled into two linear systems. 202

Figure 9-6 Sequence illustrating the method used to find the values of τ and η' in the 2D search space that best fit numerical simulation results to experimental data. Panel a: The algorithm first runs an extensive array of numerical simulations to fully map out contours of constant peak velocity magnitude v_{\max} (solid contours), and peak velocity radial position (dashed contours) for any given applied magnetic field strength and frequency. Panel b: The experimentally measured values of peak velocity magnitude and peak velocity radial position for the applied magnetic field strength and frequency are subtracted from the contours. Panel c: The intersection of the two contours labeled zero is the point in $\tau - \eta'$ space that best matches simulation to experiment. 204

Figure 9-7 Scatter plot showing the different fit values of τ and η' for the MSG W11 water-based ferrofluid experimental magnetic field strengths and frequencies listed in Table 9-1. 208

Figure 9-8 Comparison of experimentally measured (red thick dotted curves) and numerical simulations for ferrofluid spin-up velocity profiles in a non-uniform 300 Hz rotating magnetic field (black thin solid curves) for MSG W11 water-based ferrofluid. The numerical plots were generated using the fit values for τ and η in Table 9-1. 209

Figure 9-9 Comparison of experimentally measured (red thick dotted curves) and numerical simulations for ferrofluid spin-up velocity profiles in a non-uniform 400 Hz rotating magnetic field (black thin solid curves) for MSG W11 water-based ferrofluid. The numerical plots were generated using the fit values for τ and η in Table 9-1. 209

Figure 9-10 Comparison of experimentally measured (red thick dotted curves) and numerical simulations for ferrofluid spin-up velocity profiles in a non-uniform 500 Hz rotating magnetic field (black thin solid curves) for

| | |
|--|-----|
| MSG W11 water-based ferrofluid. The numerical plots were generated using the fit values for τ and η in Table 9-1. | 210 |
| Figure 9-11 Comparison of the experimental data (red thick dotted curve), numerical simulations with $\eta' = 0$ (dashed curve) and with $\eta' \neq 0$ (solid curve) for ferrofluid spin-up velocity profiles in a non-uniform 300 Hz rotating magnetic field with 6 A (rms) input current for MSG W11 water-based ferrofluid. | 210 |
| Figure 9-12 Numerical simulations with $\eta' = 0$ for MSG W11 water-based ferrofluid spin-up velocity profiles in a non-uniform 300 Hz rotating magnetic field with 6 A (rms) input current for various values of τ | 211 |
| Figure 9-13 Simulated flow and spin velocity of MSG W11 water-based ferrofluid in non-uniform rotating magnetic field with 300 Hz and 5 A rms input current to each winding of the 4 pole motor using $\tau = 20\mu s$ and $\eta' = 4 \times 10^{-9} Nm$ | 213 |
| Figure 9-14 Simulated real and imaginary parts of r component of the magnetic field \vec{H} of MSG W11 water-based ferrofluid in non-uniform rotating magnetic field with 300 Hz and 5 A rms input current to each winding of the 4 pole motor using $\tau = 20\mu s$ and $\eta' = 4 \times 10^{-9} Nm$ | 214 |
| Figure 9-15 Simulated real and imaginary parts of ϕ component of the magnetic field \vec{H} of MSG W11 water-based ferrofluid in non-uniform rotating magnetic field with 300 Hz and 5 A rms input current to each winding of the 4 pole motor using $\tau = 20\mu s$ and $\eta' = 4 \times 10^{-9} Nm$ | 215 |
| Figure 9-16 Simulated real and imaginary parts of r component of the magnetization \vec{M} of MSG W11 water-based ferrofluid in non-uniform rotating magnetic field with 300 Hz and 5 A rms input current to each winding of the 4 pole motor using $\tau = 20\mu s$ and $\eta' = 4 \times 10^{-9} Nm$ | 216 |
| Figure 9-17 Simulated real and imaginary parts of ϕ component of the magnetization \vec{M} of MSG W11 water-based ferrofluid in non-uniform rotating magnetic field with 300 Hz and 5 A rms input current to each winding of the 4 pole motor using $\tau = 20\mu s$ and $\eta' = 4 \times 10^{-9} Nm$ | 217 |
| Figure 9-18 Simulated r and ϕ components of the body force density \vec{F} of MSG W11 water-based ferrofluid in non-uniform rotating magnetic field | |

with 300 Hz and 5 A rms input current to each winding of the 4 pole motor
using $\tau = 20\mu s$ and $\eta' = 4 \times 10^{-9} Nm$ 218

Figure 9-19 Simulated z component of the volume torque density \bar{T} and the
body force density contribution $\bar{r} \times \bar{F}$ of MSG W11 water-based ferrofluid
in non-uniform rotating magnetic field with 300 Hz and 5 A rms input
current to each winding of the 4 pole motor using $\tau = 20\mu s$ and
 $\eta' = 4 \times 10^{-9} Nm$ 219

Figure 9-20 Torque simulations with MSG W11 ferrofluid just inside the spindle
in a uniform rotating magnetic field at 100, 200, 300, 400 and 500 Hz with
 $\eta' = 1.66 \times 10^{-9} [N \cdot s]$ and $\tau = 3 \times 10^{-5} [s]$ by the surface integral and volume
integral methods of section 9.1. 220

Figure 9-21 Comparison of experimentally measured (cross mark) and
numerically calculated (circle and plus marks) torque with MSG W11
ferrofluid just inside the spindle in a uniform rotating magnetic field at 100,
200, 300, 400 and 500 Hz. Simulation uses the value of $\eta' = 1.66 \times 10^{-9}$
 $[N \cdot s]$ and $\tau = 3 \times 10^{-5} [s]$ 221

Figure 9-22 Torque simulations with MSG W11 ferrofluid just inside the spindle
in a non-uniform rotating magnetic field at 100, 200, 300, 400 and 500 Hz
with $\eta' = 1.66 \times 10^{-9} [N \cdot s]$ and $\tau = 8 \times 10^{-6} [s]$ by the surface integral and
volume integral methods of section 9.1. 223

Figure 9-23 Comparison of experimentally measured (cross mark) and
numerically calculated (circle and plus marks) torques with MSG W11
ferrofluid just inside the spindle in a non-uniform rotating magnetic field at
100, 200, 300, 400 and 500 Hz. Simulations use the values of $\eta' =$
 $1.66 \times 10^{-9} [N \cdot s]$ and $\tau = 8 \times 10^{-6} [s]$ 224

Figure 9-24 Comparison of experimentally measured (cross marks) and
numerically calculated (plus marks) torque with MSG W11 ferrofluid
outside the spindle in a uniform rotating magnetic field at 100, 200, 300,
400 and 500 Hz. Simulations use the value of $\eta' = 1.66 \times 10^{-9} [N \cdot s]$ and $\tau =$
 $2.5 \times 10^{-5} [s]$ 226

Figure 9-25 Comparison of experimentally measured (cross mark) and
numerically calculated (plus mark) torque with MSG W11 ferrofluid outside
the spindle in a non-uniform rotating magnetic field at 100, 200, 300, 400
and 500 Hz. Simulations use the value of $\eta' = 1.66 \times 10^{-9} [N \cdot s]$ and $\tau =$
 $1.6 \times 10^{-5} [s]$ 228

List of Tables

Table 2-1: Physical properties of ferrofluids and non-magnetic fluids at 18 °c.
 The mass densities were calculated by using the mass measured with an Acculab VI-3mg micro-scale and the volume measured by a VWR 89000-396 5 ml graduated container. The surface tensions were measured using a K10ST Krüss Tensionmeter. The viscosities were measured using a CSL500 rheometer from TA instruments configured in a Couette cell geometry. The viscosities were determined by performing a controlled shear rate sweep. 33

Table 2-2 Magnetic properties of water-based and oil-based ferrofluids. An ADE Technologies Model 880 Digital Measurement System (DMS) vibrating sample magnetometer (VSM) was used to measure the magnetization curve for each sample..... 41

Table 2-3 Calculated Brownian, Néel and effective relaxation time constants of water-based ferrofluids and oil based ferrofluid. The nanoparticle sizes used in relaxation time constant calculations were obtained from the VSM and TEM estimated particle diameter range from Table 2-2. 44

Table 2-4 Speed of sound measurements for water-based ferrofluids, oil-based ferrofluid, and non-magnetic fluids at a temperature of 18° Celsius. The results of two different methods of measuring the speed of sound agree to within less than 4%. The value of the speed of sound in water at 18° Celsius is 1482 m/s[37] as reported in the literature which exceeds our measured velocity by less than 1.4%..... 51

Table 3-1 Physical and flow properties for water-based and oil-based ferrofluids used for planar Couette flow..... 61

Table 3-2 Physical and flow properties for water-based and oil-based ferrofluids used for Taylor-Couette flow measurements. 62

Table 3-3 Physical properties and skin depths at $f = 500$ Hz for water, water-based and oil-based ferrofluids used in experiments. 63

Table 6-1 Peak measured viscometer torques ($\mu\text{N}\cdot\text{m}$) /gauss in a uniform rotating magnetic field 141

Table 7-1 Peak measured spindle torque ($\mu\text{N}\cdot\text{m}$) per Gauss in a non-uniform rotating magnetic field. The peak field at the radius of 58 mm of the 4 pole motor stator winding is 47.65 Gauss (peak/rms) per Ampere (peak/rms). 153

Table 8-1 Acoustic impedance of ferrofluids and non-magnetic materials. *: The values of air and polycarbonate are quoted from DOP2000 Model 2125/2032 User's manual, Signal Processing S.A., Switzerland, section 22. †: The acoustic impedances $Z=pc$ are estimated using the values of density and speed of sound from Table 2-1 and 157

| | |
|---|-----|
| Table 9-1 Best fit values of τ and η' for different applied non-uniform magnetic field strengths using the 4 pole motor stator winding for MSG W11 water-based ferrofluid. | 207 |
| Table 9-2 Numerical simulation of maximum velocity position with $\eta' = 0$ for MSG W11 water-based ferrofluid spin-up velocity profiles in a non-uniform 300 Hz rotating magnetic field with 6 A (rms) input current for various values of τ . The percentage value of r_{\max}/R is given using $R = 0.047$ mm for the plastic inner radius. | 211 |

Chapter 1. Introduction to Ferrofluids

1.1 Background and Research Motivations

Ferrofluids [1] are suspensions of permanently magnetized colloidal particles immersed in a suitably chosen carrier fluid. In the presence of time-varying magnetic fields, ferrofluid particles will rotate in order to align their magnetic dipole moment with the applied field, but because of the fluid viscosity, the magnetization \vec{M} will lag behind the time-varying magnetic field \vec{H} . With \vec{M} not parallel to \vec{H} , there is a body-torque on the ferrofluid with volume density, given by $\mu_0 \vec{M} \times \vec{H}$ (with $\mu_0 = 4\pi \times 10^{-7}$ Henries/m the magnetic permeability of free space), which can drive fluid flow. At the same time, there is a body-force on the ferrofluid given by $\mu_0 (\vec{M} \cdot \nabla) \vec{H}$, which is non-zero in a non-uniform magnetic field which can also drive the fluid flow. In this thesis, research focuses on the theory, measurement and applications of the magnetization dynamics and the effects of magnetic force and torque densities on ferrofluid flow in uniform and non-uniform rotating magnetic fields.

Ferrofluids are stable colloidal suspensions of permanently magnetized nanoparticles in a carrier liquid like water or oil. Each particle is typically made from magnetite (Fe_3O_4) coated with a monolayer of surfactant to prevent the particles from agglomerating under van der Waals attraction forces.

Furthermore, the ~10 nanometer particle diameter is small enough to ensure that the particles remain dispersed by Brownian motion and do not agglomerate under gravity and magnetic interactions. Ferrofluids are therefore stable suspensions that exhibit superparamagnetic susceptibilities with suspended magnetic particles constituting typically up to 10% of the total fluid volume.

Ferrofluids are a scientifically and commercially important realization of magnetically polarizable systems. As such, they are characterized by the presence and effect of long-range body-couples and non-symmetric viscous stresses, as well as more exotic phenomena, such as couple stresses representing the direct-contact transport of microstructure angular momentum. Due to their physical, chemical and magnetic properties, ferrofluids are of increasing interest in the design of magneto-responsive colloidal extractants [2-4], microfluidic pumps and actuators driven by alternating or rotating magnetic fields [5-9] , and in biological applications such as drug delivery vectors, magnetic cell sorting schemes, and magnetocytolysis treatment of localized tumors [10, 11].

The phenomenon of spin-up flow of ferrofluid has received considerable attention [12-17] during the early development of the field of ferrohydrodynamics. Experiments were carried out by placing a sample of ferrofluid in a cylindrical container subjected to a rotating magnetic field. Regardless of the field source used, the basic observations are the same. In a stationary cylindrical container, the ferrofluid is observed to rotate rigid-body-like in a direction which depends on the applied magnetic field amplitude and frequency. Such essentially rigid-body motion is observed at the free surface of the fluid throughout the inner core of fluid and extends right up to a thin boundary layer next to the stationary cylindrical vessel wall.

The general observation in the literature is that the ferrofluid and magnetic field rotate in opposite directions. However, some authors [13-15] report observations where the ferrofluid switches between co-rotation and counter-rotation with respect to the applied magnetic field depending on magnetic field amplitude and frequency. Explicitly, [14] reports co-rotation of field and fluid for low applied fields and counter-rotation for high applied magnetic fields, whereas [13] and [15] observe counter-rotation for low applied magnetic fields and co-rotation for higher applied fields. We have made similar

observations in our laboratory, where a water-based ferrofluid placed in a cylindrical container and subjected to the uniform rotating magnetic field generated by a three-phase two-pole rotating magnetic machine stator is observed to co-rotate with the applied magnetic field for low stator winding current amplitude and counter-rotate with respect to the magnetic field for higher stator winding current amplitudes.

The confusion regarding field and fluid rotation sense, and the applicability of various theoretical analyses [18-22], is compounded when one considers that all available observations are made at the free-surface of the opaque ferrofluid using various types of tracer particles on the surface. Some magnetic fluids were even not true ferrofluids because the particles were too large. It is clear that this will be problematic and probably not representative of the bulk-flow situation when one considers that curvature-driven flows have been observed at ferrofluid free surfaces [17]. Thus, there remains a need for accurate, direct measurements of bulk-flow related quantities to explain these conflicting reports. Such measurable quantities explained in this thesis are the total torque required to restrain a stationary hollow cylinder containing ferrofluid and spin-up velocity profile in rotating magnetic field.

Observations of counter-rotation of field and fluid led [13] to investigate the direction in which the cylindrical container would rotate if it could freely do so. This represents an indirect measurement of the magnetic torque applied on the ferrofluid. One would expect the counter-rotating fluid to drag the cylindrical container with it, but experiments show the container co-rotating with the field whereas the fluid counter-rotates. Such observations have since been corroborated by [14] and [17]. However, all these observations are of a qualitative nature, not having directly measured the actual torque required to restrain the container. Hence, the motivation of our contribution – to obtain direct quantitative measurements of the torque required to restrain the

cylindrical container during spin-up flow of a ferrofluid and to directly measure the bulk flow of ferrofluid in uniform and non-uniform rotating magnetic fields.

There are a number of ways in which magnetic nanoparticles can be used for biomedical applications [43-46]: a) Magnetic nanoparticles can bind to drugs, proteins, enzymes, antibodies, or organisms; b) Magnetic nanoparticles can be directed to organs, tissues, or tumors using an external magnet for therapeutic effect; and c) Dissipation in alternating and rotating magnetic fields can cause heating of magnetic nanoparticles for use in hyperthermia. These applications require better understanding of ferrohydrodynamics.

The theory of the magnetic susceptibility tensor can help to understand the magnetic permeability change and the power dissipation in ferrofluids, which can be applied to bio-imaging applications such as Magnetic Resonance Imaging (MRI) and to hyperthermia treatments.

1.2 Scope of the Thesis

Chapter 2 presents a summary of some useful magnetic, rheological and physical properties of the ferrofluids used in experiments and computer simulations as well as a brief description of the experimental techniques used to measure these properties.

Chapter 3 describes the system of governing ferrohydrodynamic equations that are solved in this thesis.

Chapter 4 describes the magnetoeffective viscosity of ferrofluid planar Couette and Poiseuille flows. Analysis shows the different behavior of ferrofluid under uniform magnetic field intensity \bar{H} (current driven) and magnetic flux density \bar{B} (flux driven) on planar Couette flow and on planar Poiseuille flow.

Chapter 5 describes some bio-medical applications of ferrofluid which can be analyzed by the complex magnetic susceptibility tensor that is derived in this chapter from the magnetic relaxation equation. The real and imaginary parts of the complex magnetic susceptibility tensor represent the energy storage and dissipation in the ferrofluid. Applications to magnetic resonance imaging, hyperthermia, and other biomedical applications are discussed. Impedance measurements in this chapter show a change of magnetic susceptibility in a uniform rotating magnetic field.

Chapter 6 presents torque experiments of ferrofluid in a uniform rotating magnetic field using a Couette viscometer. The measurements are taken for 3 cases: ferrofluid inside a spindle, ferrofluid outside a spindle, and ferrofluid simultaneously inside and outside a spindle. This experimental data proves that the magnetization \bar{M} is not parallel to the magnetic field \bar{H} , which drives the flow by a volume torque density term $\mu_0 \bar{M} \times \bar{H}$. The rotating magnetic field setups are described in Appendix A

Chapter 7 presents viscometer torque experiments of ferrofluid in a non-uniform rotating magnetic field. Experimental measurements show a stronger effect in a non-uniform rotating magnetic field than in a uniform rotating magnetic field, which is due to the non-zero body force density term $\mu_0 (\bar{M} \cdot \nabla) \bar{H}$ in the non-uniform rotating magnetic field.

Chapter 8 presents spin-up velocity profile measurements of ferrofluid in uniform and non-uniform rotating magnetic fields. Experimental data also shows a stronger effect from the non-uniform rotating magnetic field. The strength of the magnetic field at the container wall is maximum for a non-uniform rotating magnetic field. This causes the velocity profile to be near

maximum close to the container wall and forms an essentially rigid body motion velocity profile in a non-uniform rotating magnetic field.

Chapter 9 uses FEMLAB software to compare the predictions of an iterative finite element numerical simulation with the experimentally measured torque and spin-up flows in Chapters 6-8, in order to determine best fit values of magnetization relaxation time and ferrofluid spin viscosity. Fitting the simulation with the experimental data of spin-up velocity profiles in the non-uniform rotating magnetic field shows that the spin viscosity, η' , has a non-zero value in the range of $\sim 1-11.8 \times 10^{-9}$ [N·s]. The value of relaxation time $\tau \approx 1.3-30$ [μ s] and was determined by fitting the torque experimental data with the simulation.

Chapter 10 summarizes the accomplishments and contributions of this thesis and also lists some interesting topics for future research.

Chapter 2. Physical and Magnetic Properties of Ferrofluids

Three types of commercial ferrofluids were obtained from Ferrotec Corporation, (Nashua, NH): water-based ferrofluids MSGW11 and EMG705 and an oil-based ferrofluid EFH1. Physical properties of these ferrofluids were measured because of a lack of literature values: the mass density ρ [kg/m^3], viscosity η [$N\cdot s/m^2$], and surface tension γ [N/m]. For comparison, the physical properties of non-magnetic fluids are also measured: de-ionized (DI) water and Nytro, a commercial transformer oil. The magnetization curves of these ferrofluids were measured by using an ADE Technologies Digital Measurement Systems (DMS) Vibrating Sample Magnetometer (VSM). From the magnetization curves the saturation magnetization $\mu_0 M_s$ [*Tesla*], volume fraction of magnetic particles ϕ , magnetic susceptibility χ , magnetic particle diameter d , and magnetic Brownian, Néel and effective relaxation time constants ($\tau_B, \tau_N, \tau_{eff}$ [s]) were determined. The particle size and distribution of these ferrofluids were also measured using Transmission Electron Microscopy (TEM). The speed of sound in the ferrofluids and other non-magnetic fluids were measured by an Ultrasonic Velocity Profiler (UVP) in order to calibrate ultrasound velocity measurements.

2.1 Physical Properties

2.1.1 Mass Density

The measured room temperature mass densities of each of the sample ferrofluids used in our work and other non-magnetic fluids are listed in Table

2-1. All the mass density values we report are within the range given in Ferrotec Corporation's data sheets.

2.1.2 Surface Tension

The coefficient of surface tension is a measure of the force necessary to hold a fluid interface together. The surface tension values listed in Table 2-1 were obtained by using a K10ST Krüss Tensionmeter. This apparatus first dips a small metal plate slightly below the surface of the fluid sample and records the force required to pull the plate out, which determines the surface tension value.

2.1.3 Viscosity

The viscosity values listed in Table 2-1 were obtained using a CSL500 rheometer from TA instruments configured in a Couette cell geometry. The rheometer performs a controlled shear rate sweep to determine the viscosity of the suspension. Because ferrofluids act like Newtonian fluids if no magnetic fields are applied, the resulting shear-strain to shear-rate profile is a straight line with constant slope. The ratio of the shear-strain to the shear-rate given by the slope of the measured profile is the viscosity of the fluid. In Table 2-1 we note that the EFH1 oil-based ferrofluid has a viscosity of 7.27 cP (0.00727 Ns/m²), which is about 3.6 times as viscous as the MSG W11 water-based ferrofluid and 2.9 times as viscous as the EMG705 water-based ferrofluid.

Table 2-1: Physical properties of ferrofluids and non-magnetic fluids at 18 °C. The mass densities were calculated by using the mass measured with an Acculab VI-3mg micro-scale and the volume measured by a VWR 89000-396 5 ml graduated container. The surface tensions were measured using a K10ST Krüss Tensionmeter. The viscosities were measured using a CSL500 rheometer from TA instruments configured in a Couette cell geometry. The viscosities were determined by performing a controlled shear rate sweep.

| Material | ρ , [kg/m ³] | γ , [mN/m] | η , [Ns/m ²] |
|----------------------|-------------------------------|-------------------|-------------------------------|
| DI-water | 998 | 71.9 | 0.00101 |
| Nyro Transformer Oil | 890 | 23.4 | 0.01026 |
| EMG705 (water-base) | 1194 | 42.1 | 0.00248 |
| MSG W11 (water-base) | 1200 | 39.1 | 0.00202 |
| EFH1 (oil-based) | 1221 | 24.8 | 0.00727 |

2.2 Magnetization Characteristics

In determining the magnetic properties of a ferrofluid, it is important to differentiate between the externally applied field and the field inside the ferrofluid. The difference between the external magnetic field H_e and the internal magnetic field H_i is described by the demagnetization factor, D , given by

$$H_i = H_e - MD \quad (2.1)$$

The demagnetization field arises due to effective magnetic charge induced on the surface of a magnetic material, with magnetization M , which partially cancels the externally applied magnetic field. For the internal magnetic field to be uniform for a uniform external magnetic field within the ferrofluid sample, the ferrofluid container shape must be an ellipsoid of revolution such as a

sphere, infinitely long cylinder or a prolate or oblate spheroid. However, for other non-ellipsoidal containers, such as the finite length cylinder used in our measurements, (2.1) is approximately true.

Magnetization curves of the ferrofluids were measured using an ADE Technologies Model 880 Digital Measurement Systems (DMS) Vibrating Sample Magnetometer. Ferrofluid samples were placed in the DMS plastic sample containers of interior height ≈ 3 mm , diameter ≈ 5.7 mm and volume ≈ 0.076 ml, whose dimensions approximate those of an oblate spheroid with major to minor axis ratio of $n = 2.4$. The demagnetizing factor D corresponding to an oblate spheroid is [87]

$$D = \frac{1}{2} \left[\frac{n^2}{(n^2 - 1)^{3/2}} \arcsin \frac{\sqrt{n^2 - 1}}{n} - \frac{1}{n^2 - 1} \right]. \quad (2.2)$$

Using (2.2) and $n = 2.4$ we obtain a demagnetization factor of $D = 0.211$. This value and (2.1) were used to calculate the internal magnetic field used in the abscissa of the magnetization curves shown in Figure 2-1, Figure 2-2 and Figure 2-3. All VSM data were taken at room temperature, $T = 299$ K with sample volume $V \approx 0.073$ ml. EMG705 has a saturation magnetization of 206 Gauss and the sample volume is approximately 0.073 ml; MSG W11 has a saturation magnetization of 154 Gauss and the sample volume is approximately 0.073 ml; EFH1 has a saturation magnetization of 421 Gauss and the sample volume is approximately 0.071 ml. The approximate saturation magnetization and sample volume are given at the top of Figure 2-1 to Figure 2-3.

The vibrating sample magnetometer measures the sample magnetization in emu (electromagnetic units). The magnetization $\mu_0 \bar{M}$ in units of Gauss (10^{-4}

Tesla) is related to emu as $Gauss = \frac{emu}{4\pi V(ml)}$, where V [ml] is the ferrofluid

sample volume in units of milliliters and is given at the top of Figure 2-1 to Figure 2-3.

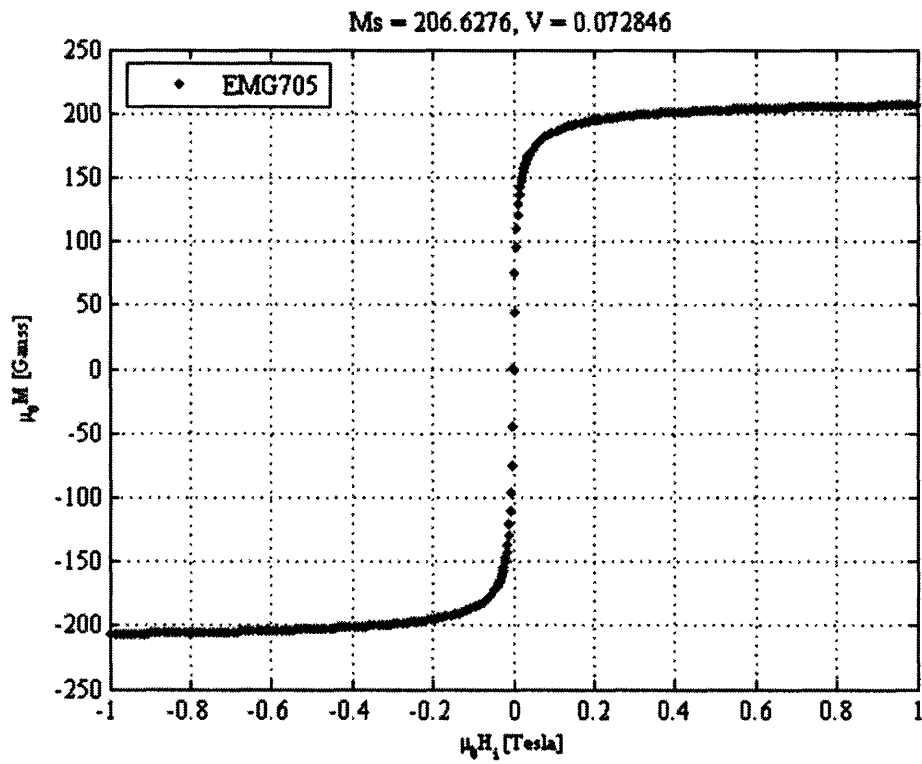


Figure 2-1 Measured magnetization curve for EMG705 water-based ferrofluid

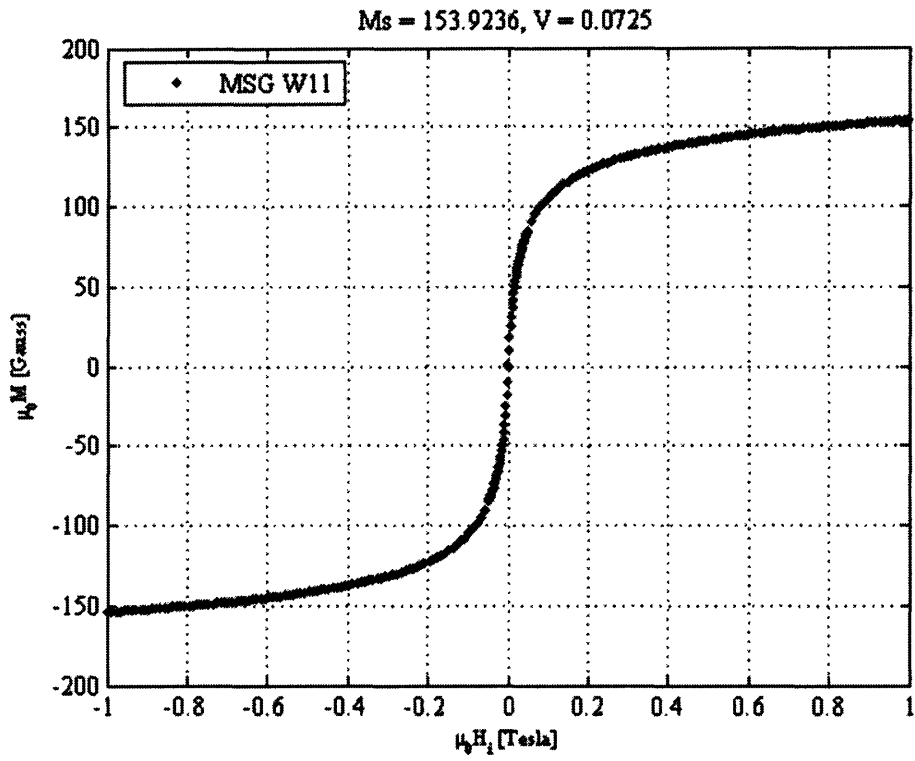


Figure 2-2 Measured magnetization curve for MSG W11 water-based ferrofluid

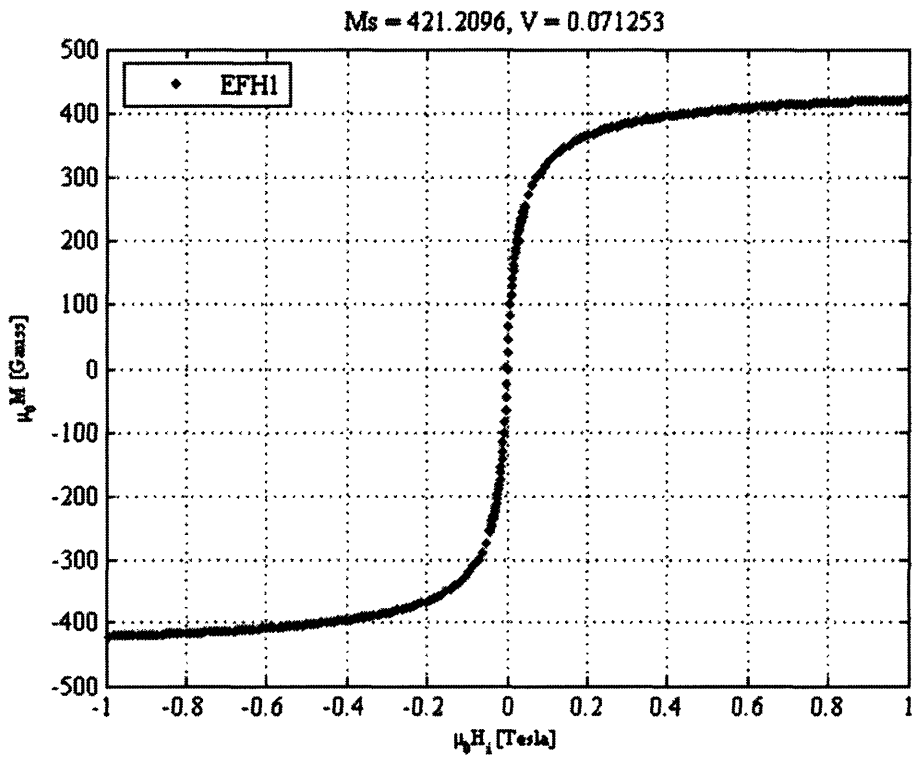


Figure 2-3 Measured magnetization curve for EFH1 oil-based ferrofluid

In our magnetization experiments the externally applied field H_e increases until the saturation magnetization M_s is reached. The same field magnitudes are also applied in the opposite direction to demonstrate that ferrofluids in a DC magnetic field do not exhibit hysteresis. This is a result of the random reorientation of the free magnetic particles in the carrier fluid, removing any memory from the fluid that would contribute to hysteresis.

The saturation magnetization of each ferrofluid was assumed to equal the magnetization value at the largest applied internal magnetic field. The volume fraction of each ferrofluid was calculated from

$$\phi = \frac{M_s}{M_d}, \quad (2.3)$$

where M_d is the domain magnetization (446 kA/m for magnetite or $\mu_0 M_d = 5602 \text{ [Gauss]} = 0.5602 \text{ [Tesla]}$).

In order to determine the initial magnetic susceptibility, the slope of the low-field linear region was also determined. The Langevin curves in Figure 2-1, Figure 2-2 and Figure 2-3 do not have enough precision in the low-field region to accurately determine the slope. For this reason, the low-field linear regions were separately measured for the water-based ferrofluids and the oil-based ferrofluid and are shown in Figure 2-4, Figure 2-5 and Figure 2-6. The slopes, corresponding to the magnetic susceptibilities χ , were determined through a simple linear least squares fit of the linear region data.

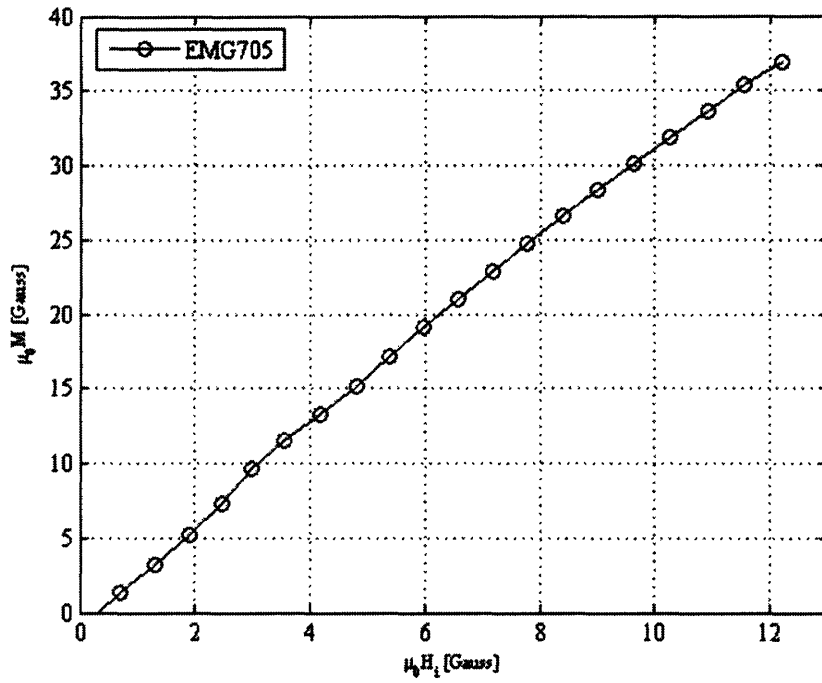


Figure 2-4 Measured magnetization linear region for EMG705 water-based ferrofluid, $\chi \approx 3.14$.

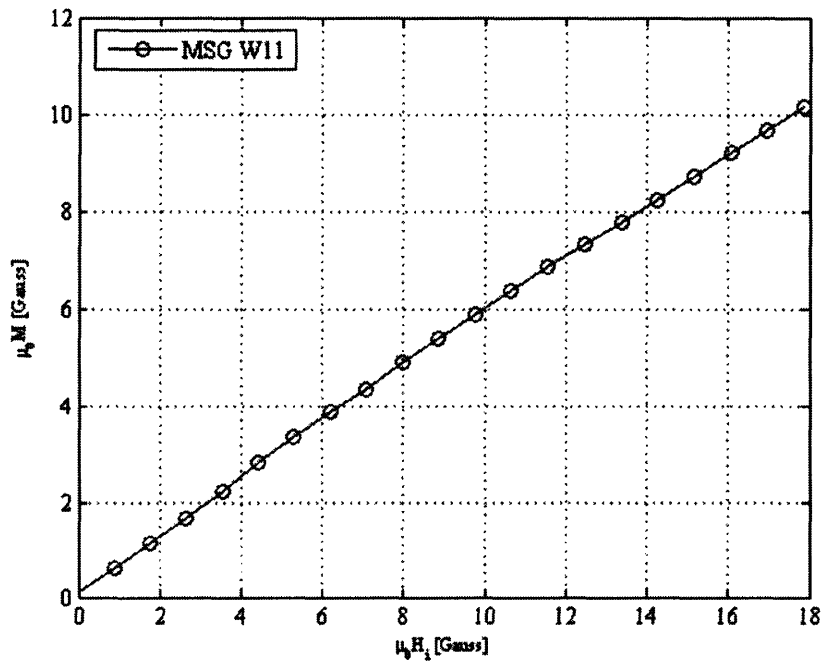


Figure 2-5 Measured magnetization linear region for MSG W11 water-based ferrofluid, $\chi \approx 0.56$.

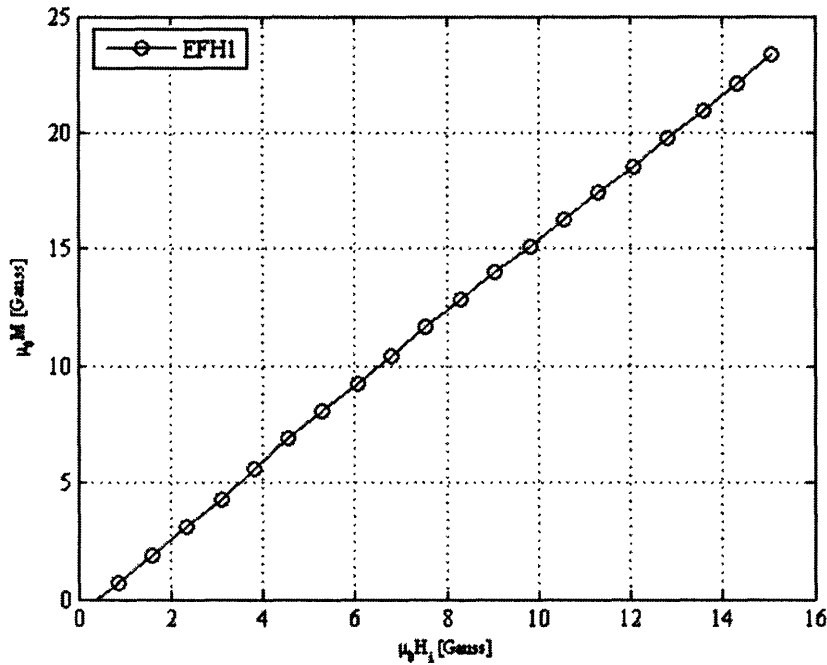


Figure 2-6 Measured magnetization linear region for EFH1 oil-based ferrofluid, $\chi \approx 1.59$.

2.3 Magnetic Particle Size

For a monodisperse ferrofluid the Langevin equation describes the equilibrium magnetization for a given applied magnetic field [1]:

$$\frac{M}{M_s} = L(\alpha) = \coth \alpha - \frac{1}{\alpha}, \quad (2.4)$$

where $\alpha = M_d V_p \mu_0 H / kT$, M_d is the domain magnetization, H is the magnetic field within the particle, V_p is the magnetic core volume per particle, T is the absolute temperature in Kelvin, and $k = 1.38 \times 10^{-23}$ J/K is Boltzmann's constant. Using this expression, and the data contained in Figure 2-1 and Figure 2-4, the minimum and maximum particle-size diameters for EMG705 water-based ferrofluid was estimated. The minimum and maximum particle-size diameters for MSG W11 water-based ferrofluid and EFH1

oil-based ferrofluid were also estimated using the data contained in the saturation and linear regions of the magnetization curves.

Assuming the particles were spheres of diameter d , the minimum particle diameters for ferrofluids were estimated by fitting the saturation data of Figure 2-1, Figure 2-2 and Figure 2-3 to the Langevin curve high-field asymptote:

$$\lim_{\alpha \gg 1} L(\alpha) \approx \left(1 - \frac{1}{\alpha}\right) = \left(1 - \frac{6}{\pi} \frac{kT}{\mu_o M_d H d^3}\right), \quad (2.5)$$

The maximum particle diameters for the water-based ferrofluids and oil-based ferrofluid were obtained by using the low-field limit of the Langevin curve:

$$\lim_{\alpha \ll 1} L(\alpha) \approx \frac{\alpha}{3} = \frac{\pi}{18} \frac{\mu_o M_d H d^3}{kT} = \frac{\chi H}{M_s}, \quad (2.6)$$

and the values of the initial susceptibilities, $\chi = M / H$, were obtained from the slopes of Figure 2-4, Figure 2-5 and Figure 2-6.

For suspensions that are non-dilute with respect to the magnetic cores ($\phi \geq 10\%$), Shliomis has proposed a correction to equation (2.6) to account for the effect of dipole-dipole interactions

$$\frac{\chi(2\chi+3)}{\chi+1} = \frac{\pi}{6} \phi \frac{\mu_o M_d^2 d^3}{kT}. \quad (2.7)$$

For higher magnetic volume fraction ferrofluids, (2.7), rather than (2.6), should be used to estimate the largest particle diameter.

The resulting particle diameter ranges thus obtained are summarized in Table 2-2. Note that these diameters are only estimates. More accurate measurements were obtained using a JEOL 2011 Transmission Electron Microscope (TEM), also listed in Table 2-2.

Table 2-2 Magnetic properties of water-based and oil-based ferrofluids. An ADE Technologies Model 880 Digital Measurement System (DMS) vibrating sample magnetometer (VSM) was used to measure the magnetization curve for each sample.

| Ferrofluid | Saturation magnetization $\mu_0 M_s$, [Gauss] | Magnetic susceptibility χ | Volume fraction, [%] $\phi = \frac{\mu_0 M_s}{\mu_0 M_d}$ | Estimated particle diameter (VSM), [nm] | Particle diameter (TEM), [nm] |
|--------------------------|---|-----------------------------------|--|---|---------------------------------|
| EMG705 (water-based) | 206.6 | 3.14 | 3.69 | 7.9-16.9 | 4.8-19.5 mean: 15.6±5.3(StD) |
| MSG W11 (water-based) | 153.9 | 0.56 | 2.75 | 5.5-12.4 | 6.3-27.6 mean: 9.4±3.4(StD) |
| EFH1 (oil-based) | 421.2 | 1.59 | 7.52 | 6.9-13.3 | * |

*** The particle diameter value for EFH1 oil-based ferrofluid is absent because the uncontaminated TEM images were unavailable due to incomplete evaporation of the oil-based ferrofluid, which causes an unsuccessful deposit of the oil-based ferrofluid particles on the copper sample holder.**

2.4 Relaxation Times

In studying the dynamics of ferrofluids in time-varying magnetic fields, one must consider how the local magnetization changes, or “relaxes,” due to fluid convection, particle rotation, and applied fields. The simplest relaxation equation for an incompressible, magnetically linear ferrofluid undergoing simultaneous magnetization and reorientation due to fluid convection at flow velocity \bar{v} and spin angular velocity $\bar{\omega}$ is Shliomis' first magnetization equation [25]:

$$\frac{\partial \bar{M}}{\partial t} + \bar{v} \cdot \nabla \bar{M} + \bar{M} \nabla \cdot \bar{v} - \bar{\omega} \times \bar{M} + \frac{1}{\tau_{eff}} [\bar{M} - \bar{M}_0] = 0, \quad (2.8)$$

where τ_{eff} is the effective relaxation time constant and \bar{M}_0 is the equilibrium magnetization generally given by the Langevin equation of (2.4). Equation (2.8) is applicable under conditions not far removed from magnetization equilibrium [26-28].

The two commonly accepted mechanisms by which ferrofluid magnetic particles relax are Brownian motion, resulting from collisions between the magnetic particles and the constituent molecules of the suspending medium, and Néel relaxation, resulting from rearrangement of the magnetic domains without rotation of the particle. The characteristic time describing Brownian motion is [1]

$$\tau_B = \frac{4\pi\eta_0 R^3}{kT}, \quad (2.9)$$

where η_0 is the shear viscosity of the suspending fluid, and $R = R_p + \delta$ is the hydrodynamic radius being the sum of the magnetic particle radius, R_p , and the surfactant layer thickness, δ . In estimating the Brownian relaxation time we assume the surfactant layer thickness is approximately $\delta = 2 \text{ nm}$ [4].

The Néel relaxation time is given as [1]

$$\tau_N = \tau_0 e^{\left(\frac{KV_p}{kT}\right)}, \quad (2.10)$$

where τ_0 is a characteristic time of the magnetic material (10^{-9} s for magnetite), V_p is the magnetic volume of the particle, and K is the anisotropy constant of the magnetic domains, which spans the range of about 23,000 to 100,000 Joule/m³ for magnetite and depends on the size of particle. K increases as particle size decreases and here we use a representative value of $K = 78,000$ Joules/m³ for 12.6 nm diameter magnetic nanoparticles [23].

These two relaxation processes occur in parallel and the shortest time constant dominates the effective relaxation time constant. Therefore, the effective time constant describing magnetic particle relaxation is given by [1]

$$\frac{1}{\tau_{eff}} = \frac{1}{\tau_B} + \frac{1}{\tau_N} \Rightarrow \tau_{eff} = \frac{\tau_B \tau_N}{\tau_B + \tau_N}. \quad (2.11)$$

The resulting Brownian, Néel, and effective relaxation times thus obtained are summarized in Table 2-3. The calculated effective relaxation times have a wide range because of the strong dependence on particle diameter and ferrofluid particles have a wide distribution of size as given in Table 2-2. Direct experimental determination of these relaxation times would be preferable and should be the subject of future work.

Table 2-3 Calculated Brownian, Néel and effective relaxation time constants of water-based ferrofluids and oil based ferrofluid. The nanoparticle sizes used in relaxation time constant calculations were obtained from the VSM and TEM estimated particle diameter range from Table 2-2.

| Ferrofluid | τ_B , [μs] | τ_N , [s] | τ_{eff} , [μs] |
|--------------------------|------------------------------|---|----------------------------------|
| EMG705 (water-based) | 7.59-8.59 (VSM) | 1.30×10^{-7} - 4.78×10^{11} (VSM) | 0.12-8.59 (VSM) |
| | 0.64-12.2 (TEM) | 2.98×10^{-9} - 5.85×10^{22} (TEM) | 0.0030-12.2 (TEM) |
| MSG W11 (water-based) | 0.66-3.38 (VSM) | 5.16×10^{-9} -0.147 (VSM) | 0.0051-3.38 (VSM) |
| | 0.84-24.2 (TEM) | 1.18×10^{-8} - 1.19×10^{81} (TEM) | 0.012-24.2 (TEM) |
| EFH1 (oil-based) | 3.57-14.28 (VSM) | 2.56×10^{-8} -12.0 (VSM) | 0.025-14.3 (VSM) |

2.5 Transmission Electron Microscope Measurements

The Transmission Electron Microscope (TEM) measurements were taken using a JEOL 2011 high contrast digital TEM, which can perform TEM scans from nanometers to microns. The TEM images for water-based ferrofluids are shown in Figure 2-7 and Figure 2-8. The particle sizes listed in Table 2-2 were obtained by image processing of Figure 2-7 and Figure 2-8. All the clear particle images were selected from the TEM images to determine particle size distributions. Table 2-2 shows that EMG705 water-based ferrofluid has a mean particle diameter of 9.4 nm with standard deviation of ± 3.4 nm. MSG W11 water-based ferrofluid has a mean particle diameter of 15.6 nm with standard deviation of ± 5.3 nm. The particle diameter values for EFH1 oil-based ferrofluid are absent because the uncontaminated TEM images were unavailable due to incomplete evaporation of the oil-based ferrofluid, which causes an unsuccessful deposit of the oil-based ferrofluid particle on the copper sample holder.

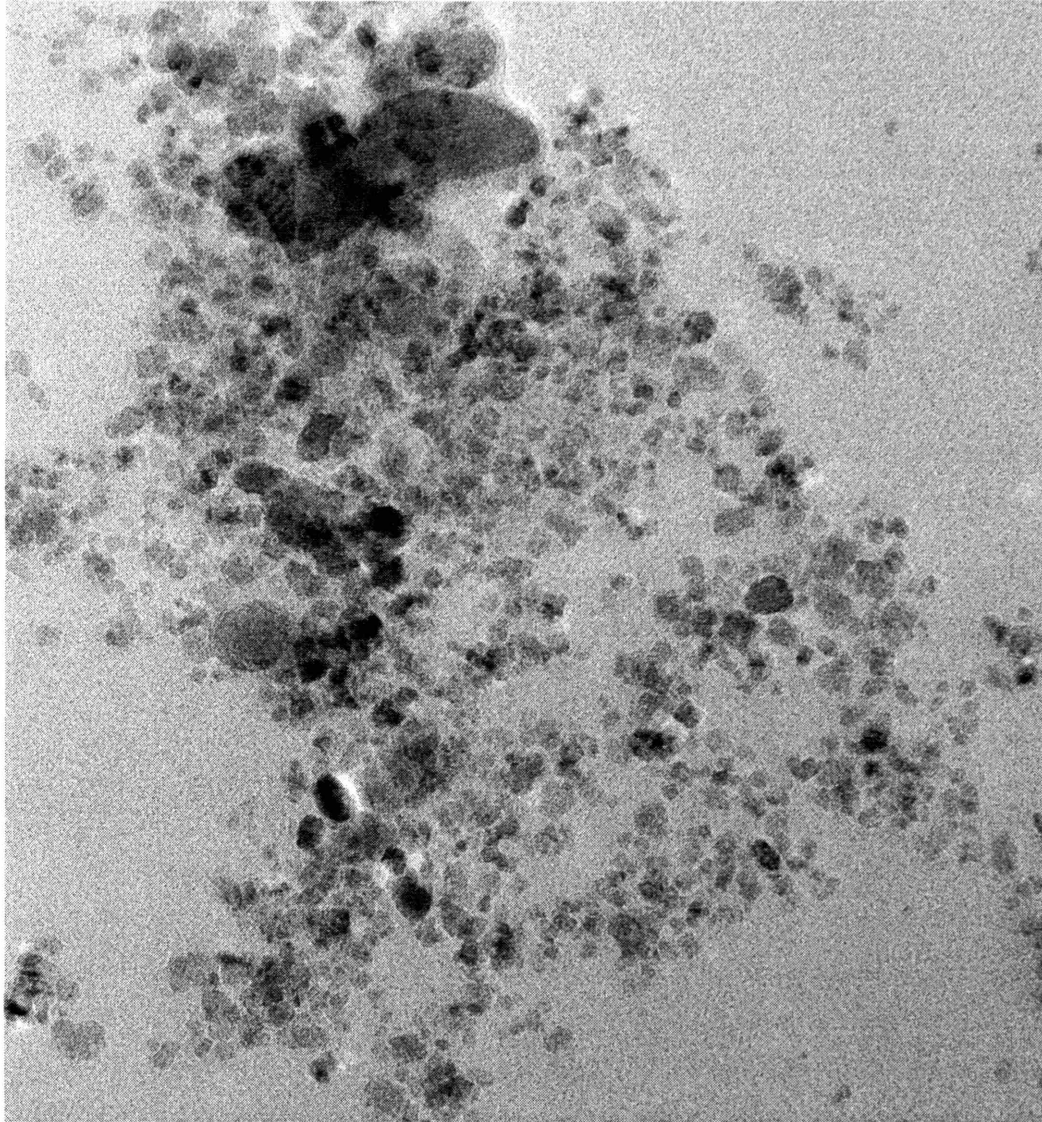
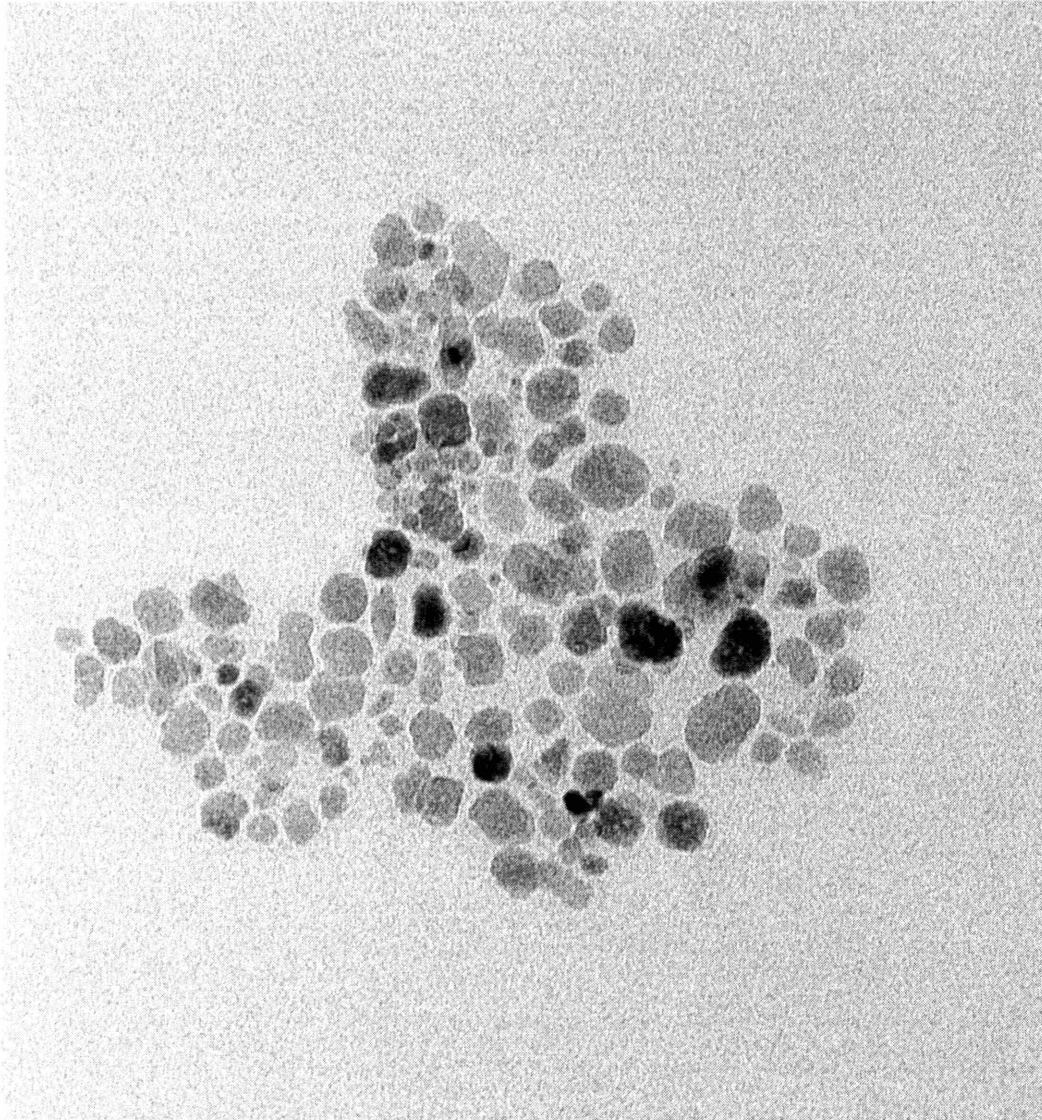


Image4.tif
Print Mag: 221000x @ 7. in
10:20 11/23/05

100 nm
Direct Mag: 50000x
CMSE E. M. FACILITY

Figure 2-7 Transmission Electron Microscope image of EMG705 water-based ferrofluid (50,000 magnification). The magnetic nanoparticles have a mean diameter of 9.4 nm and a standard deviation of ± 3.4 nm.



pic3.tif
Print Mag: 468000x @ 7. in
15:24 10/27/05

20 nm
Direct Mag: 60000x
CMSE E. M. FACILITY

Figure 2-8 Transmission Electron Microscope image of MSG W11 water-based ferrofluid (60,000 magnification). The magnetic nanoparticles have a mean diameter of 15.6 nm and a standard deviation of ± 5.3 nm.

2.6 Speed of Sound Measurements

The speed of sound for the ferrofluid samples are an essential property for the spin-up velocity profile measurements in chapter 9 using an ultrasound velocimeter. The speed of sound measurements of water-based ferrofluids, oil-based ferrofluid and other non-magnetic fluids such as deionized (DI) water and a commercial transformer oil for reference were taken with two different methods by using a Signal Processing Corporation's DOP 2000 pulsed Doppler ultrasound velocimeter. All the speed of sound measurements were taken in a fluid sample container provided by Signal Processing Corporation specifically designed for measuring the speed of sound in fluids. As shown in Figure 2-9, the cylindrical chamber holds a calibrated micrometer and an insertable ultrasound probe at diametrically opposite ends on the perimeter. The distance between the ends of the ultrasound probe and the micrometer was precisely controlled by the micrometer.

The signal processing method suggested by Signal Processing Corporation measures the differential change of the ultrasound echo correlation signal due to a known incremental change in the distance between the face of the ultrasound probe and the reflecting face of the micrometer. The ratio between the nominal change in round-trip distance and actual change in distance leads to an estimate of the speed of sound of the fluid sample in the container chamber. However, the results of speed of sound from the Signal Processing method were not repeatable enough to inspire trust without corroboration from an independent experiment. While the technique usually yields reasonable results, a small error or disturbance in turning the micrometer can lead to non-physically high measured speeds of sound.

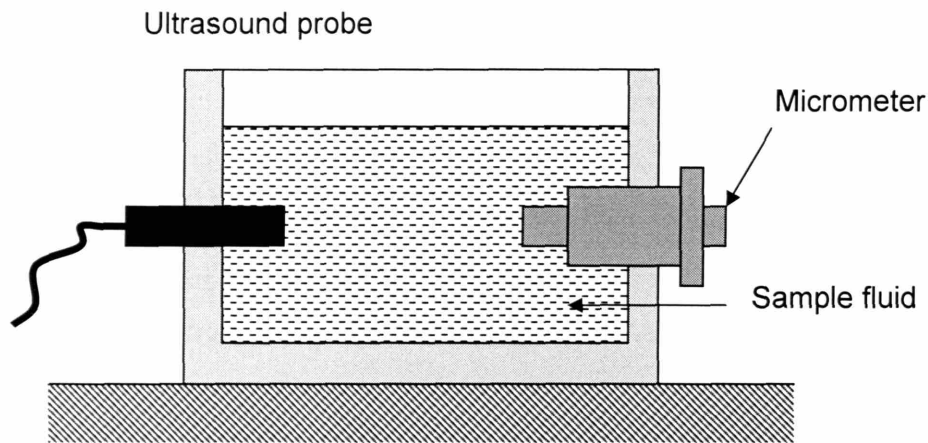


Figure 2-9 Schematic cross-section showing the container used to measure the speed of sound in the sample fluids.

The Echo Referring method (MIT's relative method) uses the same experimental setup as the Signal Processing method. Instead of a change in the distance between the ultrasound probe and the micrometer, the Echo Referring method uses a fixed distance, which avoids any disturbance from turning the micrometer. By this method, the micrometer was maintained at a known fixed position and the distance between the two reflecting surfaces was a fixed distance. The echo correlation signals for all the different fluid samples were recorded in sequence as shown in Figure 2-10. The nominal speed of sound in the DOP 2000 was set as the speed of sound in water, $v_{s_nominal} = v_{s_water}$. By evaluating the echo correlation signals and the round-trip travel time of sound in the sample fluid, the effective distances were estimated as:

$$D_{eff} = t_{sample} v_{s_nominal} \quad (2.12)$$

where D_{eff} is the estimated effective distance, t_{sample} is the one way travel time of sound in the sample fluid, and $v_{s_nominal}$ is the nominal speed of sound in the DOP 2000 setup.

The actual distance between the two surfaces of the ultrasound probe and micrometer were:

$$D_{act} = t_{sample} v_{s_sample} \quad (2.13)$$

where D_{act} is the estimated actual distance, and v_{s_sample} is the speed of sound of the sample. The actual distance equals the effective distance when a fluid with known speed of sound, as DI water, was used and the nominal speed of sound was set as the known speed of sound.

Combining (2.12) and (2.13) yields

$$v_{s_sample} = \frac{D_{act} v_{s_nominal}}{D_{eff}} \quad (2.14)$$

Because the effective distance for the various ferrofluid samples is estimated by the echo signal and the speed of sound is determined relative to a reference fluid sample (e.g., de-ionized water), this method was called the Echo Referring Method (or MIT method). Table 2-4 shows that the results of the two techniques of measuring the speed of sound at 18° Celsius differ by less than 4%, which falls well within practical engineering approximation. Moreover, scientific reference quotes a value of 1476 m/s for the speed of sound in water at a temperature of 18° Celsius [37], which again differs from our relatively simple measurement by less than 1%. The agreement between the two measurement techniques, as well as the close agreement with the accepted value for the speed of sound in water inspires confidence in the measured values of the speed of sound in the ferrofluid samples.

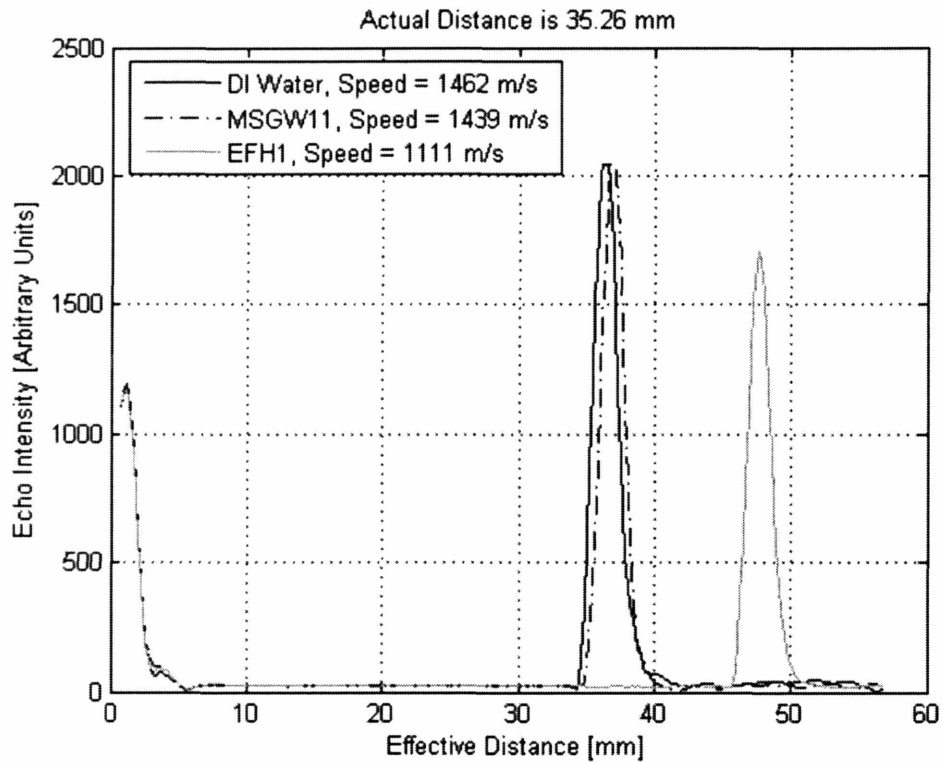


Figure 2-10 Echo intensity image of DI water, MSG W11 water-based ferrofluid and EFH1 oil-based ferrofluid. The speed of sound in the DOP 2000 was set as the speed of sound in water, $v_{s_nominal}$. By evaluating the echo correlation signals and the round-trip travel time of sound in the sample fluid, the effective distances were estimated. Using equation (2.14) the speeds of sound for all samples were calculated, where the actual distance was measured using the micrometer. Note the echoes close to 0 distance are the transducer echo, which is from the transducer impedance mismatching with the plastic container wall/ferrofluid interface.

Table 2-4 Speed of sound measurements for water-based ferrofluids, oil-based ferrofluid, and non-magnetic fluids at a temperature of 18° Celsius. The results of two different methods of measuring the speed of sound agree to within less than 4%. The value of the speed of sound in water at 18° Celsius is 1476 m/s [37] as reported in the literature which exceeds our measured velocity by less than 1%.

| Material | Speed of sound, [m/s] Signal Processing Method | Speed of sound, [m/s] Echo Referring (MIT) Method | Difference, [%] |
|-----------------------|---|--|------------------------|
| DI-water | 1459 | 1462 | -0.21 |
| Nyro | 1456 | 1403 | 3.64 |
| EMG705 (water-based) | 1487 | 1432 | 3.70 |
| MSG W11 (water-based) | 1487 | 1439 | 3.23 |
| EFH1 (oil-based) | 1143 | 1116 | 2.36 |

Chapter 3. Theoretical Background and Governing Equations

The ferrohydrodynamic governing equations are the electro-magnetic field equations, the fluid mechanical conservation of linear and angular momentum equations including magnetic force and torque density equations, together with a magnetization relaxation constitutive law. These equations are applied to the description of ferrofluid behavior in static, oscillating, and rotating uniform and non-uniform magnetic fields. Boundary conditions provide all the additional requirements to make the set of ferrohydrodynamic equations complete.

3.1 Maxwell's Equations

Ferrohydrodynamic experiments are conducted at low frequencies, typically up to 500 Hz, and at low velocity much less than the speed of light, so that the analysis is accurate in the magnetoquasistatic limit (MQS). In the magnetoquasistatic limit, Ampere's law reduces to

$$\nabla \times \bar{H} = 0 \quad (3.1)$$

where \bar{H} [Amp/m] is the magnetic field. The volume current density source term and the displacement current density correction term of Ampere's law are ignored as ferrofluid is non-conductive and is operated in the MQS regime.

Then the irrotational magnetic field can be replaced by the gradient of a magnetic scalar potential Ψ [Amp] as

$$\bar{H} = -\nabla\Psi \quad (3.2)$$

Gauss's law for the magnetic flux density requires that the divergence of magnetic flux density equals zero.

$$\nabla \cdot \bar{B} = 0 \quad (3.3)$$

where \bar{B} is the magnetic flux density [Tesla]. The constitutive relation of magnetic flux density, magnetic field and magnetization is

$$\bar{B} = \mu_0 (\bar{H} + \bar{M}) \quad (3.4)$$

where $\mu_0 = 4\pi \times 10^{-7}$ [henry/m] is the magnetic permeability in free space and \bar{M} is the magnetization of ferrofluid [Amp/m]. Combining Ampere's law (3.2), Gauss' law for magnetic field (3.3) and the constitutive relation (3.4), yields

$$\nabla^2 \Psi = \nabla \cdot \bar{M} \quad (3.5)$$

which is Poisson's equation with an effective magnetic charge density term as $-\mu_0 \nabla \cdot \bar{M}$.

3.2 Magnetization Relaxation Equation

The ferrofluid magnetization relaxation equation used in this work is Shliomis' first relaxation equation [25]

$$\frac{\partial \bar{M}}{\partial t} + \bar{v} \cdot \nabla \bar{M} + \bar{M} (\nabla \cdot \bar{v}) - \bar{\omega} \times \bar{M} + \frac{1}{\tau_{eff}} (\bar{M} - \bar{M}_0) = 0 \quad (3.6)$$

where τ_{eff} [s] is the effective relaxation time constant given in section 2.4, \bar{v} [m/s] is the ferrofluid linear flow velocity, $\bar{\omega}$ [1/s] is the ferrofluid spin velocity which is an average particle rotation angular velocity, and \bar{M}_0 [Amp/m] is the equilibrium magnetization. This is valid when $\Omega \tau \ll 1$, where Ω [1/s] is the angular frequency of the applied magnetic field. Shliomis' second magnetization relaxation equation, derived microscopically using the Fokker-Planck equation in the mean field approximation, considers $\Omega \tau \gg 1$. More recently, Shliomis has derived a more complicated third magnetization equation from irreversible thermodynamics which describes magnetoviscosity in the entire range of magnetic field strength and flow vorticity. It is stated that this new magnetization equation is an improvement over that of the first and

second equations by being valid even far from equilibrium. In our study, the first Shliomis magnetization relaxation equation, (3.6), in the low frequency limit can approximately state the dynamic relation of \bar{H} and \bar{M} as in our work $\tau \sim 10^{-5}$ s and the magnetic frequency of operation is typically up to 500 Hz so that at most $\Omega\tau \approx 0.03$. In the low field strength limit the equilibrium magnetization can be replaced by $\bar{M}_0 = \chi_0\bar{H}$, where χ_0 is the initial susceptibility of ferrofluid as described in sections 2.2-2.3. Further substitution of the equilibrium magnetization relation into (3.6) leads to the expression,

$$\frac{\partial \bar{M}}{\partial t} + (\bar{v} \cdot \nabla) \bar{M} - \bar{\omega} \times \bar{M} + \frac{1}{\tau} (\bar{M} - \chi_0 \bar{H}) = 0 \quad (3.7)$$

where the ferrofluid is considered incompressible so that $\nabla \cdot \bar{v} = 0$.

3.3 Fluid Dynamic Equations

The fluid dynamic equations are given by conservation of linear and angular momentums. Conservation of linear momentum is [1]

$$\rho \frac{D\bar{v}}{Dt} = -\nabla p' + \bar{F} + 2\zeta \nabla \times \bar{\omega} + (\eta + \lambda - \zeta) \nabla (\nabla \cdot \bar{v}) + (\eta + \zeta) \nabla^2 \bar{v} \quad (3.8)$$

where ρ [kg/m³] is the ferrofluid mass density, p' [N/m²] is the dynamical pressure including gravity effects, $p' = p - \rho(\bar{r} \cdot \bar{g})$, \bar{r} [m] is a position vector with respect to an arbitrary origin, \bar{g} [m/s²] is the acceleration of gravity, \bar{F} [N/m³] is the magnetic force density, ζ [Ns/m²] is the vortex viscosity and from microscopic theory for dilute suspensions obeys the approximate relationship, $\zeta = 1.5\eta\phi$, where ϕ is the volume fraction of particles of section 2.2 also being in reference [25], η is the dynamic shear viscosity [Ns/m²], and λ [Ns/m²] is the bulk viscosity. Conservation of angular momentum is [1]

$$J \frac{D\bar{\omega}}{Dt} = \bar{T} + 2\zeta(\nabla \times \bar{v} - 2\bar{\omega}) + (\eta' + \lambda')\nabla(\nabla \cdot \bar{\omega}) + \eta'\nabla^2\bar{\omega} \quad (3.9)$$

where J [kg/m] is the moment of inertia density, \bar{T} [N/m²] is the magnetic torque density, η' [Ns] is the shear coefficient of spin viscosity, and λ' [Ns] is the bulk coefficient of spin viscosity. Furthermore, we take the force density and the torque density in the fluid dynamic equations to be time average values given that the applied magnetic field is oscillating or rotating. Thus, the time average body force density is given as $\bar{F} = \langle \mu_0 (\bar{M} \cdot \nabla) \bar{H} \rangle$ and the time average body torque density is given as $\bar{T} = \langle \mu_0 \bar{M} \times \bar{H} \rangle$, where the delimiters $\langle \rangle$ denote time average values of body force and torque densities. Using complex notation in the sinusoidal steady state, the time average values are easily calculated as $\langle AB \rangle = \frac{1}{2} \text{Re} \{ \hat{A} \hat{B}^* \}$, where $A = \text{Re} \{ \hat{A} e^{j\Omega t} \}$, $B = \text{Re} \{ \hat{B} e^{j\Omega t} \}$, \hat{A} and \hat{B} are arbitrary complex amplitudes, and $\Omega = 2\pi f$ is the radian frequency [29].

This set of three vector differential equations, (3.7)-(3.9), governs the ferrohydrodynamic behavior of isothermal ferrofluids.

In our study we consider the ferrofluid to be incompressible so that the conservation of mass equation

$$\frac{\partial \rho}{\partial t} + \nabla \cdot (\rho \bar{v}) = 0 \quad (3.10)$$

reduces to

$$\nabla \cdot \bar{v} = 0, \quad \rho = \text{constant} \quad (3.11)$$

3.4 Boundary Conditions

In principle, all that is required to solve (3.5), (3.7), (3.8) and (3.9) for a given flow situation and applied magnetic field is a complete set of boundary conditions.

For Maxwell's equations, the boundary conditions are

$$\bar{n} \cdot \|\bar{B}\| = 0, \quad \bar{n} \times \|\bar{H}\| = \bar{K} \quad (3.12)$$

where \bar{n} is the unit vector normal to the boundary and \bar{K} [Amp/m] is the surface current density at the boundary, and $\|\ \|$ denotes the jump value across the boundary.

Further considering Poisson's equation (3.5), a simple boundary condition given below is

$$\Psi|_{BC} = \Psi_0 \quad (3.13)$$

where Ψ_0 is the magnetic scalar value at the boundary, which is specified by the applied magnetic field or the surface current density at the boundary. More detail is discussed in section 9.2.3 with equation (9.61).

In the sinusoidal steady state the magnetization relaxation equation of (3.7) does not impose any spatial boundary conditions. The magnetization is rewritten in terms of the magnetic scalar potential Ψ , the linear velocity \bar{v} and the spin velocity $\bar{\omega}$, which gives the particular solution to Poisson's equation of (3.5).

For the fluid dynamic equations, the linear momentum equation requires an initial condition and two vector boundary conditions, commonly accepted to be the same as in classical fluid mechanics. For a rigid and stationary boundary, the no-penetration and no slip boundary conditions are:

$$\bar{n} \cdot \|\bar{v}\| = 0, \quad \bar{n} \times \|\bar{v}\| = 0 \quad (3.14)$$

where $\|\bar{v}\|$ represents the jump in fluid velocity across the boundary.

As with the translational velocity field, (3.9) describing spin velocity requires an initial condition as well as two vector boundary conditions. The appropriate boundary conditions for the spin field, on the other hand, are still a subject of debate. However, because most analyses of ferrofluid behavior neglect the effect of “spin-diffusion” by setting $\eta' = \lambda' = 0$, thereby reducing the second-order internal angular momentum equation (3.9) to zero order and thus not requiring any boundary conditions on the spin field, $\bar{\omega}$, the spin-boundary condition has not received as much attention as the translational velocity boundary condition. Including non-zero spin viscosity, various possible spin velocity boundary conditions are imaginable, depending on assumptions for the particle/wall interaction effects. In this contribution we analyze two of these possibilities: (i) The “spin–no-slip” boundary condition and (ii) spin–vorticity matching at surfaces. The spin-no-slip boundary condition:

$$\bar{n} \cdot \|\bar{\omega}\| = 0, \quad \bar{n} \times \|\bar{\omega}\| = 0 \quad (3.15)$$

corresponds to the assumption that particle/wall interactions are so strong that no relative spin between the particle and surface is possible. Spin/vorticity matching boundary conditions:

$$\left\| \bar{\omega} - \frac{1}{2} \nabla \times \bar{v} \right\| = 0 \quad (3.16)$$

corresponds to the assumption that antisymmetric stresses vanish at the wall. In this case, ferrofluid nanoparticles roll along the particle/wall interface. We treat both boundary conditions in (3.15) and (3.16) simultaneously by writing the boundary condition as

$$\left\| \bar{\omega} - \gamma \frac{1}{2} \nabla \times \bar{v} \right\| = 0 \quad (3.17)$$

where γ is the spin boundary condition selector. When $\gamma = 0$ the general boundary condition gives the “spin-no-slip” boundary condition of (3.15) and when $\gamma = 1$ the general boundary condition gives the “spin-vorticity” boundary condition of (3.16).

3.5 Turbulence in Planar Couette Flow and Taylor

Instability in Taylor-Couette Flow

Our study is focused on the hydrodynamics of ferrofluid in an oscillating or rotating magnetic field in planar or cylindrical geometry. With the turbulence and instability analysis below, our work is at low velocity and combined with the experimental geometry gives a Reynolds’ number that is much less than the critical Reynolds’ number for turbulence and our Taylor number is less than the critical Taylor number. Therefore, in our analysis without turbulence, planar Couette flow just has one velocity component along the channel and without instability the Taylor-Couette flow just has one velocity component in the angular direction. This simplifies our simulation and helps us to understand the fundamental mechanisms of complex ferrofluid flow behavior under oscillating and rotating magnetic fields.

Two shear-driven flows bear the name of Couette: the flow between infinite parallel planes translating at different velocities while maintaining a constant separation is called planar Couette flow, while the flow between differentially rotating concentric cylinders is called cylindrical Couette flow, or more commonly, Taylor-Couette flow. At high velocity there may be turbulence in planar Couette flow and Taylor instability in Taylor-Couette flows.

The turbulence for planar Couette flow depends only on the distance d between the plates, the relative velocity U of the plates, and the kinematic viscosity ν ($\nu = \eta / \rho$, where η is the flow viscosity and ρ is the mass density), which are combined into a single non-dimensional parameter, the Reynolds number defined as

$$\text{Re} = Ud / \nu \quad (3.18)$$

Commonly, laminar flow occurs at low Reynolds' numbers, where viscous forces are dominant, and is characterized by smooth, constant fluid motion, while turbulent flow, on the other hand, occurs at high Reynolds' numbers and is dominated by inertial forces, producing random eddies, vortices and other flow fluctuations. The transition between laminar and turbulent flow is often indicated by a critical Reynolds number, Re_c , which depends on the exact flow configuration and must be determined experimentally. Within a certain range around this point there is a region of gradual transition where the flow is neither fully laminar nor fully turbulent, and predictions of fluid behavior can be difficult. Ordinarily for a planar geometry, the critical Reynolds' number is generally accepted to be 2300 [34-36]. When the Reynolds' number is smaller than 2000, the flow is laminar flow. When the Reynolds' number is greater than 4000, the flow is turbulent flow. A Reynolds' number between 2000 and 4000 is in the transition region. A critical speed can also be calculated from the critical Reynolds' number as

$$U_c = \frac{\text{Re}_c \nu}{d} \quad (3.19)$$

Table 3-1 presents the physical and flow properties of planar Couette ferrofluid flow by assuming the gap of the planar channel is 0.01 m with a representative velocity 0.1 m/s .

Table 3-1 Physical and flow properties for water-based and oil-based ferrofluids used for planar Couette flow.

| Ferrofluid | ρ , [kg/m ³] | η , [N·s/m ²] | Re (d=0.01 m, U = 0.1 m/s) |
|-----------------------|-------------------------------|--------------------------------|----------------------------|
| EMG705 (water-based) | 1,194 | 0.00248 | 481.45 |
| MSG W11 (water-based) | 1,200 | 0.00202 | 594.06 |
| EFH1 (oil-based) | 1,221 | 0.00727 | 167.95 |

The planar Couette flow in our work is laminar flow, because our Reynolds' number is much less than the critical Reynolds' number of 2000.

In contrast, cylindrical geometry Taylor-Couette flow has curvature effects so that both the inner and outer radii R_{in} and R_{out} (or the gap width $d = R_{out} - R_{in}$ and the average radius $R = (R_{in} + R_{out})/2$) play a role. Because the rotating flow introduces a Coriolis term into the equation, the flow depends on the angular velocities of both the inner and outer cylinders, ω_{in} and ω_{out} . The five dimensional parameters can be combined into three non-dimensional parameters in various ways. Here we choose $\beta = R_{in} / R_{out}$, $\mu = \omega_{out} / \omega_{in}$, and $Re = R_{in} \omega_{in} d / \nu$. A more general parameter, Taylor's number, is defined as

$$T_a = \frac{4\omega_{in}^2 R_{in}^4 (1-\mu)(1-\mu/\beta^2)}{\nu^2 (1-\beta^2)^2} \quad (3.20)$$

which determines instability from the properties of Taylor Couette flow. A critical Taylor's number for Taylor instability is given as T_c . When the Taylor's number of a Taylor-Couette flow is greater than the critical Taylor's number, instability occurs. A critical spin velocity of the inner cylinder can be calculated for a given critical Taylor's number as,

$$\omega_{inc} = \frac{\nu(1-\beta^2)}{2R_{in}^2} \sqrt{\frac{T_c}{(1-\mu)(1-\mu/\beta^2)}} \quad (3.21)$$

Table 3-2 presents the physical and flow properties of ferrofluids. The Taylor's numbers in Table 3-2 are calculated from (3.20) by assuming the spin velocity ω_{in} is 50 rpm = 5.2 rads/s and $\omega_{out} = 0$ (stationary container). In our Taylor-Couette flow experiments, we have two cylinder sizes. The inner cylinder is a 10 ml syringe with 13.9 mm diameter and a 20 ml syringe with diameter 18.2 mm. The outer cylinder is a 200 ml beaker with diameter 52.2 mm. Here $\beta = 0.27$ for the 10 ml syringe and $\beta = 0.35$ for the 20 ml syringe, and $\mu = 0$ for all cases as the beaker is stationary.

Table 3-2 Physical and flow properties for water-based and oil-based ferrofluids used for Taylor-Couette flow measurements.

| Ferrofluid | ρ , [kg/m ³] | η , [N·s·m ⁻²] | T (10ml syringe) | T (20ml syringe) |
|----------------------|-------------------------------|---------------------------------|--------------------|--------------------|
| EMG705 (water-based) | 1,194 | 0.00248 | 17414 | 19348 |
| MSG W11 | 1,200 | 0.00202 | 18181 | 20294 |
| EFH1 | 1,221 | 0.00727 | 24041 | 26835 |

The critical Taylor number is $T_c = 3.31 \times 10^5$ for $\mu = 0$ [36]. In our work the Taylor numbers in Table 3-2 are smaller than the critical Taylor's number, so that our spin-up flow is stable.

3.6 Skin Depth

Skin depth δ is the distance to which an incident magnetic field penetrates into an ohmic conductor.

$$\delta = \sqrt{\frac{2}{\sigma\mu\omega}} = \sqrt{\frac{1}{\pi\sigma\mu f}} \quad (3.22)$$

where σ [siemen/m] is conductivity, μ [henry/m] is the magnetic permeability, $\omega = 2\pi f$ [rad/s] is the radian frequency and f [Hz] is the frequency of the applied magnetic field. Table 3-3 gives the physical properties and the skin depth for water and ferrofluids we used. Because the skin depth of our experiments shown in Table 3-3 is much greater than the size of the experiment geometry, there is no significant skin depth decay in our work.

Table 3-3 Physical properties and skin depths at $f = 500$ Hz for water, water-based and oil-based ferrofluids used in experiments.

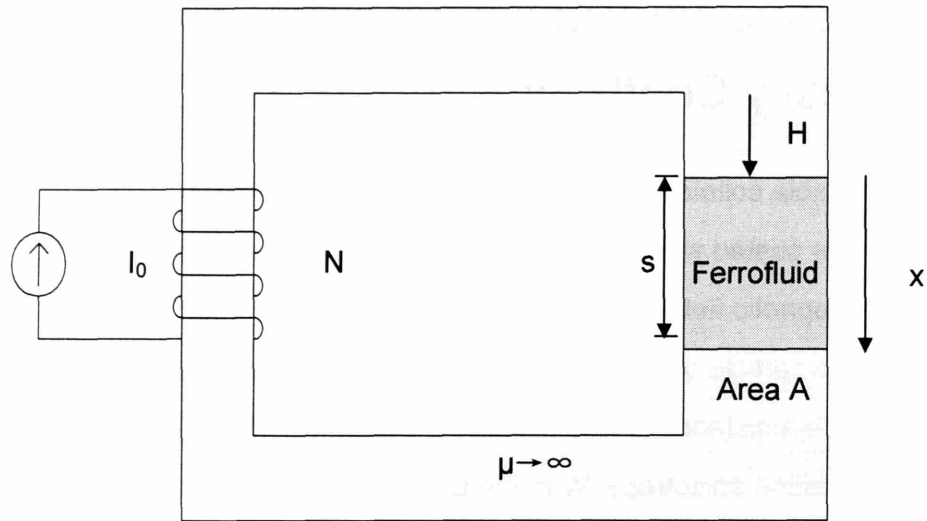
| Material | f, [Hz] | μ , [Henry·m ⁻¹] | σ , [siemen/m] | δ , [m] |
|-----------|---------|----------------------------------|--|----------------|
| DI-water | 500 | $4\pi \times 10^{-7}$ | 5.5×10^{-6} | 9597 |
| Tap water | 500 | $4\pi \times 10^{-7}$ | $5.5 \times 10^{-4} \sim 5 \times 10^{-2}$ | 100~1000 |
| EMG705 | 500 | 5.20×10^{-6} | $5.5 \times 10^{-4} \sim 5 \times 10^{-2}$ | 47.2~472 |
| MSG W11 | 500 | 1.96×10^{-6} | $5.5 \times 10^{-4} \sim 5 \times 10^{-2}$ | 80.6~806 |
| EFH1 | 500 | 3.25×10^{-6} | $5.5 \times 10^{-4} \sim 5 \times 10^{-2}$ | 62.6~626 |

Chapter 4. Effective Magnetoviscosity with Zero Spin Viscosity Coefficients ($\eta' = 0, \lambda' = 0$)

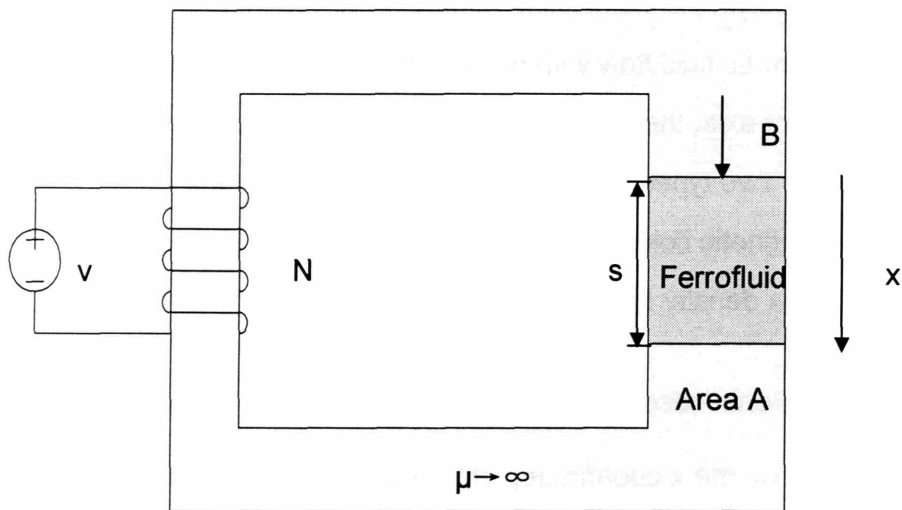
Ferrofluids are stable colloidal suspensions consisting of single-domain magnetic particles coated with a surfactant and immersed in a carrier fluid. A homogeneous magnetic field tends to orient the magnetic moment of a colloidal magnetic particle of a magnetic fluid in the direction of the applied magnetic field with resistance to free rotation of the particle from fluid viscosity or magnetic crystalline anisotropy. With the Brownian and Néel relaxation effects and hydrodynamic forces, antisymmetric stress between the magnetic particle and the carrier fluid affects the effective magnetoviscosity of the magnetic fluid. By applying Shliomis' first magnetization relaxation equation to planar-Couette magnetic fluid flow with an applied uniform DC magnetic field transverse to the duct axis, the effective magnetoviscosity and particle spin velocity are derived. Two types of uniform DC magnetic fields are applied, imposed uniform magnetic field H as shown in Figure 4-1(a) and imposed uniform magnetic flux density B as shown in Figure 4-1(b).

For both one dimensional cases in Figure 4-1, because $\nabla \cdot \bar{B} = 0$, with all fields only depending only on the x coordinate, B_x must be spatially uniform.

However, as shown in Figure 4-1(a), the magnetic field \bar{H} is driven by $\oint \bar{H} \cdot d\bar{l} = NI_0$ in the ferrofluid. Because the spin velocity $\bar{\omega}$ is spatially uniform for planar Couette flow as will be shown in the following analysis, the magnetic field \bar{H} is spatially uniform in the ferrofluid. For other flows, such as Poiseuille flow, the spin velocity is a function of position, so that the magnetic field \bar{H} is not constant in the ferrofluid. As shown in Figure 4-1(b) the magnetic flux density $\bar{B} = \Lambda_0 / A$ is spatially uniform when the exciting coil has constant voltage, but the magnetic field \bar{H} can be spatially varying.



(a)



(b)

Figure 4-1 (a) With a constant DC current source the DC magnetic field H is spatially constant in the ferrofluid, $H = NI_0 / s$ for planar Couette flow because the spin velocity is uniform and B will be a spatial constant that depends on the fluid spin velocity $\bar{\omega}$. For non-Couette flow $NI = \int_0^s H_x dx$ (b) With an impulse voltage source, $v = \Lambda_0 \delta(t)$, the DC magnetic flux Λ_0 is imposed and the DC magnetic flux density B is spatially uniform in the ferrofluid, $B = \Lambda_0 / A$, where H depends on the fluid spin velocity and is spatially constant only for Couette flow.

4.1 Governing equations for Planar Couette Flow

4.1.1 Magnetic Field and Magnetization

For the planar duct Couette flow, with magnetic fluid confined between rigid walls as shown in Figure 4-2, the top surface is driven at velocity V and the volume is magnetically stressed by a uniform x directed DC magnetic field H_x (Figure 4-1(a)) or magnetic flux density B_x (Figure 4-1(b)), as shown in Figure 4-2. The flow velocity \bar{v} and the spin velocity $\bar{\omega}$ are of the form

$$\bar{v} = v_z(x)\bar{i}_z, \quad \bar{\omega} = \omega_y(x)\bar{i}_y, \quad (4.1)$$

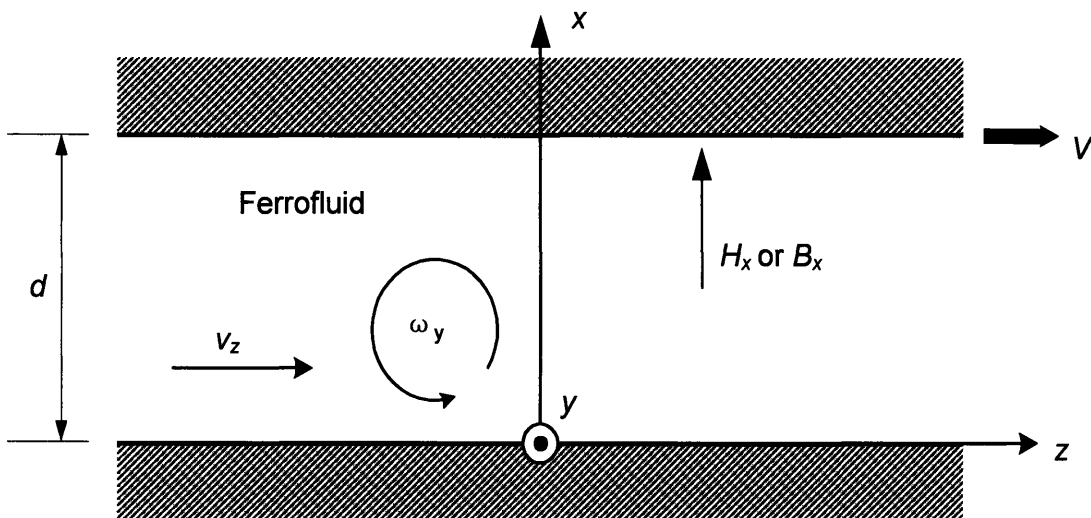


Figure 4-2 A planar ferrofluid layer between rigid walls, in planar Couette flow driven by the $x=d$ surface moving at velocity V , is magnetically stressed by a uniform x directed DC magnetic field H_x or magnetic flux density B_x .

The imposed magnetic field H_x or magnetic flux density B_x do not depend on the y and z coordinates for the magnetic circuits shown in Figure 4-1 and Figure 4-2. We assume that the gap d is sufficiently small that the externally imposed current or magnetic flux sources impose magnetic field variables and flow variables that are independent of y and z and can only

vary with x . Gauss's law for the magnetic flux density $\bar{B} = \mu_0(\bar{H} + \bar{M})$ and Ampere's law for the magnetic field \bar{H} with zero current density are

$$\nabla \cdot \bar{B} = 0 \Rightarrow \frac{dB_x}{dx} = 0 \Rightarrow B_x = \text{constant} \quad (4.2)$$

$$\nabla \times \bar{H} = 0 \Rightarrow \frac{dH_z}{dx} = \frac{dH_y}{dx} = 0 \Rightarrow H_y, H_z = \text{constant} \quad (4.3)$$

In the absence of y and z directed surface currents on the $x=0$ and $x=d$ planes, $H_y = H_z = 0$. Therefore, in the DC steady state, the total magnetic field inside the magnetic fluid layer is of the form

$$\bar{H} = H_x(x) \bar{i}_x \quad (4.4)$$

and in terms of imposed external uniform magnetic flux density B_x the total magnetic flux density inside the magnetic fluid layer has the form

$$\bar{B} = B_x \bar{i}_x + B_z(x) \bar{i}_z \quad (4.5)$$

where because of the lack of a surface current source, $H_z = 0$ from (4.3), and B_z is only due to z directed magnetization, M_z , due to fluid motion. For planar Couette flow we will find that H_x in (4.4) is independent of x .

For low magnetic fields, Shliomis' first magnetization relaxation equation for magnetization \bar{M} in a magnetic field \bar{H} is given as (3.7). At low fields the magnetic fluid obeys a linear constitutive law in equilibrium with constant magnetic susceptibility χ_0 , $\bar{M} = \chi_0 \bar{H}$.

Using (4.4) and (4.5) in (3.7), the magnetization components in terms of imposed uniform magnetic field H_x are

$$M_x = \frac{\chi_0 H_x}{[(\omega_y \tau)^2 + 1]}, M_z = \frac{-\chi_0 H_x \omega_y \tau}{[(\omega_y \tau)^2 + 1]} \quad (4.6)$$

and the magnetization components in terms of imposed external uniform magnetic flux density B_x are

$$M_x = \frac{\chi_0 B_x / \mu_0}{[(\omega_y \tau)^2 + 1 + \chi_0]}, M_z = \frac{-\chi_0 B_x \omega_y \tau / \mu_0}{[(\omega_y \tau)^2 + 1 + \chi_0]} \quad (4.7)$$

4.1.2 Magnetic Force and Torque Density

The magnetic force density is given by $\bar{F} = \mu_0(\bar{M} \cdot \nabla)\bar{H}$ and the magnetic torque density is given by $\bar{T} = \mu_0(\bar{M} \times \bar{H})$. Using (4.6), the magnetic force and torque density with imposed uniform magnetic field H_x are of the form

$$\bar{F} = \mu_0(\bar{M} \cdot \nabla)\bar{H} = \mu_0 M_x \frac{dH_x}{dx} \bar{i}_x = 0 \quad (4.8)$$

$$\bar{T} = \mu_0(\bar{M} \times \bar{H}) = \mu_0 M_z H_x \bar{i}_y = \frac{-\chi_0 \mu_0 \omega_y \tau H_x^2}{(\omega_y \tau)^2 + 1} \bar{i}_y \quad (4.9)$$

Using (4.7), the magnetic force and torque density with imposed external uniform magnetic flux density B_x are of the form

$$\bar{F} = \mu_0(\bar{M} \cdot \nabla)\bar{H} = \mu_0 M_x \frac{d}{dx} \left(\frac{B_x}{\mu_0} - M_x \right) \bar{i}_x = -\bar{i}_x \frac{d}{dx} \left(\frac{1}{2} \mu_0 M_x^2 \right) = 0 \quad (4.10)$$

$$\bar{T} = \mu_0(\bar{M} \times \bar{H}) = (M_z B_x - \mu_0 M_x M_z) \bar{i}_y = \frac{-\chi_0 \omega_y \tau B_x^2 [(\omega_y \tau)^2 + 1]}{\mu_0 [(\omega_y \tau)^2 + 1 + \chi_0]^2} \bar{i}_y \quad (4.11)$$

Note, that the right hand side of (4.10) is zero, because in (4.10) B_x is constant from (4.2) and we will show that under DC conditions and with $\eta' = 0$ that ω_y is also constant as will be shown in Section 4.2, so that M_x and M_z in (4.7) do not depend on x .

4.1.3 Planar Couette Flow

For an incompressible fluid and for the assumed flow solutions in (4.1),

$\nabla \cdot \bar{v} = 0, \nabla \cdot \bar{\omega} = 0$. The coupled linear and angular momentum conservation equations with force density \bar{F} and torque density \bar{T} for a fluid in a gravity field $-g\bar{i}_x$ are given in (3.8) and (3.9).

For low Reynolds' number flows so that inertia is negligible; in the DC steady state; and neglecting spin viscosity ($\eta' = 0$), pressure gradient and gravity effects; the flow and spin velocity equations are

$$0 = \bar{F} + 2\zeta \nabla \times \bar{\omega} + (\zeta + \eta) \nabla^2 \bar{v} \quad (4.12)$$

$$0 = \bar{T} + 2\zeta (\nabla \times \bar{v} - 2\bar{\omega}) \quad (4.13)$$

where in (4.12), the force density is zero from (4.8) and (4.10). Using the solution form of (4.1), the flow and spin velocity equations reduce to

$$(\zeta + \eta) \frac{d^2 v_z}{dx^2} + 2\zeta \frac{d\omega_y}{dx} = 0 \quad (4.14)$$

$$T_y - 2\zeta \left(\frac{dv_z}{dx} + 2\omega_y \right) = 0 \quad (4.15)$$

In the absence of magnetic field ($H_x = 0$) or magnetic flux density ($B_x = 0$),

$T_y = 0$ and with the boundary conditions that $v_z(x=0) = 0$ and $v_z(x=d) = V$,

the solution for flow and spin velocities are

$$v_{z0}(x) = \frac{Vx}{d}, \quad \omega_{y0} = -\frac{V}{2d} \quad (4.16)$$

With imposed external magnetic field (H_x) as shown in Figure 4-1(a) or

magnetic flux density (B_x) as shown in Figure 4-1(b), the spin velocity (ω_y) is

spatially uniform as shown in the following section 4.2, which makes the torque

density (T_y) spatially uniform from (4.2), (4.3), (4.9) and (4.11). Therefore, integration of (4.15) gives the solution for the flow velocity of the form

$$v_z(x) = \left(\frac{T_y}{2\zeta} - 2\omega_y \right) x + C \quad (4.17)$$

Using the boundary conditions that

$$\begin{aligned} v_z(x=0) = 0 &\Rightarrow C = 0 \\ v_z(x=d) = V &\Rightarrow \left(\frac{T_y}{2\zeta} - 2\omega_y \right) = \frac{V}{d} \end{aligned} \quad (4.18)$$

the flow and spin velocities are

$$\begin{aligned} v_z(x) &= \frac{Vx}{d} \\ \omega_y &= \frac{T_y}{4\zeta} - \frac{V}{2d} \end{aligned} \quad (4.19)$$

where T_y is given by (4.9) for H_x imposed magnetic field and (4.11) for B_x imposed magnetic field. Equation (4.19) shows that for planar Couette flow the magnetic field does not change the flow velocity profile from (4.16) but does change the spin velocity.

4.1.4 Shear Stress

The general Cauchy stress tensor equation for flow is

$$\bar{\bar{T}} = -p\bar{\bar{I}} + \eta[\nabla\bar{v} + \nabla\bar{v}^T] + \lambda(\nabla \cdot \bar{v})\bar{\bar{I}} + \zeta\bar{\bar{\varepsilon}} \cdot (\nabla \times \bar{v} - 2\bar{\omega}) \quad (4.20)$$

where $\bar{\bar{T}}$ is the pressure viscous-stress tensor, $\bar{\bar{I}}$ is the unit isotropic dyadic,

$$\lambda \text{ is the bulk viscosity, and } \bar{\bar{\varepsilon}} \text{ is the polyadic, } \varepsilon_{ijk} = \begin{cases} +1 & ijk = xyz, yzx \text{ or } zxy \\ -1 & ijk = xzy, yxz \text{ or } zyx \\ 0 & i = j, i = k \text{ or } j = k \end{cases}$$

Using the solution form of (4.16) and (4.19) with the assumption of incompressible flow ($\nabla \cdot \bar{v} = 0$), the shear stress at the $x = 0$ interface is

$$T_{zx} = (\eta + \zeta) \frac{dv_z}{dx} + 2\zeta\omega_y = (\eta + \zeta) \frac{V}{d} + 2\zeta\omega_y \quad (4.21)$$

which has no direct magnetic stress.

The Maxwell stress tensor $\left(T_{ij} = H_i B_j - \frac{1}{2} \delta_{ij} \mu_0 H_k H_k \right)$ in general has no surface shear stress contribution $(T_{zx} = H_z B_x)$ in the absence of surface currents, because tangential \bar{H} (H_z) and normal \bar{B} (B_x) are continuous across the $x=0$ interface. In the absence of magnetic field ($H_x = 0$) or magnetic flux density ($B_x = 0$), the shear force at the $x=0$ interface is obtained by substituting (4.16) into (4.21)

$$T_{zx0} = \eta \frac{V}{d} \quad (4.22)$$

The change of the shear force due to the magnetic field gives the change in the flow viscosity, $\Delta\eta$, as

$$\Delta T_{zx} = T_{zx} - T_{zx0} = \zeta \left(\frac{V}{d} + 2\omega_y \right) = \Delta\eta \frac{V}{d} \Rightarrow \Delta\eta = \zeta \left(1 + \frac{2\omega_y d}{V} \right) = \frac{T_y}{2} \frac{d}{V} \quad (4.23)$$

where T_y is given by (4.9) for H_x imposed magnetic field and (4.11) for B_x imposed magnetic field.

4.2 Spin Velocity and Effective Viscosity Solutions for Planar Couette Flow

4.2.1 The Solution for an Imposed External Magnetic Field H_x

Using the solution form of the torque density from (4.9) in (4.14) and (4.15), the solution of the spin velocity ω_y , when H_x is imposed, is found by solving the 3rd order equation

$$2\omega_y + \frac{\chi_0 \mu_0 \omega_y \tau H_x^2}{2\zeta \left[(\omega_y \tau)^2 + 1 \right]} + \frac{V}{d} = 0 \quad (4.24)$$

Defining the non-dimensional parameters $r = \Delta\eta / (2\zeta) = \left(\frac{1}{2} + \frac{\omega_y d}{V} \right)$ and

$P_H = \frac{\mu_0 \chi_0 H_x^2 \tau}{4\zeta}$, equation (4.24) can be rewritten as the 3rd order equation

$$r^3 - r^2 + \left[\frac{1}{4} + \frac{1 + P_H}{(V\tau/d)^2} \right] r - \frac{P_H}{2(V\tau/d)^2} = 0 \quad (4.25)$$

Solving equation (4.25) for a real root, the effective viscosity for magnetic fluid in an imposed magnetic field can be found. This solution is given by Shliomis [25] and Rosensweig [1], although note that equation (4.25) corrects a few small errors in Rosensweig's expression (equation (8.96)). Figure 4-3 plots

$\frac{\Delta\eta}{2\zeta}$ vs. P_H and also corrects minor errors in Rosensweig's plot (Figure 8.11).

The effective viscosity $\Delta\eta$ has non-physical multiple values when the applied magnetic field and flow parameters P_H and $\frac{V\tau}{d}$ exceed critical values. This may be because the analysis assumes the spin viscosity to be $\eta' = 0$, which may be non-physical.

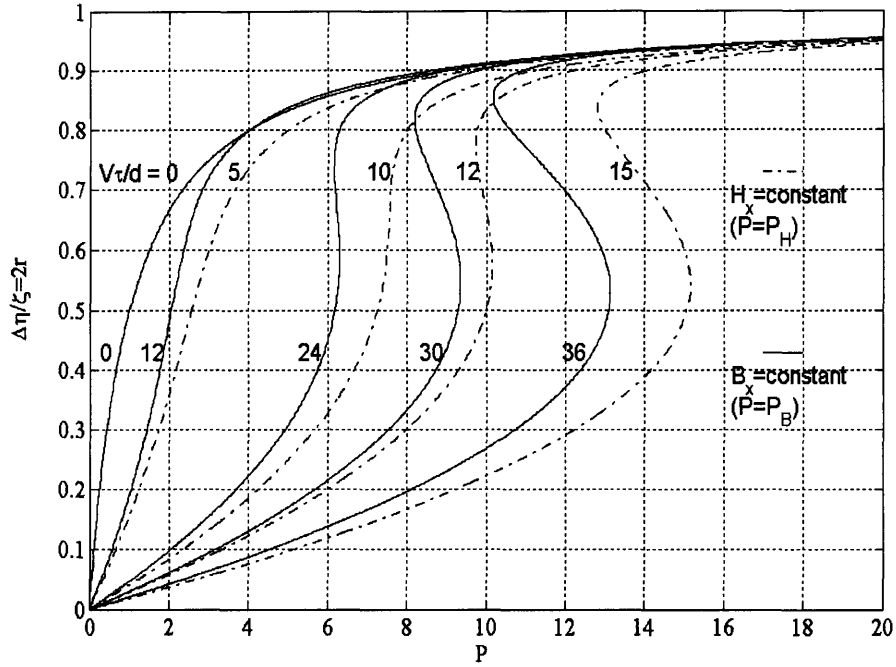


Figure 4-3 The solution for the change in magnetoviscosity for planar Couette flow

versus related magnetic field parameter $\left(P_H = \frac{\mu_0 \chi_0 H_x^2 \tau}{4\zeta} \right)$ and magnetic flux density

parameter $\left(P_B = \frac{\chi_0 B_x^2 \tau}{\mu_0 (1 + \chi_0)^2 4\zeta} \right)$ for various values of $\frac{V\tau}{d}$. For imposed magnetic

flux density B_x , $\chi_0 = 1.55$ for oil-based magnetic fluid Ferrotec EFH1 [40, 41].

Note that for this case of constant H_x , that $B_x = \mu_0 (H_x + M_x)$ and that even though B_x is spatially constant it does depend on ω_y . Using the solution of

M_x from (4.6) in $B_x = \mu_0 (H_x + M_x)$, B_x is

$$B_x = \mu_0 (H_x + M_x) = \mu_0 H_x \left(1 + \frac{\chi_0}{[(\omega_y \tau)^2 + 1]} \right) \quad (4.26)$$

Non-dimensionalizing (4.26) with non-dimensional parameter $P_H = \frac{\mu_0 \chi_0 H_x^2 \tau}{4\zeta}$

and $B_0^2 = \frac{4\zeta\mu_0}{\chi_0\tau}$, equation (4.26) can be written as

$$\frac{B_x^2}{B_0^2} = \left(1 + \frac{\chi_0}{[(\omega_y \tau)^2 + 1]} \right)^2 P_H \quad (4.27)$$

Figure 4-4 shows the relationship of related magnetic field and magnetic flux density. With an imposed constant magnetic field H_x , the magnetic flux density B_x is still a spatial constant but depends on the spin velocity. It is also shown in Figure 4-4 that the magnetic flux density B_x has non-physical multiple values when the applied magnetic field and flow parameters P_H and $\frac{V\tau}{d}$ exceed critical values. This again indicates that taking the spin viscosity value of $\eta' = 0$ may be non-physical.

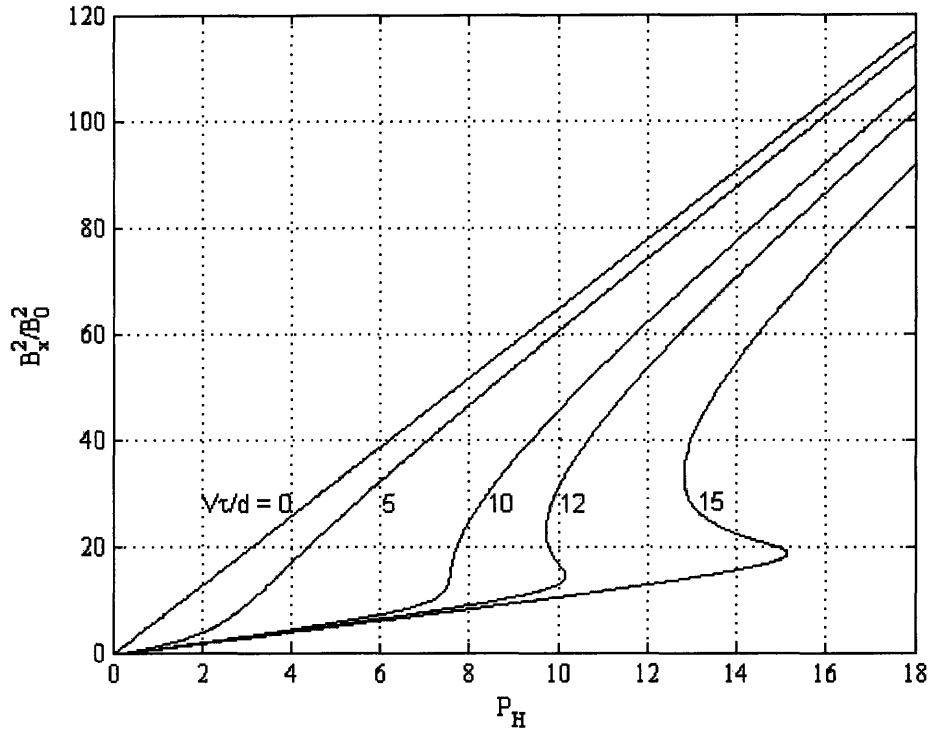


Figure 4-4 The magnetic flux density parameter $\left(\frac{B_x}{B_0}\right)^2$ versus magnetic field

parameter $P_H = \frac{\mu_0 \chi_0 H_x^2 \tau}{4\zeta}$ for an imposed constant magnetic field H_x for planar

Couette flow for various $\frac{V\tau}{d}$, where $\chi_0 = 1.55$ for oil based ferrofluid Ferrotec EFH1.

4.2.2 The Solution for an Imposed External Magnetic Flux Density

B_x

Using the solution form of the torque density from (4.11) in (4.14) and (4.15), the solution of the spin velocity ω_y is found by solving the 5th order equation

$$2\omega_y + \frac{\chi_0 \omega_y \tau \left[(\omega_y \tau)^2 + 1 \right] B_x^2}{2\mu_0 \zeta \left[(\omega_y \tau)^2 + 1 + \chi_0 \right]^2} + \frac{V}{d} = 0 \quad (4.28)$$

Defining the non-dimensional parameters $r = \Delta\eta/(2\zeta) = \left(\frac{1}{2} + \frac{\omega_y d}{V}\right)$ and

$P_B = \frac{\chi_0 B_x^2 \tau}{\mu_0 (1 + \chi_0)^2 4\zeta}$, equation (4.28) can be rewritten as the 5th order equation

$$\begin{aligned} \left(r - \frac{1}{2}\right)^5 + \frac{1}{2}\left(r - \frac{1}{2}\right)^4 + \frac{[(1 + \chi_0)^2 P_B + 2(1 + \chi_0)]}{(V\tau/d)^2} \left(r - \frac{1}{2}\right)^3 + \\ \frac{(1 + \chi_0)}{(V\tau/d)^2} \left(r - \frac{1}{2}\right)^2 + \frac{[(1 + \chi_0)^2 (P_B + 1)]}{(V\tau/d)^4} \left(r - \frac{1}{2}\right) + \frac{(1 + \chi_0)^2}{2(V\tau/d)^4} = 0 \end{aligned} \quad (4.29)$$

Solving equation (4.29) for a real root, the effective viscosity for magnetic fluid in an imposed magnetic flux density can be found. Figure 4-3 also shows the solution for magnetoviscosity versus P_B for various values of $\frac{V\tau}{d}$ taking $\chi_0 = 1.55$ for oil-based magnetic fluid Ferrotec EFH1 [40, 41].

Note again that B_x is a spatial and temporal constant and that $H_x = \frac{B_x}{\mu_0} - M_x$

is also a spatial and temporal constant for planar Couette flow but varying with flow spin velocity ω_y . Using the solution of M_x from (4.7) in $H_x = \frac{B_x}{\mu_0} - M_x$,

H_x is

$$H_x = \frac{B_x}{\mu_0} - M_x = \frac{B_x}{\mu_0} \left(1 - \frac{\chi_0}{[(\omega_y \tau)^2 + 1 + \chi_0]}\right) \quad (4.30)$$

Non-dimensionalizing (4.30) with non-dimensional parameter

$P_B = \frac{\chi_0 B_x^2 \tau}{\mu_0 (1 + \chi_0)^2 4\zeta}$ and $H_0^2 = \frac{4\zeta}{\chi_0 \mu_0 \tau}$, equation (4.26) can be written as

$$\frac{H_x^2}{H_0^2} = (1 + \chi_0)^2 \left(1 - \frac{\chi_0}{[(\omega_y \tau)^2 + 1 + \chi_0]}\right)^2 P_B \quad (4.31)$$

Figure 4-5 shows the relationship of magnetic flux density parameter P_B and magnetic field parameter $\left(\frac{H_x}{H_0}\right)^2$ for various $\frac{V\tau}{d}$. With an imposed constant magnetic flux density B_x , the magnetic field H_x is still a spatial constant but depends on the spin velocity. It is also shown in Figure 4-5 that the magnetic field H_x has non-physical multiple values when the applied magnetic flux density and flow parameters P_B and $\frac{V\tau}{d}$ exceed critical values. This may be because the analysis uses the spin viscosity value of $\eta' = 0$, which may be non-physical.

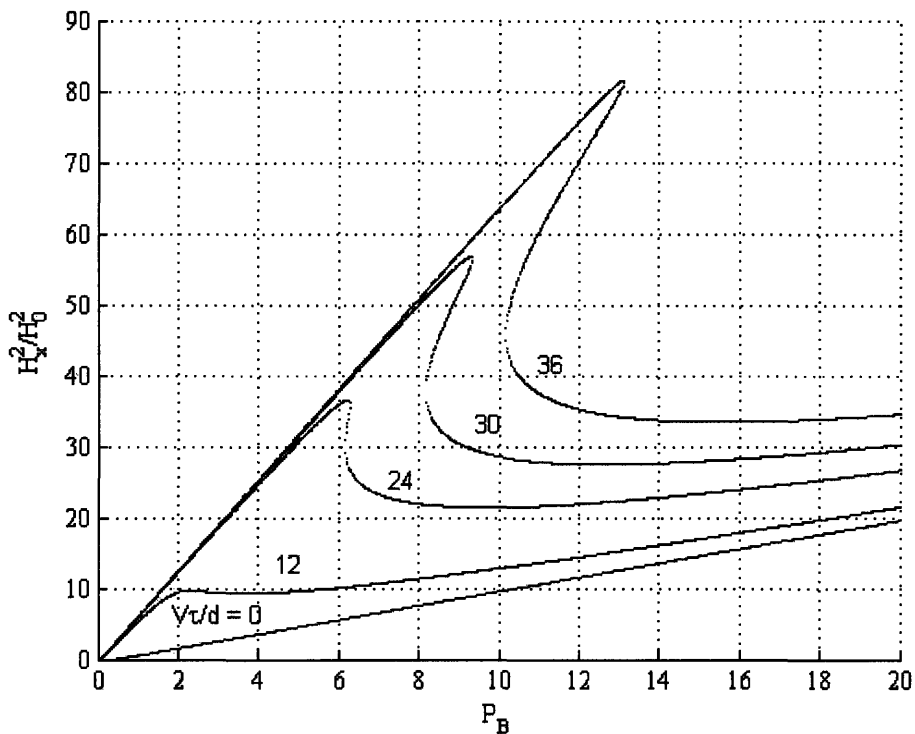


Figure 4-5 The relationship of related magnetic flux density parameter

$$P_B = \frac{\chi_0 B_x^2 \tau}{\mu_0 (1 + \chi_0)^2 4 \zeta} \text{ and magnetic field parameter } \left(\frac{H_x}{H_0}\right)^2 \text{ for an imposed magnetic}$$

flux density B_x for various values of $\frac{V\tau}{d}$, where $\chi_0 = 1.55$ for oil based ferrofluid Ferrotec EFH1.

4.3 Effective Viscosity Solutions for Planar Poiseuille Flow

The difference between a planar Couette flow and a planar Poiseuille flow is the driving source for the flow. A planar Couette flow has flow driven by a surface moving at a constant velocity as shown in Figure 4-2, while a planar Poiseuille flow is driven by a constant pressure gradient, $\frac{\partial p}{\partial z}$, along the planar channel as shown in Figure 4-6.

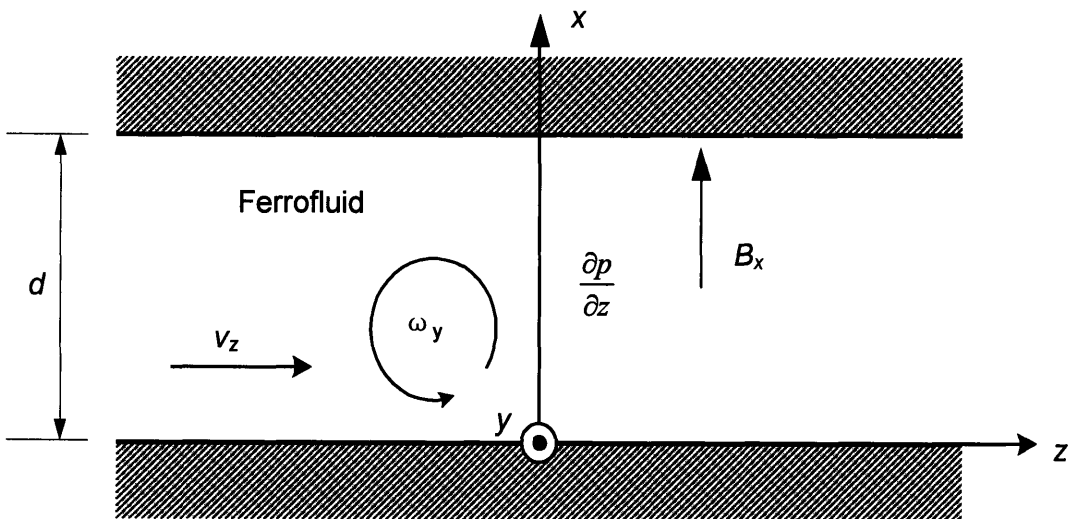


Figure 4-6 A planar ferrofluid layer between rigid stationary walls, in planar Poiseuille flow driven by the constant pressure gradient, $\frac{\partial p}{\partial z}$, along the planar channel, is magnetically stressed by a uniform x directed DC magnetic flux density B_x .

4.3.1 Governing Equations and Boundary Conditions for Planar Poiseuille Flow

The governing equations of magnetic field and magnetization for a planar Poiseuille flow are the same as the equations for a planar Couette flow as

given in section 4.1.1. The magnetic force and torque density equations for a planar Poiseuille flow are of the same form as for a planar Couette flow as given in section 4.1.2.

A planar Poiseuille flow also has the same coupled linear and angular momentum conservation equations as planar Couette flow with force density \bar{F} and torque density \bar{T} for a fluid in a gravity field $-g\bar{i}_x$ given in (3.8) and (3.9). The primary difference in the solutions between planar Couette and Poiseuille flows is that for Poiseuille flow ω_y is a function of x . For low Reynolds' number flows, so that inertia is negligible, in the DC steady state, and neglecting spin viscosity ($\eta' = 0$) and gravity effects, the flow and spin velocity equations are

$$0 = -\nabla p + \bar{F} + 2\zeta \nabla \times \bar{\omega} + (\zeta + \eta) \nabla^2 \bar{v} \quad (4.32)$$

$$0 = \bar{T} + 2\zeta (\nabla \times \bar{v} - 2\bar{\omega}) \quad (4.33)$$

where in (4.32), the force density is set to zero from (4.8) and (4.10). Using the solution form of (4.1), the flow and spin velocity equations reduce to

$$(\zeta + \eta) \frac{d^2 v_z}{dx^2} + 2\zeta \frac{d\omega_y}{dx} - \frac{\partial p}{\partial z} = 0 \quad (4.34)$$

$$T_y - 2\zeta \left(\frac{dv_z}{dx} + 2\omega_y \right) = 0 \quad (4.35)$$

The boundary conditions for the velocity at $x = 0$ and $x = d$ are

$$v_z(x = 0) = v_z(x = d) = 0 \quad (4.36)$$

From symmetry we have the boundary values of the spin velocity and the velocity derivative as

$$\omega_y(x = 0) = -\omega_y(x = d) \quad (4.37)$$

$$\frac{dv_z}{dx}(x=0) = -\frac{dv_z}{dx}(x=d) \quad (4.38)$$

Also by symmetry the spin velocity value at $x = \frac{d}{2}$ must be zero

$$\omega_y \left(x = \frac{d}{2} \right) = 0 \quad (4.39)$$

The spin velocity $\omega_y(x)$ is thus an odd function of x , and the flow velocity

$v_z(x)$ is an even function of x around $x = \frac{d}{2}$.

4.3.2 Effective Viscosity Solutions for Planar Poiseuille Flow

Taking the derivative of (4.35) respect to x to replace the velocity term in (4.34), the solution of the spin velocity ω_y is found by solving the differential equation of

$$2\eta \frac{d\omega_y}{dx} - \frac{\zeta + \eta}{2\zeta} \frac{dT_y}{dx} + \frac{\partial p}{\partial z} = 0 \quad (4.40)$$

where the torque density T_y is given as (4.11) for an imposed uniform

external magnetic flux density B_x . Equation (4.40) is then integrated to yield

$$2\eta\omega_y - \frac{\zeta + \eta}{2\zeta} T_y + \frac{\partial p}{\partial z} x + C = 0 \quad (4.41)$$

Using the symmetry condition (4.39), the value of constant C is

$$C = -\frac{\partial p}{\partial z} \frac{d}{2} \quad (4.42)$$

Using the solution of torque density from (4.11) in (4.41) the solution of the spin velocity ω_y is found by solving the 5th order equation dependent on x

$$2\eta\omega_y + \frac{\zeta + \eta}{2\zeta} \frac{\chi_0 \omega_y \tau B_x^2 \left[(\omega_y \tau)^2 + 1 \right]}{\mu_0 \left[(\omega_y \tau)^2 + 1 + \chi_0 \right]^2} + \frac{\partial p}{\partial z} \left(x - \frac{d}{2} \right) = 0 \quad (4.43)$$

Defining the non-dimensional parameters $r = \omega_y \tau$, $K = \frac{\tau d}{2\eta} \frac{\partial p}{\partial z}$ and

$P_p = \frac{\chi_0 B_x^2 \tau (\zeta + \eta)}{\mu_0 4 \zeta \eta}$, equation (4.43) can be rewritten as

$$r + \frac{P_p (r^2 + 1) r}{(r^2 + 1 + \chi_0)^2} + K \left(\frac{x}{d} - \frac{1}{2} \right) = 0 \quad (4.44)$$

which is a 5th order equation

$$\begin{aligned} r^5 + K \left(\frac{x}{d} - \frac{1}{2} \right) r^4 + [2(1 + \chi_0) + P_p] r^3 + 2K \left(\frac{x}{d} - \frac{1}{2} \right) (1 + \chi_0) r^2 \\ + [(1 + \chi_0)^2 + P_p] r + K \left(\frac{x}{d} - \frac{1}{2} \right) (1 + \chi_0)^2 = 0 \end{aligned} \quad (4.45)$$

Using the solution from (4.45) in (4.35) the flow velocity is

$$v_z(x) = \int \left(\frac{T_y}{2\zeta} - 2\omega_y \right) dx \quad (4.46)$$

Using the expression for T_y from (4.11) and non-dimensional parameters

$r = \omega_y \tau$, $K = \frac{\tau d}{2\eta} \frac{\partial p}{\partial z}$, $P_p = \frac{\chi_0 B_x^2 \tau (\zeta + \eta)}{\mu_0 4 \zeta \eta}$ and $P_B = \frac{\chi_0 B_x^2 \tau}{2\zeta \mu_0}$, equation (4.46) can

be rewritten as

$$\begin{aligned} \frac{v_z \tau}{d}(x) &= \int \left(\frac{-\chi_0 B_x^2 \tau \omega_y \tau \left[(\omega_y \tau)^2 + 1 \right]}{2\zeta \mu_0 \left[(\omega_y \tau)^2 + 1 + \chi_0 \right]^2} - 2\omega_y \tau \right) d \left(\frac{x}{d} \right) \\ &= - \int \left(\frac{2\eta P_p}{\zeta + \eta} \frac{\omega_y \tau \left[(\omega_y \tau)^2 + 1 \right]}{\left[(\omega_y \tau)^2 + 1 + \chi_0 \right]^2} + 2\omega_y \tau \right) d \left(\frac{x}{d} \right) \\ &= - \int \left(\frac{2\eta P_p}{\zeta + \eta} \frac{[r^3 + r]}{\left[r^2 + 1 + \chi_0 \right]^2} + 2r \right) d \left(\frac{x}{d} \right) = - \int \left(\frac{2P_p}{1.5\phi + 1} \frac{[r^3 + r]}{\left[r^2 + 1 + \chi_0 \right]^2} + 2r \right) d \left(\frac{x}{d} \right) \end{aligned} \quad (4.47)$$

where ζ [Ns/m^2] is the vortex viscosity and from microscopic theory for dilute suspensions obeys the approximate relationship, $\zeta = 1.5\eta\phi$, where ϕ is the volume fraction of particles of section 2.2 [25].

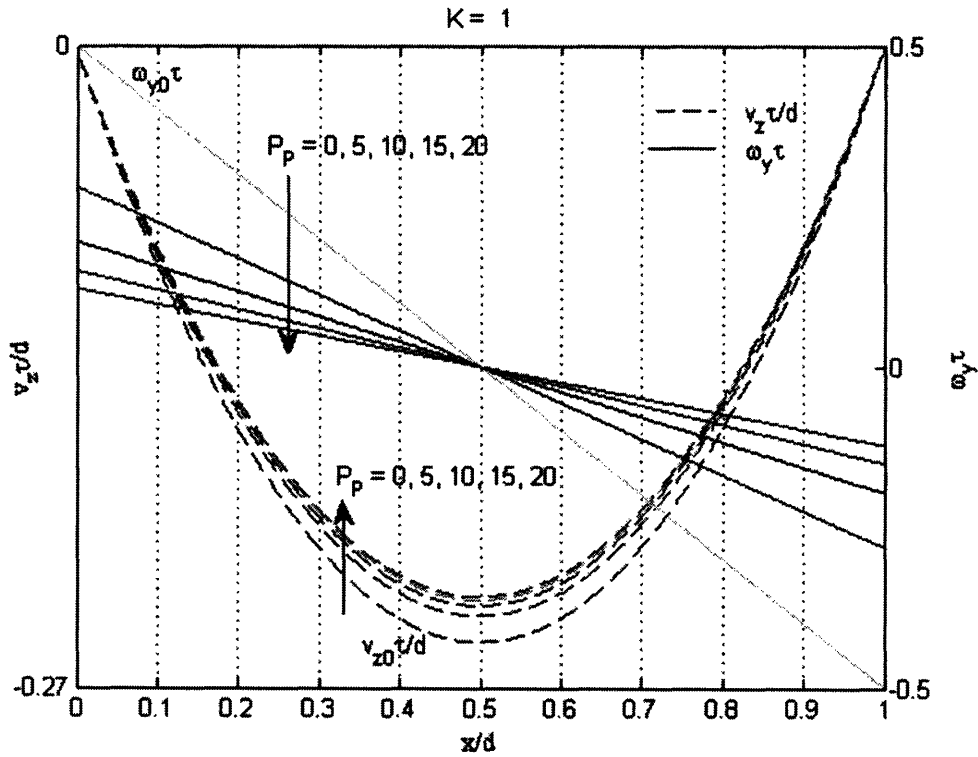


Figure 4-7 Calculated spin velocity profiles (solid lines) and flow velocity profiles (dashed lines) as a function of x for various magnetic flux density parameter values of

$$\left(P_p = \frac{\chi_0 B_x^2 \tau (\zeta + \eta)}{\mu_0 4 \zeta \eta} \right) \text{ for } K=1, \chi_0=1.55 \text{ and } \phi=7.52\% \text{ for EFH1 oil-based}$$

ferrofluid.

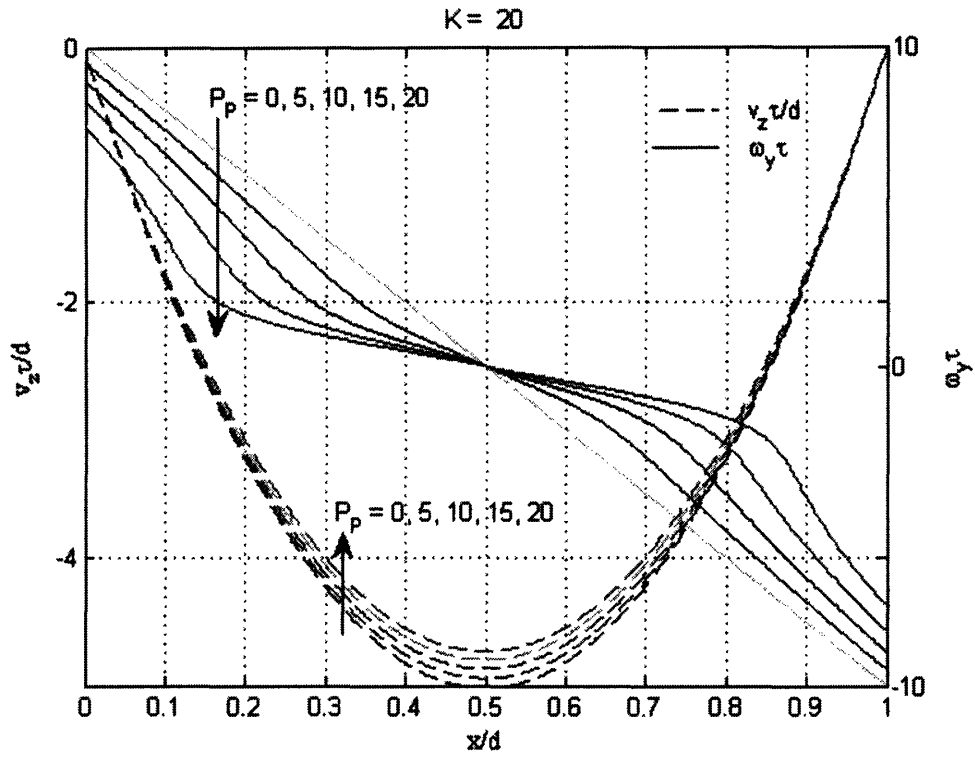


Figure 4-8 Calculated spin velocity profiles (solid lines) and flow velocity profiles (dashed lines) as a function of x for various magnetic flux density parameter values of

$$\left(P_p = \frac{\chi_0 B_x^2 \tau (\zeta + \eta)}{\mu_0 4 \zeta \eta} \right) \text{ for } K = 20, \chi_0 = 1.55 \text{ and } \phi = 7.52\% \text{ for EFH1 oil-based}$$

ferrofluid.

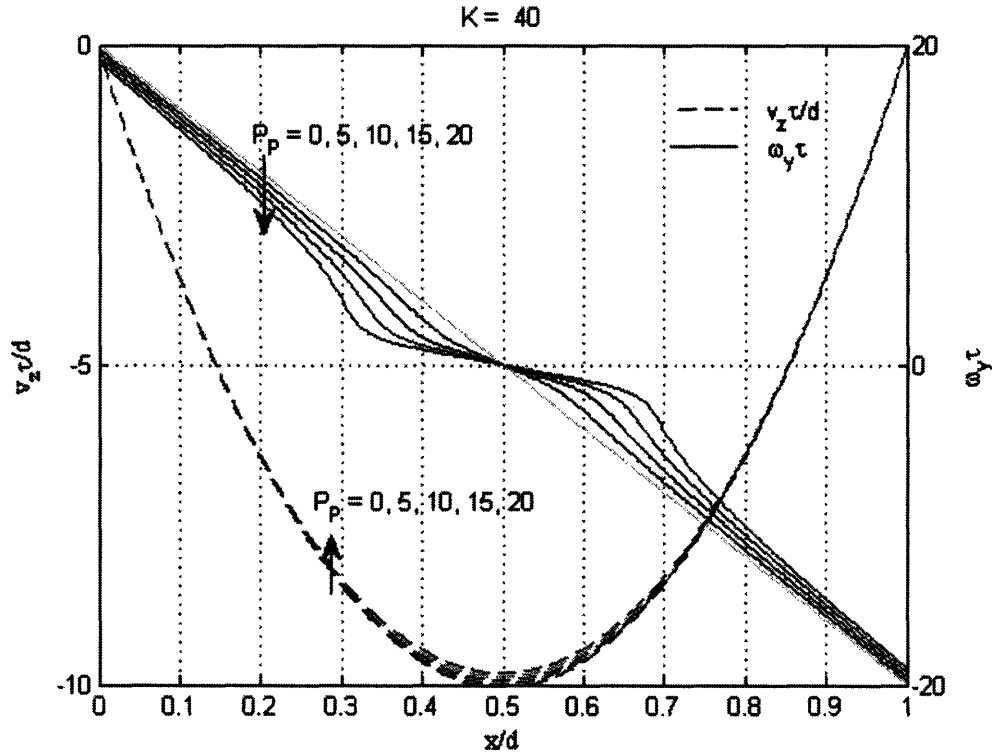


Figure 4-9 Calculated spin velocity profiles (solid lines) and flow velocity profiles (dashed lines) as a function of x for various magnetic flux density parameter values of $\left(P_p = \frac{\chi_0 B_x^2 \tau (\zeta + \eta)}{\mu_0 4 \zeta \eta} \right)$ for $K = 40$, $\chi_0 = 1.55$ and $\phi = 7.52\%$ for EFH1 oil-based ferrofluid.

Figure 4-7 to Figure 4-9 show the spin velocity profiles from the fifth order equation (4.45) and flow velocity profiles from (4.47) for various values of magnetic flux density parameter $P_p = \frac{\chi_0 B_x^2 \tau (\zeta + \eta)}{\mu_0 4 \zeta \eta}$ with $K = 1, 20, 40$. As a check it is also shown in Figure 4-7 that with $B_x = 0$ ($P_p = 0$), the flow velocity and spin velocity profiles calculated from (4.47) and (4.45) reduce to the usual Poiseuille flow as given in (4.50) as v_{z0} and ω_{y0} .

From (4.21) the shear stress at each surface is

$$T_{zx}|_{x=0,d} = (\eta + \zeta) \left. \frac{dv_z}{dx} \right|_{x=0,d} + 2\zeta \omega_y|_{x=0,d} \quad (4.48)$$

In the absence of magnetic flux density ($B_x = 0$), $T_y = 0$, and from (4.35) the relation between flow and spin velocities is

$$\frac{dv_{z0}}{dx} = -2\omega_{y0} \quad (4.49)$$

where the sub zero denotes the values in the absence of magnetic flux density. Substituting (4.49) into (4.34) and using the boundary condition (4.36) the solution for the velocity profiles of Poiseuille flow and spin velocities in the absence of magnetic field is

$$\begin{aligned} v_{z0} &= \frac{1}{2\eta} \frac{\partial p}{\partial z} (x^2 - dx) \\ \omega_{y0} &= -\frac{1}{2\eta} \frac{\partial p}{\partial z} \left(x - \frac{d}{2} \right) \end{aligned} \quad (4.50)$$

which yields the boundary values at $x = 0$ as

$$\omega_{y0}(x=0) = \frac{d}{4\eta} \frac{\partial p}{\partial z}, \quad \frac{dv_{z0}}{dx}(x=0) = -\frac{d}{2\eta} \frac{\partial p}{\partial z} \quad (4.51)$$

and at $x = d$ as

$$\omega_{y0}(x=d) = -\frac{d}{4\eta} \frac{\partial p}{\partial z}, \quad \frac{dv_{z0}}{dx}(x=d) = \frac{d}{2\eta} \frac{\partial p}{\partial z} \quad (4.52)$$

From (4.48) the shear stress at the $x = 0$ interface with $B_x = 0$ is

$$T_{zx}|_{x=0} = (\eta + \zeta) \left. \frac{dv_{z0}}{dx} \right|_{x=0} + 2\zeta \omega_{y0}|_{x=0} = \eta \frac{dv_{z0}}{dx} = -\frac{d}{2} \frac{\partial p}{\partial z} \quad (4.53)$$

while the shear stress with $B_x \neq 0$ at the $x = 0$ interface is

$$T_{zx}|_{x=0} = (\eta + \zeta) \left. \frac{dv_z}{dx} \right|_{x=0} + 2\zeta \omega_y|_{x=0} \quad (4.54)$$

Substituting (4.35) and (4.41) into (4.54) and evaluating the values at $x = 0$, the shear stress reduces to

$$T_{zx}|_{x=0} = \frac{\zeta + \eta}{2\zeta} T_y|_{x=0} - 2\eta\omega_y|_{x=0} = -\frac{d}{2} \frac{\partial p}{\partial z} \quad (4.55)$$

so that the magnetic field does not change the shear stress at each interface of a planar Poiseuille flow.

However, the magnetic field does change the flow and spin velocity profile. We define the effective viscosity, η_{eff} , from the ratio of the mechanical power necessary to drive the flow with/without magnetic field

$$\frac{\eta_{eff}}{\eta} = \frac{\int_0^d -\frac{\partial p}{\partial z} v_{z0}(x) dx}{\int_0^d -\frac{\partial p}{\partial z} v_z(x) dx} = \frac{\int_0^d v_{z0}(x) dx}{\int_0^d v_z(x) dx} = \frac{Q_0}{Q} \quad (4.56)$$

where Q is the volume flow rate per depth with magnetic field, $Q = \int_0^d v_z(x) dx$,

and Q_0 is the volume flow rate per depth without magnetic field

$$Q_0 = \int_0^d v_{z0}(x) dx.$$

Figure 4-10 shows the relationship of the magnetoviscosity and the related

magnetic flux density parameter $P_p = \frac{\chi_0 B_x^2 \tau (\zeta + \eta)}{\mu_0 4\zeta \eta}$ for various pressure

gradient parameter values of $K = \frac{\tau d}{2\eta} \frac{\partial p}{\partial z}$ of the planar Poiseuille flow ferrofluid.

Figure 4-10 also shows that with the same pressure gradient, higher magnetic field magnitude has a stronger effect on magnetoviscosity and with the same applied magnetic field magnitude, higher pressure gradient has a lesser effect on magnetoviscosity.

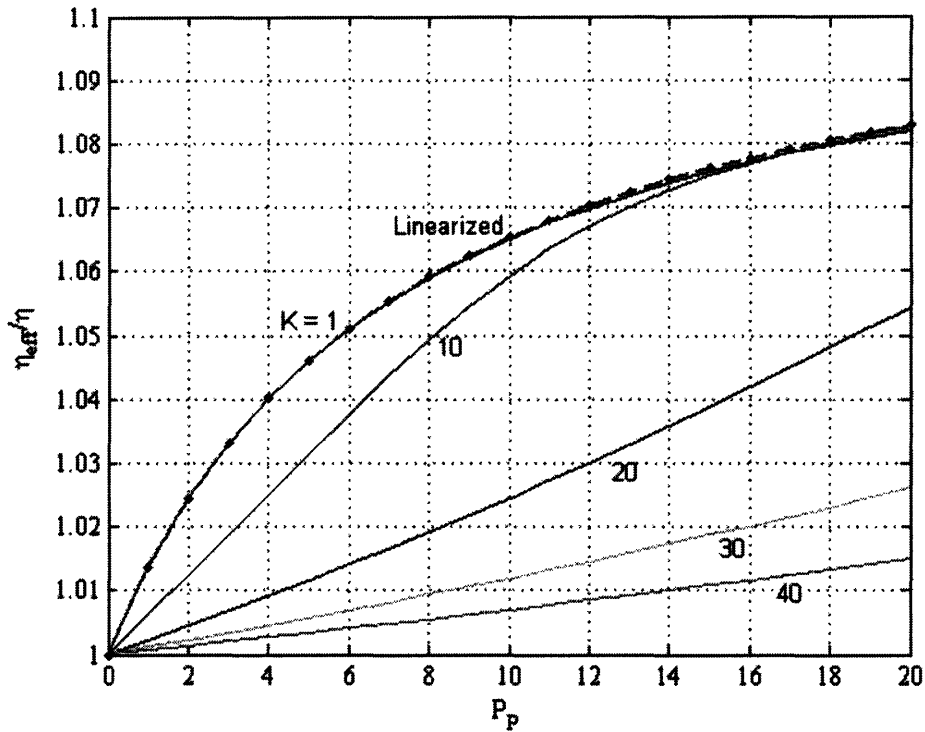


Figure 4-10 The solution for magnetoviscosity versus related magnetic flux density

parameter $\left(P_p = \frac{\chi_0 B_x^2 \tau (\zeta + \eta)}{\mu_0 4 \zeta \eta} \right)$ for various pressure gradient parameter values of

$K = \frac{\tau d}{2\eta} \frac{\partial p}{\partial z}$. The linearized magnetoviscosity curve in the small spin velocity limit [85]

(* markers) overlaps with the magnetoviscosity curve with $K = 1$, $\chi_0 = 1.55$ and

$\phi = 7.52\%$ for EFH1 oil-based ferrofluid.

As a check it is shown in Figure 4-10 that the linearized magnetoviscosity curve in the small spin velocity limit [85] (* markers) from (4.58) overlaps with the magnetoviscosity with $K = 1$ curve. The linearized magnetoviscosity with small spin velocity limit was given as [85]

$$\tilde{\eta}_{eff} = \tilde{\eta} - \frac{\alpha \tilde{\zeta}}{2\tilde{\zeta} - \alpha} \quad (4.57)$$

where $\tilde{\eta}_{eff} = \frac{2\eta_{eff}}{\mu_0 H_0^2 \tau}$ is normalized effective viscosity, $\tilde{\eta} = \frac{2\eta}{\mu_0 H_0^2 \tau}$ is

normalized viscosity, $\tilde{\zeta} = \frac{2\zeta}{\mu_0 H_0^2 \tau}$ is normalized vortex viscosity and

$\alpha = -\frac{\chi_0}{(1+\chi_0)^2} \left(\frac{B}{\mu_0 H_0} \right)^2$ is the first order term of normalized torque density \tilde{T}_y

in the small spin velocity limit [85]. Note that α [85] has a 1/2 factor which is from the time average value in the sinusoidal steady state. In the DC magnetic field the 1/2 is removed. Unnormalized (4.57) with nondimensional parameters

$P_p = \frac{\chi_0 B_x^2 \tau (\zeta + \eta)}{\mu_0 4 \zeta \eta}$, the linearized magnetoviscosity curve in the small spin

velocity limit can be rewritten as

$$\frac{\eta_{eff}}{\eta} = 1 + \frac{1.5\phi}{1 + \frac{(1+1.5\phi)(1+\chi_0)^2}{P_p}} \quad (4.58)$$

where ϕ is the volume fraction of particles.

Analysis of effective magnetoviscosity show that in a planar Couette flow magnetic fields change the magnetoviscosity of ferrofluid by changing the shear stress at the planar channel walls, but keeping the velocity profile unchanged, and in a planar Poiseuille flow magnetic fields change the magnetoviscosity of ferrofluid by changing the velocity profile and keeping the shear stresses at the planar channel walls unchanged.

Analytic solutions of effective magnetoviscosity using ferrohydrodynamic equations with spin viscosity $\eta' = 0$ in planar Couette flow show multiple non-physical values of flow viscosities and magnetic field solutions. These nonphysical solutions are probably because assuming a zero spin viscosity $\eta' = 0$ is nonphysical. Governing ferrohydrodynamic equations with spin

viscosity $\eta' \neq 0$ results in nonlinear differential equations, which makes analytic solutions impossible. However, numerical simulations of the governing ferrohydrodynamic equations with nonzero spin viscosity, $\eta' \neq 0$, will be presented in Chapter 9.

Chapter 5. Complex Magnetic Susceptibility Tensor and Applications

There are many ways in which magnetic nanoparticles can be used for biomedical applications such as [43-46]: a) Magnetic nanoparticles and their surface coating can bind to drugs, proteins, enzymes, antibodies, or organisms; b) Magnetic nanoparticles can be directed to organs, tissues, or tumors using an external magnet for therapeutic effect; c) Dissipation in alternating and rotating magnetic fields can cause heating of magnetic nanoparticles for use in hyperthermia treatment; and d) Magnetic resonance imaging can be enhanced and externally controlled by magnetic field effects due to magnetic nanoparticles magnetization and motion.

Such chemotherapeutic applications require nanoparticles to be able to pass through organ and tissue capillary systems without threat of vessel embolism and be able to transport pharmacologically active materials with an effective release mechanism of the drug at the target site. All components for the magnetic nanoparticle carrier system must be nontoxic, biodegradable, and removable [47].

From the magnetization relaxation equation (3.6), we define the magnetic susceptibility tensor and derive the generalized three dimensional magnetic susceptibility tensor for ferrofluid in the sinusoidal steady state in an oscillating or rotating magnetic field which determines the total magnetic field distribution inside and outside the ferrofluid and affects ferrofluid and magnetic nanoparticle motions. The real part of the complex magnetic susceptibility contributes to self and mutual inductances of ferrofluid while the imaginary part of the complex magnetic susceptibility contributes to ferrofluid loss. The inductance and resistance of the ferrofluid depends on and can thus be externally controlled by the spin velocity and frequency of the applied magnetic

field. By controlling the ferrofluid magnetic susceptibility, we can for example control magnetic resonance imaging (MRI) contrast and ferrofluid power dissipation that can change the temperature of the surrounding region, which can be used in hyperthermia treatments.

5.1 Brief Summary of Current Research.

5.1.1 Magnetocytolysis

Classical hyperthermia induces damage to cells and tissues, enhances radiation injury to tumor cells, and improves chemotherapeutic efficacy. A local thermal effect is desired within cancerous tissues while leaving normal tissues unaffected [48, 49]. Heating between 41 C° and 46 C° generally reduces the viability of cancer cells without harming healthy cells and increases cancer cell sensitivity to radiation and chemotherapy.

Temperatures up to 56 C° (thermoablation) lead to cell death [48-50]. Magnetic materials for hyperthermia of biological tissues have been used since at least the late 1950s. Over a nanoparticle diameter range of 5–10 nm, the effective relaxation time of (3.6) in magnetite varies over two orders of magnitude. Ferrofluid subdomain particles (10 nm diameter) absorb more power and reach higher temperature at reasonable AC magnetic fields than by hysteresis heating of multidomain particles of 1 μm size scale [50-54].

Small amounts of magnetic fine particles in radio frequency (RF) magnetic fields can easily rise in temperature to cause cell death. For example, for a magnetic field intensity of 6.5 kA/m at 300 kHz, Néel relaxation has peak dissipated power density of about 10^{10} W/m^3 for magnetite nanoparticles of about 9 nm radius, decreasing to about 10^8 W/m^3 at 7 nm radius and to 10^6 W/m^3 at 12 nm radius. Hysteresis losses are about 10^6 W/m^3 at 9 nm nanoparticle radius, rising to about 10^{10} W/m^3 for nanoparticles larger than

about 10 nm particle radius. Calculations and confirming measurements show that a temperature rise of about 16 C° in about 30 minutes results from a 3 mm radius sphere of crushed magnetite embedded in a gel in a magnetic field of 17.6 kA/m at 300 kHz [55].

To study the biological effects of AC magnetic field stressed ferrofluids, both in vivo and in vitro studies have been done in cancer cell lines and spontaneously induced tumors in animal models [54]. The term Magnetic Fluid Hyperthermia (MFH), which uses AC magnetic fields to heat target areas containing magnetic fluids, is suggested for this new cancer treatment method. It has been shown [56] that MFH is able to inactivate tumor cells in vitro to at least the same extent as water bath hyperthermia and that there is no cytotoxic effect of intracellularly administered dextran-ferrite magnetic particles [57, 58]. An in vivo study [59] using transplants of a mammary carcinoma showed that high doses of MFH were able to induce tumor control in 44% of the cases up to 30 days after therapy.

Trials carried out on human and mouse macrophages (leukocytes, white blood cells) without a magnetic field and in a constant magnetic field did not observe any cytolysis or toxic effects [60]. Under an alternating magnetic field of 100 Gauss at a frequency of 1 MHz, the temperature of a concentrated ferrofluid increases from 37 C° to 80 C° in about 2 minutes. Magnetocytolysis experiments were carried out using very low concentrations of magnetic nanoparticles, such that no increase in the temperature of the bulk solution was reported. After being subjected to alternating fields for 5 minutes, it was observed that 40–50% of the mouse and human macrophages are killed, but only 3–6 hours after application of the oscillating field. It was found that binding of the magnetic nanoparticles to the cell membrane is essential for cytolysis. For iron oxide nanoparticles of 10 nm diameter deposited into tumors in mice and exposed to a 6500-A/m, 400-kHz magnetic field for 4 minutes, the local heating, called “magnetic thermoablation,” raised the tumor temperature to

about 71 °C from 26 °C, causing therapeutic irreversible damage to the tumor [61]. Similar measurements in mice using water-based dextran-ferrite magnetic fluid in a 9300-A/m magnetic field at 0.88 MHz raised the tumor temperature to 45 °C, with 33% tumor regression and mouse life span increases of 150% [62].

5.1.2 Drug Delivery

The use of biocompatible ferrofluids as a delivery system for therapeutic drugs is commonly called “magnetic drug targeting” [63-65]. Mitoxantrone, a chemotherapeutic agent that inhibits DNA and RNA synthesis, was ionically bound to magnetic nanoparticles and was directed to cancerous tumor sites in rabbits using a 1.7 Tesla magnet focused on the tumor. Complete tumor remissions with no adverse side effects were obtained using only 20% of the normal mitoxantrone dosage [66]. Similar success was achieved using ferrofluids labeled with iodine in a 0.6 Tesla magnetic field [67].

Magnetic targeting of anticancer drugs reversibly bound to magnetic fluids to locally advanced tumors can be achieved using magnetic fields directed to the tumor surfaces from outside the patient [54, 68]. Phase I clinical trials using this approach in patients with advanced and unsuccessfully pretreated cancers or sarcomas showed successful magnetic drug targeting with epirubin [54] and epirubicin [68]. Based on magnetic resonance tomographic techniques, pharmacokinetics, and the histological detection of magnetite, it was shown that ferrofluids could be successfully directed by externally imposed magnetic fields to the tumors in about one half of the patients. Superparamagnetic nanoparticles were surface-modified with Poly(Ethylene Glycol) (PEG) and folic acid, respectively, to improve their intracellular uptake and ability to target specific cells [69]. It was found that PEG modification of nanoparticles resulted in decreased uptake by macrophages, whereas folic acid modification did not result in any change in uptake by macrophages. However, both PEG and folic

acid modification resulted in increased internalization of magnetic nanoparticles in breast cancer cells.

5.1.3 Separations

Separation techniques are important for purification of biological materials and for identification of organisms, cells, and genomic materials. Application of a magnetic field to a suspension of magnetic nanoparticles confined between planar sheets causes the nanoparticles to self organize into a regular array of columns. The column spacing can be controlled from submicron to 100 nm by varying gap width, nanoparticle size, and concentration. Such a self-assembled array of magnetic particles was used to separate large DNA in a microchannel in about 30 minutes, in contrast to the usual pulsed field agarose gel electrophoresis method, which takes about 12–24 hours [70]. Because pore size control from about 1–100 nm can be obtained without the need for sophisticated microlithography, there are many separation applications envisioned for DNA, cells, proteins, organelles, and microparticles or nanoparticles.

Magnetic fluids have also been used as magnetically responsive extractants usable in treating aqueous media contaminated with organic compounds. In one study [70], magnetite (Fe_3O_4) nanoparticles of 7.5 nm nominal diameter coated with a 9 nm diameter bifunctional polymer layer composed of a hydrophilic Poly(Ethylene Oxide) (PEO) outer region and a hydrophobic Poly(Propylene Oxide) (PPO) inner region were prepared. With the advantages of very high surface area and decreased diffusion lengths, these magnetic fluids were shown to have high capacity for organic solutes, similar to that of analogous PEO–PPO–PEO block copolymer micelles. Efficient magnetic nanoparticle recovery using high-gradient magnetic field separation (HGMS) has been shown and incorporated into a proposed water purification process [71].

Magnetic cell sorting schemes based on quadrupole fields [72] and in microfabricated magnetic arrays [73] have been developed. The objective was to develop economical, high-throughput, high-purity, and high-recovery alternatives for separation of heterogeneous cell populations based on expression of particular surface markers.

An efficient magnetic vector/effector synthesis procedure was developed to target membrane receptors in target cells for subsequent separation. This system was used to target, separate, and count damaged red blood cells. Applications of this technology include: 1) quality testing of human blood during storage in vitro [74]; 2) studies of the evolution of red blood cell (erythrocyte) populations during parasitic pathologies such as malaria [75] and Alzheimer's disease [76]; and 3) detection of membrane modifications involved in complex biological processes such as apoptosis (programmed cell death).

5.1.4 Immunoassays

Immunoassays are widely used in biology and medicine for the determination of the composition of complex samples such as blood by labeling one of the reaction components with radioisotopes, enzymes, or fluorescent dyes. Magnetic nanoparticle labels offer advantages as they are inexpensive to produce, are stable, and can be safely and easily stored, handled, and disposed of without problems of radioactivity or environmental contamination [77].

Antibodies were coupled with magnetic nanoparticles and reacted with their solid-phase adsorbed antigen. The samples were first placed in a magnetic field of 1500 A/m and then the remanent magnetization in the absence of magnetic field was measured in a Superconducting Quantum Interference Device (SQUID) magnetometer. This measurement technique investigated the binding of Monoclonal Antibodies (MABs) to collagen type III using

Dextran-coated iron oxide nanoparticles with 13 nm mean diameter. Then polystyrene tubes used as sample containers were incubated with the antigen collagen type III so that the antigen was adsorbed onto the tube wall. The measured magnetic moment after switching off the magnetic field is entirely caused by the remanent magnetization of nanoparticles with hindered mobility because of their binding to the antigen fixed at the tube wall. Unbound nanoparticles relax by Brownian relaxation and have no net remanent magnetization. For this method to work, the Néel relaxation time must be longer than the measurement period, typically about 100 seconds, which requires larger size magnetic particles on the order of >20 nm diameter for magnetite particles [77, 78].

5.1.5 Magnetic Resonance Imaging

Magnetic materials are highly opaque to x-rays and, with 8–10% volume concentration in ferrofluid, offer comparable image quality to conventional barium sulfate [79]. Magnetic nanoparticles, conjugated to various MABs (Monoclonal Antibodies), peptides, or proteins, show potential applications for in vivo monitoring of brain intercellular communication and target-oriented magnetic resonance imaging in animal and human brains [80]. Dextran-coated superparamagnetic iron oxide is commercially available for MRI and has been used for localization and diagnosis of brain and cardiac blood obstructions and for liver lesions or tumors, where the nanoparticles tend to accumulate because of the difference in tissue fluidity and endocytotic processes (incorporation of substances into cells). Approximately 7 nm sized magnetite nanoparticles coated with polymeric starch were injected into a rat brain. The magnetic nanoparticles were well distributed within the dorsal hippocampus, demonstrating the feasibility of using magnetite nanoparticles for in vivo MRI of the rat brain. Recent research of ferrofluid bio/medical application in MRI shows dramatic impact of even low concentrations of ferrofluid on the MRI

relaxation times, the longitudinal relaxation time T1 and the spin-spin relaxation time T2, the parameters that form the basis for image contrast in most clinical applications of MRI [83].

5.1.6 Bacterial Threads of Nanomagnets

Magnetotactic bacterial threads can be used to direct the self-assembly of ordered magnetic microstructures [81]. *Bacillus subtilis* strain FJ7 is a mutant strain that can be cultured with intertwining filaments to form weblike structures. A thread was dipped into an aqueous colloidal suspension containing 10 nm diameter magnetite nanoparticles between the cell strings to form threads of magnetic materials with an estimated nanoparticle density of 10^{18} particles/cm³ and a volume fraction of about 7%.

5.2 Complex Magnetic Susceptibility Tensor

The ferrofluid magnetization relaxation equation (3.6) gives the relationship of magnetic field \vec{H} and magnetization \vec{M} in terms of ferrofluid velocity, spin velocity and initial magnetization susceptibility.

In Cartesian geometry, for ferrofluid in a planar channel like Figure 4-2, the velocity and spin velocity of ferrofluid have the form of

$$\vec{v} = v_y \vec{i}_y + v_z \vec{i}_z, \quad \vec{\omega} = \omega_x \vec{i}_x + \omega_y \vec{i}_y + \omega_z \vec{i}_z \quad (5.1)$$

where there is no x directed flow in the channel geometry shown in Figure 4-2 due to the walls at $x=0$ and $x=d$. The magnetic field and the magnetization are

$$\vec{H} = H_x \vec{i}_x + H_y \vec{i}_y + H_z \vec{i}_z \quad (5.2)$$

$$\vec{M} = M_x \vec{i}_x + M_y \vec{i}_y + M_z \vec{i}_z \quad (5.3)$$

In the sinusoidal steady state of AC oscillating or rotating magnetic fields, the magnetic field and the magnetization using complex amplitude notation are

$$\bar{H} = \text{Re}\left\{\hat{H}e^{j\Omega t}\right\}, \quad \bar{M} = \text{Re}\left\{\hat{M}e^{j\Omega t}\right\} \quad (5.4)$$

where Ω is the angular frequency of the applied magnetic field. Using complex amplitude notation, allows time derivatives to be replaced by $j\Omega$

$$\frac{\partial}{\partial t} \rightarrow j\Omega \quad (5.5)$$

By assuming that the channel structure shown in Figure 4-2 has infinite extent in the y and z directions, the partial derivatives with respect to y and z are zero

$$\frac{\partial}{\partial y} = \frac{\partial}{\partial z} = 0 \quad (5.6)$$

and all variables can only depend on x. Considering (5.1)-(5.6), the x, y and z components of the magnetization relaxation equation (3.6) are

$$\begin{aligned} \bar{i}_x : j\Omega\tau\hat{M}_x - (\omega_y\tau\hat{M}_z - \omega_z\tau\hat{M}_y) + \hat{M}_x - \chi_0\hat{H}_x &= 0 \\ \bar{i}_y : j\Omega\tau\hat{M}_y - (\omega_z\tau\hat{M}_x - \omega_x\tau\hat{M}_z) + \hat{M}_y - \chi_0\hat{H}_y &= 0 \\ \bar{i}_z : j\Omega\tau\hat{M}_z - (\omega_x\tau\hat{M}_y - \omega_y\tau\hat{M}_x) + \hat{M}_z - \chi_0\hat{H}_z &= 0 \end{aligned} \quad (5.7)$$

where all the velocity terms drop out as the second term from (3.6) equals zero when the x component of velocity equals zero from (5.1) and the partial derivatives with respect to y and z are zero from (5.6).

$$(\bar{v} \cdot \nabla) \bar{M} = \left(v_x \frac{\partial}{\partial x} + v_y \frac{\partial}{\partial y} + v_z \frac{\partial}{\partial z} \right) \bar{M} = 0 \quad (5.8)$$

The matrix form of (5.7) is

$$\begin{bmatrix} j\Omega\tau + 1 & \omega_z\tau & -\omega_y\tau \\ -\omega_z\tau & j\Omega\tau + 1 & \omega_x\tau \\ \omega_y\tau & -\omega_x\tau & j\Omega\tau + 1 \end{bmatrix} \begin{bmatrix} \hat{M}_x \\ \hat{M}_y \\ \hat{M}_z \end{bmatrix} = \chi_0 \begin{bmatrix} \hat{H}_x \\ \hat{H}_y \\ \hat{H}_z \end{bmatrix} \quad (5.9)$$

which gives the relationship of magnetic field and the magnetization of ferrofluid. The general definition of a scalar magnetic susceptibility is

$$M = \chi H, \quad \chi = \frac{M}{H} \quad (5.10)$$

where H is the magnitude of the magnetic field and M is the magnitude of the magnetization. Here we must define a complex magnetic susceptibility tensor showing the relation between the magnetic field and the magnetization with 3 dimensional components as

$$\begin{bmatrix} \hat{M}_x \\ \hat{M}_y \\ \hat{M}_z \end{bmatrix} = \bar{\bar{\chi}}_m \begin{bmatrix} \hat{H}_x \\ \hat{H}_y \\ \hat{H}_z \end{bmatrix} \quad (5.11)$$

where $\bar{\bar{\chi}}_m$ is the complex magnetic susceptibility tensor and has the form of

$$\begin{aligned} \bar{\bar{\chi}}_m &= \begin{bmatrix} \chi_{xx} & \chi_{xy} & \chi_{xz} \\ \chi_{yx} & \chi_{yy} & \chi_{yz} \\ \chi_{zx} & \chi_{zy} & \chi_{zz} \end{bmatrix} \\ &= \chi_0 \frac{\begin{bmatrix} (j\Omega\tau + 1)^2 + (\omega_x\tau)^2 & \omega_x\omega_y\tau^2 - (j\Omega\tau + 1)\omega_z\tau & \omega_x\omega_z\tau^2 + (j\Omega\tau + 1)\omega_y\tau \\ \omega_x\omega_y\tau^2 + (j\Omega\tau + 1)\omega_z\tau & (j\Omega\tau + 1)^2 + (\omega_y\tau)^2 & \omega_y\omega_z\tau^2 - (j\Omega\tau + 1)\omega_x\tau \\ \omega_x\omega_z\tau^2 - (j\Omega\tau + 1)\omega_y\tau & \omega_y\omega_z\tau^2 + (j\Omega\tau + 1)\omega_x\tau & (j\Omega\tau + 1)^2 + (\omega_z\tau)^2 \end{bmatrix}}{(j\Omega\tau + 1) \left[(j\Omega\tau + 1)^2 + (\omega_x\tau)^2 + (\omega_y\tau)^2 + (\omega_z\tau)^2 \right]} \end{aligned} \quad (5.12)$$

The magnetization of the ferrofluid can thus be controlled by varying the frequency Ω of the driving magnetic field and by controlling the ferrofluid spin velocity by application of magnetic field and/or fluid vorticity. Changing ferrofluid magnetization by changing frequency and/or spin velocity can change the net magnetic field inside and outside the ferrofluid and can thus be used for controlling MR image contrast, heating, and fluid motions.

5.3 Power Dissipation

In the sinusoidal steady state, the complex Poynting's theorem is

$$\nabla \cdot \hat{S} = \nabla \cdot \left(\frac{1}{2} \hat{E} \times \hat{H}^* \right) = \frac{1}{2} \hat{H}^* \cdot (\nabla \times \hat{E}) - \frac{1}{2} \hat{E} \cdot (\nabla \times \hat{H}^*) \quad (5.13)$$

where $\hat{S} = \frac{1}{2} \hat{E} \times \hat{H}^*$ is the complex Poynting vector with units of [watts/m²]. In

the absence of volume current density and with the neglect of the displacement current density because we are in the magnetoquasistatic limit (MQS), (5.13) reduces to

$$\nabla \cdot \hat{S} = \frac{1}{2} \hat{H}^* \cdot (-j\Omega \bar{\mu} \hat{H}) = \frac{-j\Omega \mu_0}{2} \hat{H}^* \cdot (1 + \bar{\chi}_m) \hat{H} = \frac{-j\Omega \mu_0}{2} \left(|\hat{H}|^2 + \hat{H}^* \cdot \bar{\chi}_m \hat{H} \right) \quad (5.14)$$

where $\bar{\mu} = \mu_0 (1 + \bar{\chi}_m)$ is the magnetic permeability tensor, and $\bar{\chi}_m$ is the complex magnetic susceptibility tensor.

In (5.14), $\nabla \cdot \hat{S}$ represents the power per unit volume propagating out of the ferrofluid. In the absence of volume current in ferrofluid and with the applied external magnetic field, the total power propagates into the ferrofluid. The complex power density into the ferrofluid equals the negative of $\nabla \cdot \hat{S}$ and depends on the magnetic field and complex magnetic susceptibility tensor of ferrofluid as

$$P^M = P_d + jP_s = \frac{j\Omega \mu_0}{2} \left(|\hat{H}|^2 + \hat{H}^* \cdot \bar{\chi}_m \hat{H} \right) \quad (5.15)$$

where P^M is the total complex power density into the ferrofluid [watts/m³], P_d is the dissipation power density [watts/m³] and P_s is the time rate of energy density storage in the ferrofluid [watts/m³]. In the sinusoidal steady state (oscillating or rotating magnetic field), the time average of the complex power density in the ferrofluid is

$$\langle P^M \rangle = \langle P_d \rangle + j \langle P_s \rangle = \text{Re} \left\{ \frac{j\Omega\mu_0}{2} \hat{H}^* \cdot \bar{\chi}_m \hat{H} \right\} + j \text{Im} \left\{ \frac{j\Omega\mu_0}{2} \left(|\hat{H}|^2 + \hat{H}^* \cdot \bar{\chi}_m \hat{H} \right) \right\} \quad (5.16)$$

The time average value of the dissipated power density is given as

$$\langle P_d \rangle = -\frac{\Omega\mu_0}{2} \text{Im} \left\{ \hat{H}^* \cdot \bar{\chi}_m \hat{H} \right\} \quad (5.17)$$

The time average value of the time rate of energy storage density is given as

$$\langle P_s \rangle = \frac{\Omega\mu_0}{2} \left[|\hat{H}|^2 + \text{Re} \left\{ \hat{H}^* \cdot \bar{\chi}_m \hat{H} \right\} \right] \quad (5.18)$$

where $\langle P_s \rangle$ is related to the energy density storage in the ferrofluid.

By applying an AC magnetic field (oscillating or rotating magnetic field) in the y-z plane to the geometry shown in Figure 4-2, the velocity and spin velocity given in (5.1) is simplified to

$$\bar{v} = v_y \bar{i}_y + v_z \bar{i}_z, \quad \bar{\omega} = \omega_x \bar{i}_x \quad (5.19)$$

Using complex amplitude notation, an oscillating magnetic field at 45° to the y and z axes is taken to be of the form

$$\bar{H} = H_0 \text{Re} \left\{ (\bar{i}_y + \bar{i}_z) e^{j\Omega t} \right\} \quad (5.20)$$

where H_0 is the amplitude of the magnetic field and Ω is the angular frequency of the applied magnetic field. A CW rotating magnetic field is taken to be the form

$$\bar{H} = \text{Re} \left\{ H_0 (\bar{i}_y + j\bar{i}_z) e^{j\Omega t} \right\} \text{ or } \bar{H} = \text{Re} \left\{ H_0 (-j\bar{i}_y + \bar{i}_z) e^{j\Omega t} \right\} \quad (5.21)$$

and a CCW rotating magnetic field has the form of

$$\bar{H} = \text{Re} \left\{ H_0 (\bar{i}_y - j\bar{i}_z) e^{j\Omega t} \right\} \text{ or } \bar{H} = \text{Re} \left\{ H_0 (j\bar{i}_y + \bar{i}_z) e^{j\Omega t} \right\} \quad (5.22)$$

In the absence of x directed magnetic field H_x , the time average value of the dissipated power density is

$$\begin{aligned}
\langle P_d \rangle &= -\frac{\Omega\mu_0}{2} \text{Im} \left\{ \hat{H}^* \cdot \bar{\chi}_m \hat{H} \right\} \\
&= -\frac{\Omega\mu_0}{2} \text{Im} \left\{ \left(\hat{H}_y^* \bar{i}_y + \hat{H}_z^* \bar{i}_z \right) \cdot \left[\left(\chi_{xy} \hat{H}_y + \chi_{xz} \hat{H}_z \right) \bar{i}_x + \left(\chi_{yy} \hat{H}_y + \chi_{yz} \hat{H}_z \right) \bar{i}_y + \left(\chi_{zy} \hat{H}_y + \chi_{zz} \hat{H}_z \right) \bar{i}_z \right] \right\} \\
&= -\frac{\Omega\mu_0}{2} \text{Im} \left\{ \chi_{yy} |\hat{H}_y|^2 + \chi_{zz} |\hat{H}_z|^2 + \chi_{yz} \hat{H}_z \hat{H}_y^* + \chi_{zy} \hat{H}_y \hat{H}_z^* \right\}
\end{aligned} \tag{5.23}$$

where χ_{ij} is the ij th component of the magnetic susceptibility tensor. Using

(5.12), Equation (5.23) yields

$$\begin{aligned}
\langle P_d \rangle &= \frac{-\Omega\mu_0}{2} \text{Im} \left\{ \chi_{yy} |\hat{H}_y|^2 + \chi_{zz} |\hat{H}_z|^2 + \chi_{yz} \hat{H}_z \hat{H}_y^* + \chi_{zy} \hat{H}_y \hat{H}_z^* \right\} \\
&= \frac{-\Omega\mu_0\chi_0}{2} \text{Im} \left\{ \frac{(j\Omega\tau + 1) \left(|\hat{H}_y|^2 + |\hat{H}_z|^2 \right) + \omega_x\tau \left(\hat{H}_y \hat{H}_z^* - (\hat{H}_y \hat{H}_z^*)^* \right)}{(j\Omega\tau + 1)^2 + (\omega_x\tau)^2} \right\} \\
&= \frac{-\Omega\mu_0\chi_0 \left[(\omega_x\tau)^2 - 1 - (\Omega\tau)^2 \right] \Omega\tau \left(|\hat{H}_y|^2 + |\hat{H}_z|^2 \right) + 2\omega_x\tau \left(1 - (\Omega\tau)^2 + (\omega_x\tau)^2 \right) \text{Im} \left\{ \hat{H}_y \hat{H}_z^* \right\}}{2 \left[\left(1 - (\Omega\tau)^2 + (\omega_x\tau)^2 \right)^2 + 4(\Omega\tau)^2 \right]}
\end{aligned} \tag{5.24}$$

The power of (5.24) dissipated in an oscillating magnetic field is then

$$\langle P_d \rangle = P_0 \frac{(\Omega\tau)^2 \left[1 + (\Omega\tau)^2 - (\omega_x\tau)^2 \right]}{\left[1 - (\Omega\tau)^2 + (\omega_x\tau)^2 \right]^2 + 4(\Omega\tau)^2} \tag{5.25}$$

where $P_0 = \frac{\mu_0\chi_0 H_0^2}{\tau}$ and the power dissipation in an oscillating magnetic field

is independent of the sign of spin velocity ω_x . The power dissipated in a

rotating magnetic field is

$$\begin{aligned}\langle P_d \rangle &= P_0 \frac{(\Omega\tau)(\Omega\tau - \omega_x\tau)}{1 + (\Omega\tau - \omega_x\tau)^2}, \text{ CW} \\ \langle P_d \rangle &= P_0 \frac{(\Omega\tau)(\Omega\tau + \omega_x\tau)}{1 + (\Omega\tau + \omega_x\tau)^2}, \text{ CCW}\end{aligned}\tag{5.26}$$

where $\omega_x > 0$ when the spin velocity is counter clockwise (CCW) and $\omega_x < 0$ when the spin velocity is clockwise (CW). Equation (5.26) can be generalized to

$$\langle P_d \rangle = P_0 \frac{(\Omega\tau)(\Omega\tau + \alpha|\omega_x|\tau)}{1 + (\Omega\tau + \alpha|\omega_x|\tau)^2}\tag{5.27}$$

where α is a rotation selector

$$\alpha = \begin{cases} 1, & \text{when spin velocity co-rotates with the magnetic field.} \\ -1, & \text{when spin velocity counter-rotates with the magnetic field.} \end{cases}\tag{5.28}$$

Equation (5.25) shows that the power dissipated in an oscillating magnetic field could be negative when the spin velocity is higher than $\sqrt{1 + (\Omega\tau)^2}$ as shown in Figure 5-1. Such a high spin velocity could be generated by fluid vorticity. Figure 5-1 also shows that the power dissipation increases with increasing spin velocity and the power dissipation reaches saturation of $P_d / P_0 = 1$ with increasing frequency of applied magnetic field. Equation (5.26) shows that the power dissipated in a rotating magnetic field could be negative when the spin velocity counter rotates to the rotating magnetic field with a value higher than $\Omega\tau$ as shown in Figure 5-2. Such a high spin velocity could be generated by fluid vorticity. Figure 5-2 also shows that the power dissipation reaches saturation with increasing frequency of the applied magnetic field.

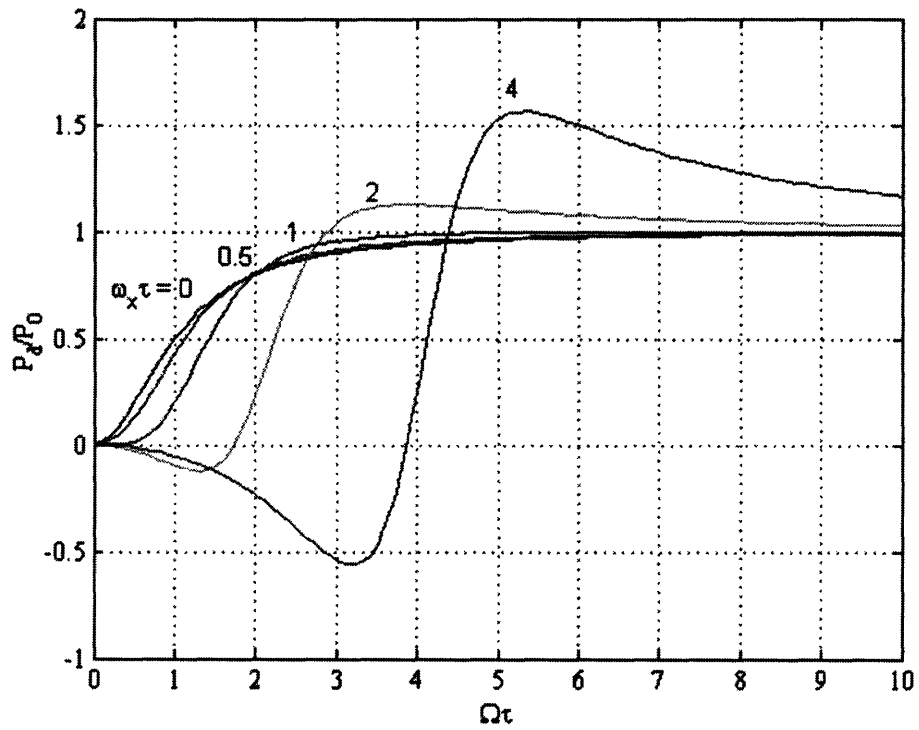


Figure 5-1 Power dissipation density in an oscillating magnetic field versus $\Omega\tau$ as a function of spin velocity $\omega_x\tau$.

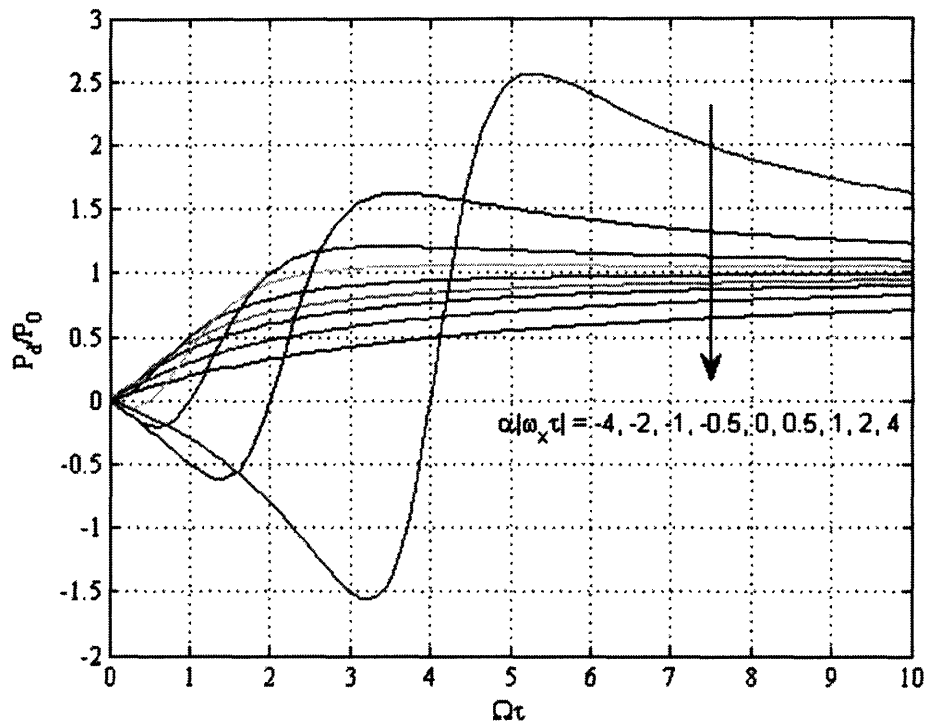


Figure 5-2 Power dissipation density in a rotating magnetic field versus $\Omega\tau$ as a function of spin velocity $\alpha|\omega_x\tau|$, where $\alpha=1$ when the spin velocity co-rotates with the magnetic field, and $\alpha=-1$ when the spin velocity counter-rotates with the magnetic field.

5.4 Impedance Measurements

A set of impedance measurements were designed to demonstrate the complex magnetic susceptibility change with changing spin velocity strength and frequency.

5.4.1 Experiment Setup And Apparatus

Impedance measurements used a 2 pole three phase AC motor stator winding, which can generate a uniform rotating or oscillating magnetic field. As shown in Figure 5-3 a 20 turn 18 gauge copper wire solenoidal coil with 1 inch (2.54

cm) diameter was placed vertically or horizontally in a VWR 400 ml plastic beaker, which was filled with MSG W11 water-based ferrofluid. The plastic beaker was placed in the center region of the 2 pole motor stator winding, which generated the uniform rotating magnetic field as discussed in Appendix A. The impedance of the coil with and without ferrofluid was measured by a HP 4192 LF (5 Hz - 13 MHz) impedance analyzer.

The measurements were taken in a uniform clockwise and counter clockwise rotating magnetic field at frequencies of 100, 200, 300, 400 and 500 Hz with an input current of 0, 1, 2, 3, 3.5, 4, 4.5 and 5 Amps rms for the 2 pole motor stator winding. In the central region of the 2-pole stator, in the absence of ferrofluid each ampere rms produces a magnetic field of 38 Gauss rms, so these input currents correspond to uniform external magnetic fields of 0, 38, 76, 114, 133, 152, 171 and 190 Gauss rms respectively at the mid-height and radial center of the stator winding. These magnetic field measurements were made in the absence of ferrofluid, and therefore reflect the external magnetic field and do not incorporate the demagnetizing effect of the ferrofluid. As comparison the impedance of the coil in air was also measured. In order to investigate the effect of a strong DC magnetic field in the vertical direction transverse to the rotating magnetic field, as might be the case in an MRI scanner, impedance measurements in a uniform rotating magnetic field were also taken with an additional DC magnetic field in the axial vertical direction of the 2 pole motor stator winding with the magnetic field strength of 300, 600 and 900 Gauss for horizontal and vertical positions of the test coil.

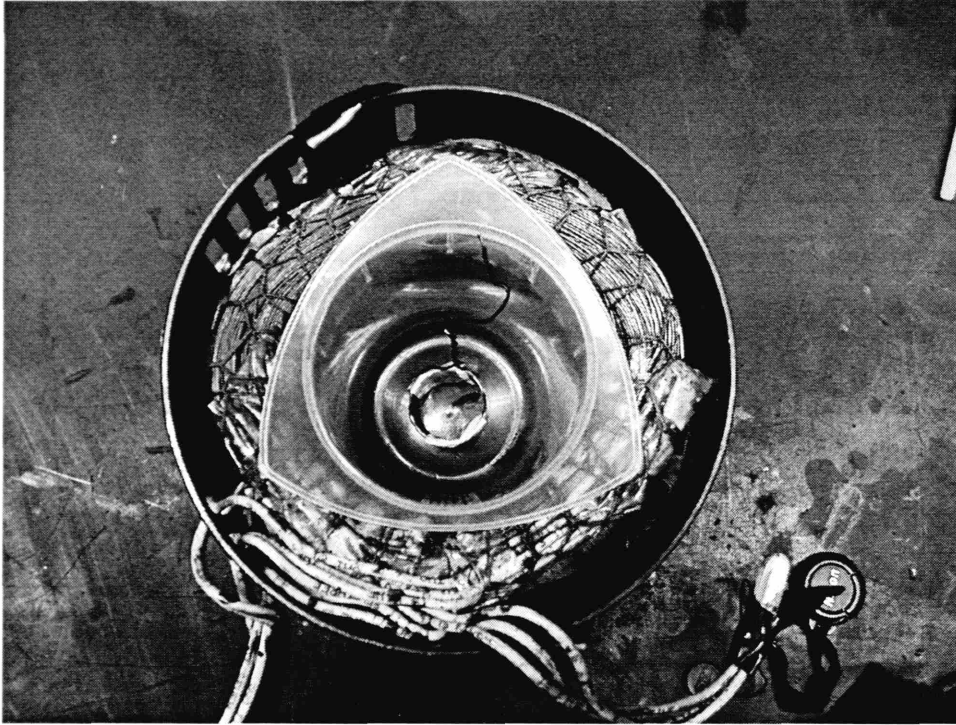


Figure 5-3 Experiment setup of the impedance measurement. A 20 turn 18 gauge copper wire solenoidal coil was placed vertically or horizontally in MSG W11 water-based ferrofluid in a VWR 400 ml plastic beaker. The beaker was centered in a uniform rotating magnetic field generated by a 2 pole three phase AC motor stator winding.

5.4.2 Complex Magnetic Susceptibility And Impedance

An N turn coil with radius r and length d submerged into ferrofluid with a complex magnetic susceptibility $\chi = \chi' - j\chi''$ has an equivalent series LR circuit as shown in Figure 5-4 where the inductance is complex.

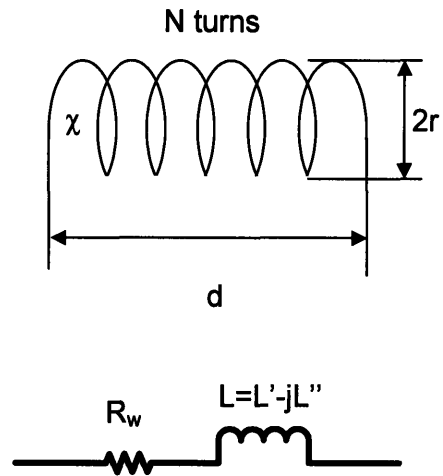


Figure 5-4 Equivalent circuit for an N turn copper wire coil submerged into ferrofluid with a complex magnetic susceptibility $\chi = \chi' - j\chi''$. R_w is the resistance of the coil winding due to the copper wire, while L is the complex inductance.

The magnetic permeability of ferrofluid with a complex magnetic susceptibility $\chi = \chi' - j\chi''$ is

$$\mu = \mu_0(1 + \chi) = \mu' - j\mu'' \quad (5.29)$$

where the real part of the magnetic permeability is $\mu' = \mu_0(1 + \chi')$ and the imaginary part of the magnetic permeability is $\mu'' = \mu_0\chi''$. The complex inductance of the N turn coil with radius r and length d submerged in the ferrofluid is

$$L = \frac{\mu\pi r^2 N^2}{d} = \frac{\pi r^2 N^2}{d}(\mu' - j\mu'') = L' - jL'' \quad (5.30)$$

where the real part of the complex inductance is $L' = \frac{\mu' \pi r^2 N^2}{d}$ and the

imaginary part of the complex inductance is $L'' = \frac{\mu'' \pi r^2 N^2}{d}$. The total

impedance of the coil is

$$Z = R_w + j\Omega_e L = R_w + R_{eff} + j\Omega_e L' = R_{total} + j\Omega_e L' \quad (5.31)$$

where the total resistance of the coil, R_{total} , includes the resistance from the coil winding, R_w , and the dissipation from the imaginary part of the complex

magnetic susceptibility, $R_{eff} = \frac{\mu_0 \Omega_e \pi r^2 N^2 \chi''}{d}$, which is also a function of the

frequency f_e of the applied terminal voltage by the HP impedance analyzer,

where $\Omega_e = 2\pi f_e$. The non-dissipative part of the inductance represents

magnetic energy storage and is given by the real part of the complex magnetic susceptibility,

$$L' = \frac{\mu' \pi r^2 N^2}{d} = \frac{\mu_0 \pi r^2 N^2}{d} (\chi' + 1) \quad (5.32)$$

The complex magnetic susceptibility of the ferrofluid can thus be determined by measuring the impedance of the coil submerged in the ferrofluid.

With the terminal voltage applied across the coil, the impedance analyzer measures the impedance change of the coil at the same frequency of the terminal voltage, which corresponds to the magnetic susceptibility change at the same frequency. Through spin velocity ω_x , due to the applied rotating magnetic field in the y-z plane in the geometry shown in Figure 4-2, the magnetic susceptibility of ferrofluid changes which thus changes the impedance across the coil.

For the vertically placed coil, the measured impedance just depends on the x component of the magnetization. From (5.12) the complex magnetic susceptibility of the vertically placed coil, χ_v , is

$$\chi_v = \chi_{xx} = \frac{\chi_0}{1 + j\Omega_e\tau} = \frac{\chi_0}{1 + (\Omega_e\tau)^2} - j \frac{\chi_0\Omega_e\tau}{1 + (\Omega_e\tau)^2} \quad (5.33)$$

From (5.31) and (5.32) the inductance L'_v and effective resistance R_{eff-v} across of the vertically placed coil are

$$\begin{aligned} L'_v &= \frac{\mu' \pi r^2 N^2}{d} = \frac{\mu_0 \pi r^2 N^2}{d} \left(\frac{\chi_0}{1 + (\Omega_e\tau)^2} + 1 \right) \\ R_{eff-v} &= \frac{\mu_0 \Omega_e \pi r^2 N^2 \chi''}{d} = \frac{\mu_0 \Omega_e \pi r^2 N^2}{d} \frac{\chi_0 \Omega_e \tau}{1 + (\Omega_e\tau)^2} \end{aligned} \quad (5.34)$$

which do not depend on the spin velocity ω_x .

The measured impedance at the radian frequency of the impedance analyzer Ω_e of the horizontally placed coil depends only on the y component of magnetization. From (5.12) the complex magnetic susceptibility of the horizontally placed coil, χ_h , is

$$\begin{aligned} \chi_h = \chi_{yy} &= \frac{\chi_0(1 + j\Omega_e\tau)}{(1 + j\Omega_e\tau)^2 + (\omega_x\tau)^2} \\ &= \frac{\chi_0 [1 + (\Omega_e\tau)^2 + (\omega_x\tau)^2]}{[1 - (\Omega_e\tau)^2 + (\omega_x\tau)^2]^2 + 4(\Omega_e\tau)^2} - j \frac{\chi_0 \Omega_e \tau [1 + (\Omega_e\tau)^2 - (\omega_x\tau)^2]}{[1 - (\Omega_e\tau)^2 + (\omega_x\tau)^2]^2 + 4(\Omega_e\tau)^2} \end{aligned} \quad (5.35)$$

Therefore, the inductance L'_h and effective resistance R_{eff-h} across the horizontally placed coil are

$$L'_h = \frac{\mu' \pi r^2 N^2}{d} = \frac{\mu_0 \pi r^2 N^2}{d} \left(\frac{\chi_0 [1 + (\Omega_e \tau)^2 + (\omega_x \tau)^2]}{[1 - (\Omega_e \tau)^2 + (\omega_x \tau)^2]^2 + 4(\Omega_e \tau)^2} + 1 \right) \quad (5.36)$$

$$R_{eff-h} = \frac{\mu_0 \Omega_e \pi r^2 N^2 \chi''}{d} = \frac{\mu_0 \Omega_e \pi r^2 N^2}{d} \frac{\chi_0 \Omega_e \tau [1 + (\Omega_e \tau)^2 - (\omega_x \tau)^2]}{[1 - (\Omega_e \tau)^2 + (\omega_x \tau)^2]^2 + 4(\Omega_e \tau)^2}$$

which depend on the spin velocity ω_x .

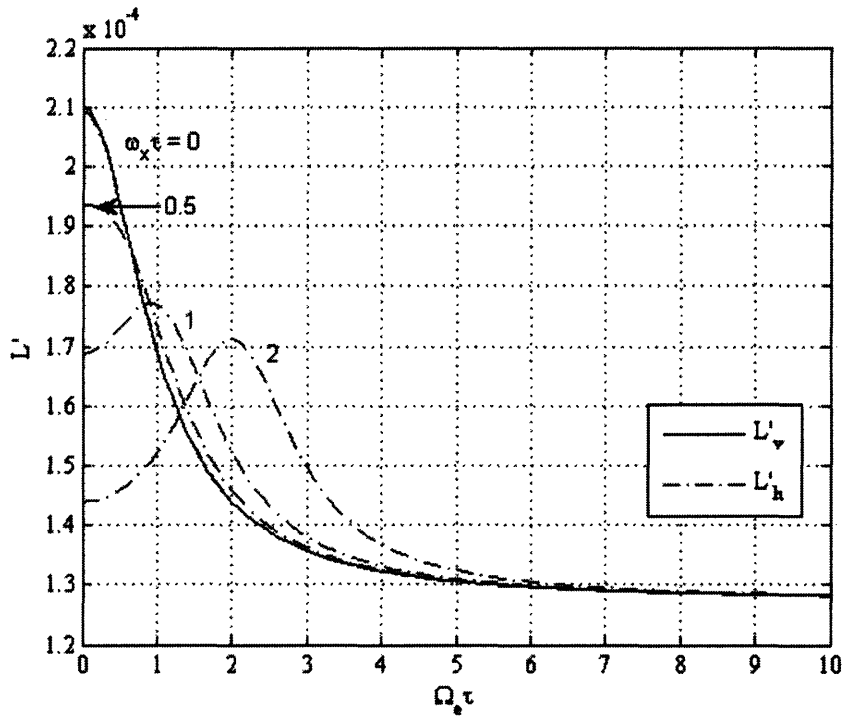


Figure 5-5 The calculated inductance of the solenoidal coil, placed vertically and horizontally in a uniform rotating magnetic field, for various spin velocities ω_x using the equilibrium magnetic susceptibility value of $\chi_0 = 0.56$ for MSG W11 water-based ferrofluid and an estimated value of relaxation time constant $\tau \approx 10 \mu\text{s}$. Note that L'_v is independent of spin velocity ω_x .

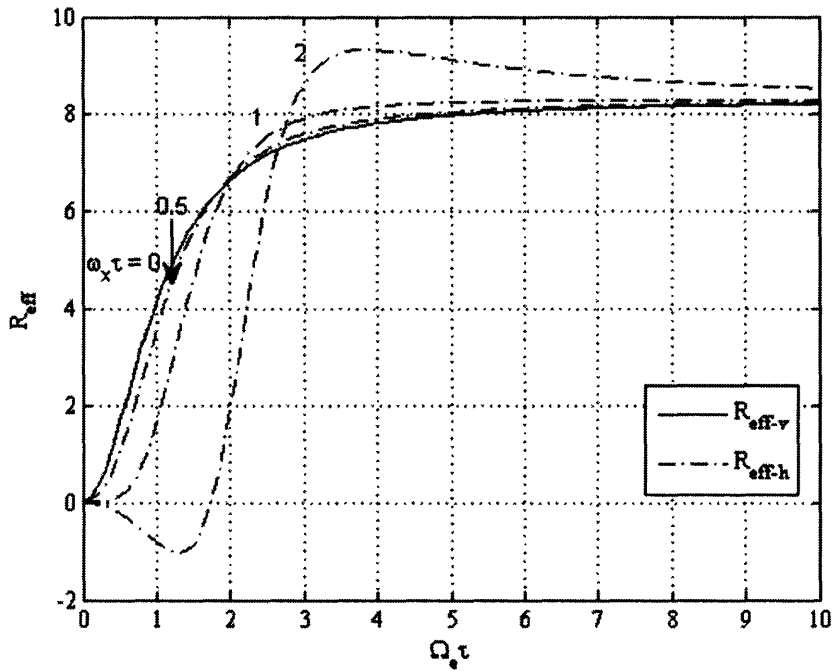


Figure 5-6 The calculated resistance of the solenoidal coil, placed vertically and horizontally in a uniform rotating magnetic field, for various spin velocities ω_x using the equilibrium magnetic susceptibility value of $\chi_0 = 0.56$ for MSG W11 water-based ferrofluid and an estimated value of relaxation time constant $\tau \approx 10 \mu\text{s}$. Note that $R_{\text{eff-v}}$ is independent of spin velocity ω_x .

Figure 5-5 and Figure 5-6 show the calculated inductance and resistance of the solenoidal coil placed vertically and horizontally in a uniform rotating magnetic field for various spin velocities ω_x . The equilibrium magnetic susceptibility value of $\chi_0 = 0.56$ and an estimated relaxation time constant value of $\tau \approx 10 \mu\text{s}$ were used for MSG W11 water-based ferrofluid. The solid curves are the inductance and resistance of the vertically placed coil and the dashed curves are the inductance and resistance of the horizontally placed coil. The inductance and resistance of the vertically placed coil do not depend on spin velocity ω_x while the inductance and resistance of the horizontally placed coil do depend on ω_x . With zero spin velocity, $\omega_x = 0$, the horizontally

placed coil has the same inductance and resistance as the vertically placed coil.

5.4.3 Experimental Results

Figure 5-7 and Figure 5-9 show the inductance change of a horizontal or vertical coil submerged in MSG W11 water-based ferrofluid in a 100 Hz, 38 and 144 Gauss uniform clockwise rotating magnetic field to generate ferrofluid spin velocity. Comparing the inductance change from the coil in air and in the ferrofluid without the rotating magnetic field shows that the MSG W11 water-based ferrofluid has an initial magnetic susceptibility of around 0.6, which reasonably agrees with the initial magnetic susceptibility 0.56 of MSG W11 water-based ferrofluid calculated from the measured magnetization curve using a VSM as shown in Table 2-2. Figure 5-7 and Figure 5-9 also show in a vertically oriented or horizontally oriented coil, that increasing the strength of the rotating magnetic field decreases the real part of the effective complex magnetic susceptibility.

Figure 5-8 and Figure 5-10 similarly show the resistance change of a horizontal or vertical coil submerged in MSG W11 water-based ferrofluid in a 100 Hz, 38 and 144 Gauss uniform clockwise rotating magnetic field. It is shown in Figure 5-8 and Figure 5-10 that the imaginary part of the effective complex magnetic susceptibility decreases with increasing rotating magnetic field strength.

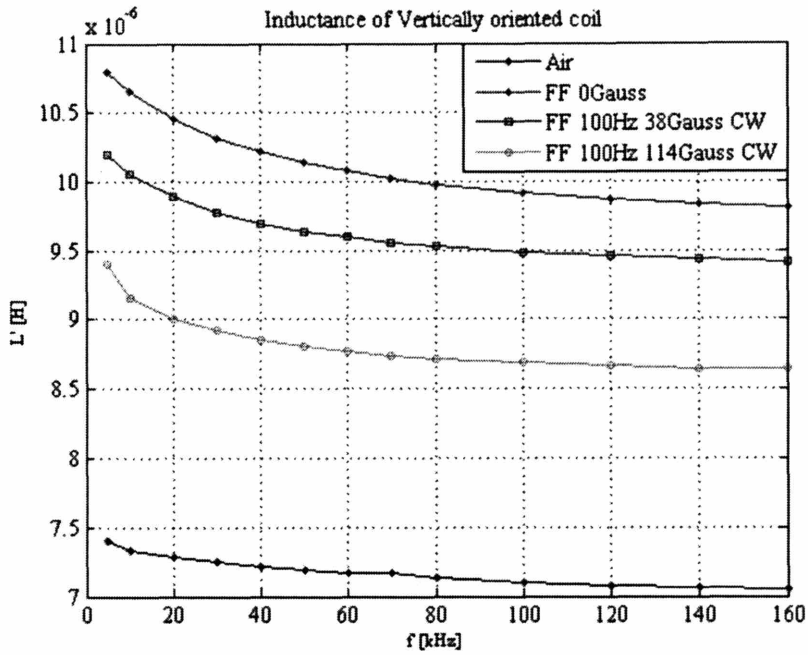


Figure 5-7 The measured inductance change of a vertically oriented coil in a uniform rotating magnetic field in the horizontal plane at 100 Hz.

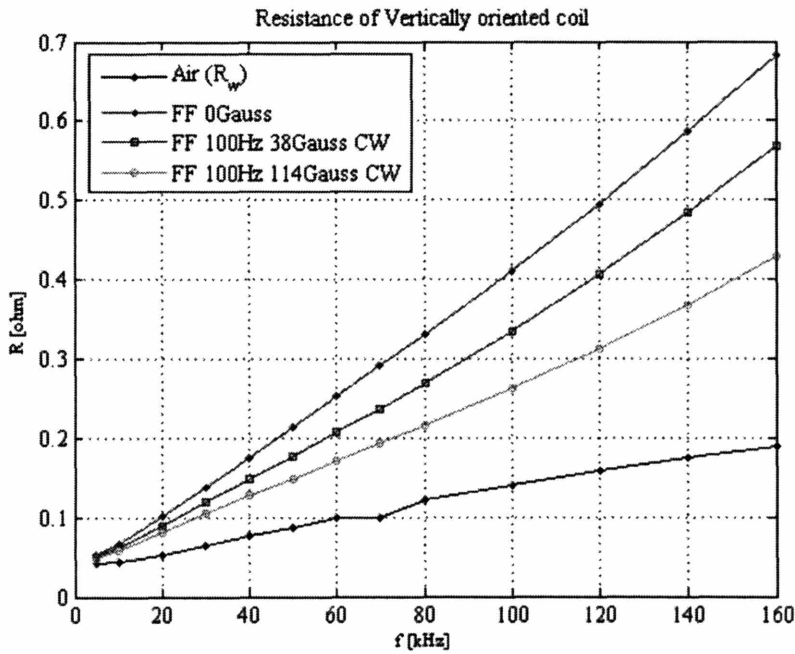


Figure 5-8 The measured resistance change of a vertically oriented coil in a uniform rotating magnetic field in the horizontal plane at 100 Hz.

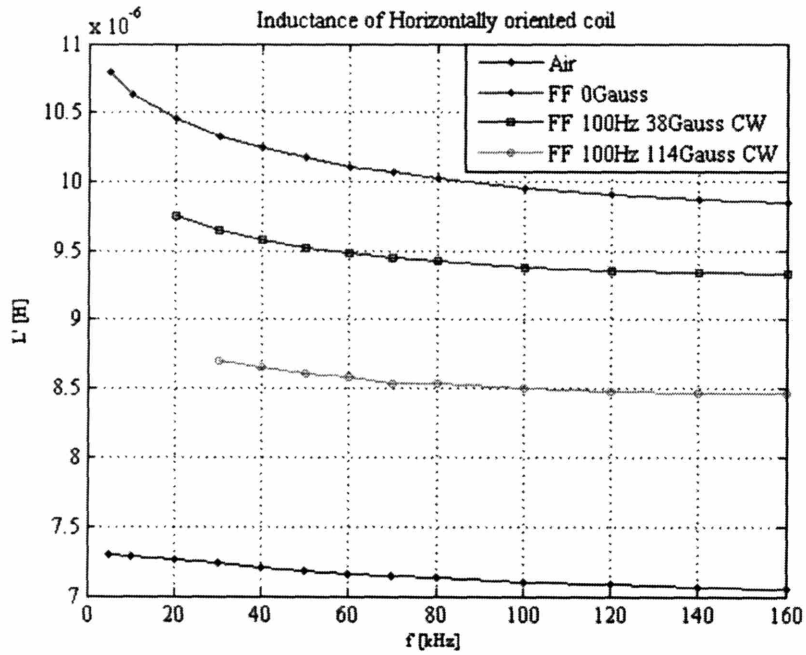


Figure 5-9 The measured inductance change of a horizontally oriented coil in a uniform rotating magnetic field in the horizontal plane at 100 Hz.

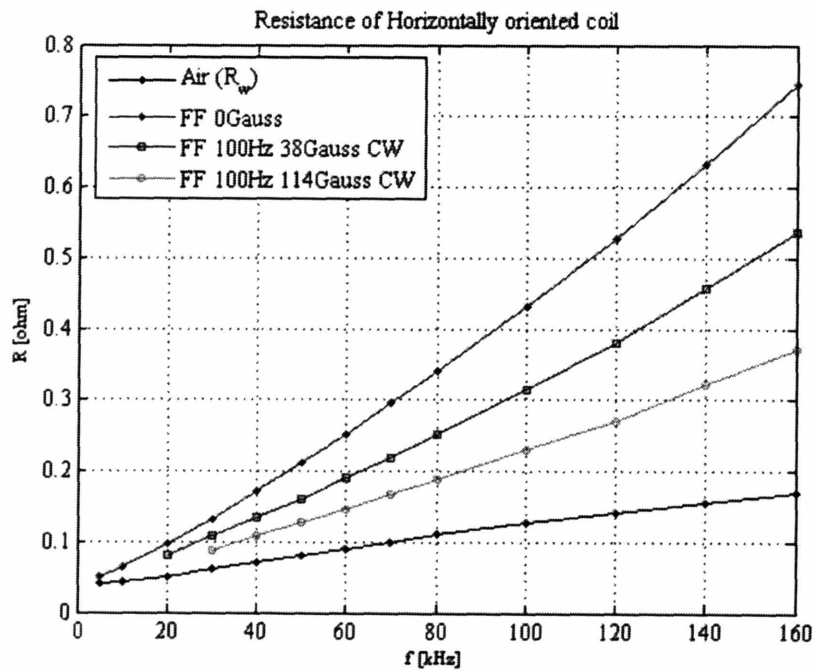


Figure 5-10 The measured resistance change of a horizontally oriented coil in a uniform rotating magnetic field in the horizontal plane at 100 Hz.

Figure 5-11 and Figure 5-13 show the inductance change of the vertical coil submerged in MSG W11 water-based ferrofluid in a 400 Hz 76 and 114 Gauss uniform clockwise rotating magnetic field in the horizontal plane with transverse DC magnetic field of 0, 300, 600, 900 Gauss. It is shown in these two figures that increasing transverse DC magnetic field decreases the real part of the effective complex magnetic susceptibility. This is probably due to the non-linear DC Langevin equilibrium magnetization characteristic of section 2.2, where the incremental magnetic susceptibility decreases as the DC magnetic field increases as the slope of the M-H characteristic decreases as H increases.

Figure 5-12 and Figure 5-14 show the resistance change of the vertical coil submerged in MSG W11 water-based ferrofluid in a 400 Hz 76 and 114 Gauss uniform clockwise rotating magnetic field with transverse DC magnetic field of 0, 300, 600, 900 Gauss. It is shown in these two figures that increasing the transverse DC magnetic field decreases the imaginary part of the effective complex magnetic susceptibility. This is probably due to the non-linear DC Langevin equilibrium magnetization characteristic of section 2.2, where the incremental magnetic susceptibility decreases as the DC magnetic field increases as the slope of the M-H characteristic decreases as H increases.

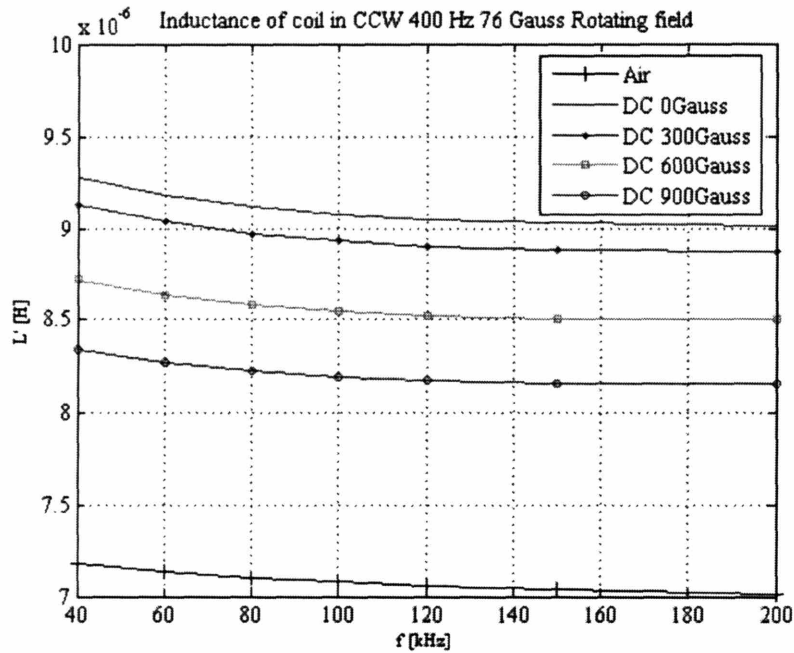


Figure 5-11 The measured inductance change of a horizontally oriented coil in a uniform rotating magnetic field in the horizontal plane at 400 Hz, 76 Gauss for various vertical DC magnetic fields.

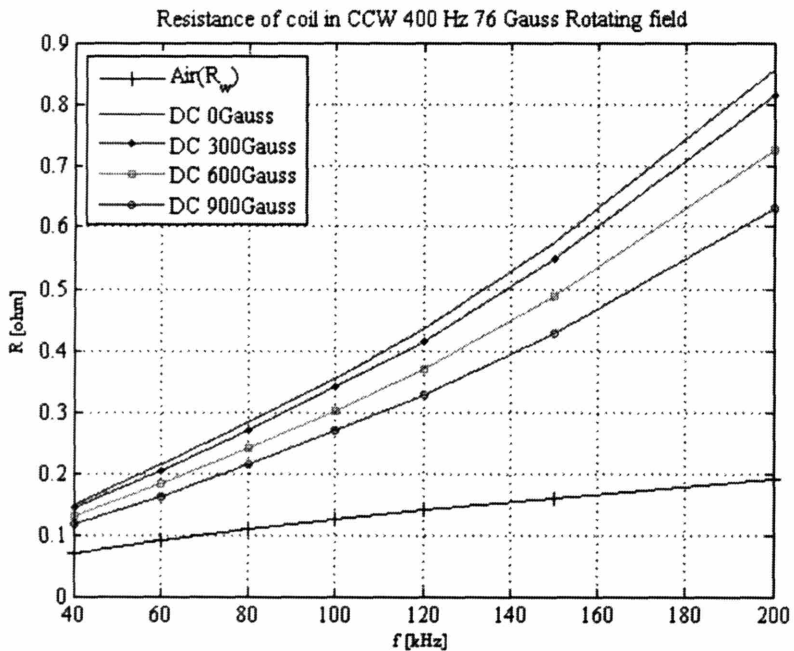


Figure 5-12 The measured resistance change of a horizontally oriented coil in a uniform rotating magnetic field in the horizontal plane at 400 Hz, 76 Gauss for various vertical DC magnetic fields.

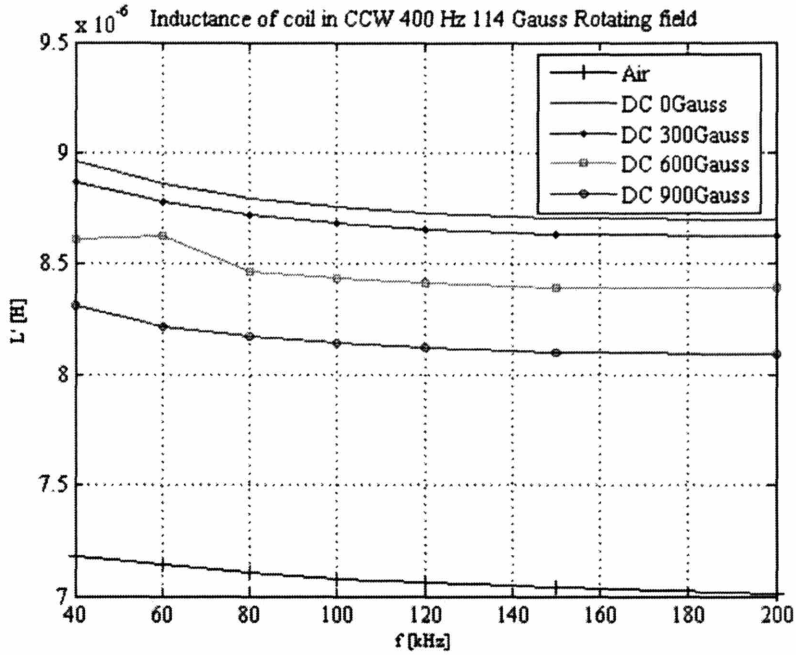


Figure 5-13 The measured inductance change of a horizontally oriented coil in a uniform rotating magnetic field in the horizontal plane at 400 Hz, 114 Gauss for various vertical DC magnetic fields.

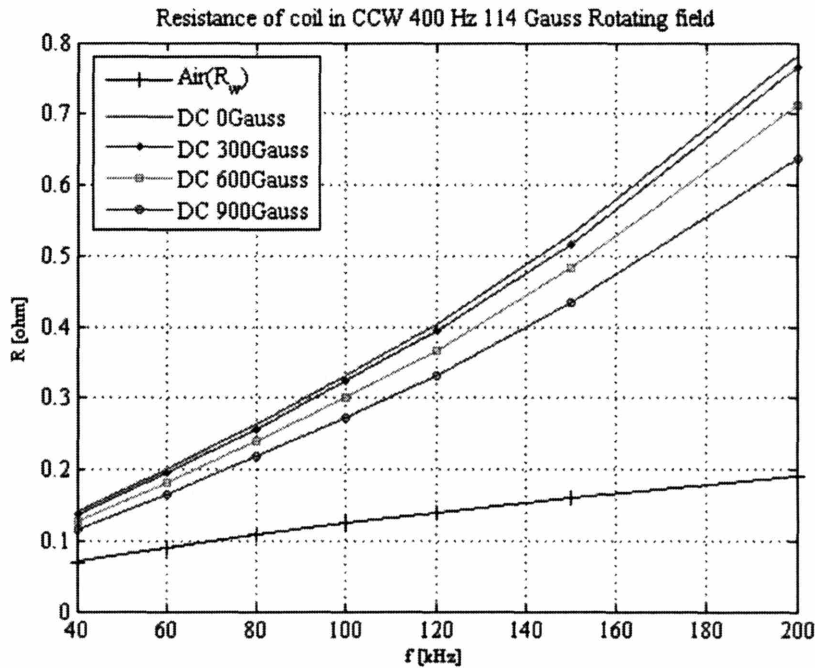


Figure 5-14 The measured resistance change of a horizontally oriented coil in a uniform rotating magnetic field in the horizontal plane at 400 Hz, 114 Gauss for various vertical DC magnetic fields.

The complex magnetic susceptibility tensor of (5.12) derived from the magnetization relaxation equation of (3.6) describes how spin velocity can change ferrofluid complex impedance. Impedance analysis of complex magnetic susceptibility change of ferrofluid in a uniform rotating magnetic field as a function of spin velocity allows calculation of dissipated power and work of oscillating and rotating magnetic fields. Such properties can be used for determining power dissipation for possible hyperthermia biomedical applications, conversion of electrical energy to mechanical work in causing fluid motion, and changes in magnetic field external to the ferrofluid which can be used to improve magnetic resonance image contrast. Preliminary experiments have shown that rotating and DC magnetic fields do change the effective inductance and resistance of a ferrofluid filled coil, but that nonlinear effects due to the equilibrium Langevin magnetization curve needs to be included in future work as the decreasing slope of the M-H characteristic as H increases causes a decrease in the equilibrium magnetic susceptibility.

Chapter 6. Viscometer Torque Measurements in Uniform Rotating Magnetic Fields

The magnetic field induced torque is measured on a rotating or stationary electrically insulating and non-magnetic cylinder in contact with water-based or oil-based ferrofluids subjected to a uniform rotating magnetic field generated by a three-phase AC 2-pole motor stator winding. From the torque measurement on the rotating cylinder with ferrofluid outside, the effective magnetoviscosity of the ferrofluid as a function of the magnetic field amplitude and rotation speed is measured and conditions for effective zero and negative magnetoviscosity are found. For a stationary cylinder, three experimental configurations are examined: 1) ferrofluid entirely within the test cylinder; 2) ferrofluid entirely outside the test cylinder; and 3) ferrofluid both inside and outside the test cylinder. For ferrofluid entirely within the test cylinder, the torque is found to scale linearly with volume, and to be a function of the applied magnetic field amplitude, frequency and direction of rotation, with torque in the same direction as the magnetic field rotation vector, in agreement with recently derived analysis [42]. For ferrofluid entirely outside the test cylinder, the torque is in the direction opposite to the magnetic field rotation vector. When the ferrofluid is both inside and outside the cylinder the measured torque is the approximate algebraic sum of the measured torques for ferrofluid entirely inside and entirely outside the test cylinder with net torque in the opposite direction to the magnetic field rotation vector.

6.1 Experimental Apparatus

A Brookfield Model LVDV-I+ Couette viscometer was used as a torque meter, shown in Figure 6-1. When a fixed rotation speed is selected, the Lexan (polycarbonate) spindle rotates counterclockwise and the viscometer will apply the necessary torque in order to keep it rotating at the specified speed. When

the magnetic field induced shear stress on the spindle is in the clockwise direction, *i.e.*, in the direction opposite to spindle rotation, it is harder to turn the spindle at the specified speed; therefore the viscometer applies a higher torque, above and beyond the torque required to shear the fluid in the absence of a field and it records an increase of effective ferrofluid viscosity. On the other hand, when the magnetic field induced shear stress on the spindle is in the counter clockwise direction, *i.e.*, in the same direction as spindle rotation, it is easier to rotate the spindle at the specified speed; therefore the viscometer applies a lower torque, as compared to the torque required to shear the fluid in the absence of a field and the viscometer records a decrease of effective ferrofluid viscosity. Furthermore, the Brookfield viscometer measures the torque value applied to the attached spindle and for ferrofluid outside the spindle calculates the viscosity of the test fluid at the applied spindle rotating speed. Both the torque and the viscosity values can be displayed at the same time. At a fixed spindle rotation speed the torque required to rotate the spindle is proportional to the fluid viscosity outside the spindle.

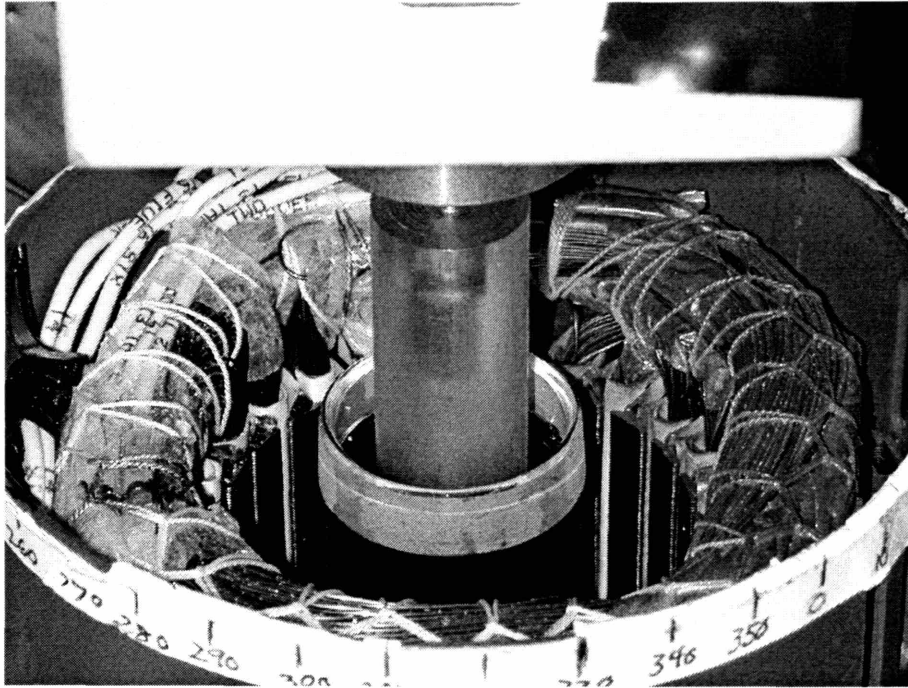


Figure 6-1 The experimental setup to measure magnetic field induced torque on a rotating or stationary Lexan spindle using the 2-pole motor stator winding to impose a uniform magnetic field. The Lexan spindle is connected to the viscometer and is centered in the beaker of ferrofluid, which is itself centered within the motor stator winding.

Figure 6-2 shows the experimental setup for the torque measurements with a stationary cylinder in a 2 pole uniform magnetic field. A 10 ml syringe was used as a test spindle which can hold ferrofluid inside. This setup was also used in the case of ferrofluid outside and both inside and outside the spindle. The rotating magnetic field setup and magnetic field measurements are described in Appendix A.

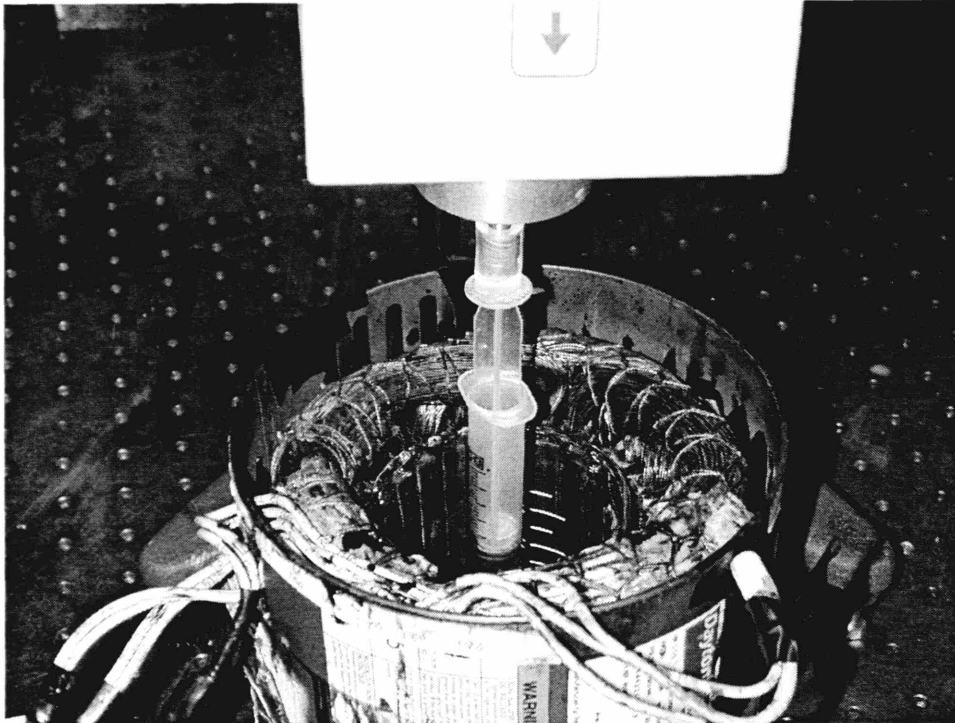


Figure 6-2 The experimental setup for spindle torque measurements with a stationary cylinder using the 2-pole motor stator winding to impose a uniform magnetic field. The 10 ml syringe, which is used as a test spindle with ferrofluid inside and/or outside, is connected to the viscometer and is centered in the beaker of ferrofluid, which is itself centered within the motor stator winding.

6.2 Viscometer Torque and Magnetoviscosity

Relationship in a Couette Viscometer

6.2.1 Viscous Shear Stress

The Couette viscometer measures the torque to maintain the fixed rotation speed of a spindle in the test fluid in the cylindrical container shown in Figure 6-3. The spindle with radius a rotates in the counter-clockwise direction with spin velocity ω , centered in the cylindrical ferrofluid container with radius b .

The fluid Reynolds' number for a cylinder of radius a rotating at angular speed

ω is $Re = \frac{\rho v a}{\eta} = \frac{\rho \omega a^2}{\eta}$, where $v = \omega a$ is the linear velocity of the spindle

surface. The Reynolds' number is a ratio of fluid inertial force to viscous force. In general, high Reynolds' number flow leads to fluid instability and turbulence [34]. The Brookfield viscometer instruction manual gives a critical Reynolds' number of $Re \approx 50$ for transition to turbulence.

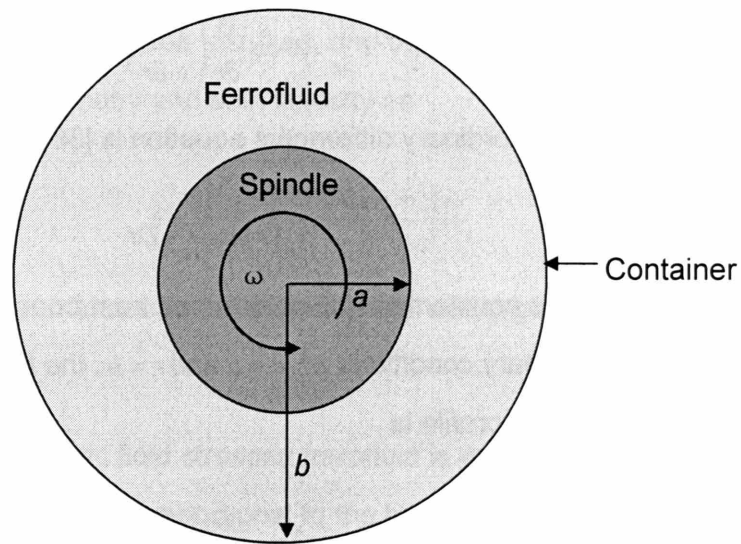


Figure 6-3 The experimental setup of the Couette viscometer. The spindle with radius a rotates in the counter-clockwise direction with spin velocity ω , centered in the cylindrical ferrofluid container with radius b .

In the absence of magnetic field, consider laminar ferrofluid flow between the two concentric cylindrical walls of the spindle with radius a and the container inner wall with radius b , where the spindle rotates with spin velocity ω as shown in Figure 6-2 and Figure 6-3. The flow velocity at the stationary container wall is $\bar{v}(r = b) = 0$, and the flow velocity at the spindle surface is

$$\bar{v}(r = a) = \omega a \bar{i}_\phi.$$

In the absence of body forces, the Navier-Stokes equation for an incompressible fluid ($\nabla \cdot \bar{v} = 0$) is given as

$$\rho \frac{D\bar{v}}{Dt} = \rho \left(\frac{\partial \bar{v}}{\partial t} + (\bar{v} \cdot \nabla) \bar{v} \right) = -\nabla p + \eta \nabla^2 \bar{v} \quad (6.1)$$

where p is the ferrofluid pressure, which is independent of ϕ , $\frac{\partial p}{\partial \phi} = 0$, and η

is the fluid viscosity. In the steady state $\frac{\partial \bar{v}}{\partial t} = 0$ and by symmetry $\frac{\partial v_\phi}{\partial \phi} = 0$. With

$\bar{v} = v_\phi(r) \bar{i}_\phi$ the Navier-Stokes equation becomes

$$[\nabla^2 \bar{v}]_\phi = 0 \Rightarrow \frac{\partial}{\partial r} \left(\frac{1}{r} \frac{\partial}{\partial r} (r v_\phi) \right) = 0 \quad (6.2)$$

The solution for this ordinary differential equation is [36]

$$v_\phi(r) = \frac{C}{r} + Dr \quad (6.3)$$

where C and D are constants to be determined from boundary conditions.

Applying the boundary conditions at $r = a$ and $r = b$, the fully-developed laminar fluid velocity profile is

$$v_\phi(r) = \frac{\omega b a^2}{b^2 - a^2} \left(\frac{b}{r} - \frac{r}{b} \right) \quad (6.4)$$

For an incompressible, isotropic, Newtonian fluid the viscous stress T_{ij}^V at a boundary is proportional to fluid viscosity as

$$T_{ij}^V = \eta \left(\frac{\partial v_i}{\partial x_j} + \frac{\partial v_j}{\partial x_i} \right) \quad (6.5)$$

where i is the direction of the stress and j is the normal direction to the stress surface. To calculate the shear stress on the spindle wall at $r = a$, with $i = \phi$ and $j = r$, the viscous shear stress is given as [84]

$$T_{\phi r}^V = \eta \left(r \frac{\partial}{\partial r} \left(\frac{v_\phi}{r} \right) \right) \Big|_{r=a} = -2\eta \frac{\omega b a^2}{b^2 - a^2} \frac{b}{r^2} \Big|_{r=a} = -2\eta \frac{\omega b^2}{b^2 - a^2} \quad (6.6)$$

The total force on the spindle is

$$f_{\phi}^V = T_{\phi r}^V 2\pi aL = -2\eta \frac{\omega b^2}{b^2 - a^2} 2\pi aL \quad (6.7)$$

where L is the effective length of the spindle submerged in the ferrofluid. The torque on the rotating spindle is then

$$L_z = f_{\phi}^V a = -\frac{4\pi a^2 b^2 \eta L \omega}{b^2 - a^2} \quad (6.8)$$

The Couette viscometer measures the torque on the rotating spindle, which is proportional to the viscosity of the test fluid, and calculates the viscosity of the test fluid in the fixed geometry and spin velocity as

$$\eta = \left| \frac{L_z}{K} \right|, \quad K = -\frac{4\pi a^2 b^2 L \omega}{b^2 - a^2} \quad (6.9)$$

where K is the constant related to the experimental setup geometry and spin velocity of the spindle.

The viscosity with magnetic field stressed ferrofluid is the effective magnetoviscosity and is also proportional to the torque on the spindle. By applying the magnetic field to the ferrofluid, an extra shear stress or torque is induced on the surface of the spindle. The Couette viscometer measures this torque and uses (6.9) to calculate the effective magnetoviscosity of the ferrofluid. Therefore, the magnetic field induces the effective viscosity η_m on the fluid viscosity shown in (6.10)

$$\eta_m = \eta + \Delta\eta = \left| \frac{L_z + L_{zm}}{K} \right| \quad (6.10)$$

where η_m is the effective magnetoviscosity of ferrofluid in the magnetic field, $\Delta\eta$ is the effective viscosity change due to the magnetic field, L_z is the viscous torque necessary to rotate the cylinder in the absence of magnetic

field and L_{zm} is the additional torque on the rotating cylinder from magnetic field induced flow.

6.2.2 Magnetic Field Shear Stress

The surface-excess magnetic torque at the wall-fluid interface may be calculated by evaluating the jump in the “magnetic stress” tensor (or the so-called Maxwell stress) across the wall-fluid interface. Use of this mathematical technique circumvents the need to know the exact distribution of magnetic fields in this region with rapidly varying magnetic properties. The Maxwell stress applicable to an incompressible ferrofluid is given by [1, 29]

$$T_{ij}^M = H_i B_j - \frac{1}{2} \delta_{ij} \mu_0 H_k H_k \quad (6.11)$$

where δ_{ij} is known as the Kronecker delta, being zero if $i \neq j$ and one if $i = j$.

We are interested in determining the ϕ -directed component of the jump in the Maxwell stress tensor across the ferrofluid-spindle wall interface at $r = a$ (the r -directed component is of no consequence as it does not contribute to the z -directed torque, which is the experimentally measurable quantity). The ϕ -directed surface magnetic force per unit area on the cylindrical wall, F_ϕ^M , is given by the jump in the ϕr -component of the Maxwell stress

$$\begin{aligned} F_\phi^M &= T_{\phi r}^M (r = a^+) - T_{\phi r}^M (r = a^-) \\ &= (B_r H_\phi)|_{r=a^+} - (B_r H_\phi)|_{r=a^-} \end{aligned} \quad (6.12)$$

However, the jump conditions on the magnetoquasistatic field require that the normal component of \bar{B} , B_r , and in the absence of surface current, the tangential component of \bar{H} , H_ϕ , be continuous across the spindle wall-fluid

interface. Therefore, there is no surface-excess magnetic force in the azimuthal direction

$$F_{\phi}^M = 0 \quad (6.13)$$

and therefore no magnetic field surface torque on the cylindrical container wall. The spindle torque is only due to the viscous force cause by magnetic field induced flow and flow induced by spindle rotation.

6.2.3 Measurement Procedure

By measurement of the total torque on the spindle with application of magnetic field, the magnetoviscosity can be evaluated. From (6.10), if the magnetic field induced flow is in the same direction as spindle rotation, the magnetoviscosity is less than the fluid viscosity as the viscometer has to exert less torque to maintain the set speed; if the magnetic field induced flow is in the opposite direction of spindle rotation, the magnetoviscosity is greater than the fluid viscosity as the viscometer has to exert greater torque to maintain the set speed; if the magnetic field induced flow is in the same direction and same speed as spindle rotation, the magnetoviscosity is zero as the viscometer exerts no torque to maintain the set speed; if the magnetic field induced flow is greater than the spindle speed and in the same direction, the magnetoviscosity is negative as the viscometer must exert an opposite torque to maintain the set speed.

For our experiments to measure the effective magnetoviscosity and to demonstrate zero and negative magnetoviscosity values, an insulating Lexan (polycarbonate) spindle was used at a fixed rotation speed of 100 rpm (counterclockwise) as shown in Figure 6-1. To measure the torque only induced by the rotating magnetic field the spindle was set to remain stationary, hence, with zero applied magnetic field no torque is required from the viscometer to restrain the spindle. Under conditions for which a clockwise

magnetic field induced shear stress arises, the viscometer exerts a balancing counter-clockwise torque to keep the spindle stationary and the viscometer records a torque increase which is registered as a positive torque, whereas for a counterclockwise shear stress a negative torque will be measured. The range of measurable torque for our Brookfield viscometer is $-10.0 \mu\text{N}\cdot\text{m}$ to $67.3 \mu\text{N}\cdot\text{m}$, where a negative torque means the viscometer exerts a clockwise torque to balance a magnetic field induced counter-clockwise torque. This occurs when the magnetic field induced counter clockwise shear stress would drive the spindle at a velocity greater than its speed with zero magnetic field.

A 2 pole motor stator winding with balanced three phase AC sinusoidal currents was used to produce clockwise and counter-clockwise uniform magnetic fields in the absence of ferrofluid (Figure 6-3). The machine inner bore has 78 mm diameter and 63.8 mm height. In the effective magnetoviscosity measurements, a Lexan spindle of 25 mm diameter was used within a beaker of ferrofluid of 38mm diameter, creating an annular gap of 6.5 mm with the spindle in the center of the beaker as shown in Figure 6-1. A metal spindle is not used in order to avoid eddy currents and 'induction motor' torque in rotating magnetic fields. 10 ml and 20 ml syringes were used in the torque measurement experiments as ferrofluid filled cylindrical spindles, having an inner diameter of 13.9 mm and 18.17 mm respectively. The syringes were filled with ferrofluid so that the height of the ferrofluid in either syringe equaled 62.41 mm. The syringes were placed so that the fluid was radially and axially centered along the axis of the motor stator winding. A 200 ml beaker was used in this experiment for the case when ferrofluid was outside the test spindle cylinder. The diameter of the beaker was 52.15 mm. Measurements were taken for both water-based and oil-based ferrofluids.

The effective magnetoviscosity measurements were taken at frequencies of 5, 10, 50, 100 and 500 Hz with an input current of 0, 1, 2, 3, 4 and 5 Amps peak for the case that ferrofluid is entirely outside the test cylinder. In the 2-pole

stator, these input currents correspond to uniform external magnetic fields of 0, 38, 76, 114, 152 and 190 Gauss peak respectively at the middle level and radial center of the stator winding. The stationary spindle torque measurements were taken at frequencies of 100, 200, 300, 400 and 500 Hz with an input current of 1, 2, 3, 3.5, 4, 4.5 and 5 Amps rms for the case that ferrofluid is entirely inside the test cylinder, entirely outside the test cylinder and both inside and outside the test cylinder. In the central region of the 2-pole stator, in the absence of ferrofluid each ampere rms produces a magnetic field of 38 Gauss rms, so these input currents correspond to uniform external magnetic fields of 0, 38, 76, 114, 133, 152, 171 and 190 Gauss rms respectively at the mid-height and radial center of the stator winding. These magnetic field measurements were made in the absence of ferrofluid, and therefore reflect the external magnetic field and do not incorporate the demagnetizing effect of the ferrofluid. The clockwise rotating magnetic field is applied for the case that ferrofluid is entirely inside the test spindle and counterclockwise for the case that ferrofluid is entirely outside the test spindle and for measurements where ferrofluid is both inside and outside the test cylinder. Under these conditions the viscometer torque will be counter-clockwise allowing the full range of torque measurements up to 67.3 $\mu\text{N}\cdot\text{m}$.

Measurements show that for ferrofluid entirely inside the test cylinder, the viscometer torque points in the same direction as the magnetic field rotation vector (co-rotation), whereas for ferrofluid entirely outside the cylinder the torque points in the direction opposite to the field rotation vector (counter-rotation). When the ferrofluid is both inside and outside the test cylinder, the measured viscometer torque is the approximate algebraic sum of the viscometer torques for ferrofluid entirely inside and entirely outside the test cylinder and is in the direction opposite to the magnetic field rotation vector.

For higher frequencies, some measurements contain fewer data points. This is either because the torque was beyond the maximum Brookfield torque of 67.3 $\mu\text{N}\cdot\text{m}$ or because the power supply across the motor winding terminals could not deliver the required current as the inductive impedance was too high. At these higher frequencies, the inductive reactance $L\Omega$ increases with field radian frequency Ω and limits the current that can be supplied to the stator winding. However by adding an appropriate capacitor, C , in series with the motor winding, a resonant circuit was created so that the capacitive reactance $1/C\Omega$ cancels the inductive reactance, *i.e.*, when $L\Omega = 1/C\Omega$, thereby eliminating current limitations at higher frequencies. This modification to the experimental setup was needed at frequencies of 400Hz and above. However, at higher resonance frequencies, the voltage across the stator winding becomes too large for safe operation

6.3 Measurements of Viscometer Torque during Spin-Up Flow

6.3.1 Effective Magnetoviscosity Measurements

Measurements with the spindle rotating at 100 rpm (counter-clockwise) with surrounding ferrofluid demonstrates that the measured spindle torque increases for co-rotation of spindle and magnetic field and decreases for counter-rotation including zero and negative values as shown in Figure 6-4. Since the spindle torque is proportional to ferrofluid viscosity like that given in equation (6.9), the zero and negative torque values correspond to zero and negative viscosity.

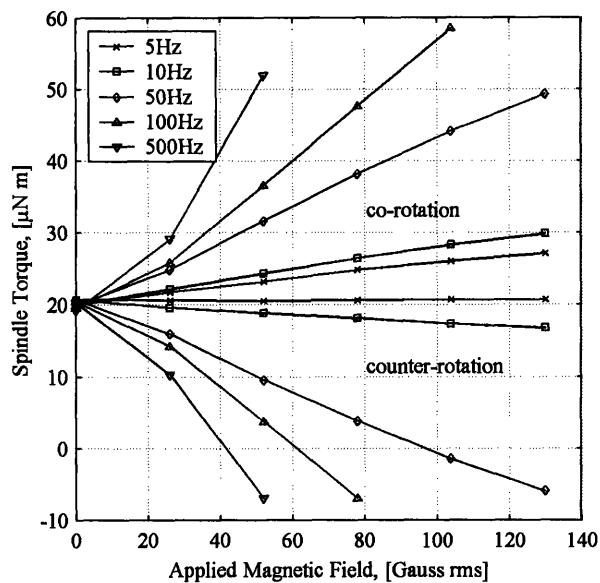


Figure 6-4 Measured spindle torque at 100 rpm counter-clockwise with surrounding water-based ferrofluid as a function of magnetic field amplitude, frequency, and direction of rotation. CCW spindle rotation shows a torque increase for co-rotation of spindle and magnetic field and a torque decrease including zero and negative values with counter-rotation, corresponding to zero and negative viscosity [33, 34, 42].

The viscometer measures the torque required to balance the viscous resistance to spindle rotation and converts it to an effective magnetoviscosity based on the spindle geometry as described in section 6.2.1; therefore the effective magnetoviscosity is directly proportional to the measured torque value. These measurements report viscometer viscosity readings that include zero and negative values as shown in Figure 6-4. Such paradoxical readings occur when the magnetic body force on the ferrofluid induced flow is in the same direction as the rotating spindle (counter clockwise) thus requiring less torque from the viscometer to turn the spindle, causing the viscometer to read out a decreased viscosity. If the ferrofluid exerts a shear stress on the spindle that equals that necessary to turn the spindle at a constant rate, no torque is required from the viscometer and it records a zero viscosity. The cylinder

rotation is then entirely due to the magnetic-field-induced flow. A greater magnetic field induced fluid shear stress requires the viscometer to reverse torque direction to maintain constant spindle rotation and the viscometer reads a negative value. When ferrofluid flow is in the opposite direction to the spindle rotation (clockwise) more torque is required from the viscometer which reads that the ferrofluid viscosity has increased.

When the spindle rotates at 100 rpm, the Reynolds' number is $Re \approx 280$, putting the flow into the turbulent region. The Brookfield viscometer instruction manual states that the measured torque will be higher than the actual torque. Thus, the measurements in Figure 6-4 provide an upper-bound for the true torque.

6.3.2 Stationary Spindle Torque Measurements

In order to more accurately investigate magnetic field induced spindle torque under laminar flow conditions, measurements were continued with a stationary spindle so that there is no torque with zero magnetic field. Therefore, any measured torque is only magnetic field induced. The rotating magnetic field causes ferrofluid flow that induces a viscous shear stress on the spindle. The flow Reynolds' number between the stationary inner and outer cylinder walls is generally small. Figure 6-5 presents representative data for the 133 Gauss rms magnetic field induced torque vs. ferrofluid volume for various frequencies in the range of 100 Hz – 500 Hz, using water-based ferrofluid with the 20 ml syringe as spindle cylinder. The essentially linear variation of magnetic torque vs. fluid volume in Figure 6-5 illustrates that the magnetic field induced torque is proportional to the volume of the ferrofluid inside the 20 ml syringe spindle. This linearity with volume indicates that free surface effects are not important as flow caused by magnetic forces due to surface deformations would not scale with volume.

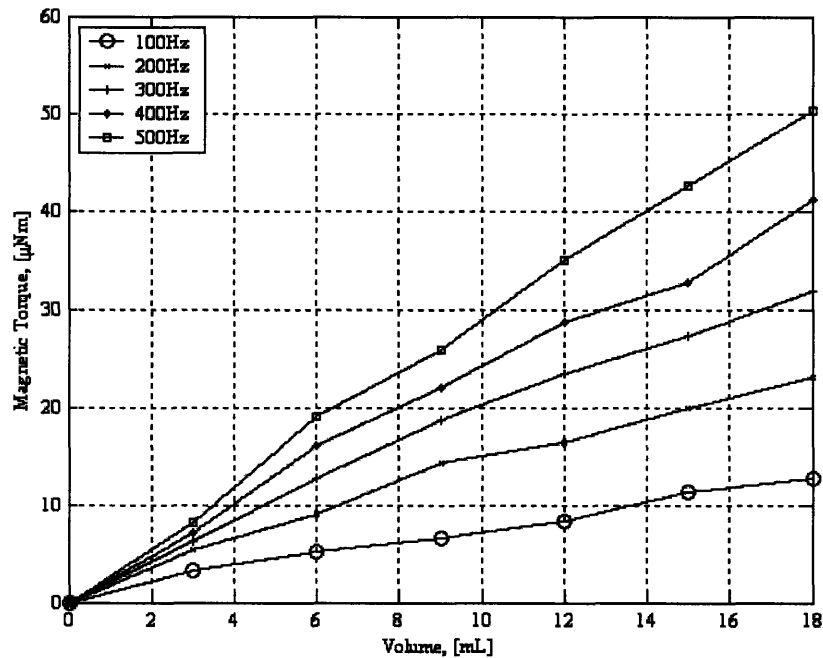


Figure 6-5 Viscometer torque required to restrain 20 ml stationary spindle syringe with water-based ferrofluid inside the spindle with 133 Gauss rms applied magnetic field as a function of volume of ferrofluid for various magnetic field frequencies.

The same sequences of experiments were repeated using water-based ferrofluid with the 10ml and 20ml syringes and oil-based ferrofluid with 10 ml and 20 ml syringes with magnetic field amplitude from 0 to 190 Gauss rms and frequency from 100 to 500 Hz with similar results.

Figure 6-6 presents the measured torque vs. magnetic field amplitude for various frequencies in the range of 100 Hz – 500 Hz, using water-based ferrofluid with the 10 ml syringe as spindle cylinder, when the ferrofluid is entirely inside the syringe, entirely outside the syringe and both inside and outside the syringe respectively. Figure 6-6 shows that the magnitude of the measured torque, and therefore the magnetic-field-induced shear stress, increases with magnetic field amplitude and frequency. At the same time Figure 6-6 also shows that the approximate measured torque, when ferrofluid

is both inside and outside the syringe, is the approximate algebraic sum of the torques for ferrofluid entirely inside and entirely outside the syringe, with net negative spindle torque indicating that the outside counter-rotation flow has larger magnitude torque than the inside co-rotation flow.

The same sequences of experiments were repeated using water-based ferrofluid with the 20 ml syringe and oil-based ferrofluid with 10 ml and 20 ml syringes with similar results as shown in Figure 6-7-Figure 6-9.

The peak measured torque values in Table 6-1 for water-based MSG W11 and oil-based EFH1 ferrofluids shows that torques in a 20 ml spindle are stronger than in a 10 ml spindle, because the 20 ml spindle has a larger radius and more ferrofluid.

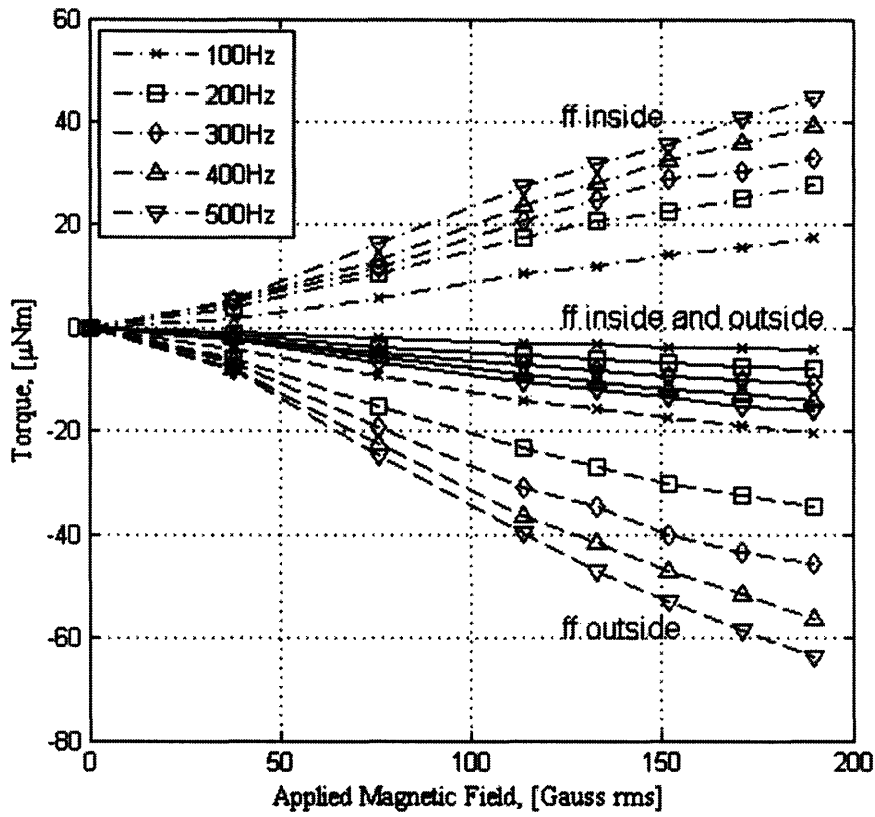


Figure 6-6 Viscometer torque required to restrain the 10 ml stationary spindle syringe with 9.5 ml MSG W11 water-based ferrofluid as a function of uniform magnetic field amplitude and frequency with ferrofluid entirely inside, entirely outside, and both inside and outside the syringe.

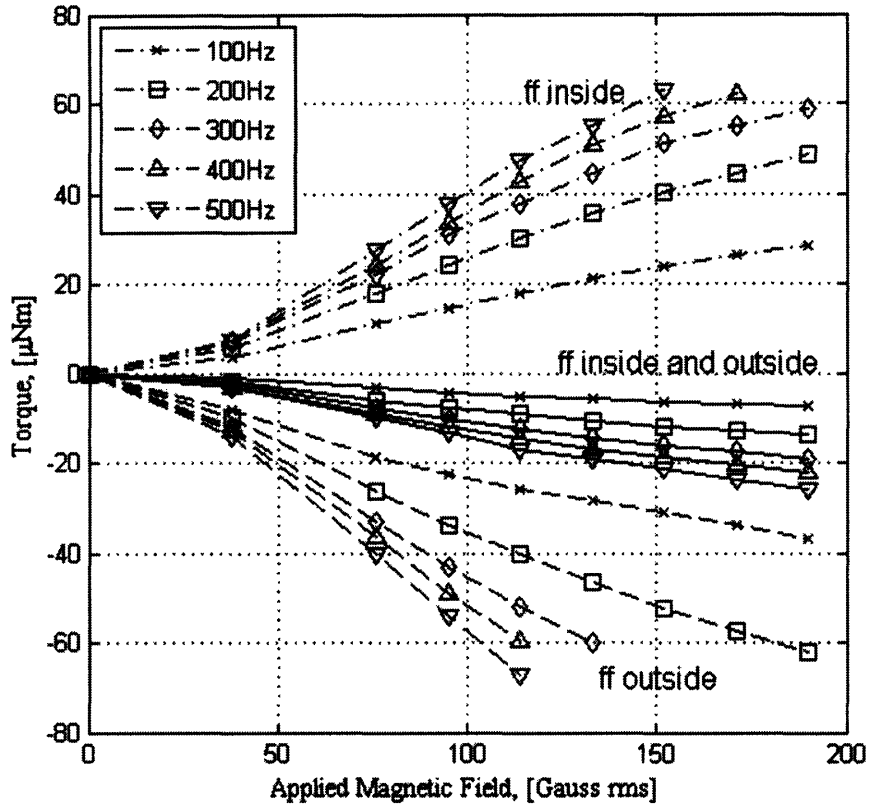


Figure 6-7 Viscometer torque required to restrain the 20 ml stationary spindle syringe with 16.5 ml MSG W11 water-based ferrofluid as a function of uniform magnetic field amplitude and frequency with ferrofluid entirely inside, entirely outside, and both inside and outside the syringe.

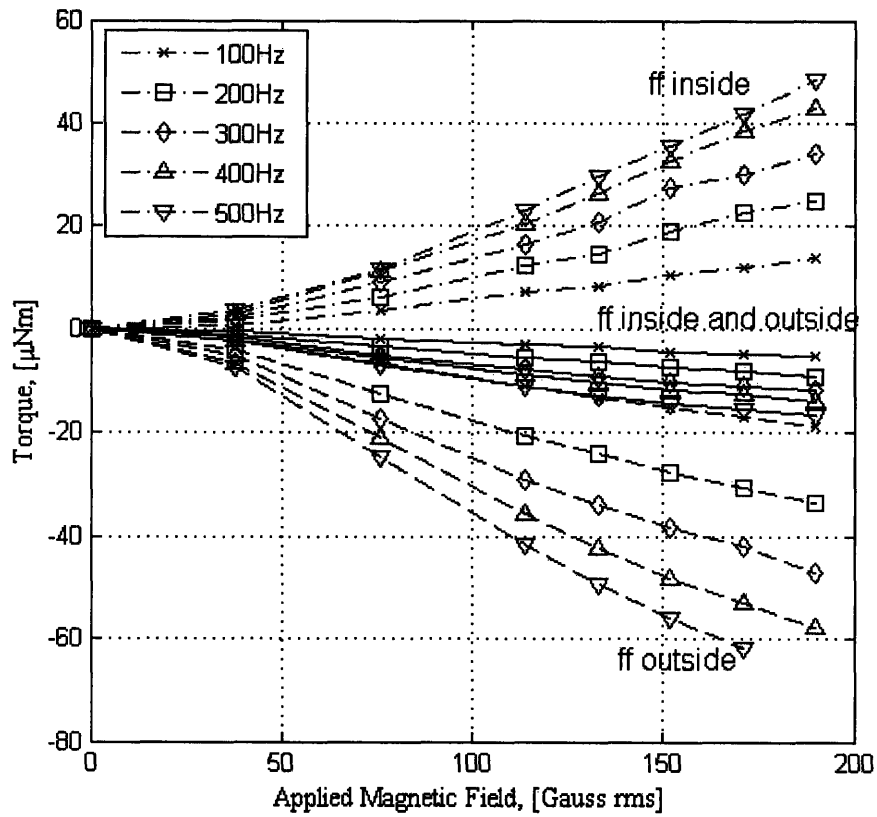


Figure 6-8 Viscometer torque required to restrain the 10 ml stationary spindle syringe with 9.5 ml EFH1 oil-based ferrofluid as a function of uniform magnetic field amplitude and frequency with ferrofluid entirely inside, entirely outside, and both inside and outside the syringe.

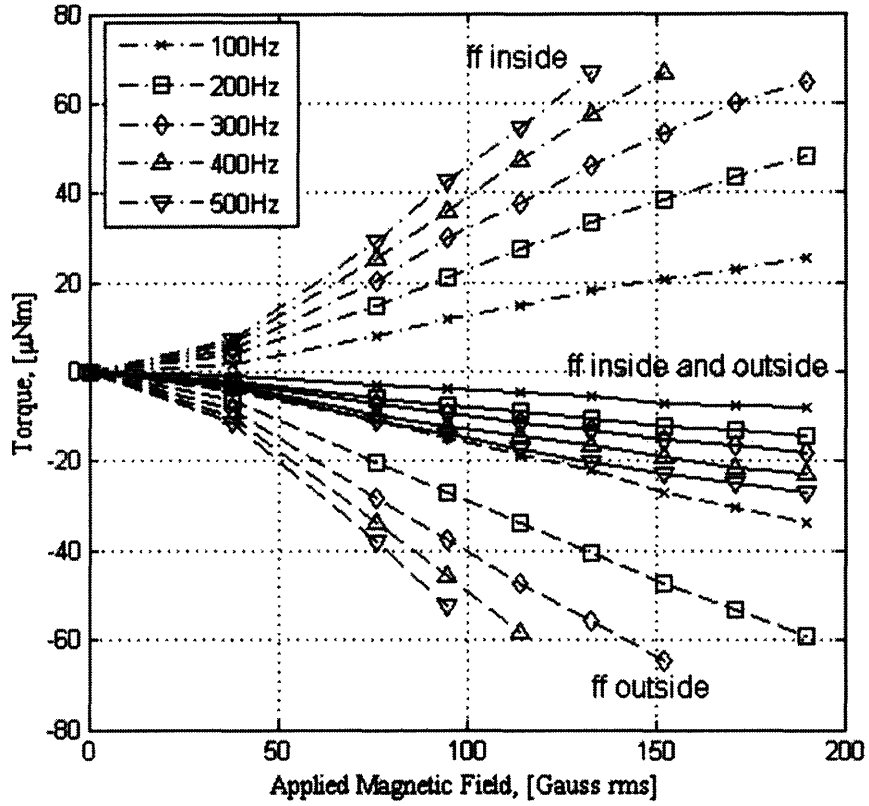


Figure 6-9 Viscometer torque required to the restrain 20 ml stationary spindle syringe with 16.5 ml EFH1 oil-based ferrofluid as a function of uniform magnetic field amplitude and frequency with ferrofluid entirely inside, entirely outside, and both inside and outside the syringe.

Table 6-1 Peak measured viscometer torques ($\mu\text{N}\cdot\text{m}$) /gauss in a uniform rotating magnetic field

| Torque Rate [$\mu\text{Nm}/\text{Gauss}$] | | 100 [Hz] | 200 [Hz] | 300 [Hz] | 400 [Hz] | 500 [Hz] |
|---|---------|----------|----------|----------|----------|----------|
| MSG W11 (water-based) 10 ml spindle | inside | 0.094 | 0.158 | 0.190 | 0.216 | 0.240 |
| | outside | 0.122 | 0.204 | 0.273 | 0.318 | 0.354 |
| | both | 0.026 | 0.049 | 0.065 | 0.079 | 0.091 |
| MSG W11 (water-based) 20 ml spindle | inside | 0.159 | 0.268 | 0.337 | 0.382 | 0.416 |
| | outside | 0.248 | 0.357 | 0.455 | 0.524 | 0.590 |
| | both | 0.046 | 0.081 | 0.110 | 0.128 | 0.148 |
| EFH1 (oil-based) 10 ml spindle | inside | 0.074 | 0.130 | 0.180 | 0.225 | 0.254 |
| | outside | 0.100 | 0.182 | 0.256 | 0.318 | 0.370 |
| | both | 0.029 | 0.049 | 0.069 | 0.079 | 0.097 |
| EFH1 (oil-based) 20 ml spindle | inside | 0.136 | 0.255 | 0.351 | 0.439 | 0.500 |
| | outside | 0.179 | 0.310 | 0.425 | 0.510 | 0.550 |
| | both | 0.047 | 0.081 | 0.099 | 0.128 | 0.152 |

Torque measurements in a uniform rotating magnetic field show the magnetization relaxation effect that the magnetization \vec{M} is not parallel to the magnetic field \vec{H} . This effect results in a torque density $\mu_0 \vec{M} \times \vec{H}$ that drives the spin-up flow and generates torque on the spindle boundary. The torque measurements in a uniform rotating magnetic field have approximately a linear relationship with the applied magnetic field strength and a smaller torque per Gauss values comparing to the torque measurements in a non-uniform rotating magnetic field discussed in the following chapter.

Chapter 7. Viscometer Torque Measurements in Non-uniform Rotating Magnetic Fields

We measure the torque required to restrain a stationary cylinder in contact with water-based ferrofluid subjected to a non-uniform rotating magnetic field generated by a three-phase AC 4-pole motor stator winding. Three experimental configurations are again examined: 1) ferrofluid entirely within the test cylinder; 2) ferrofluid entirely outside the test cylinder; and 3) ferrofluid both inside and outside the test cylinder.

7.1 Non-uniform Magnetic Field

The non-uniform magnetic field was generated by a 4 pole motor stator winding with balanced three phase AC sinusoidal currents, which produce clockwise and counter-clockwise non-uniform magnetic fields in the absence of ferrofluid with field-line patterns like those shown in Figure 7-1 that show the 4-pole structure of the stator winding. The color shows the rms strength of the magnetic flux density magnitude in Gauss and the cylindrical symmetry of the non-uniform magnetic field. Figure 7-2 shows that the theoretical and measured rms strength of the non-uniform magnetic field are linear along the stator winding radius. Figure 7-2 also indicates that each Ampere (peak/rms) of exciting current to all three phases of the 4-pole motor stator winding generates a cylindrical symmetry non-uniform magnetic field with a slope of 821.6 Gauss/m (peak/rms) along the radius of the stator winding. The 4 pole motor stator winding has an inner diameter of 116 mm and height of 65 mm. The magnetic field measurements are shown in Appendix A, which show that the peak field at the outer radius of 58 mm is 47.66 Gauss (peak/rms) per Ampere (peak/rms) current.

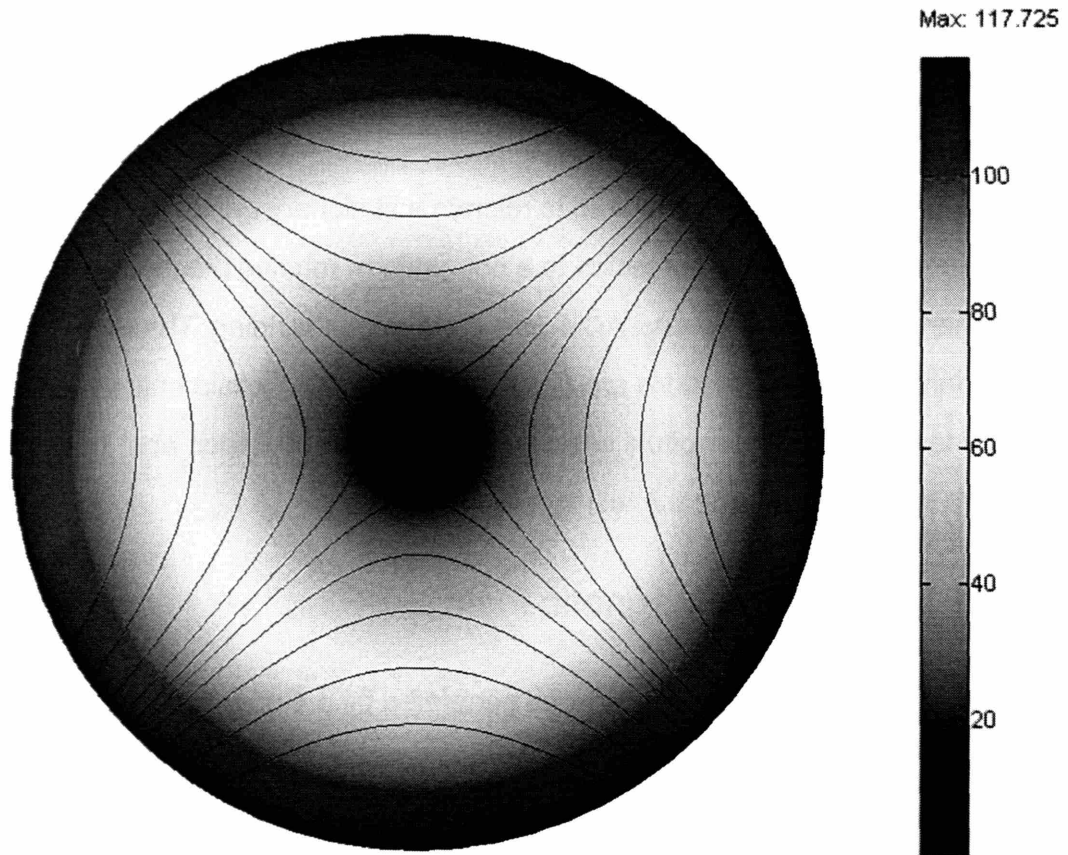


Figure 7-1 Ideal non-uniform magnetic field in a 4-pole motor stator winding with current equal to 4 Ampere peak (2.83 Amperes rms) corresponding to ~167 Gauss peak (118 Gauss rms) magnetic field at radius of 50.8 mm, which is the closest approach to the outer wall of the stator winding due to the thickness of the gaussmeter probe. The magnetic field lines indicate the 4-pole structure of the stator winding. The color shows the rms strength of the magnetic flux density in Gauss and cylindrical symmetry of the non-uniform magnetic field.

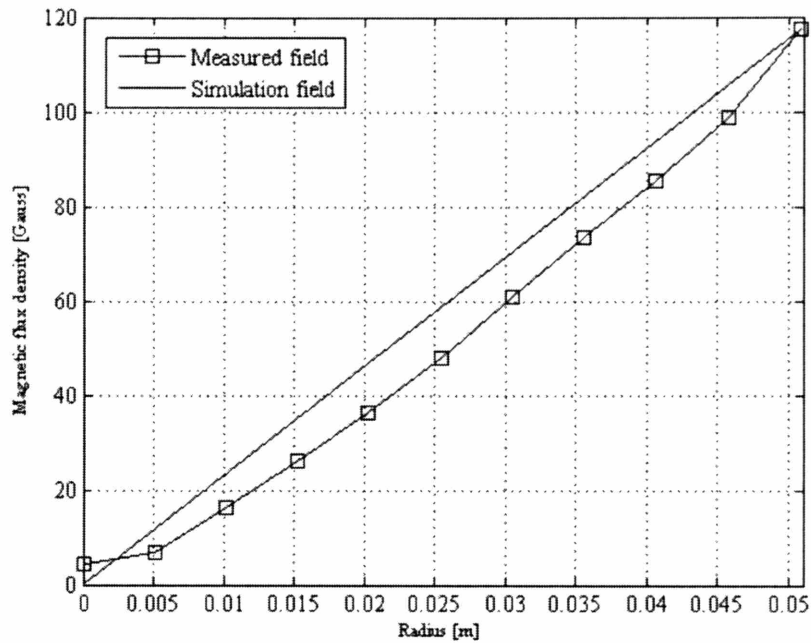


Figure 7-2 The theoretical and measured rms magnitude of a 4-pole non-uniform magnetic field strength vs. radius from the center of a 4-pole motor stator winding with current equal to 4 Amperes peak (2.83 Amperes rms).

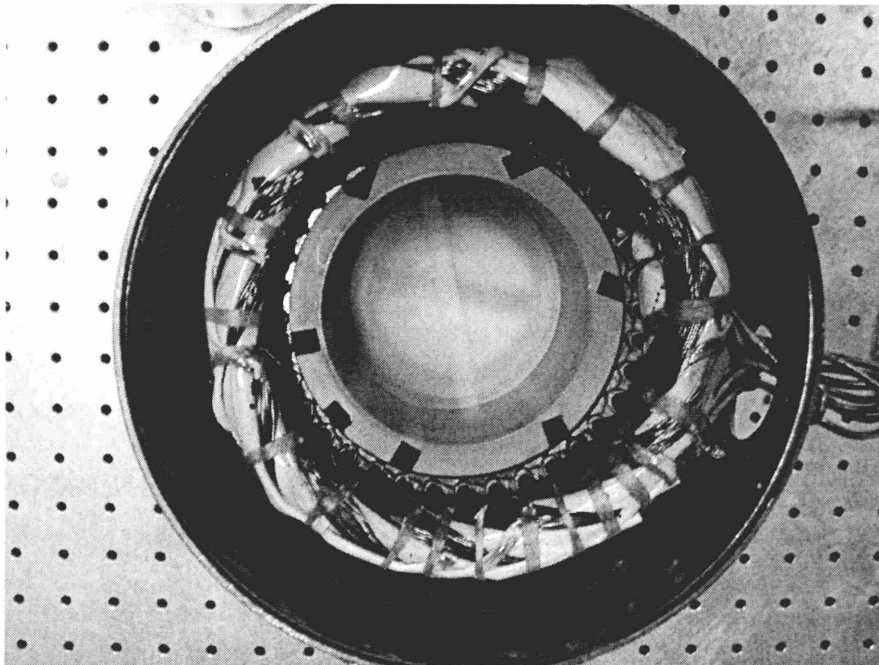


Figure 7-3 The 4-pole motor stator winding to impose a non-uniform magnetic field showing the cylindrical vessel to hold ferrofluid and the grooved channels in the outer wall to hold ultrasound transducers to measure fluid flow profiles to be described in Chapter 8.

7.2 Measurement Apparatus and Procedure

We used the same Brookfield Model LVDV-1+ Couette viscometer as a torque meter described in section 6.1. A Lexan spindle was attached to the viscometer. Under conditions for which a clockwise magnetic-field-induced shear stress arises, the viscometer exerts a balancing counter-clockwise torque to keep the spindle stationary and the viscometer records a torque increase which is registered as a positive torque, whereas for a counterclockwise shear stress a negative torque will be measured. The range of measurable torque for our Brookfield viscometer is $-10.0 \mu\text{N}\cdot\text{m}$ to $67.3 \mu\text{N}\cdot\text{m}$, where a negative torque means the viscometer exerts a clockwise torque to balance a magnetic field induced counter-clockwise torque.

A 4 pole motor stator winding with balanced three phase AC sinusoidal currents was used to produce clockwise and counter-clockwise non-uniform magnetic fields in the absence of ferrofluid as described in section 7.1. A hollow Lexan spindle was used in the torque measurement experiments as shown in Figure 7-4, having a hollow chamber with inner diameter of 86.7 mm and height of 73.2 mm which provides a volume capacity of 432 ml. The hollow spindle was filled with ferrofluid or water and attached to the viscometer through the upper solid section. The spindle was placed so that the fluid was radially and axially centered along the axis of the motor stator winding. A VWR 1000 ml beaker surrounding the spindle was used in this experiment for the case when ferrofluid or water was outside the test spindle cylinder. The inner diameter of the beaker was 104 mm, which creates an annular gap of 5.3 mm with the spindle in the center of the beaker as shown in Figure 7-5. It is necessary to have a large radius spindle as the non-uniform magnetic field has its maximum strength at the outer wall, as shown in Figure 7-1 and Figure 7-2.

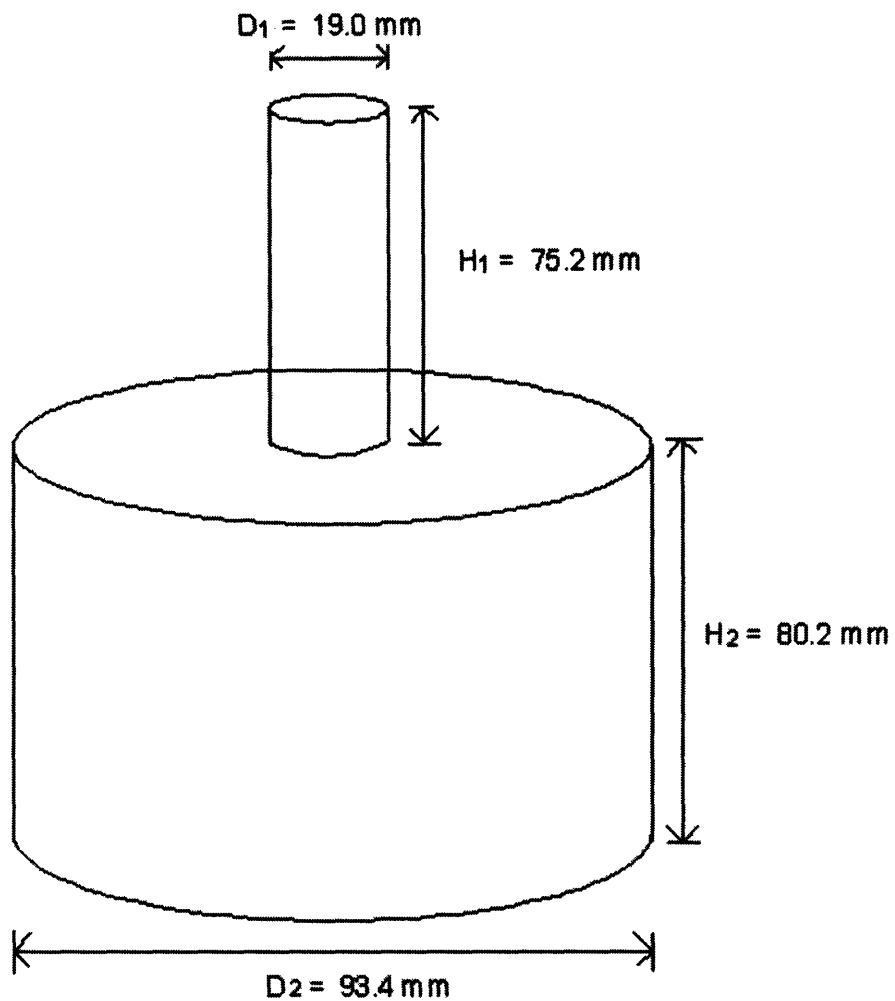


Figure 7-4 The Lexan hollow spindle. The upper section of diameter D_1 was solid and was connected to the viscometer while the lower section of diameter D_2 was hollow so that it could be filled with ferrofluid. The lower hollow section has an inside dimension with height of 73.2 mm and diameter of 86.7 mm. The dimensions shown in the figure are outside dimensions.

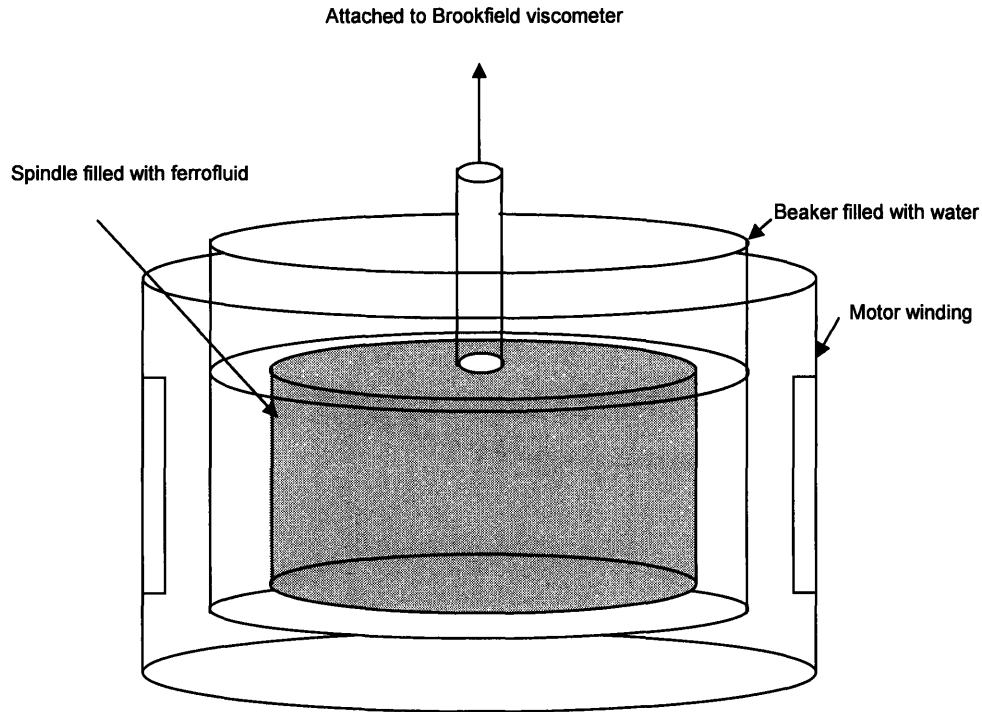


Figure 7-5 A floating force balance system used in torque measurements with a non-uniform magnetic field. For measurements with ferrofluid inside the spindle, the spindle filled with ferrofluid was submerged in a beaker filled with water to make the total weight attached to the viscometer less than 5 oz (142 g), the weight limit of the Brookfield viscometer. For measurements with ferrofluid outside the spindle, the spindle was filled with water and submerged in a beaker filled with ferrofluid to make the total weight attached to the viscometer less than 5oz. For measurements with ferrofluid both inside and outside the spindle, the spindle and the beaker were filled with ferrofluid to make the total weight attached to the viscometer less than 5 oz (142 g). The beaker used in measurements was a VWR 1000ml beaker Cat. No. 89000-212.

As shown in Figure 7-1, the non-uniform magnetic field in the 4-pole motor stator winding is very weak at the center of the winding. In order to increase the sensitivity of the torque measurement and measure the maximum torque, the hollow spindle was specially designed with a large diameter close to the diameter of the 4-pole motor stator winding to keep the ferrofluid in a stronger magnetic field region. Due to the hanging weight limitation of the Brookfield viscometer, which is 5 oz (142 g) maximum, the torque measurement can not be done with the ferrofluid filled spindle attached directly to the viscometer. A floating force balance system shown in Figure 7-5 was used in all torque measurements with a non-uniform magnetic field in order to balance the total weight attached to the viscometer. In the case of ferrofluid inside the spindle, the beaker was filled with water at the same height as the ferrofluid inside the spindle; in the case of ferrofluid outside the spindle the surrounding beaker was filled with ferrofluid at the same height of water inside the spindle and in the case of ferrofluid both inside and outside the spindle, both spindle and beaker were filled with ferrofluid to the same height. Using buoyancy with liquid inside or outside the spindle the hanging weight on the viscometer was kept below 5 oz.

Measurements were taken at frequencies of 50, 100, 150, 200, 300, 400 and 500 Hz with an input current of 0, 0.25, 0.5, 0.75, 1, 1.25, 1.5, 1.75, 2 and 2.5 Amps rms for the case that ferrofluid is entirely inside the spindle, entirely outside the spindle and both inside and outside the spindle. Each Ampere rms in each phase of the input current to the 4 pole motor stator winding corresponds to a magnetic field magnitude that increased linearly with radius with a slope of 821.6 Gauss/m rms along the radius with rms magnetic field at the spindle outer wall with inside radius of $R = 43.4$ mm of 35.7 Gauss rms. These input currents correspond to non-uniform external magnetic fields of 0, 8.9, 17.9, 26.8, 35.7, 44.6, 53.6, 62.5, 71.4 and 89.3 Gauss rms respectively at the middle height and outer radius of $R = 43.4$ mm of the inside of the beaker.

These magnetic field measurements were made in the absence of ferrofluid, and therefore reflect the external magnetic field and do not incorporate the demagnetizing effect of the ferrofluid. For a long cylinder of ferrofluid with magnetic susceptibility χ the internal magnetic field H_i is given in terms of the external magnetic field H_o by the expression $H_i = H_o - MD$ so that

$H_i = H_o / (1 + \chi / 2)$, where $D = 1/2$ is the cylindrical demagnetization factor of an infinitely long cylinder. The clockwise magnetic field is applied for the case that ferrofluid is entirely inside the spindle and counterclockwise for the case that ferrofluid is entirely outside the spindle and both inside and outside the spindle. Under these conditions the viscometer torque will be counter-clockwise allowing the full range of torque measurements up to 67.3 $\mu\text{N}\cdot\text{m}$.

Measurements show that for ferrofluid entirely inside the test cylinder the torque points in the same direction as the magnetic field rotation vector (co-rotation), whereas for ferrofluid entirely outside the cylinder the torque points in the direction opposite to the field rotation vector (counter-rotation). When the ferrofluid is both inside and outside the test cylinder, the measured torque is the approximate algebraic sum of the torques for ferrofluid entirely inside and entirely outside the test cylinder, with net torque opposite to the magnetic field rotation vector. For higher frequencies, some trials contain fewer data points. This is either because the torque was beyond the maximum Brookfield torque or because the voltage across the motor winding terminals was too high, precluding safe operation at higher input currents.

7.3 Experimental Measurements in Non-uniform Rotating Magnetic Fields

Torque measurements with ferrofluid inside the spindle in a clockwise rotating non-uniform magnetic field are shown in Figure 7-6. For the measurement with

ferrofluid just inside the spindle, measured torques on the spindle inner wall increase with increasing applied magnetic field frequency and field amplitude as show in Figure 7-6. The measurements show that saturation values of torque are reached at high frequency of about 500 Hz. Increasing frequency higher than 500 Hz does not significantly increase the torque magnitude.

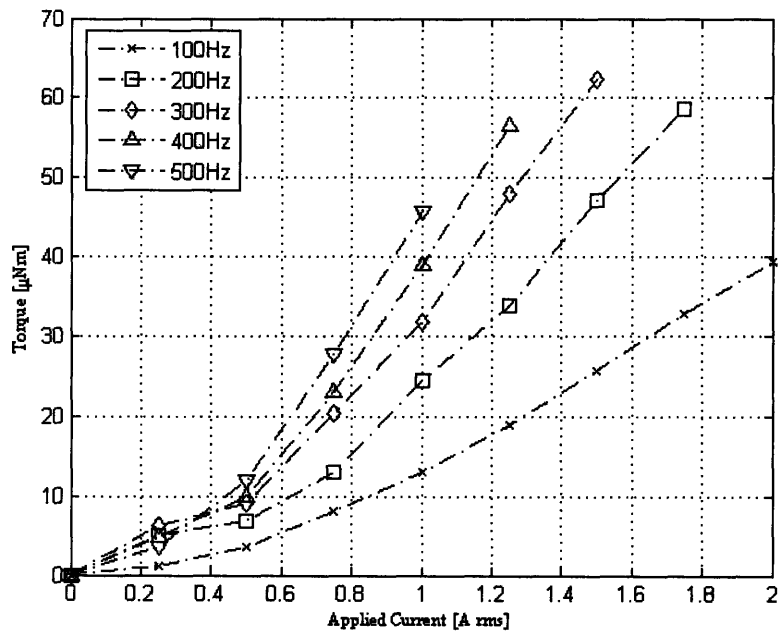


Figure 7-6 Torque measurements with 432 ml MSG W11 water based ferrofluid inside the stationary hollow spindle with clockwise rotating non-uniform magnetic field.

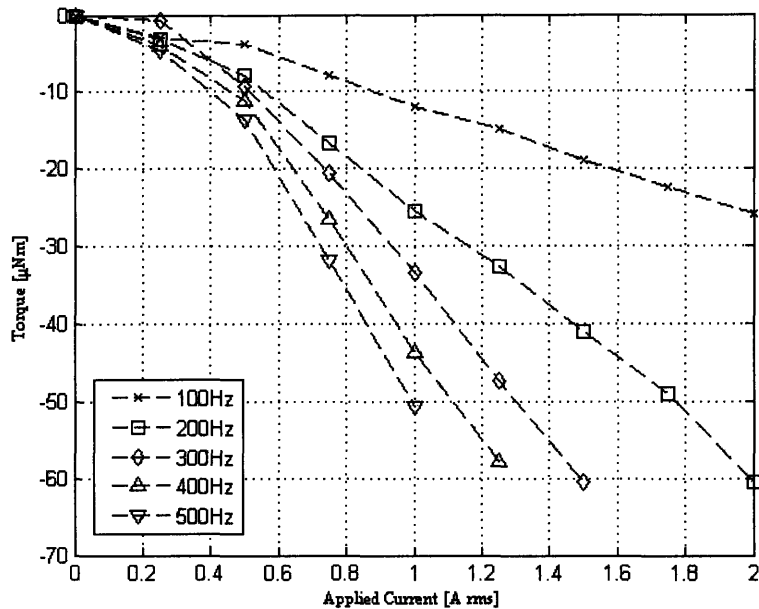


Figure 7-7 Torque measurements with 250 ml MSG W11 water based ferrofluid outside the stationary hollow spindle with counter-clockwise rotating non-uniform magnetic field.

Figure 7-7 shows the torque measurement with ferrofluid outside the spindle with a counter-clockwise rotating magnetic field. The measured torque on the spindle outer wall increases with increasing applied magnetic field frequency and field amplitude. It also shows saturation of spindle torque with increasing frequency at about 500 Hz.

Figure 7-8 shows the torque measured on the spindle wall when MSG W11 ferrofluid is simultaneously inside and outside the spindle wall. For comparison, the measurements of ferrofluid inside or outside the spindle from Figure 7-6 and Figure 7-7 are also shown in the same figure. Because of the limitations of our apparatus, measurements for higher frequency and stronger magnetic field are absent for the cases of ferrofluid just inside the spindle and just outside the spindle. Measurements with ferrofluid both inside and outside the spindle magnitude show torque magnitudes increase with increasing frequency and increasing magnetic field amplitude.

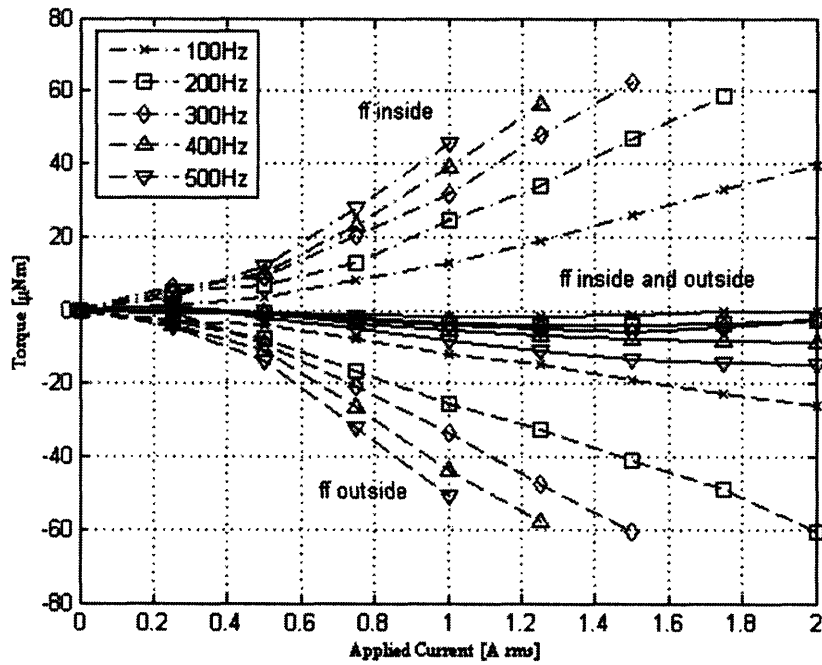


Figure 7-8 Torque measurement with MSG W11 water based ferrofluid of 432 ml inside, 250 ml outside and both inside and outside the stationary hollow spindle in rotating non-uniform magnetic fields.

Table 7-1 Peak measured spindle torque ($\mu\text{N}\cdot\text{m}$) per Gauss in a non-uniform rotating magnetic field. The peak field at the radius of 58 mm of the 4 pole motor stator winding is 47.65 Gauss (peak/rms) per Ampere (peak/rms).

| Torque Rate [$\mu\text{Nm}/\text{Gauss}$] | 100 [Hz] | 200 [Hz] | 300 [Hz] | 400 [Hz] | 500 [Hz] |
|---|----------|----------|----------|----------|----------|
| MSG W11 (water-based) inside | 0.702 | 0.949 | 0.962 | 1.143 | 1.199 |
| MSG W11 (water-based) outside | 0.634 | 0.972 | 1.064 | 1.271 | 1.383 |
| MSG W11 (water-based) both | 0.069 | 0.117 | 0.185 | 0.248 | 0.300 |

Table 7-1 shows the peak measured torque per Gauss of MSG W11 water-based ferrofluid in a non-uniform rotating magnetic field, which is

stronger than the torque rate in a uniform rotating magnetic field as shown in Table 6-1. The torque measurements in the uniform rotating magnetic field shown in section 6.3.2, increase approximately linearly with the strength of the applied magnetic field, while the torque measurements in the non-uniform rotating magnetic field shown in Figure 7-6 to Figure 7-8 has an approximately non-linear dependence on the strength of the applied magnetic field. Because ferrofluid in a uniform rotating magnetic field has a zero body force density, $\mu_0 (\vec{M} \cdot \nabla) \vec{H}$, the only drive source for the torque driven flow is the volume torque density $\mu_0 \vec{M} \times \vec{H}$. Ferrofluid in a non-uniform rotating magnetic field is subject to the volume torque density, while the body force density $\vec{F} = \mu_0 (\vec{M} \cdot \nabla) \vec{H}$ makes an additional contribution to the torque $\vec{r} \times \vec{F}$, which makes the torque have a stronger dependence on the strength of the applied magnetic field. The numerical simulations in Chapter 9 demonstrate the effects of volume torque density and body force density contributions to the total torque.

Chapter 8. Spin-up Flow Velocity Measurements In A Non-uniform Rotating Magnetic Field

Spin-up flow phenomena of MSG W11 water-based ferrofluid in a rotating non-uniform magnetic field generated by a three-phase AC 4-pole motor stator winding was investigated with a Signal Processing DOP2000 ultrasound velocimeter. The velocity distribution in the bulk of a ferrofluid cannot be measured by laser Doppler or streak path techniques due to the opacity of ferrofluids. Pulsed ultrasound velocimetry allows, however, for the real-time measurement of velocity profiles in opaque fluids. Experimental measurements of the velocity field in the bulk of the ferrofluid provides the information required to answer many of the questions that arise from reviewing the ferrofluid spin-up literature. Investigations of ferrofluid spin-up flow in the literature do not report the flow field inside the bulk of the ferrofluid, being limited to studying only the flow profile on the free-surface of the opaque ferrofluid by recording the motion of various kinds of floating tracer beads and particles. Unlike previous research reported in the literature which are restricted to optical observations at the top ferrofluid/air interface, the ultrasound technique overcomes the difficulty that the ferrofluid opacity poses, enabling us to measure the velocity profiles in the bulk of the ferrofluid.

8.1 Measurement Apparatus

A Signal Processing SA DOP 2000, model 2125 Ultrasonic Doppler Velocimeter was used to measure the bulk velocity of ferrofluid in non-uniform rotating magnetic fields. The DOP2000 Velocimeter uses a pulsed ultrasonic echo technique to instantaneously measure velocity profiles along the ultrasonic beam, Doppler energy profiles, echo profiles, spectral density (FFT), histograms, and the flow rate in flowing liquids. The pulsed ultrasound technique uses reflections off of small tracer particles or air bubbles

suspended in the fluid flow. The technique then uses the time of flight of the reflected ultrasound beams to estimate the velocity of the tracer particles. Each ultrasound probe measures the component of the velocity along the emitted beam at every point along the beam. The velocity measured by the velocimeter is positive if the flow is away from the probe and negative if the flow is towards the ultrasound probe. The DOP2000 computes and displays in real time these data profiles based on the analysis of a user specified number of gates placed along the ultrasonic beam. The digital ultrasonic synthesizer can generate any emitting frequencies between 0.45 MHz and 10.5 MHz. The DOP2000 also includes a variable spatial resolution filter that allows the size of the sampling volume to be adapted to the application and therefore improves the signal to noise ratio of the measurements. The DOP2000 also provides the multiple channels function, which operates each channel and probe at a different time frame of a time period and allows multiple channels to work simultaneously without any interference. Combining the readings of multiple probes at various positions and angles allows the measurement of the velocity at many points in the flow field. In ferrofluid applications, tracer particles of sizes around 50-200 microns must be added to the fluid. The 5-15 nm ferrofluid particles are too small to scatter the ultrasound effectively. Commonly used particles include plastic polyethylene spheres, corn pollen, and hollow spheres of SiO₂. In our experiments we found it necessary to add GrilTex-P1 latex particles, produced by EMS chemie, Switzerland, to the ferrofluid to improve the quality of the reflected ultrasound signal. These copolyamide spherical particles with an average diameter of 50 μm have a density of 1.1 g/cc and are practically neutrally buoyant in water-based ferrofluid. During the course of the experiments, we would, however, stir the ferrofluid vigorously by hand once every day to prevent the particles from settling, thus maintaining the dispersion of tracer particles necessary for a high level of ultrasonic echoes. The pulsed ultrasound technique has the advantage of non-disruptive measurement of the flow profile. The ultrasound probes can

be placed in the outside walls of the ferrofluid container without contacting the ferrofluid. However, this increases ultrasound energy losses because the signal must couple from the probe to the container wall and from the container wall into the fluid. Walls made out of materials that have an acoustic impedance similar to that of ferrofluids (like Plexiglas) can maximize transmissivity between the container wall and the ferrofluid. As shown in Figure 8-1, a cylindrical polycarbonate container with an inner diameter of 91.9 mm and height of 60 mm was used in the spin-up velocity profile experiments, which was designed to fit snugly into the 116 mm diameter bore of the three phase, 4-pole motor stator winding in order to guarantee that the ferrofluid is radially centered along the axis of the stator winding. The container has a wall thickness of 10 mm, in order to hold the ultrasound probe. To maintain high magnetic field uniformity, the container was also centered vertically within the stack of the stator's iron core. Table 8-1 lists the acoustic impedance of ferrofluids and non-magnetic materials.

Table 8-1 Acoustic impedance of ferrofluids and non-magnetic materials. *: The values of air and polycarbonate are quoted from DOP2000 Model 2125/2032 User's manual, Signal Processing S.A., Switzerland, section 22. †: The acoustic impedances $Z=\rho c$ are estimated using the values of density and speed of sound from Table 2-1 and

Table 2-3.

| Material | Speed of sound, c, [m/s] Signal Processing Method | Density, ρ , [kg/m ³] | Acoustic impedance†, Z, [MRayls] = [10 ⁶ kg·m ⁻² ·s ⁻¹] |
|--|---|--|---|
| Ferrofluid | | | |
| Air* | c_B , [μ s] 344 | ρ_N , [kg/m ³] 1.29 | 0.0004 [μ s] |
| Polycarbonate (Lexan)* EMG705 | 2270 7.59-8.59 (VSM) | 1220 1.30×10 ⁻⁷ -4.78×10 ¹¹ (VSM) | 2.77 0.12-8.59 (VSM) |
| (water-based) DI-water | 1459 0.64-12.2 (TEM) | 998 2.98×10 ⁻⁹ -5.85×10 ²² (TEM) | 0.0030-12.2 (TEM) |
| EMG705 (water-based) MSG W11 | 1487 0.66-3.38 (VSM) | 1194 5.16×10 ⁻⁹ -0.1474 (VSM) | 0.0051-3.38 (VSM) |
| (water-based) MSG W11 (water-based) | 1487 0.84-24.2 (TEM) | 1200 1.18×10 ⁻⁸ -1.19×10 ⁸¹ (TEM) | 0.012-24.2 (TEM) |
| EFH1 (oil-based) EFH1 (oil-based) | 1143 3.57-14.28 (VSM) | 1221 2.56×10 ⁻⁸ -12.0 (VSM) | 0.025-14.3 (VSM) |

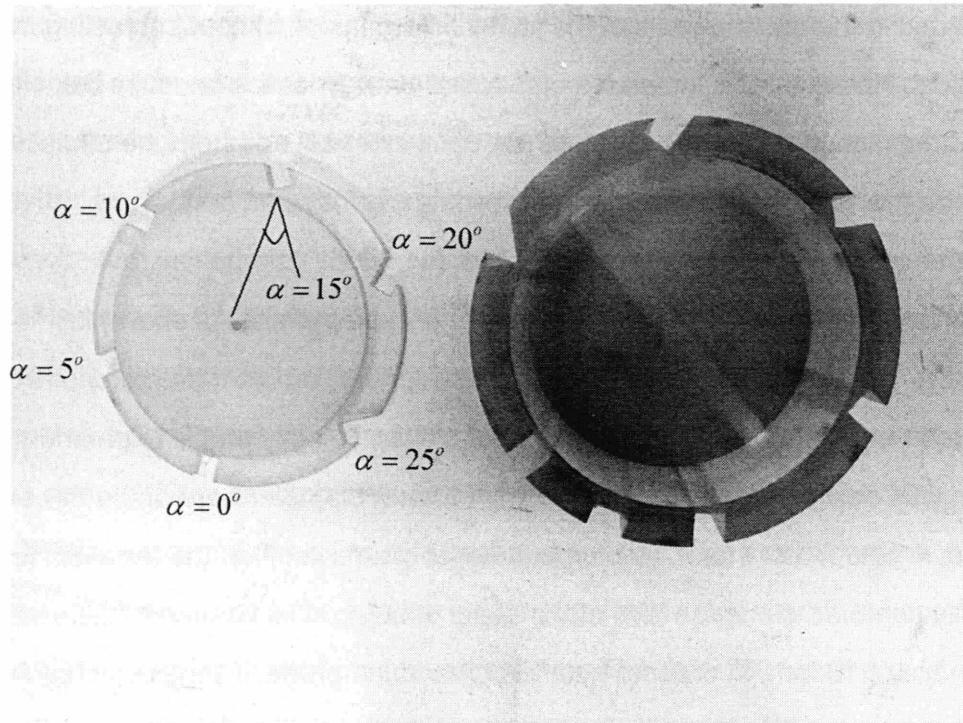


Figure 8-1 Cylindrical polycarbonate container for spin-up velocity profile measurements in a non-uniform rotating magnetic field. Right: slots in the container wall with angles of 0° , 5° , 10° , 15° , 20° , 25° with respect to normal and radius to measure v_r and v_ϕ components and a slot at the bottom center diameter of the container for measurement of v_z . Left: container cover prevents a free surface interface by covering and contacting a fully filled container.

8.2 Measurement Setup and Procedure

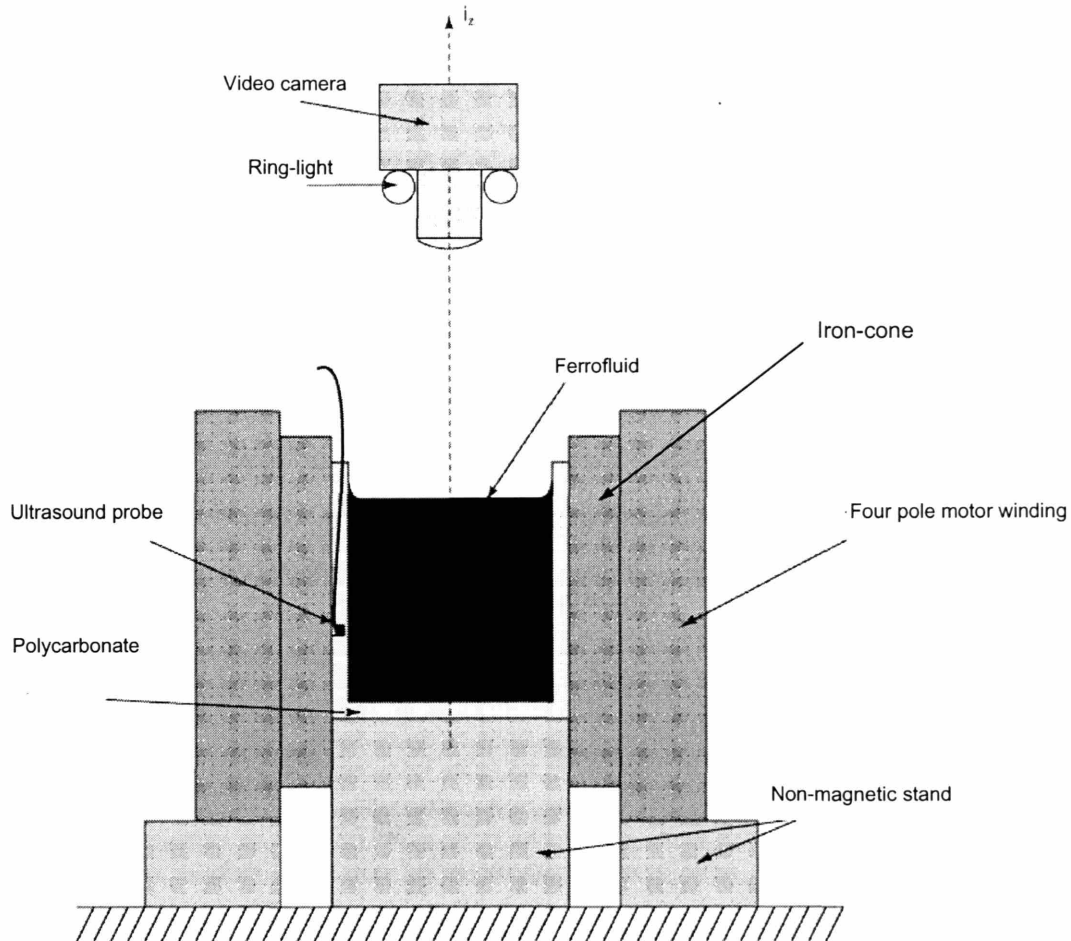


Figure 8-2 Configuration of motor stator and cylindrical vessel for the spin-up flow profile measurement experiments. A three-phase, 4-pole motor stator winding was used to excite a rotating non-uniform magnetic field. The ring-light and video camera record the surface velocity profile at the same time as the UVP velocity profile was taken.

Figure 8-2 shows the experimental setup used to investigate the flow in the bulk of a cylindrical container of water-based ferrofluid with a free top surface undergoing spin-up flow driven by a non-uniform counter-clockwise rotating magnetic field. The field was produced by the stator winding of a 4-pole three-phase motor stator winding. The polycarbonate cylindrical vessel was filled to a height of 60 mm with water-based ferrofluid and was placed radially and axially centered in the stator winding. A video camera placed directly

above the experiment was used to also monitor the surface velocity profile at the ferrofluid/air interface. Measurements were also performed with a stationary top on the ferrofluid surface so that there was no free air/ferrofluid interface and therefore no surface flow. Channels were grooved at different angles from the radial normal to the cylinder's lateral side to house the ultrasound velocimeter probes. The grooved channels have a thin thickness of intact wall (< 5 mm) so that the ultrasound probe does not directly contact the ferrofluid. Ultrasound gel was used at the interface of the ultrasound probe and the vessel wall to couple the ultrasound signal to the bulk of the ferrofluid more effectively.

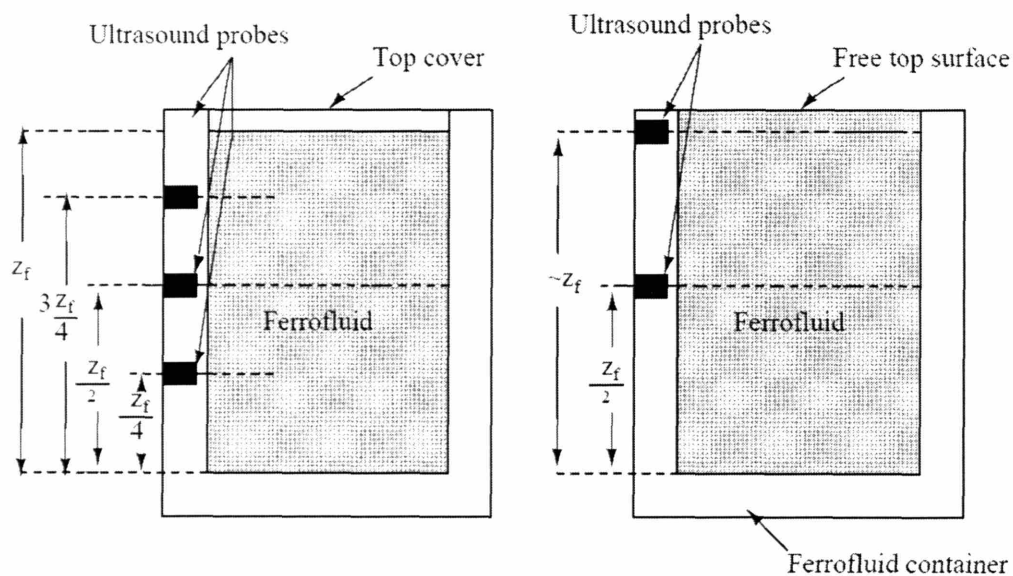


Figure 8-3 The placement of the ultrasound probes at different heights (values of z) in containers of ferrofluid with and without a top cover. The top cover of the left cylindrical container forces zero flow at $z = z_f$ and reduces surface shear stress effects, whereas in the right container the absence of the top cover allows the free top surface to develop surface shear stress driven flows.

Spin-up velocity profile measurements were taken in the container with and without a top cover at different heights. Figure 8-3 shows the placement of probes at different heights z on the container wall. The left container in Figure

8-3, has a top cover to eliminate the free air/ferrofluid interface, has zero surface flow velocity and reduces surface shear stress effects. The right container in Figure 8-3, is without a top cover and has a free air/ferrofluid interface that allows surface shear stress driven flows. Rosensweig's model for the spin-up flow of magnetic fluid in a uniform magnetic field considers the interfacial deformation of a free ferrofluid surface having contact angle θ with a container wall [17]. The deformation of the ferrofluid results in a magnetic surface shear stress driven flow. The surface-driven flow is believed to be usually stronger than that produced by the spin diffusion model which was recently treated by Rinaldi [31]. The volume flow field resulting from the surface-driven model, however, remained unmeasured until recently [86]. Rosensweig conducted a careful set of experiments with concave, flat and convex free surface shapes by respectively under-filling, filling to the brim, and slightly over-filling a container with ferrofluid. In a uniform rotating magnetic field, he reports counter-rotation for concave surface shapes, no rotation for flat surface shapes, and co-rotation for convex surface shapes. Rosensweig concludes that this observed behavior constitutes evidence that surface stress rather than a volume torque density drives the spin-up flow [17]. Rosensweig, however, observed only the flow velocity at the top free surface of the ferrofluid, and the flow in the bulk of the ferrofluid was not known.

The non-uniform magnetic fields inside the 4 pole motor stator winding were generated with balanced-three-phase-sinusoidal currents to create clockwise or counter-clockwise non-uniform rotating magnetic fields as described in section 7.1. Measurements were taken at frequencies of 50, 100, 200, 300, 400 and 500 Hz with an input current of 1, 2, 3, 4, 5, 6, 7, 8 and 9 *Ampères* (rms) for the cases that the ferrofluid container is uncovered with a free surface or is with a stationary top so that there is no free surface with the probe placed at mid-container height. The currents at higher frequencies were limited to lower values of amperes to avoid overheating and damage to the stator

winding. These magnetic field measurements were made in the absence of ferrofluid, and therefore reflect the external magnetic field and do not incorporate the demagnetizing effect of the ferrofluid. The non-uniform magnetic field magnitude values and demagnetizing effect are discussed in section 7.2. The 10 mm non-magnetic wall thickness of the polycarbonate cylindrical container separates the ferrofluid from the stator iron. We added 1 gram of Latex tracer particles to every 0.1 liters of water-based ferrofluid or equivalently less than 1% by weight. This amount of tracer particles produced much higher reflected echo signals than obtained by introducing air bubbles, significantly improving the quality and repeatability of the measurements without perceptibly changing the velocity flow profiles in the experiments. The tracer particle/ ferrofluid suspension requires more than 24 hours to sedimentate enough Latex tracer particles to the bottom of the cylindrical container to cause significant degradation of the reflected ultrasound signals. Our experience shows, however, that the signal quality can be maintained at its initial quality by simply vigorously stirring the suspension by hand at the start of every day of measurements after the experimental sample has been left unstirred overnight. Further stirring during the day was not necessary. Also, we have found it important to prevent the ferrofluid from heating up (to ~ 35 °C) during the tests to avoid temperature-gradient-driven, thermal-convection bulk flows in the fluid. The currents flowing in the stator winding's coils heat up the whole stator due to ohmic losses in the copper winding. Special care was taken after each set of tests to turn off the currents and allow enough time (~15 minutes) for the motor stator to cool down to room temperature; an electric fan helped accelerate the slow cooling process. The polycarbonate material of the cylindrical ferrofluid container also acted as a heat insulator. These combined measures assured that the ferrofluid remained at a practically uniform and constant temperature throughout an experimental test set.

8.3 Measurement of The Spin-up Flow Velocity Profile

The velocimeter measures only the component of the velocity parallel to the axis of the ultrasound probe. The device records the parallel component of the velocity as a function of time at every point along the path of the ultrasound beam. Due to the finite thickness of the ultrasound beam, the velocity recorded at every point is the average of the velocity over a small volume. The geometry necessary to interpret the ultrasound velocimeter data can be derived from Figure 8-4 which shows a top view of the ferrofluid vessel in the spin-up experiment. The ultrasound probe was inserted into the outer cylinder wall at an angle $\alpha = 25^\circ$ from the radial direction at a height $z = 30$ mm from the bottom of the ferrofluid (*i.e.*, approximately in the middle of the 60 mm height of ferrofluid in the vessel). The probe issues an ultrasonic beam and measures the component of fluid velocity parallel to the direction of the beam at every point along the beam. Thus the z- and r- components of the fluid velocity can be measured directly by ultrasound beams pointing in the vertical and radial directions respectively. It was proved in the measurement that the z- and r- components of the fluid velocity are very small, thus the z- and r- components of the fluid velocity are treated as zero in the following analysis. Measurement of the ϕ -component of the velocity requires processing of the velocity measured on the ultrasound beam path shown in Figure 8-4. From the figure we see that the radius r at a point on the ultra-sound beam path is given by,

$$r = \sqrt{(x^2 + (R \sin \alpha)^2)} \quad (8.1)$$

The velocity measured at a point in the fluid is most generally given by,

$$\bar{v}(r, z) = v_r(r, z)\bar{i}_r + v_\phi(r, z)\bar{i}_\phi + v_z(r, z)\bar{i}_z \quad (8.2)$$

On the ultrasound beam path this general expression can be rewritten as,

$$\bar{v}(r, z) = v_r(r, z) \left(\frac{x}{r} \bar{i}_x + \frac{R \sin \alpha}{r} \bar{i}_y \right) + v_\phi(r, z) \left(-\frac{R \sin \alpha}{r} \bar{i}_x + \frac{x}{r} \bar{i}_y \right) + v_z(r, z) \bar{i}_z \quad (8.3)$$

However, the velocity measured by the velocimeter at points on the ultrasound beam path shown in Figure 8-4 has at most only r - and ϕ -components,

because the z -component of the velocity is perpendicular to the r - ϕ plane.

The ultrasound probe shown in Figure 8-4 measures only the x -component of the fluid velocity at every point along the beam path. Therefore the velocity profile measured by the velocimeter, v_m , is given by,

$$v_m(x) = \bar{v}(r, z) \cdot \bar{i}_x = v_r(r) \frac{x}{\sqrt{x^2 + (R \sin \alpha)^2}} - v_\phi(r) \frac{R \sin \alpha}{\sqrt{x^2 + (R \sin \alpha)^2}} \quad (8.4)$$

This means that to deduce the velocity profile $v_\phi(r, z)$ from the ultrasound velocimeter profile we must first directly measure the radial component of the velocity $v_r(r, z)$ and then use the expression,

$$v_\phi(r) = v_r(r) \frac{x}{R \sin \alpha} - v_m(x) \frac{\sqrt{x^2 + (R \sin \alpha)^2}}{R \sin \alpha} \quad (8.5)$$

The radial component of velocity, $v_r(r)$, is easily measured by directing the ultrasound beam in the radial direction so that $\alpha = 0$.

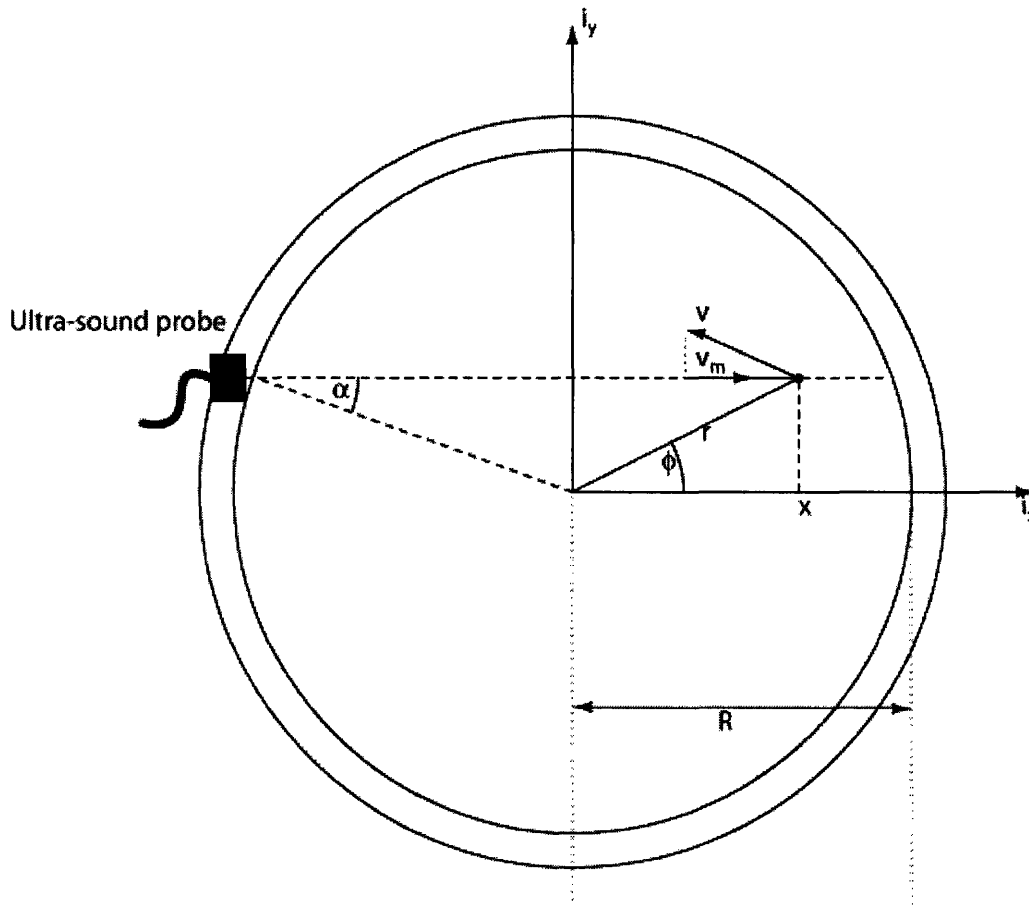


Figure 8-4 Geometry for spin-up flow profile measurement experiments. The ultrasound probe measures the component of the fluid velocity v_m along the probe's axis.

8.4 Spin-up Velocity Profile Measurements

8.4.1 MSG W11 Water-based Ferrofluid With Top Cover

The spin-up velocity profiles measured in the bulk of the water-based ferrofluid are shown in Figure 8-5 to Figure 8-7 for applied rotating magnetic field frequency of 300, 400 and 500 Hz for various magnetic field amplitudes without a free surface. The figure shows that when subject to a counter-clockwise rotating magnetic field the bulk ferrofluid in the cylindrical vessel undergoes rigid-body-like counter-clockwise rotation at the constant

angular velocity. Only in a layer near the walls of the cylinder does the no-slip condition force the fluid flow to differ from rigid-body rotation. At any given frequency, higher values of the applied magnetic field strength lead to higher rotational velocities.

Figure 8-8 and Figure 8-9 show the effects of applied magnetic field strength and rotation frequency on the observed bulk rotational speed Ω of the ferrofluid. We used the slopes of the linear region of the measured velocity profiles as an estimate for the bulk ferrofluid rotational speed. For low frequencies of applied rotating magnetic field the bulk rotational speed of the ferrofluid increases with the applied rotating magnetic field frequency. We measured the maximum velocity and its radial position in ferrofluid bulk rotation at each value of applied rotating magnetic field strength. Figure 8-8 shows that at higher frequencies the rigid-body rotation of the ferrofluid saturates or begins to decrease slowly with applied frequency for any given rotating magnetic field strength. On the other hand, the bulk rotational speed of the ferrofluid $\Omega = \frac{v_{\phi}}{r}$ was observed to increase monotonically with applied rotating magnetic field strength as shown in Figure 8-9.

The no-slip condition applies at the top and bottom stationary surfaces of the covered cylindrical container. We measured the velocity profiles at $z = z_f/4$ and $z = 3z_f/4$ and at the center, $z = z_f/2$, of the cylindrical container. This investigation of the dependence of the azimuthal velocity profile on z shows the symmetry of the covered spin-up flow. As expected, the experimental data in Figure 8-10 to Figure 8-12 demonstrate that there are higher flow rates at the vertical center of the cylindrical container than near the top and bottom faces of the cylindrical container where the flow velocity goes to zero. Ideally, the curves for $z = z_f/4$ and $z = 3z_f/4$ should completely overlap in both figures. Experimental results show some discrepancy, especially in Figure 8-10 due to experimental error. The ferrofluid in the container is, however, observed to

consistently co-rotate with the applied non-uniform rotating magnetic field. Most significantly, these experiments demonstrate that there is significant rotational flow in the bulk of the ferrofluid in the absence of any free surfaces.

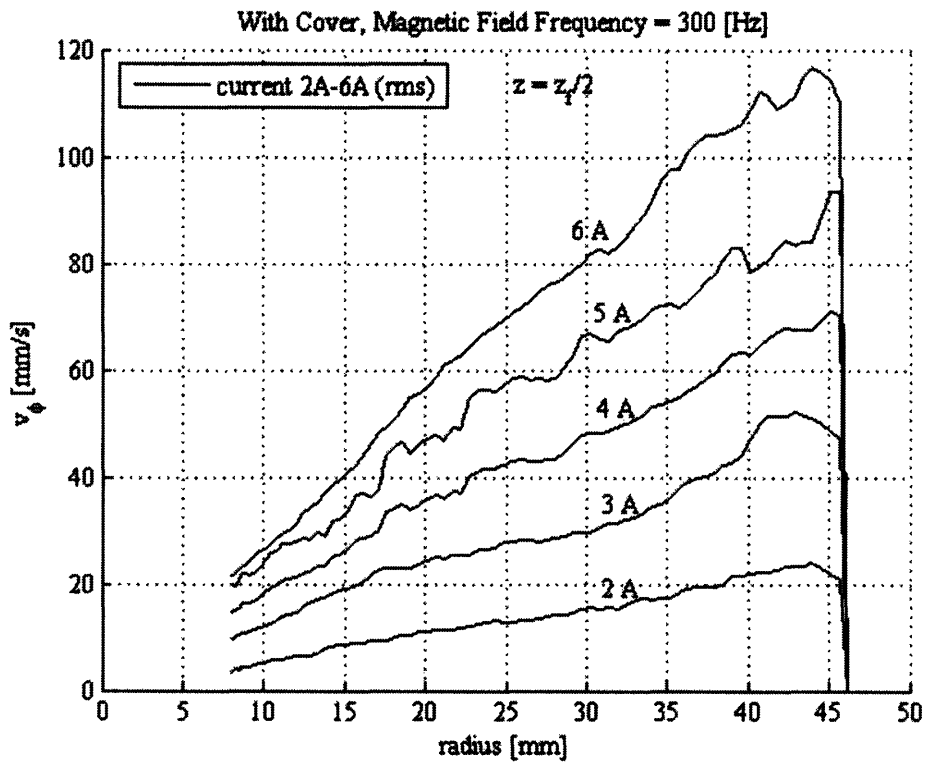


Figure 8-5 The azimuthal component of spin-up flow profiles at $z = z_1/2$ for MSG W11 water-based ferrofluid excited by a non-uniform magnetic field rotating counter-clockwise at 300 Hz. Counter-clockwise velocities increase with increasing applied magnetic field (increasing current in A rms). In the central region the flow profiles resemble the linear profile of a fluid in rigid body co-rotation with the applied magnetic field. The velocity is zero at the $r = R = 46$ mm stationary wall. The cylindrical container was covered so that there were no free ferrofluid surfaces.

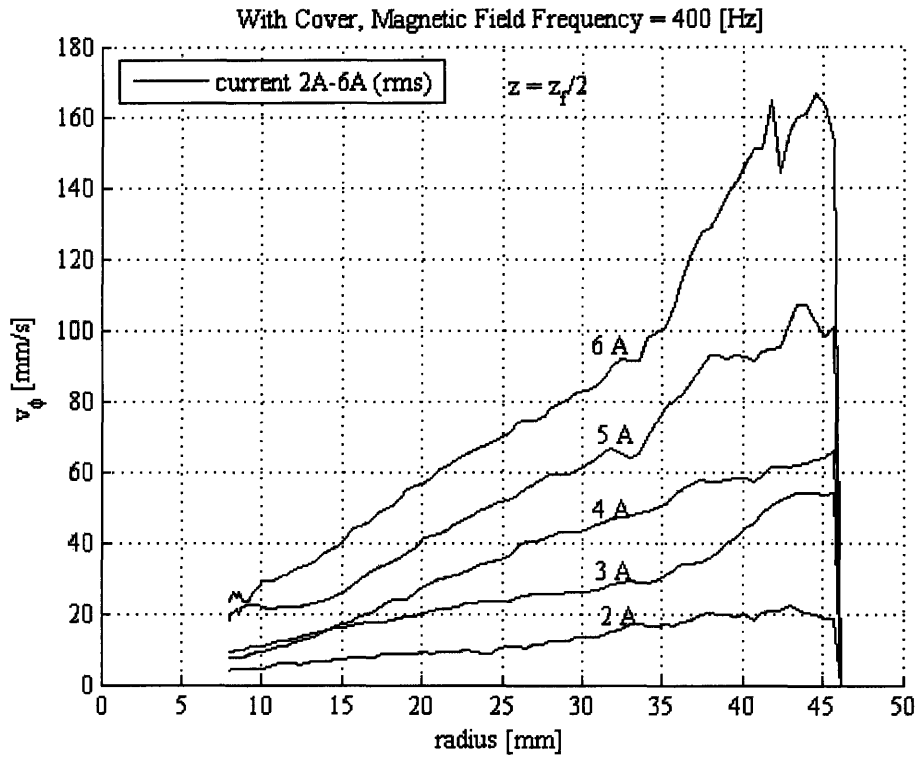


Figure 8-6 The azimuthal component of spin-up flow profiles at $z = z_f/2$ for MSG W11 water-based ferrofluid excited by a non-uniform magnetic field rotating counter-clockwise at 400 Hz. Counter-clockwise velocities increase with increasing applied magnetic field (increasing current in A rms). The cylindrical container was covered so that there were no free ferrofluid surfaces.

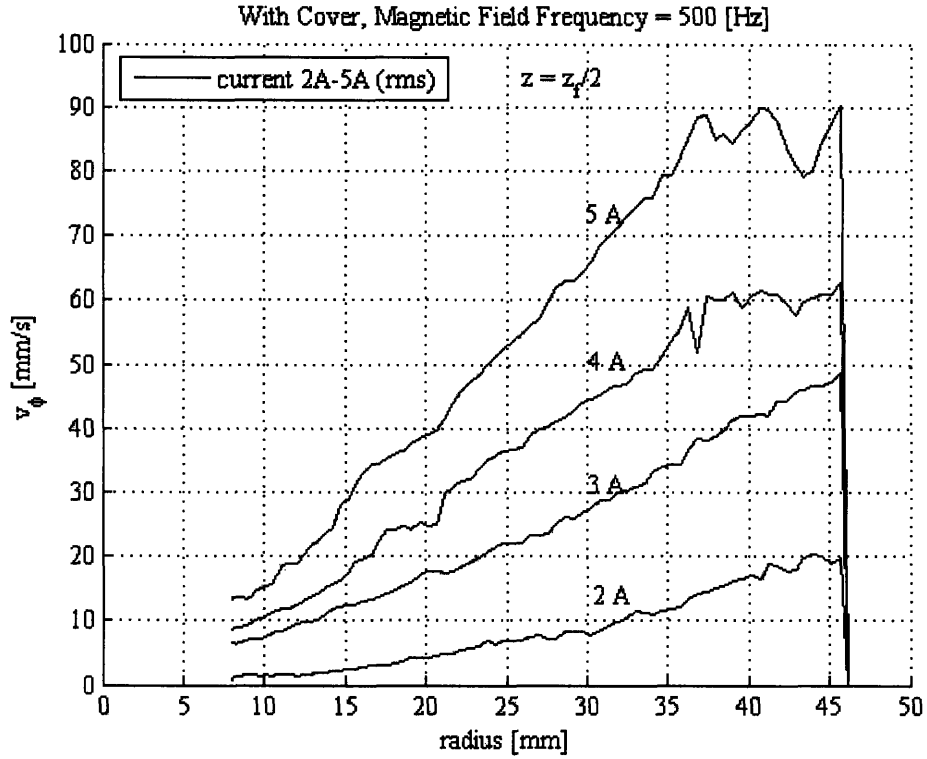


Figure 8-7 The azimuthal component of spin-up flow profiles at $z = z_f/2$ for MSG W11 water-based ferrofluid excited by a non-uniform magnetic field rotating counter-clockwise at 500 Hz. Counter-clockwise velocities increase with increasing applied magnetic field (increasing current in A rms). The cylindrical container was covered so that there were no free ferrofluid surfaces.

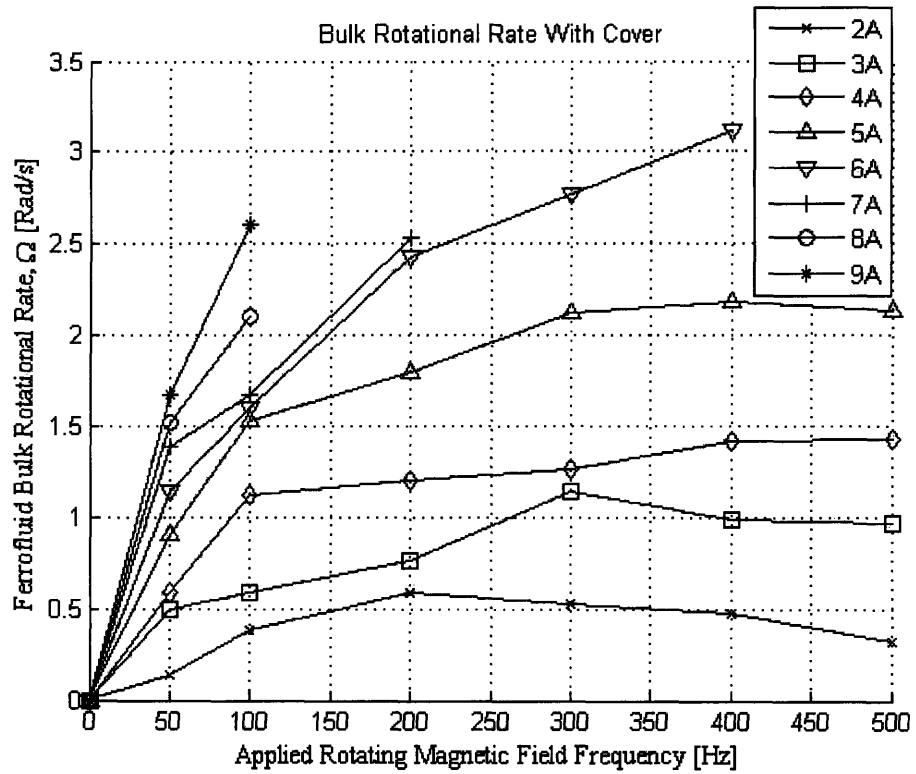


Figure 8-8 Relation between the bulk rotational rate in the central region of the MSG W11 ferrofluid, $\Omega = v_{\phi}/r$, and the frequency of the applied rotating magnetic field for various magnetic field strengths. The ultrasound probe was placed at height $z = z/2$ in the outside wall of a cylindrical container with a top cover.

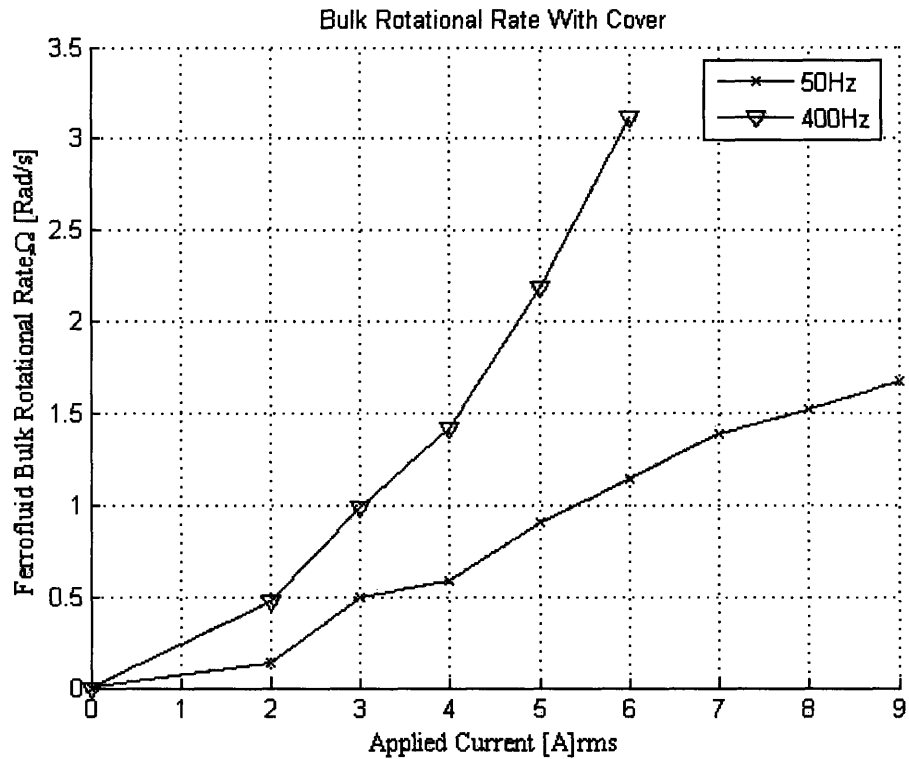


Figure 8-9 Relation between the bulk rotational rate in the central region of the MSG W11 ferrofluid, $\Omega = v_{\phi}/r$, and the applied currents for various magnetic field frequencies. The ultrasound probe was placed at height $z = z/2$ in the outside wall of a cylindrical container with a top cover. The rate of rotation increases monotonically with applied field strength for the investigated range of magnetic field strength.

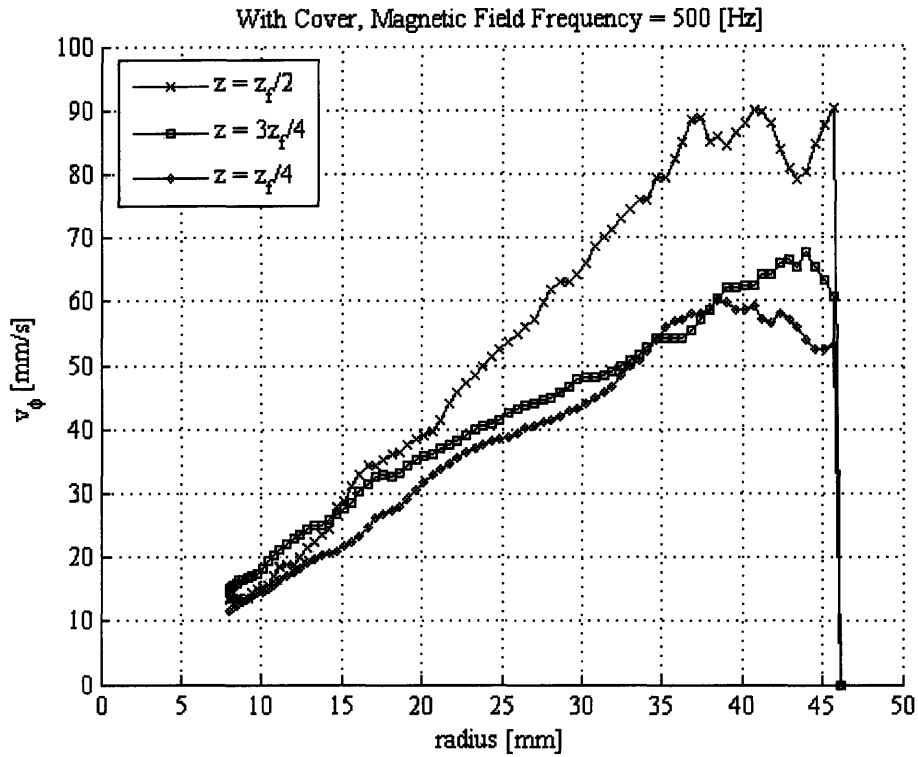


Figure 8-10 The azimuthal component of spin-up flow profiles at $z = z_f/2$, $z = 3z_f/4$ and $z = z_f/4$ for MSG W11 water-based ferrofluid excited by a non-uniform magnetic field rotating counter-clockwise at 500 Hz with balanced 3 phase currents of 5 A (rms). The cylindrical container was covered so that there were no free ferrofluid surfaces.

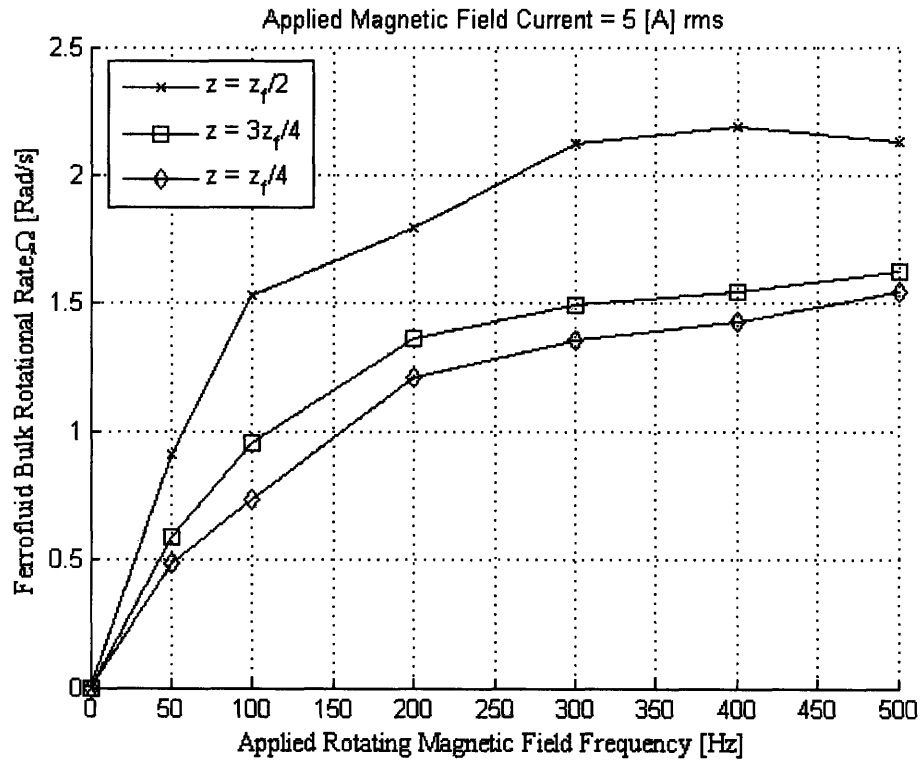


Figure 8-11 Relation between the bulk rotational rate in the central region of the MSG W11 ferrofluid, $\Omega = v_w/r$, and the applied rotating magnetic field frequency with current of 5 A (rms) at various heights. The ultrasound probes were placed at heights $z = z_r/4$, $z = z_r/2$ and $z = 3z_r/4$ with a top cover.

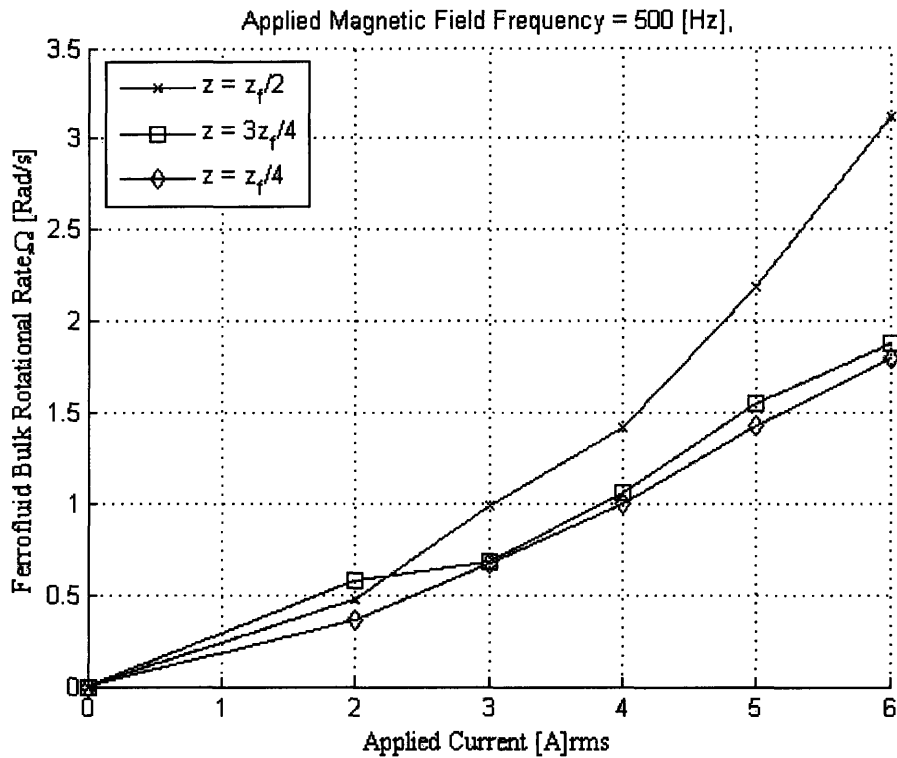


Figure 8-12 Relation between the bulk rotational rate in the central region of the MSG W11 ferrofluid, $\Omega = v_\phi/r$, and the applied current at applied rotating magnetic field frequency of 500 Hz for various heights. The ultrasound probes were placed at heights $z = z_f/4$, $z = z_f/2$ and $z = 3z_f/4$ with a top cover.

8.4.2 MSG W11 Water-based Ferrofluid Without Top Cover

Spin-up flow velocity profiles of MSG W11 water-based ferrofluid were also taken without a cover on the container in a counter-clockwise rotating non-uniform magnetic field, so that there was a free ferrofluid top surface. The air/ferrofluid interface at the surface of the vessel with no top is observed to co-rotate in the counter-clockwise direction which is different from the observation that surface flow counter-rotates in a uniform rotating magnetic field [82]. Figure 8-13 to Figure 8-15 show that bulk flows have the near-same azimuthal velocity profile and rotational rate for non-uniform rotating magnetic

field without and with a free air/ferrofluid interface. Our experiments also show that even though the free air/ferrofluid interface velocity co-rotates to the bulk flow, the effect of the free surface shear stress has little effect on the bulk flow of ferrofluid.

Figure 8-16 shows the optically observed rotational speeds on the surface of the ferrofluid. The surface of ferrofluid co-rotates with counter-clockwise rotating non-uniform magnetic field. The surface rotational speed is approximately the same as the bulk rotational speed, being up to about 3 rad/s as shown in Figure 8-14 to Figure 8-16.

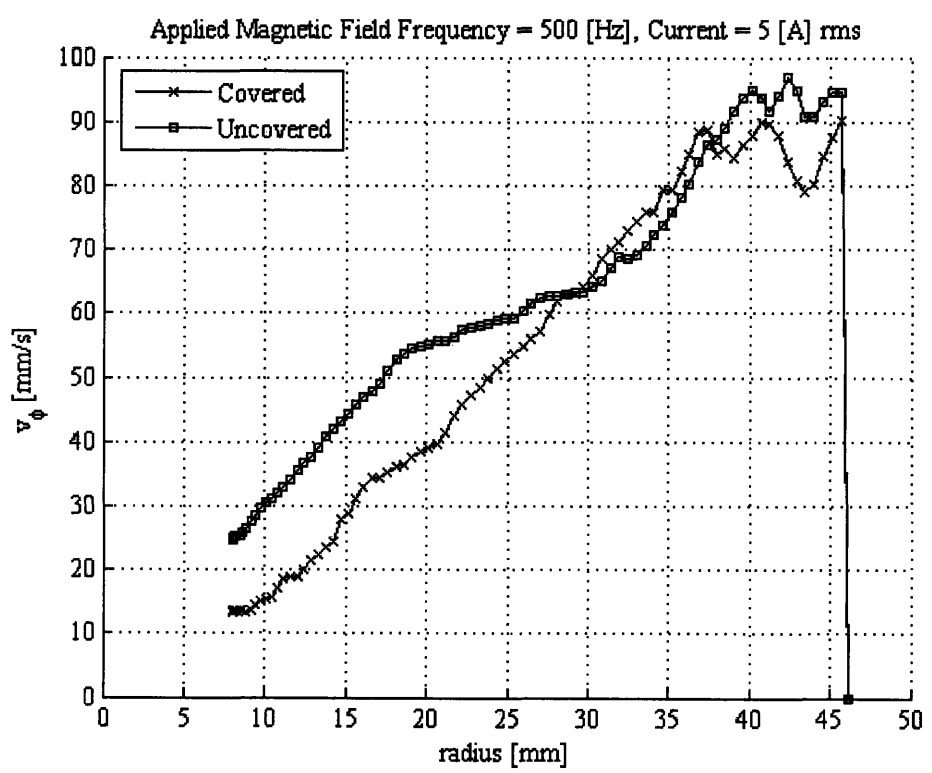


Figure 8-13 The azimuthal component of spin-up flow profiles at $z = z_r/2$, for MSG W11 water-based ferrofluid excited by a non-uniform magnetic field rotating counter-clockwise at 500 Hz with balanced 3 phase currents of 5 A (rms). The cylindrical container with free and covered ferrofluid surfaces had similar velocity variations with radius at $z = z_r/2$.

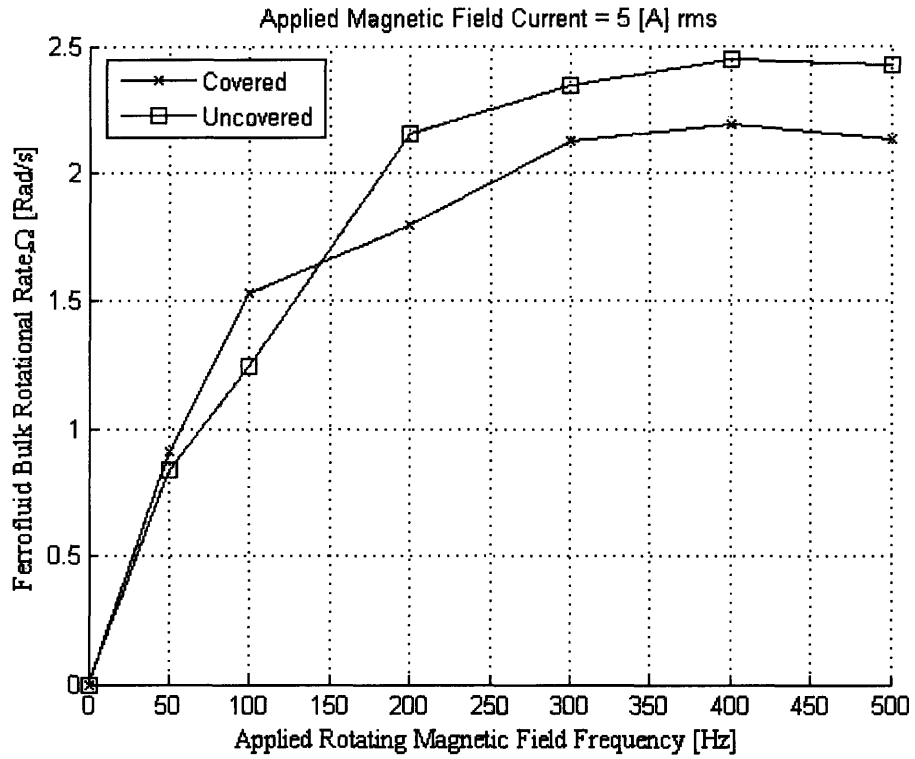


Figure 8-14 Relation between the co-rotating bulk rotational rate in the central region of the MSG W11 ferrofluid, $\Omega = v_{\phi}/r$, and the applied CCW rotating magnetic field frequency for balanced 3 phase currents of 5 A (rms). The ultrasound probe was placed at height $z = z/2$.

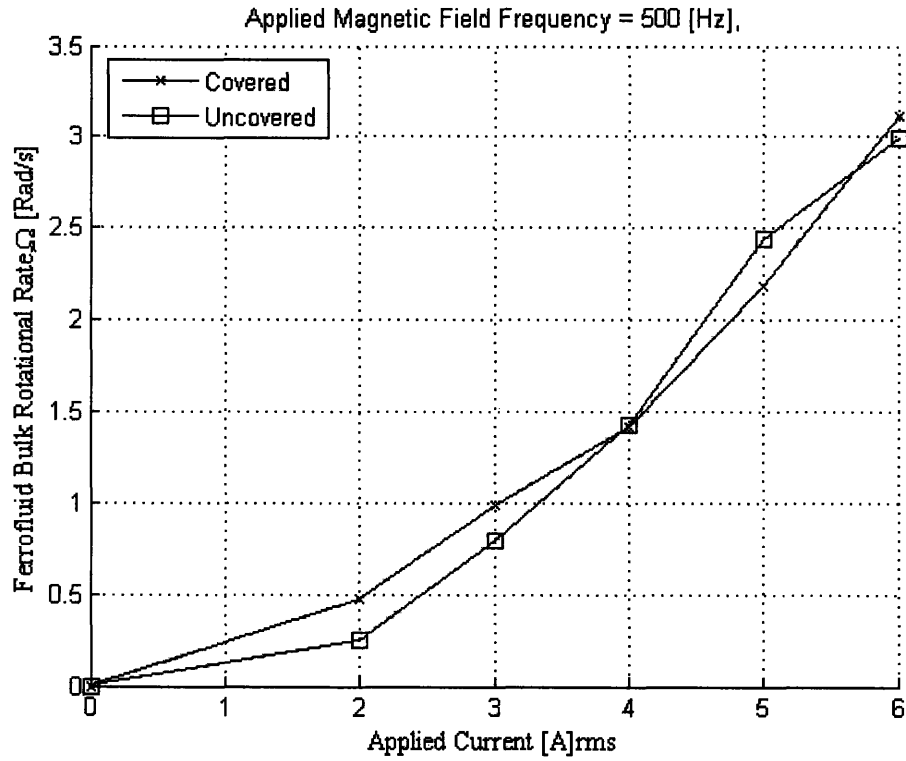


Figure 8-15 Relation between the co-rotating bulk rotational rate in the central region of the MSG W11 ferrofluid, $\Omega = v_\phi/r$, and the applied CCW rotating magnetic field frequency of 500 Hz for various magnetic field 3 phase balanced currents (rms). The ultrasound probe was place at height $z = z/2$.

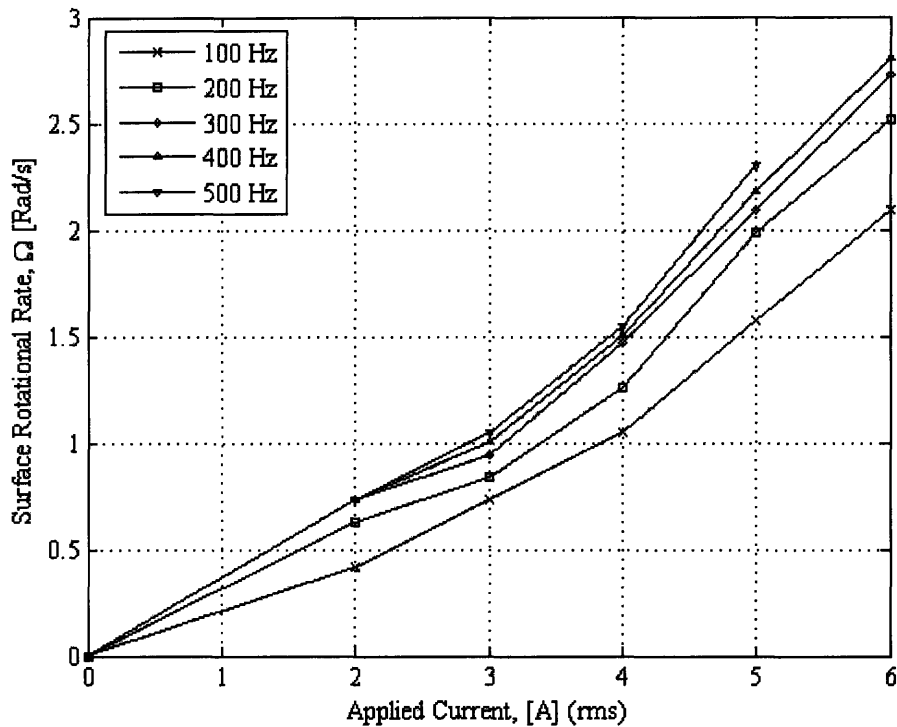


Figure 8-16 The co-rotational rates visually observed on the free top surface of MSG W11 water-based ferrofluid as a function of the frequency of the applied CCW rotating non-uniform magnetic field.

Figure 8-17 shows the azimuthal flow profiles at $z=z_f/2$ without a free surface for MSG W11 water-based ferrofluid excited by a uniform magnetic field rotating counter-clockwise at 200Hz [82]. Comparing the velocity profile in a uniform rotating magnetic field [82] with the velocity profile in a non-uniform rotating magnetic field discussed in this chapter shows that the peak velocities of velocity profiles in a uniform rotating magnetic field appear at the positions at approximately $r = (0.6\sim 0.8) R$, where R is the radius of the container, and the peak velocities of velocity profiles in a non-uniform rotating magnetic field appear at positions at approximately $r = 0.9 R$. The reason is that in a non-uniform rotating magnetic field with a field pattern as Figure 7-1 the magnetic field strength is linearly related to the radius, thus close to the container wall the magnetic body force density and volume torque density

have a stronger contribution to the spin-up flow and makes the peak velocity value appear at a position close to the container wall, even though the velocity at the wall is zero. It is also shown that the spin-up flow velocity profile in a non-uniform rotating magnetic field has a higher peak velocity rate of about 0.51 mm/s per Gauss than 0.25 mm/s per Gauss in a uniform rotating magnetic field shown in Figure 8-17. The reason is that the spin-up flow in a uniform rotating magnetic field has only the volume torque density $\mu_0 \bar{M} \times \bar{H}$ to drive the fluid, while spin-up flow in a non-uniform rotating magnetic field is driven by both the volume torque density $\mu_0 \bar{M} \times \bar{H}$ and the body force density $\mu_0 (\bar{M} \cdot \nabla) \bar{H}$. The body force density in a non-uniform magnetic field is strongest near the outer wall of ferrofluid container.

Additional measurements of flow profiles appear in Appendix B.

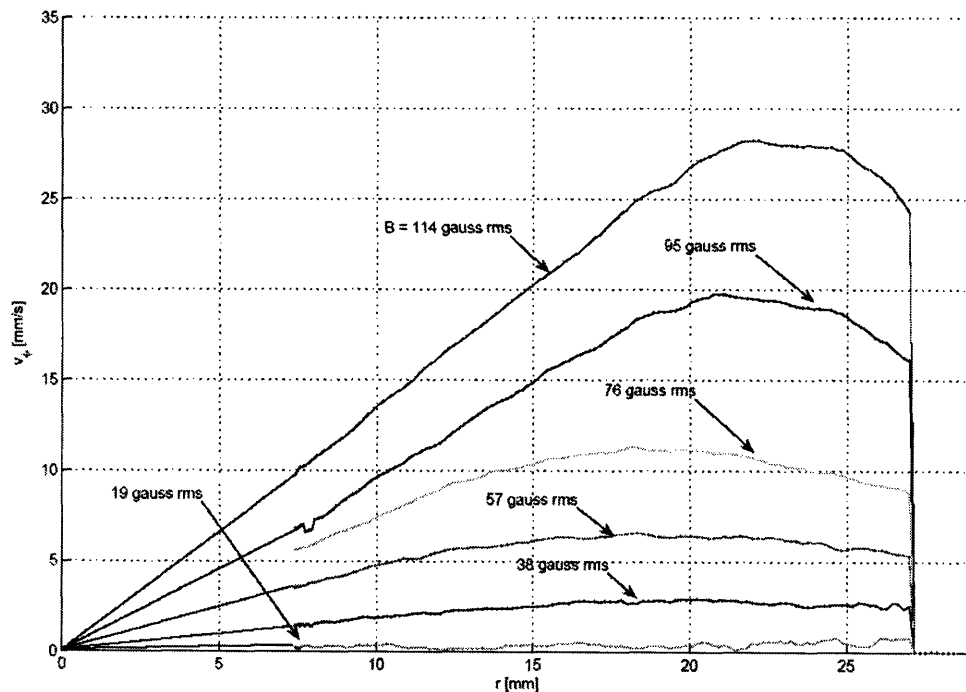


Figure 8-17 Azimuthal flow profiles at $z=z_r/2$ for MSG W11 water-based ferrofluid excited by a magnetic field rotating counter-clockwise at 200Hz. This flow profile results when water-based ferrofluid in a container without a free surface was placed in a uniform rotating applied magnetic field [82].

Chapter 9. Numerical Simulations for Torque Measurements and Spin-up Flow Velocity Measurements

Governing ferrohydrodynamic equations were modified for one dimensional problems and solved by numerical simulations for torque and spin-up flow velocity profiles in uniform and non-uniform rotating magnetic fields. For the torque computation in a uniform rotating magnetic field for ferrofluid inside the spindle, numerical simulation results show agreement with the measured torque in a uniform rotating magnetic field, where the torque on the spindle wall equals the total volume torque density integrated over the ferrofluid volume with zero body force density, \bar{F} . For the torque computation in a non-uniform rotating magnetic field, numerical simulation results show that the torque on the spindle wall equals the sum of the total volume torque density integrated over the ferrofluid volume and the torque due to the body force density, $\bar{r} \times \bar{F}$ integrated over the ferrofluid volume. Numerical simulations of spin-up flow velocity in a non-uniform rotating magnetic field are also discussed in this chapter.

9.1 Torque on a Cylindrical Boundary in a Rotating Magnetic Field

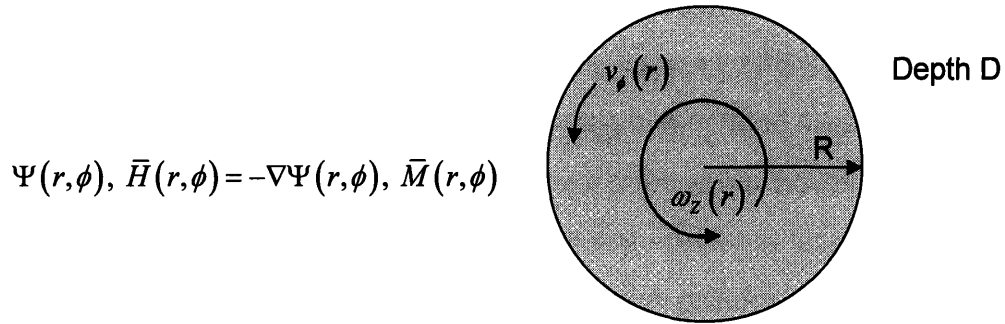


Figure 9-1 Ferrohydrodynamic induced torque on hollow spindle wall with ferrofluid inside spindle. Spindle has a radius R and Depth D.

As discussed in chapter 6 and chapter 7 with ferrofluid in a rotating magnetic field, the total torque on a ferrofluid filled spindle was measured using the viscometer torque meter. At the same time, the torque on the surface of the spindle inner wall can be evaluated by the total azimuthal shear force on the inside surface wall. Figure 9-1 shows in a cylindrical geometry that ferrofluid inside a spindle in a rotating magnetic field has an azimuthal velocity $v_\phi(r)$, and a spin velocity $\omega_z(r)$, where both the velocity and spin velocity are functions of the radius, r . The total surface torque on a spindle with radius R, height D and ferrofluid inside the spindle is given as

$$\begin{aligned} L_{sz} &= f_\phi \Big|_{r=R} R + \iint C_{rz} dS = R \iint F_{s\phi} dS + \iint C_{zr} dS = R \iint T_{\phi r} dS + \iint C_{zr} dS \\ &= \iint (T_{\phi r} R + C_{zr}) R d\phi dz = RD \int_0^{2\pi} (T_{\phi r} R + C_{zr}) d\phi \end{aligned} \quad (9.1)$$

where L_{sz} is the total z directed torque on the surface of the spindle wall with units of $[N \cdot m]$, f_ϕ is the total force on the spindle inner surface with units $[N]$, $F_{s\phi}$ is the total surface force density on the spindle inner surface with units

$[\text{N}/\text{m}^2]$, $T_{\phi r}$ is the total shear stress on the spindle inner surface with units of $[\text{N}/\text{m}^2]$, C_{zr} is the couple-stress on the spindle inner surface in the z direction with units of $[\text{N}/\text{m}]$, R is the radius of the spindle and D is the ferrofluid height in the spindle. The relation between total force, force density and the shear stress is given as

$$f_{\phi} = \iint F_{s\phi} dS = \iint T_{\phi r} dS = \int_{\phi=0}^{2\pi} \int_{z=0}^D T_{\phi r} R d\phi dz \quad (9.2)$$

where the surface force density equals the shear stress tensor as

$$F_{s\phi} = T_{\phi r} \quad (9.3)$$

for the cylindrical geometry shown in Figure 9-1. From (9.1), the torque on the spindle inner surface will be evaluated in section 9.1.1. The numerical simulation software, Femlab from Comsol, requires that the torque on the spindle inner surface be evaluated in a Cartesian geometry, as will be shown in section 9.1.2.

9.1.1 Torque Evaluation in Cylindrical Geometry

In cylindrical geometry, the total shear stress includes the Cauchy shear stress from fluid dynamics and the Maxwell stress tensor. Here as discussed in section 6.2.2, the jump in Maxwell stress tensor has no contribution on the azimuthal force, so that we only evaluate the Cauchy shear stress tensor. The Cauchy shear stress tensor is [1]

$$T_{\phi r} = \eta \left(r \frac{\partial}{\partial r} \left(\frac{v_{\phi}}{r} \right) + \frac{1}{r} \frac{\partial v_r}{\partial \phi} \right) + 2\zeta \left(\frac{1}{2} (\nabla \times \bar{v})_z - \omega_z \right) \quad (9.4)$$

where the z component of half the vorticity $\bar{\Omega} = \frac{1}{2} \nabla \times \bar{v}$ is

$$\Omega_z = \frac{1}{2} (\nabla \times \bar{v})_z = \frac{1}{2r} \left[\frac{\partial (rv_{\phi})}{\partial r} - \frac{\partial v_r}{\partial \phi} \right] \quad (9.5)$$

The total shear stress tensor is given as

$$\begin{aligned} T_{\phi r} &= \eta \left(r \frac{\partial}{\partial r} \left(\frac{v_\phi}{r} \right) + \frac{1}{r} \frac{\partial v_r}{\partial \phi} \right) + \zeta \left[\frac{\partial (rv_\phi)}{\partial r} - \frac{\partial v_r}{\partial \phi} \right] - 2\zeta\omega_z \\ &= (\eta + \zeta) \frac{\partial v_\phi}{\partial r} + (\eta - \zeta) \left(\frac{1}{r} \frac{\partial v_r}{\partial \phi} - \frac{v_\phi}{r} \right) - 2\zeta\omega_z \end{aligned} \quad (9.6)$$

Because the shear stress tensor is evaluated at the $r = R$ surface, (9.6) can be simplified by applying the boundary condition at that surface, which is

$$\bar{v} = 0, \quad \bar{\omega} = \frac{1}{2} \gamma (\nabla \times \bar{v}) \quad (9.7)$$

where γ is a boundary condition selector as described by (3.17) in section

3.4. The shear stress tensor at the boundary can be simplified to

$$\begin{aligned} T_{\phi r} &= (\eta + \zeta) \frac{\partial v_\phi}{\partial r} + (\eta - \zeta) \left(\frac{1}{r} \frac{\partial v_r}{\partial \phi} \right), \quad \text{when } \gamma = 0 \\ T_{\phi r} &= \eta \left(\frac{\partial v_\phi}{\partial r} + \frac{1}{r} \frac{\partial v_r}{\partial \phi} \right), \quad \text{when } \gamma = 1 \end{aligned} \quad (9.8)$$

The total couple-stress on the r directed normal surface in the z direction is

$$C_{zr} = \eta' \frac{\partial \omega_z}{\partial r} \quad (9.9)$$

The total torque on the inner surface of the spindle with ferrofluid inside can be evaluated by applying (9.8) and (9.9) in (9.1).

$$L_{sz} = \begin{cases} = 2\pi RD \left[(\eta + \zeta) R \frac{\partial v_\phi}{\partial r} + \eta' \frac{\partial \omega_z}{\partial r} \right] \Big|_{r=R}, & \text{when } \gamma = 0 \\ = 2\pi RD \left[\eta R \left(\frac{\partial v_\phi}{\partial r} + \frac{1}{r} \frac{\partial v_r}{\partial \phi} \right) + \eta' \frac{\partial \omega_z}{\partial r} \right] \Big|_{r=R}, & \text{when } \gamma = 1 \end{cases} \quad (9.10)$$

Using the assumption that both velocity and spin velocity are functions of r as shown in Figure 9-1, (9.10) reduces to

$$L_{sz} = \begin{cases} = 2\pi RD \left[(\eta + \zeta) R \frac{\partial v_\phi}{\partial r} + \eta' \frac{\partial \omega_z}{\partial r} \right] \Big|_{r=R}, & \text{when } \gamma = 0 \\ = 2\pi RD \left[\eta R \frac{\partial v_\phi}{\partial r} + \eta' \frac{\partial \omega_z}{\partial r} \right] \Big|_{r=R}, & \text{when } \gamma = 1 \end{cases} \quad (9.11)$$

For problems with ferrofluid outside the spindle and ferrofluid simultaneously inside and outside the spindle in cylindrical geometry, the same shear stress method can be used to evaluate the torque on the inner and outer surface of the spindle.

9.1.2 Torque Evaluation in Cartesian Geometry

Because the finite element software used to solve the ferrohydrodynamic equations, Comsol Multiphysics, requires equations to be solved in Cartesian coordinates, transformations from cylindrical geometry to Cartesian geometry was necessary. To calculate the total ϕ directed force density in Cartesian geometry,

$$\bar{F}_s = F_{s\phi} \bar{i}_\phi = -F_{s\phi} \sin \phi \bar{i}_x + F_{s\phi} \cos \phi \bar{i}_y \quad (9.12)$$

$$F_{sx} = \bar{F}_s \cdot \bar{i}_x = F_{s\phi} \bar{i}_\phi \cdot \bar{i}_x = -F_{s\phi} \sin \phi \Rightarrow F_{s\phi} = -\frac{F_{sx}}{\sin \phi} \quad (9.13)$$

$$F_{sy} = \bar{F}_s \cdot \bar{i}_y = F_{s\phi} \bar{i}_\phi \cdot \bar{i}_y = F_{s\phi} \cos \phi \Rightarrow F_{s\phi} = \frac{F_{sy}}{\cos \phi} \quad (9.14)$$

where F_{sx} and F_{sy} are the x and y directed surface force densities with units of $[N/m^2]$.

Generally the surface force density is calculated by the stress tensor as:

$$F_{si} = T_{ij} n_j \quad (9.15)$$

where F_{si} is the i directed surface force density with units $[N/m^2]$, T_{ij} is the Cauchy stress tensor component stress in the i direction on a surface with

normal in the j direction and n_j is the j directed normal direction. In this notation i, j could be any combination of x, y, z for Cartesian geometry or r, ϕ, z for cylindrical geometry.

In cylindrical geometry the normal direction of the surface on the spindle inner wall is the r direction. Transforming to Cartesian coordinates the normal direction is

$$\bar{n} = \bar{i}_r = \cos \phi \bar{i}_x + \sin \phi \bar{i}_y \quad (9.16)$$

The x and y components of the normal direction are given as

$$n_x = \cos \phi, \quad n_y = \sin \phi \quad (9.17)$$

Further, the x and y directed surface force density components are evaluated by the stress tensor as

$$\begin{aligned} F_{sx} &= T_{xj} n_j = T_{xx} n_x + T_{xy} n_y \\ F_{sy} &= T_{yj} n_j = T_{yx} n_x + T_{yy} n_y \end{aligned} \quad (9.18)$$

where $n_z = 0$ for cylindrical surfaces and T_{ij} is the magnetic field shear stress plus the fluid Cauchy stress tensor. As discussed in section 6.2.2, the magnetic field shear stress has no contribution on surface torque on the cylindrical container wall, T_{ij} is just the fluid Cauchy stress tensor which is given as

$$T_{ij} = -p \delta_{ij} + \eta \left(\frac{\partial v_i}{\partial x_j} + \frac{\partial v_j}{\partial x_i} \right) + \lambda \frac{\partial v_k}{\partial x_k} \delta_{ij} + 2\zeta \epsilon_{ijk} (\Omega_k - \omega_k) \quad (9.19)$$

where p is the pressure in the ferrofluid [N/m^2], η is the dynamic viscosity of ferrofluid with units of [$N \cdot s/m^2$], v_i is the i th component of velocity with units of [m/s], λ is the bulk viscosity with units of [$N \cdot s/m^2$], ζ is the vortex viscosity with units of [$N \cdot s/m^2$] where $\zeta = 1.5\eta\phi$ from microscopic theory for dilute

suspensions, $\bar{\Omega} = \frac{1}{2} \nabla \times \bar{v}$ is half of the vorticity and represents the fluid rate of rotation in the absence of magnetic force with units of [1/s] and $\bar{\omega}$ is the spin velocity of ferrofluid with units of [1/s]. δ_{ij} is the Kronecker delta and ε_{ijk} is the alternating unit tensor, defined as

$$\delta_{ij} = \begin{cases} 0 & i \neq j \\ 1 & i = j \end{cases}, \quad \varepsilon_{ijk} = \begin{cases} +1 & ijk = xyz, yzx \text{ or } zxy \\ -1 & ijk = xzy, yxz \text{ or } zyx \\ 0 & i = j, i = k \text{ or } j = k \end{cases} \quad (9.20)$$

From (9.19) and using the incompressible fluid condition, $\nabla \cdot \bar{v} = 0$, the stress components of T_{xx} and T_{yy} are evaluated with $\delta_{xx} = \delta_{yy} = 1$ and

$$\varepsilon_{xxk} = \varepsilon_{yyk} = 0 \text{ as}$$

$$\begin{aligned} T_{xx} &= -p + \eta \left(2 \frac{\partial v_x}{\partial x} \right) \\ T_{yy} &= -p + \eta \left(2 \frac{\partial v_y}{\partial y} \right) \end{aligned} \quad (9.21)$$

where the third term in (9.19) is eliminated because the ferrofluid was taken as an incompressible fluid so that $\nabla \cdot \bar{v} = 0$. The shear stress component of T_{xy}

and T_{yx} are

$$\begin{aligned} T_{xy} &= \eta \left(\frac{\partial v_x}{\partial y} + \frac{\partial v_y}{\partial x} \right) + 2\zeta (\Omega_z - \omega_z) = \eta \left(\frac{\partial v_x}{\partial y} + \frac{\partial v_y}{\partial x} \right) - \frac{T_z}{2} \\ T_{yx} &= \eta \left(\frac{\partial v_x}{\partial y} + \frac{\partial v_y}{\partial x} \right) - 2\zeta (\Omega_z - \omega_z) = \eta \left(\frac{\partial v_x}{\partial y} + \frac{\partial v_y}{\partial x} \right) + \frac{T_z}{2} \end{aligned} \quad (9.22)$$

where T_z is the z component of torque density \bar{T} in the ferrofluid with units of [N•m/m³] related to fluid velocity and spin velocity as

$$\bar{T} = \mu_0 \bar{M} \times \bar{H} = -4\zeta \left(\frac{1}{2} \nabla \times \bar{v} - \bar{\omega} \right) \quad (9.23)$$

The z component of the torque, T_z , is

$$T_z = -4\zeta(\Omega_z - \omega_z) \quad (9.24)$$

Combining (9.18) to (9.24), the x directed surface force density is then

$$F_{sx} = \left(2\eta \frac{\partial v_x}{\partial x} + p\right) \cos \phi + \left[\eta \left(\frac{\partial v_x}{\partial y} + \frac{\partial v_y}{\partial x}\right) - \frac{T_z}{2}\right] \sin \phi \quad (9.25)$$

Similarly the y directed surface force density is

$$F_{sy} = \left(2\eta \frac{\partial v_y}{\partial y} + p\right) \sin \phi + \left[\eta \left(\frac{\partial v_x}{\partial y} + \frac{\partial v_y}{\partial x}\right) + \frac{T_z}{2}\right] \cos \phi \quad (9.26)$$

The surface force density in the azimuthal direction is then

$$F_{s\phi} = -\sin \phi F_{sx} + \cos \phi F_{sy} \quad (9.27)$$

Replacing terms in (9.27) from (9.25) and (9.26), (9.27) reduces to

$$F_{s\phi} = \eta \left(\frac{\partial v_y}{\partial y} + \frac{\partial v_x}{\partial x}\right) \sin 2\phi + \eta \left(\frac{\partial v_x}{\partial y} - \frac{\partial v_y}{\partial x}\right) \cos 2\phi + \frac{T_z}{2} \quad (9.28)$$

The other component of (9.1) is the couple-stress, C_{zr} , which was evaluated from the couple-stress dyadic

$$C_{ij} = \eta' \left(\frac{\partial \omega_i}{\partial x_j} + \frac{\partial \omega_j}{\partial x_i}\right) + \lambda' \frac{\partial \omega_k}{\partial x_k} \delta_{ij} \quad (9.29)$$

where η' is the shear coefficient of spin viscosity [$N \cdot s$] and λ' is the bulk coefficient of spin viscosity [$N \cdot s$].

The component of total couple-stress in the z direction on the r directed normal surface is

$$\begin{aligned} C_{zr} &= \eta' \left(\frac{\partial \omega_r}{\partial z} + \frac{\partial \omega_z}{\partial r}\right) = \eta' \frac{\partial \omega_z}{\partial r} \\ &= \eta' \left(\frac{\partial \omega_z}{\partial x} \frac{\partial x}{\partial r} + \frac{\partial \omega_z}{\partial y} \frac{\partial y}{\partial r}\right) = \eta' \left(\frac{\partial \omega_z}{\partial x} \cos \phi + \frac{\partial \omega_z}{\partial y} \sin \phi\right) \end{aligned} \quad (9.30)$$

The total torque on the inner surface of the spindle with ferrofluid inside can be evaluated as shown by applying (9.28) and (9.30) into (9.1)

$$L_{sz} = RD \int_0^{2\pi} R \left[2\eta \left(\frac{\partial v_x}{\partial x} + \frac{\partial v_y}{\partial y} \right) \sin \phi \cos \phi + \eta \left(\frac{\partial v_x}{\partial y} + \frac{\partial v_y}{\partial x} \right) \cos 2\phi - \frac{T_z}{2} \right] d\phi \\ + RD \int_0^{2\pi} \eta' \left(\frac{\partial \omega_z}{\partial x} \cos \phi + \frac{\partial \omega_z}{\partial y} \sin \phi \right) d\phi \quad (9.31)$$

where all the values are evaluated at $r = R$. The integration in (9.31) can be easily calculated by a boundary integral in the numerical simulation.

At the same time, the total torque on the inner surface of the spindle with ferrofluid inside can be evaluated by integrating the torque density and the contribution of the force density throughout the volume of ferrofluid. Magnetic field \bar{H} and magnetization \bar{M} cause a force density $\bar{F} = \mu_0 \bar{M} \cdot \nabla \bar{H}$ and torque density $T = \mu_0 \bar{M} \times \bar{H}$ in the ferrofluid, which are the source of the total torque at the inner surface of the spindle wall. The total torque can be computed by integrating the torque and force density throughout the volume of ferrofluid.

$$L_{vz} = \iiint (T_z + (\bar{r} \times \bar{F})_z) r d\phi dr dz = 2\pi D \int_0^R (T_z + F_\phi r) r dr \quad (9.32)$$

where L_{vz} is the total volume torque integrated throughout the whole volume of ferrofluid, T_z is the z directed torque density in the ferrofluid volume and F_ϕ is the azimuthal force density in the ferrofluid volume. In the case of ferrofluid only inside the spindle, the total torque on the inner surface of the spindle, L_{sz} , balances the total volume torque, L_{vz} , integrated from the torque density $T = \mu_0 \bar{M} \times \bar{H}$ and the contribution of the force density $\bar{F} = \mu_0 \bar{M} \cdot \nabla \bar{H}$ throughout the volume of ferrofluid, which would have the same value as the

total torque integrated throughout the whole volume of ferrofluid. The torque balance relation is

$$L_{sz} = L_{vz} \quad (9.33)$$

Solving for the torque by two different methods provides a good check on the numerical simulation and will be demonstrated in section 9.3.

For problems with ferrofluid outside the spindle and ferrofluid simultaneously inside and outside the spindle, the same shear stress method can be used to calculate the torque on the inner and outer surfaces of the spindle wall with all the terms in (9.31) being evaluated with r equal to the value at the inner and outer wall surfaces. (9.33) is still true because the total volume torque throughout the volume of ferrofluid is just balanced by the surface torque on the boundaries. The torque balance equation has to be written as

$$\sum_s L_{sz} = L_{vz} \quad (9.34)$$

where the left hand side of (9.34) is the sum of all the surface torques on the boundaries of the ferrofluid.

9.2 Governing Equations for Numerical Simulation

The theoretical background and governing equations were introduced in chapter 3. The three sets of ferrohydrodynamic equations describe the electro-magnetic and fluid mechanical behavior in static and rotating uniform and non-uniform magnetic fields. The equations in chapter 3 can be simplified for numerical simulations to model experiments.

9.2.1 Assumption for Numerical Simulation

For our torque and spin-up velocity experiments, ferrofluid was stressed by a rotating uniform or non-uniform magnetic field in a cylindrical geometry as shown in Figure 9-1. We assume the electrically insulating spindles and

surrounding containers are placed in the center of the rotating magnetic field with heights much greater than the radius. With this assumption, our setup is symmetric in the z direction and for simplicity we ignore the axial dependence on z . In the AC sinusoidal steady state (oscillating or rotating) magnetic field using complex amplitude notation, the magnetic field, $\bar{H}(r, \phi)$, the magnetization, $\bar{M}(r, \phi)$, and the magnetic scalar potential, $\Psi(r, \phi)$, in Maxwell's equations in section 3.1 are of the form

$$\begin{aligned}\Psi &= \text{Re}\left\{\hat{\Psi}(r)e^{j(\omega t - n\phi)}\right\}, \quad \bar{H} = -\nabla\Psi = \text{Re}\left\{\hat{H}(r)e^{j(\omega t - n\phi)}\right\} \\ \bar{M} &= \text{Re}\left\{\hat{M}(r)e^{j(\omega t - n\phi)}\right\}\end{aligned}\tag{9.35}$$

where $\hat{H}(r)$ is the vector complex amplitude of the magnetic field, which is only a function of r , $\hat{M}(r)$ is the vector complex amplitude of the magnetization, $\hat{\Psi}(r)$ is the complex amplitude of the scalar potential and n is the number of pole pairs of the magnetic field. When $n = 1$, a 2 pole motor stator winding is used to generate a uniform rotating magnetic field, and when $n = 2$, a 4 pole motor stator winding is used to generate a non-uniform rotating magnetic field.

As shown in Figure 9-1, the velocity and spin-velocity in the magnetization relaxation equation in section 3.2 and the fluid dynamic equations in section 3.3 are of the form

$$\bar{v} = v_\phi(r)\bar{i}_\phi, \quad \bar{\omega} = \omega_z(r)\bar{i}_z\tag{9.36}$$

where by symmetry the velocity just has the azimuthal component depending on r and the spin velocity just has an axial component depending on r . We assume no hydrodynamic dependence on ϕ and z coordinates.

9.2.2 Differential Equations for Numerical Simulation

In cylindrical geometry, Poisson's equation (3.5) is written as

$$\frac{1}{r} \frac{\partial}{\partial r} \left(r \frac{\partial \Psi}{\partial r} \right) + \frac{1}{r^2} \frac{\partial^2 \Psi}{\partial \phi^2} + \frac{\partial^2 \Psi}{\partial z^2} = \frac{1}{r} \frac{\partial}{\partial r} (r M_r) + \frac{1}{r} \frac{\partial M_\phi}{\partial \phi} + \frac{\partial M_z}{\partial z} \quad (9.37)$$

which reduces to

$$\frac{1}{r} \frac{\partial \Psi}{\partial r} + \frac{\partial^2 \Psi}{\partial r^2} + \frac{1}{r^2} \frac{\partial^2 \Psi}{\partial \phi^2} = \frac{\partial M_r}{\partial r} + \frac{M_r}{r} + \frac{1}{r} \frac{\partial M_\phi}{\partial \phi} \quad (9.38)$$

where the third terms on both side of (9.37) drop out because there is no z dependence for the assumed forms of the magnetic scalar potential and magnetization in (9.35). Using the complex amplitude notation in (9.35), (9.37) reduces to

$$\frac{1}{r} \frac{\partial \hat{\Psi}}{\partial r} + \frac{\partial^2 \hat{\Psi}}{\partial r^2} + \frac{1}{r^2} (-n^2) \hat{\Psi} = \frac{\partial \hat{M}_r}{\partial r} + \frac{\hat{M}_r}{r} + \frac{1}{r} (-jn) \hat{M}_\phi \quad (9.39)$$

where the $\frac{\partial}{\partial \phi}$ term in (9.37) reduces to $-jn$ from the complex amplitude notation in (9.35).

Neglecting inertial terms due to assumed viscous dominated flow, the linear momentum equation (3.8) reduces to

$$-\nabla p' + \bar{F} + 2\zeta \nabla \times \bar{\omega} + (\eta + \zeta) \nabla^2 \bar{v} = 0 \quad (9.40)$$

where the first term on the left hand side of (3.8) drops out for low Reynolds' number flows and the fourth term in the right hand side of (3.8) drops out as we assume that the ferrofluid is incompressible as in (3.11), which makes $\nabla \cdot \bar{v} = 0$.

In cylindrical geometry the ϕ component of (9.40) is

$$-\frac{\partial p'}{\partial \phi} + F_\phi - 2\zeta \frac{\partial \omega_z}{\partial r} + (\eta + \zeta) \left[\frac{\partial}{\partial r} \left(\frac{1}{r} \frac{\partial}{\partial r} (r v_\phi) \right) + \frac{1}{r^2} \frac{\partial^2 v_\phi}{\partial \phi^2} + \frac{2}{r^2} \frac{\partial v_r}{\partial \phi} + \frac{\partial^2 v_\phi}{\partial z^2} \right] = 0 \quad (9.41)$$

Applying the form of velocity and spin velocity in (9.36), (9.41) reduces to

$$F_\phi - 2\zeta \frac{\partial \omega_z}{\partial r} + (\eta + \zeta) \left(\frac{\partial^2 v_\phi}{\partial r^2} + \frac{1}{r} \frac{\partial v_\phi}{\partial r} - \frac{v_\phi}{r^2} \right) = 0 \quad (9.42)$$

where the first and the last three terms drop out in (9.41) because there is no ϕ and z dependence on the fluid mechanical terms, and F_ϕ is the ϕ component of the time average force density in the ferrofluid, which is a function of the magnetic field and the magnetization in the ferrofluid.

In the sinusoidal steady state, the angular momentum equation (3.9) reduces to

$$\bar{T} + 2\zeta (\nabla \times \bar{v} - 2\bar{\omega}) + \eta' \nabla^2 \bar{\omega} = 0 \quad (9.43)$$

where the term on the left hand side of (3.9) drops out for low Reynolds' number flows. In cylindrical geometry, the z component of (9.43) is

$$T_z + 2\zeta \left(\frac{1}{r} \frac{\partial}{\partial r} (r v_\phi) - 2\omega_z \right) + \eta' \left(\frac{1}{r} \frac{\partial}{\partial r} \left(r \frac{\partial \omega_z}{\partial r} \right) + \frac{1}{r^2} \frac{\partial^2 \omega_z}{\partial \phi^2} + \frac{\partial^2 \omega_z}{\partial z^2} \right) = 0 \quad (9.44)$$

Applying the form of velocity and spin velocity in (9.36), (9.44) reduces to

$$T_z + 2\zeta \left(\frac{\partial v_\phi}{\partial r} + \frac{v_\phi}{r} - 2\omega_z \right) + \eta' \left(\frac{\partial^2 \omega_z}{\partial r^2} + \frac{1}{r} \frac{\partial \omega_z}{\partial r} \right) = 0 \quad (9.45)$$

where the last two terms in (9.44) drop out as there is no variation in ϕ and z , and T_z is the z component of the torque density in the ferrofluid, which is a function of the magnetic field and the magnetization of the ferrofluid.

Equations (9.39), (9.42) and (9.45) form the general differential equations for the numerical simulation. The three general differential equations have three unknown variables, the complex amplitude of magnetic scalar potential $\hat{\Psi}(r)$, the azimuthal velocity $v_\phi(r)$, and the axial spin velocity $\omega_z(r)$, all of which

only have dependence on r . To solve the general differential equations, it is necessary to find the expressions of the time average force density F_ϕ and torque density T_z in the ferrofluid, which is governed by the magnetization equation (3.7).

In cylindrical geometry in the sinusoidal steady state, the magnetization relaxation equation (3.7) was separated into r and ϕ components,

$$\begin{aligned}\bar{i}_r: \frac{\partial M_r}{\partial t} + \frac{v_\phi}{r} \left(\frac{\partial M_r}{\partial \phi} - M_\phi \right) + \omega_z M_\phi + \frac{1}{\tau} (M_r - \chi_0 H_r) &= 0 \\ \bar{i}_\phi: \frac{\partial M_\phi}{\partial t} + \frac{v_\phi}{r} \left(\frac{\partial M_\phi}{\partial \phi} + M_r \right) - \omega_z M_r + \frac{1}{\tau} (M_\phi - \chi_0 H_\phi) &= 0\end{aligned}\quad (9.46)$$

Applying the form of the magnetization from (9.35) and the form of velocity and spin velocity from (9.36), (9.46) reduces to

$$\begin{aligned}\bar{i}_r: \hat{M}_r \left[j \left(\Omega - n \frac{v_\phi}{r} \right) + \frac{1}{\tau} \right] + \left(\omega_z - \frac{v_\phi}{r} \right) \hat{M}_\phi &= \frac{\chi_0 \hat{H}_r}{\tau} \\ \bar{i}_\phi: \hat{M}_\phi \left[j \left(\Omega - n \frac{v_\phi}{r} \right) + \frac{1}{\tau} \right] - \left(\omega_z - \frac{v_\phi}{r} \right) \hat{M}_r &= \frac{\chi_0 \hat{H}_\phi}{\tau}\end{aligned}\quad (9.47)$$

Solving (9.47) in terms of the magnetic field, H_r and H_ϕ , the r and ϕ components of the magnetization are

$$\begin{aligned}\hat{M}_r &= \frac{\left[j \left(\Omega - n \frac{v_\phi}{r} \right) + \frac{1}{\tau} \right] \frac{\chi_0 \hat{H}_r}{\tau} - \left(\omega_z - \frac{v_\phi}{r} \right) \frac{\chi_0 \hat{H}_\phi}{\tau}}{\left[j \left(\Omega - n \frac{v_\phi}{r} \right) + \frac{1}{\tau} \right]^2 + \left(\omega_z - \frac{v_\phi}{r} \right)^2} \\ \hat{M}_\phi &= \frac{\left[j \left(\Omega - n \frac{v_\phi}{r} \right) + \frac{1}{\tau} \right] \frac{\chi_0 \hat{H}_\phi}{\tau} + \left(\omega_z - \frac{v_\phi}{r} \right) \frac{\chi_0 \hat{H}_r}{\tau}}{\left[j \left(\Omega - n \frac{v_\phi}{r} \right) + \frac{1}{\tau} \right]^2 + \left(\omega_z - \frac{v_\phi}{r} \right)^2}\end{aligned}\quad (9.48)$$

where the magnetic field terms can be replaced by the magnetic scalar potential. By applying the complex amplitude definition of (9.35) into the magnetic scalar potential gradient equation (3.2), the magnetic field terms are

$$\hat{H}_r = -\frac{\partial \hat{\psi}}{\partial r}, \quad \hat{H}_\phi = \frac{jn}{r} \hat{\psi} \quad (9.49)$$

Using (9.49) to replace the magnetic field terms in (9.48), the magnetization components in terms of the magnetic scalar potential are

$$\begin{aligned} \hat{M}_r &= \frac{-\left[j\left(\Omega - n\frac{v_\phi}{r}\right) + \frac{1}{\tau} \right] \frac{\chi_0}{\tau} \frac{\partial \hat{\psi}}{\partial r} - \left(\omega_z - \frac{v_\phi}{r}\right) \frac{\chi_0}{\tau} \frac{jn}{r} \hat{\psi}}{\left[j\left(\Omega - n\frac{v_\phi}{r}\right) + \frac{1}{\tau} \right]^2 + \left(\omega_z - \frac{v_\phi}{r}\right)^2} \\ \hat{M}_\phi &= \frac{-\left(\omega_z - \frac{v_\phi}{r}\right) \frac{\chi_0}{\tau} \frac{\partial \hat{\psi}}{\partial r} + \left[j\left(\Omega - n\frac{v_\phi}{r}\right) + \frac{1}{\tau} \right] \frac{\chi_0}{\tau} \frac{jn}{r} \hat{\psi}}{\left[j\left(\Omega - n\frac{v_\phi}{r}\right) + \frac{1}{\tau} \right]^2 + \left(\omega_z - \frac{v_\phi}{r}\right)^2} \end{aligned} \quad (9.50)$$

where the magnetization components depend on the magnetic scalar potential, velocity and spin velocity.

The time average force density and torque density in ferrofluid are given in terms of the magnetic field and the magnetization as shown in section 3.3. The force density and the torque density are given as time average values because in the fluid dynamic equations the applied magnetic field is oscillating or rotating and time averages result in time independent fluid and spin velocities. The time average force density is

$$\bar{F} = \langle \mu_0 \bar{M} \cdot \nabla \bar{H} \rangle \quad (9.51)$$

where the delimiters $\langle \rangle$ denote time average value. Using complex amplitude notation, (9.51) is rewritten as

$$\bar{F} = \frac{1}{2} \text{Re} \left\{ \mu_0 \hat{M} \cdot \nabla \hat{H}^* \right\} \quad (9.52)$$

The azimuthal component of the force density is

$$F_\phi = \frac{\mu_0}{2} \text{Re} \left\{ \hat{M}_r \frac{\partial \hat{H}_\phi^*}{\partial r} + \frac{\hat{M}_\phi}{r} \frac{\partial \hat{H}_\phi^*}{\partial \phi} + \hat{M}_z \frac{\partial \hat{H}_\phi^*}{\partial z} + \frac{\hat{M}_\phi \hat{H}_r^*}{r} \right\} \quad (9.53)$$

By applying (9.49), (9.53) is rewritten as

$$F_\phi = \frac{\mu_0}{2} \text{Re} \left\{ \frac{jn}{r^2} \hat{M}_r \hat{\Psi}^* - \frac{jn}{r} \hat{M}_r \frac{\partial \hat{\Psi}^*}{\partial r} + \left(\frac{n}{r} \right)^2 \hat{M}_\phi \hat{\Psi}^* - \frac{\hat{M}_\phi}{r} \frac{\partial \hat{\Psi}^*}{\partial r} \right\} \quad (9.54)$$

The radial component of the force density is

$$F_r = \frac{\mu_0}{2} \text{Re} \left\{ \hat{M}_r \frac{\partial \hat{H}_r^*}{\partial r} + \frac{\hat{M}_\phi}{r} \frac{\partial \hat{H}_r^*}{\partial \phi} + \hat{M}_z \frac{\partial \hat{H}_r^*}{\partial z} - \frac{\hat{M}_\phi \hat{H}_\phi^*}{r} \right\} \quad (9.55)$$

which is written in terms of the magnetic scalar potential, $\hat{\Psi}$, as

$$F_r = \frac{\mu_0}{2} \text{Re} \left\{ -\hat{M}_r \frac{\partial^2 \hat{\Psi}^*}{\partial r^2} + \frac{jn}{r^2} \hat{M}_\phi \hat{\Psi}^* - \frac{jn}{r} \hat{M}_\phi \frac{\partial \hat{\Psi}^*}{\partial r} \right\} \quad (9.56)$$

The time average torque density in the ferrofluid is

$$\bar{T} = \langle \mu_0 \bar{\mathbf{M}} \times \bar{\mathbf{H}} \rangle \quad (9.57)$$

The axial component of the torque density is

$$T_z = \frac{\mu_0}{2} \text{Re} \left\{ \hat{M}_r \hat{H}_\phi^* - \hat{M}_\phi \hat{H}_r^* \right\} \quad (9.58)$$

In terms of the magnetic scalar potential the torque density is

$$T_z = \frac{\mu_0}{2} \text{Re} \left\{ \frac{-jn}{r} \hat{M}_r \hat{\Psi}^* - \hat{M}_\phi \frac{\partial \hat{\Psi}^*}{\partial r} \right\} \quad (9.59)$$

Combining (9.50) with (9.54) and (9.59) gives the expressions of the time average force density F_ϕ and torque density T_z in the ferrofluid in terms of the complex amplitude of magnetic scalar potential $\hat{\Psi}(r)$, the azimuthal velocity $v_\phi(r)$, and the axial spin velocity $\omega_z(r)$, which are the only variables in the general differential equations of the numerical simulation. These

differential equations together with the constitutive expressions simply express the ferrohydrodynamic governing equations in a way, which can be solved numerically.

9.2.3 Boundary Conditions for Numerical Simulations

The boundary conditions in section 3.4 are modified for numerical simulation with the assumptions given in section 9.2.1.

For the case of ferrofluid inside a spindle two boundaries are present: in the center of the cylindrical geometry, at $r = 0$, and on the spindle wall, at $r = R$, where R is the radius of the test spindle.

The boundary condition at $r = 0$ for the magnetic scalar potential is

$$\hat{\Psi}(r = 0) = 0 \quad (9.60)$$

where the complex amplitude expression is used to match the differential equations, and the magnetic scalar potential equals zero in the center because from (9.49) the magnetic field at the center must be finite. The boundary condition at $r = R$ for the magnetic scalar potential is given from (9.49) as

$$\hat{H}_\phi(r = R) = \frac{jn}{r} \hat{\psi}(r = R) = -K_z \Rightarrow \hat{\psi}(r = R) = \frac{jr}{n} K_z \quad (9.61)$$

where K_z is the surface current density in the axial direction. The boundary condition for the velocity and spin velocity at $r = R$ are

$$\begin{aligned} v_\phi(r = R) &= 0 \\ \omega_z(r = R) &= \frac{\gamma}{2} (\nabla \times \bar{v})_z \Big|_{r=R} = \frac{\gamma}{2r} \frac{\partial}{\partial r} (rv_\phi) \Big|_{r=R} \end{aligned} \quad (9.62)$$

where γ is the spin boundary condition selector as described in (3.17).

9.3 Numerical Simulation Types

The ferrohydrodynamic nonlinear governing equations have a singularity point at $r = 0$ as shown in section 9.2. Because the oscillating or rotating magnetic fields are described with complex amplitudes, solving the differential equations requires complex number computation. All these make the ferrohydrodynamic equations a non-linear complex variable system, which can only be solved by numerical simulation.

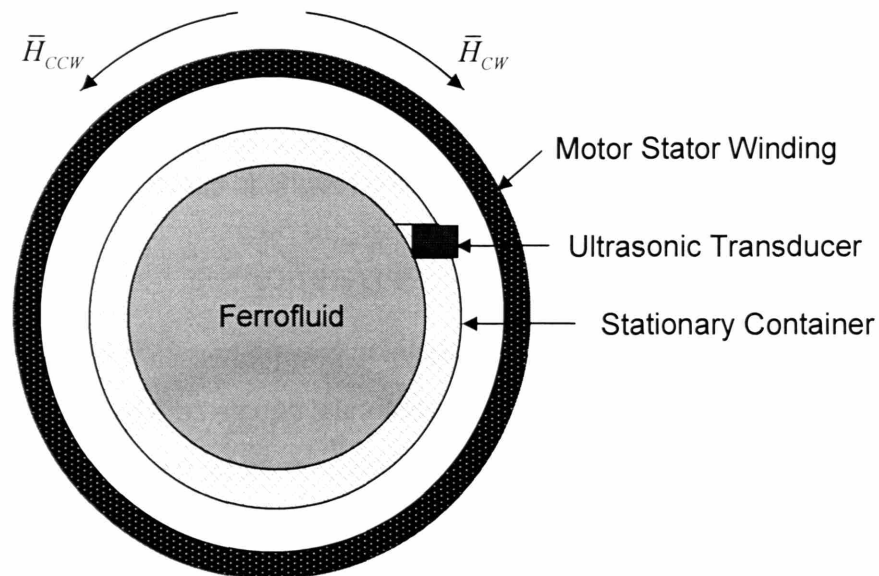


Figure 9-2 Experiment setup for velocity profile and torque measurements with ferrofluid inside the spindle with clockwise (\bar{H}_{CW}) or counter clockwise (\bar{H}_{CCW}) rotating magnetic fields.

Based on ferrofluid locations involving torque measurements and spin-up profile measurements, the numerical simulations are of two types, one region problem and multi-region problem. Velocity profile measurements and torque measurements with ferrofluid just inside the spindle shown in Figure 9-2 belong to the first type of simulation as a one region problem with one boundary at the container inner wall for velocity profile measurements and the

spindle inner wall for the torque measurements. A flow velocity and spin velocity value at the outer boundary combined with a surface current density boundary condition on the magnetic field at the stator winding provide all the necessary information to solve the hydrodynamic equations and magnetic field equations as shown in section 9.2.3.

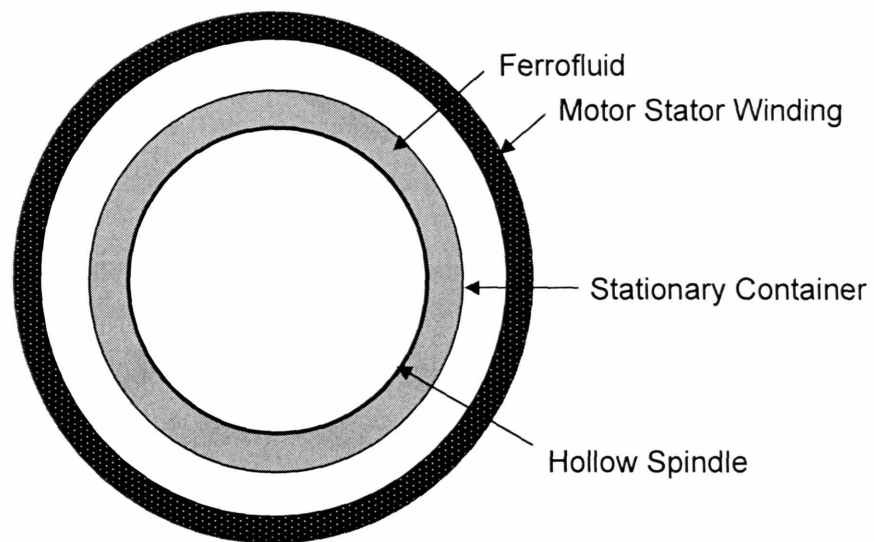


Figure 9-3 Experiment setup for torque measurements with ferrofluid just outside the spindle in the annulus gap between the spindle and the container wall.

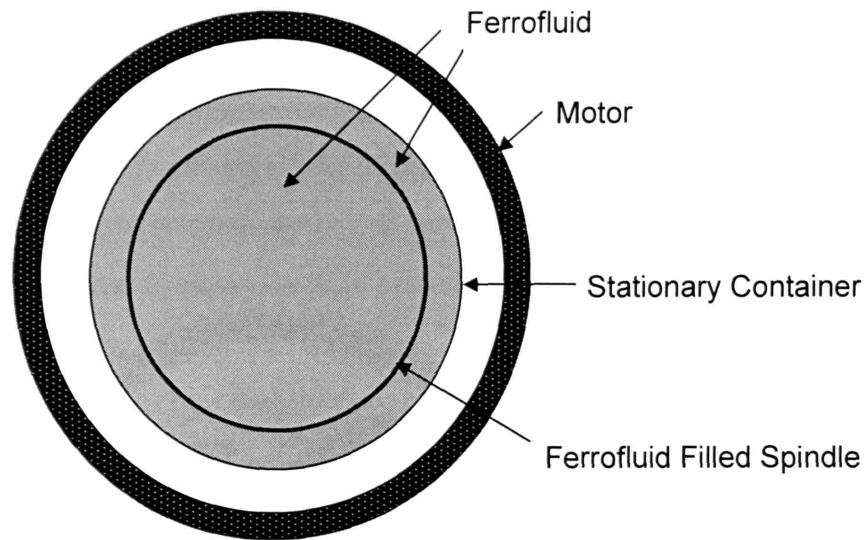


Figure 9-4 Experiment setup for torque measurements with ferrofluid simultaneously inside and outside the spindle. Ferrofluid was filled in the hollow spindle and the annulus gap between the spindle and the container, so that the simulation is a two region problem.

Torque measurements with ferrofluid just outside the spindle, as shown in Figure 9-3, and torque measurements with ferrofluid simultaneously inside and outside the spindle as shown in Figure 9-4 require a two region simulation as they require separate computational solutions in two regions in the numerical simulation with an interior boundary condition at the spindle wall, which needs specification of the boundary conditions for the velocity and the spin velocity. The magnetic scalar potential is continuous across the interior boundaries, so that the simulation does not require an additional boundary condition for the magnetic scalar potential at the interior boundary.

9.4 Numerical Simulation Software and Algorithms

FEMLAB, the numerical finite element multiphysics package from Comsol, was used to perform the numerical simulations. The FEMLAB multiphysics package is an interactive environment for modeling scientific and engineering applications described by partial differential equations (PDEs) and boundary conditions. It offers a complete multiphysics modeling environment, which can simultaneously solve any combination of physics. Based on the proven finite element method, the FEMLAB multiphysics package provides unprecedented speed and accuracy for challenging multiphysics applications through its high-performance solvers. This software package possesses three important features that allowed the ferrohydrodynamics solution outlined in the previous section. First, FEMLAB allowed the definition and solution of general partial differential equations. Second, it handles complex numbers and variables in differential equations. Third, problem definition in FEMLAB is not limited to a graphical user interface. A scripting language allows definition of FEMLAB models in terms of simple commands that can be incorporated into MATLAB scripts.

We approach the numerical solution for the full ferrohydrodynamic governing equations by decoupling the system non-linear differential equations into two linear systems that are easily solved by FEMLAB finite element models. The schematic diagram in Figure 9-5 illustrates the iterative procedure used to numerically solve the full set of governing ferrohydrodynamic equations. The algorithm starts with initial guesses for the body torque and force densities as functions of radius. The assumed forms for $T_z(r)$ and $F_\phi(r)$ are then used to numerically solve the fluid mechanical governing equations given by (9.42) and (9.45) for $v_\phi(r)$ and $\omega_z(r)$. These results are subsequently input into the magnetization constitutive equations (9.50). The electro-magnetic governing equations given by the expressions in (9.39) are numerically solved for the

magnetic potential complex amplitude $\hat{\Psi}(r)$. Knowledge of $\hat{\Psi}(r)$ determines the magnetic field intensity components $\hat{H}_r(r)$, $\hat{H}_\phi(r)$ and magnetization $\hat{M}_r(r)$, $\hat{M}_\phi(r)$ and consequently a new estimate of the body torque and force densities by (9.54) and (9.59). The new estimate can be used as input to the fluid mechanics governing equations to produce new estimates for the velocity and spin velocity. The algorithm allows this iterative procedure to continue until the successive estimates converge on a final value and further iterations have negligible effect on the solution.

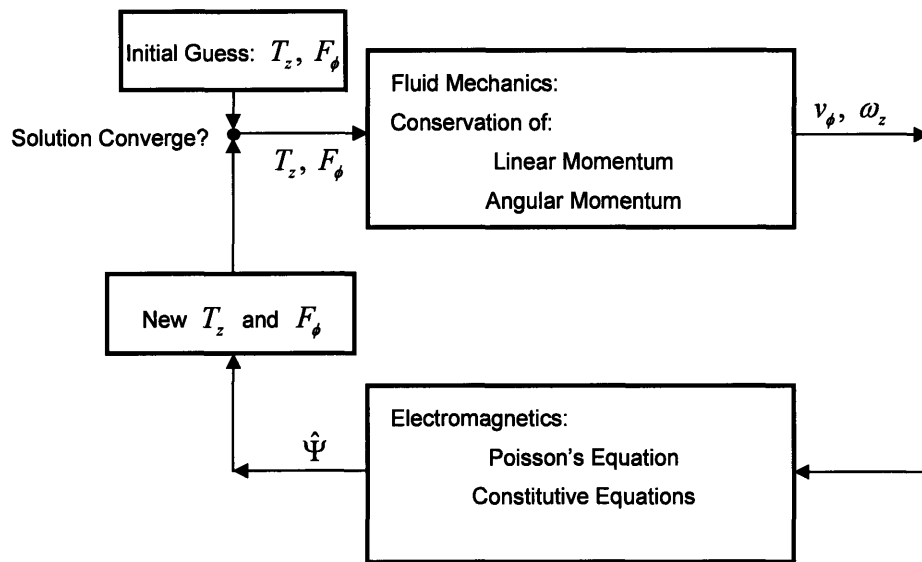


Figure 9-5 Schematic of algorithm to numerically solve the governing ferrohydrodynamic equations using Femlab. By guessing an initial functional form for the force and torque densities, the ferrohydrodynamic equations are decoupled into two linear systems.

Table 2-2 contains the parameters used for FEMLAB numerical simulations, when all the physical and magnetic properties of the ferrofluid are known. Most of the required properties of ferrofluids, like the density, viscosity, low-field

magnetic susceptibility and saturation magnetization, were measured directly through independent experimental techniques described in Chapter 2. The magnetic relaxation time τ and the spin-viscosity η' are difficult to measure directly. Theoretical considerations for finding estimates of η' are based on dilute limit approximations and may not apply at the magnetic nanoparticle concentration levels used in the studies we present in this thesis. Figure 9-6, illustrates the method used to search for values of τ and η' that best match the results of the numerical simulation to ultrasound velocity measurements. The algorithm first fully maps out a region in $\tau - \eta'$ space for each value of experimentally applied magnetic field strength and frequency. The algorithm runs hundreds of numerical simulations and stores all the solution data for subsequent processing. The code usually ran over a few days and nights on a dedicated computer. Once the solution space is mapped, the algorithm could plot contours of constant peak profile velocity v_{\max} and contours of relative constant peak velocity radial position r_{\max} / R as illustrated in panel a of Figure 9-6. Each experimental result for a given applied magnetic field strength and frequency corresponds to the intersection of a particular v_{\max} contour and a r_{\max} / R contour. This is seen more clearly in panel b of the figure, where the contours are offset by the experimentally measured values. The algorithm can easily compute the intersection of the contours labeled zero shown in panel c.

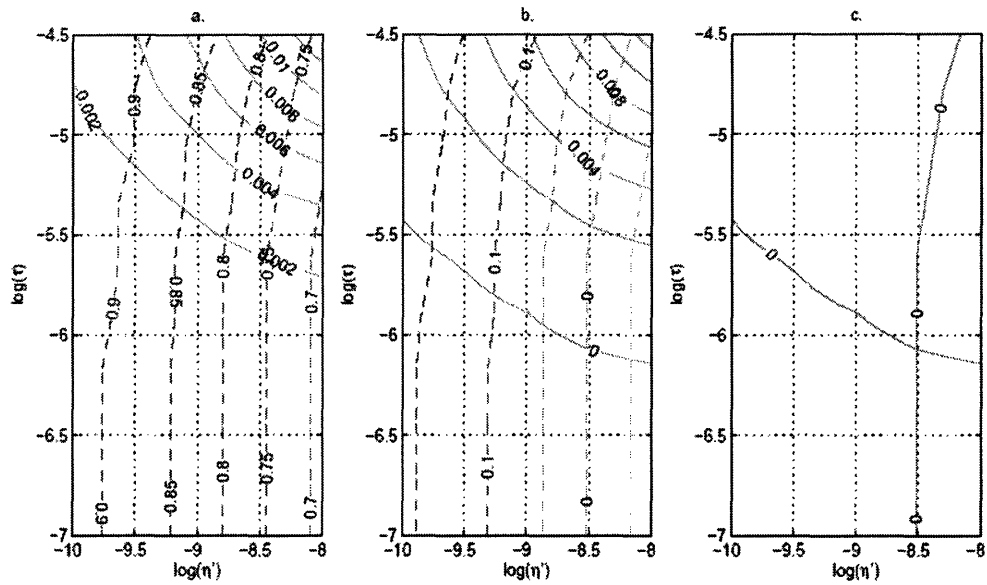


Figure 9-6 Sequence illustrating the method used to find the values of τ and η' in the 2D search space that best fit numerical simulation results to experimental data. **Panel a:** The algorithm first runs an extensive array of numerical simulations to fully map out contours of constant peak velocity magnitude v_{\max} (solid contours), and peak velocity radial position (dashed contours) for any given applied magnetic field strength and frequency. **Panel b:** The experimentally measured values of peak velocity magnitude and peak velocity radial position for the applied magnetic field strength and frequency are subtracted from the contours. **Panel c:** The intersection of the two contours labeled zero is the point in $\tau - \eta'$ space that best matches simulation to experiment.

9.5 Simulation Results

9.5.1 One Regional Simulations

One region simulations include torque simulation for the ferrofluid inside the spindle in a uniform rotating magnetic field, spin-up velocity profile simulation in a non-uniform rotating magnetic field, and torque simulation for the ferrofluid inside the spindle in a non-uniform rotating magnetic field. The one region simulation starts with the spin-up velocity profile simulation in a non-uniform rotating magnetic field. Matching the simulation result for the spin-up velocity profile using the method discussed in section 9.4 with the experiment data, determines two important parameters, magnetic relaxation time τ and spin viscosity η' .

9.5.1.1 Spin-up Velocity Profile Simulation in a Non-uniform Rotating Magnetic field

By fitting the experiment data discussed in chapter 8, the value of relaxation time, τ , and the spin viscosity, η' , were estimated as $\tau \approx (1.3-30) \times 10^{-6}$ [s] and $\eta' \approx (1-11.8) \times 10^{-9}$ [N•s] for MSG W11 water-based ferrofluid. If we assume that Brownian processes dominate the relaxation time constant, *i.e.*, $\tau = \tau_B = 3V\eta / kT$, these relaxation time values result in particle diameter of 5.5~17.0 nm with average value of 11.2 nm, which agree with our VSM measurements listed in Table 2-2.

The spin viscosity value can be estimated [1] by $\eta' \sim \eta l^2$, where l is the characteristic diffusion length which has the same order of magnitude as the average distance between the solid particles defined by the approximate

dilute-limit relationship, $\frac{l}{d} = \left(\frac{\pi}{6\phi}\right)^{\frac{1}{3}}$, where d is particle diameter and ϕ is the volume fraction of magnetic nanoparticles in the ferrofluid. For example, the MSG W11 water-based ferrofluid with volume fraction $\phi = 2.75\%$ yields $\frac{l}{d} = 2.67$. With $d = 5.5 - 12.4$ nm and viscosity $\eta = 0.00202$ [N-s/m²], the spin viscosity is $\eta' = 0.436 - 2.214 \times 10^{-16}$ [N-s]. Such a small number for spin viscosity has resulted with most researchers using the approximation of $\eta' = 0$. However, with $\eta' = 0$ the numerical simulations do not agree with our experiments as shown in the following section.

The preceding calculation of ferrofluid physical parameters from flow data illustrates the sensitivity of key ferrofluid properties like the magnetization relaxation time and the spin viscosity to small variations in particle size and diffusion length respectively. Although ferrofluids are modeled as continua of mono-dispersed non-interacting nanoparticles, they are more accurately characterized by a distribution of particle sizes around an average value. Moreover, it has been suggested that the magnetic particles agglomerate to form long chains of particles due to the interaction between the particles when magnetic fields are applied [38]. Other authors report microscopic failures of colloidal stability even in relatively weak magnetic fields, ~ 10 gauss, resulting in the separation of ferrofluids into two liquids of different particle concentrations [39].

Table 9-1 Best fit values of τ and η' for different applied non-uniform magnetic field strengths using the 4 pole motor stator winding for MSG W11 water-based ferrofluid.

| Frequency | Current | 2 [A] (rms) | 3 [A] (rms) | 4 [A] (rms) | 5 [A] (rms) | 6 [A] (rms) |
|-----------|-------------------|----------------------|----------------------|-----------------------|----------------------|-----------------------|
| 300 [Hz] | τ [μ s] | 6.2 | 8.1 | 12.3 | 21.8 | 30.0 |
| | η' [N·s] | 1.6×10^{-9} | 3.5×10^{-9} | 5.3×10^{-9} | 4.0×10^{-9} | 11.8×10^{-9} |
| 400 [Hz] | τ [μ s] | 2.0 | 7.3 | 4.5 | 14.5 | 11.2 |
| | η' [N·s] | 1.0×10^{-9} | 2.1×10^{-9} | 1.7×10^{-9} | 9.0×10^{-9} | 4.5×10^{-9} |
| 500 [Hz] | τ [μ s] | 1.3 | 5.6 | 7.9 | 18.0 | * |
| | η' [N·s] | 1.3×10^{-9} | 2.4×10^{-9} | 4.67×10^{-9} | 6.0×10^{-9} | * |

***: The best fit values of τ and η' for MSG W11 water-based ferrofluid at 500 Hz 6 A**

(rms) are absent because applying 6 A (rms) at 500 Hz results in a winding high voltage (~ 150 V), above the safe limitation of the apparatus. All the simulations used the

boundary condition of $\gamma = 0$. Using the boundary condition of $\gamma = 1$, the theory

predicts a slight increase of $\frac{\zeta}{\eta} = 1.5\phi$ in the fit values which for MSG W11 water-based

ferrofluid with $\phi = 2.75\%$ gives an approximate 4% increase in torque.

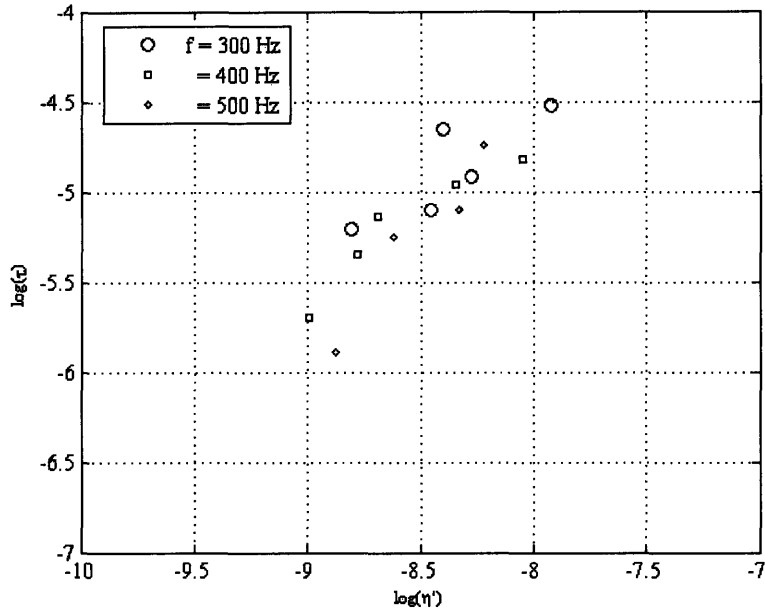


Figure 9-7 Scatter plot showing the different fit values of τ and η' for the MSG W11 water-based ferrofluid experimental magnetic field strengths and frequencies listed in Table 9-1.

Table 9-1 and Figure 9-7 summarize the best fit values of τ and η' used in Figure 9-8 to Figure 9-10 to fit all experimental data points close to the numerical simulation results. Figure 9-8 to Figure 9-10 compare measured spin-up velocity profiles and simulation results for MSG W11 water-based ferrofluid in applied magnet fields with frequencies of 300, 400 and 500 Hz at magnitude corresponding to the applied current of 2, 3, 4, 5 and 6 A rms. The relationship of applied current and the non-uniform magnetic field magnitude was discussed in section 7.1. Note that each figure uses a different value of τ and η' for the theoretical curves as summarized in Table 9-1.

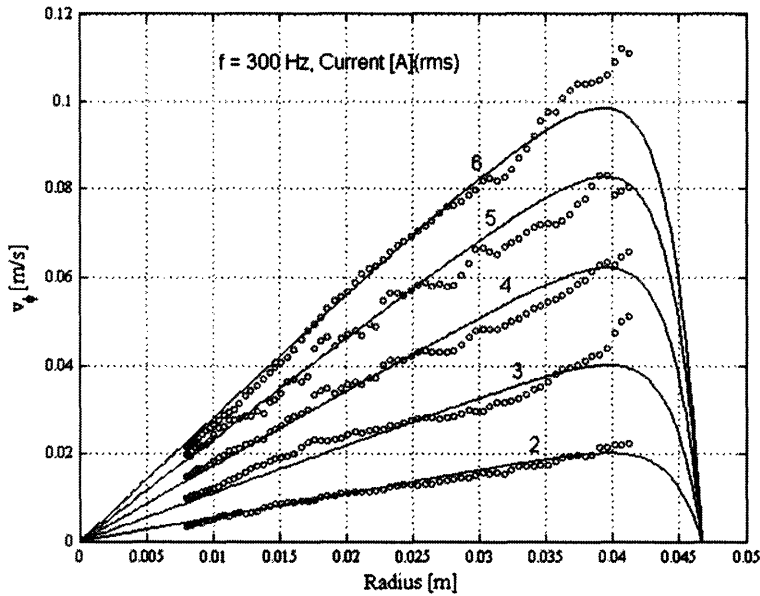


Figure 9-8 Comparison of experimentally measured (red thick dotted curves) and numerical simulations for ferrofluid spin-up velocity profiles in a non-uniform 300 Hz rotating magnetic field (black thin solid curves) for MSG W11 water-based ferrofluid.

The numerical plots were generated using the fit values for τ and η' in Table 9-1.

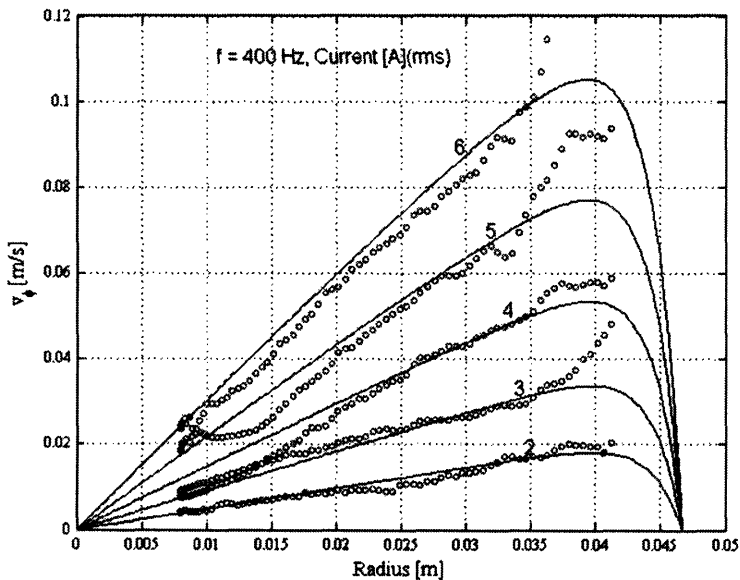


Figure 9-9 Comparison of experimentally measured (red thick dotted curves) and numerical simulations for ferrofluid spin-up velocity profiles in a non-uniform 400 Hz rotating magnetic field (black thin solid curves) for MSG W11 water-based ferrofluid.

The numerical plots were generated using the fit values for τ and η' in Table 9-1.

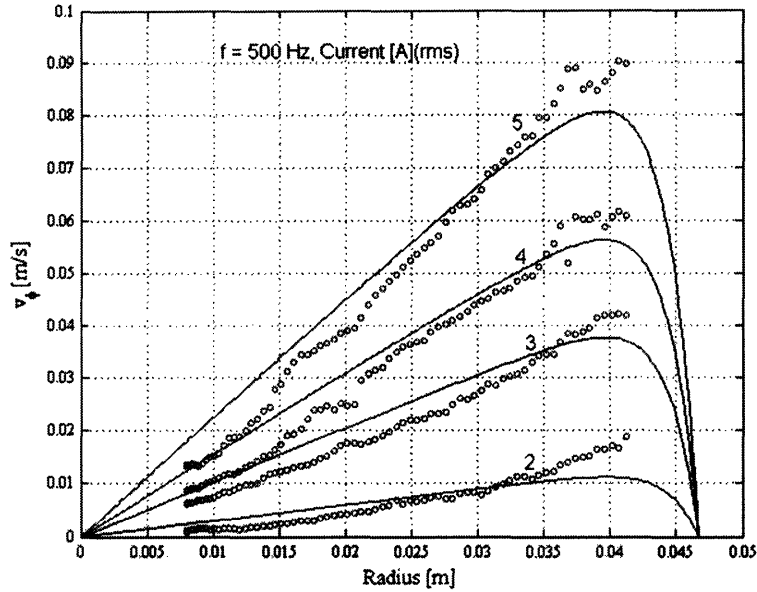


Figure 9-10 Comparison of experimentally measured (red thick dotted curves) and numerical simulations for ferrofluid spin-up velocity profiles in a non-uniform 500 Hz rotating magnetic field (black thin solid curves) for MSG W11 water-based ferrofluid.

The numerical plots were generated using the fit values for τ and η' in Table 9-1.

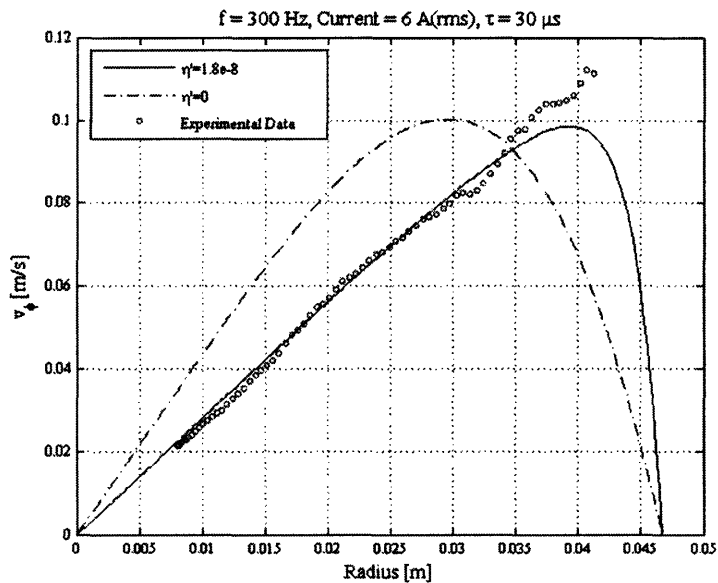


Figure 9-11 Comparison of the experimental data (red thick dotted curve), numerical simulations with $\eta' = 0$ (dashed curve) and with $\eta' \neq 0$ (solid curve) for ferrofluid spin-up velocity profiles in a non-uniform 300 Hz rotating magnetic field with 6 A (rms) input current for MSG W11 water-based ferrofluid.

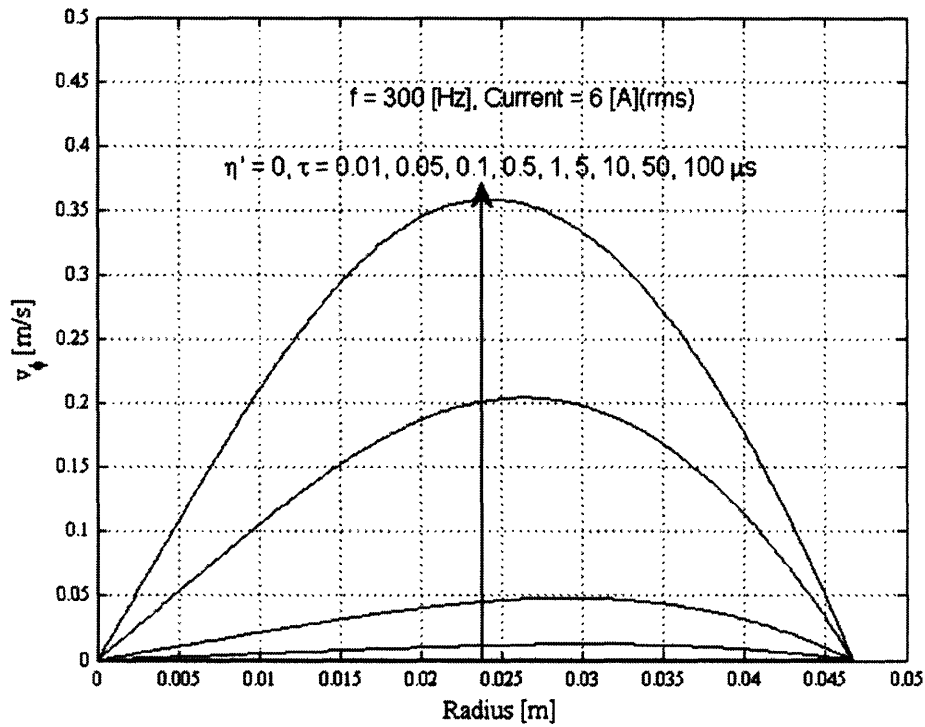


Figure 9-12 Numerical simulations with $\eta' = 0$ for MSG W11 water-based ferrofluid spin-up velocity profiles in a non-uniform 300 Hz rotating magnetic field with 6 A (rms) input current for various values of τ .

Table 9-2 Numerical simulation of maximum velocity position with $\eta' = 0$ for MSG W11 water-based ferrofluid spin-up velocity profiles in a non-uniform 300 Hz rotating magnetic field with 6 A (rms) input current for various values of τ . The percentage value of r_{max}/R is given using $R = 0.047$ mm for the plastic inner radius.

| τ [μ s] | 0.01 | 0.05 | 0.1 | 0.5 | 1 | 5 | 10 | 50 | 100 |
|-------------------|-------|-------|-------|-------|-------|-------|-------|-------|-------|
| r_{max} [m] | 0.035 | 0.032 | 0.032 | 0.031 | 0.031 | 0.03 | 0.029 | 0.026 | 0.024 |
| r_{max}/R | 74.4% | 68.4% | 67.4% | 66.4% | 65.9% | 64.4% | 61.9% | 55.9% | 51.4% |

Figure 9-11 and Figure 9-12 show that numerical simulations with $\eta' = 0$ for various values of τ for MSG W11 water-based ferrofluid spin-up velocity profiles in a non-uniform 300 Hz rotating magnetic field with 6 A (rms) input current have maximum velocity position at around 50%-75% of the container inner radius which does not agree with the experimental data with the maximum velocity very close to the container inner radius. Table 9-2 shows the maximum velocity position of the numerical simulations with $\eta' = 0$ for various values of τ for MSG W11 water-based ferrofluid spin-up velocity profiles in a non-uniform 300 Hz rotating magnetic field with 6 A (rms) input current.

9.5.1.2 Simulated Flow and Field Solutions

Figure 9-13 to Figure 9-19 present the simulated solutions for various field and flow variables.

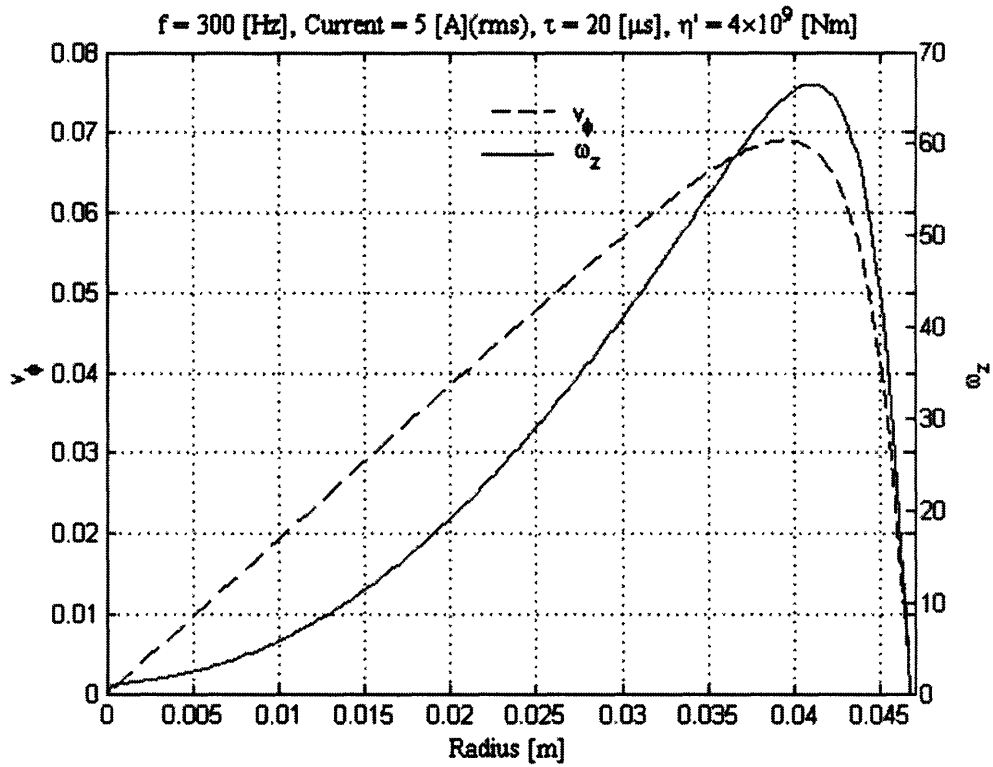


Figure 9-13 Simulated flow and spin velocity of MSG W11 water-based ferrofluid in non-uniform rotating magnetic field with 300 Hz and 5 A rms input current to each winding of the 4 pole motor using $\tau = 20 \mu s$ and $\eta' = 4 \times 10^{-9} Nm$.

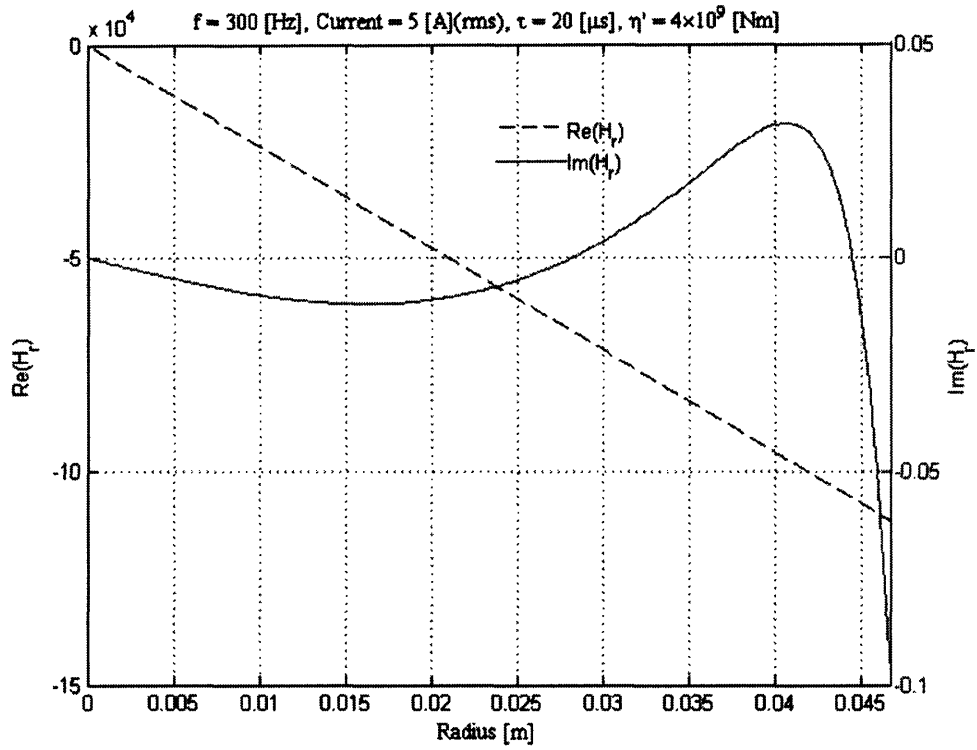


Figure 9-14 Simulated real and imaginary parts of r component of the magnetic field \bar{H} of MSG W11 water-based ferrofluid in non-uniform rotating magnetic field with 300 Hz and 5 A rms input current to each winding of the 4 pole motor using $\tau = 20 \mu$ s and $\eta' = 4 \times 10^{-9}$ Nm.

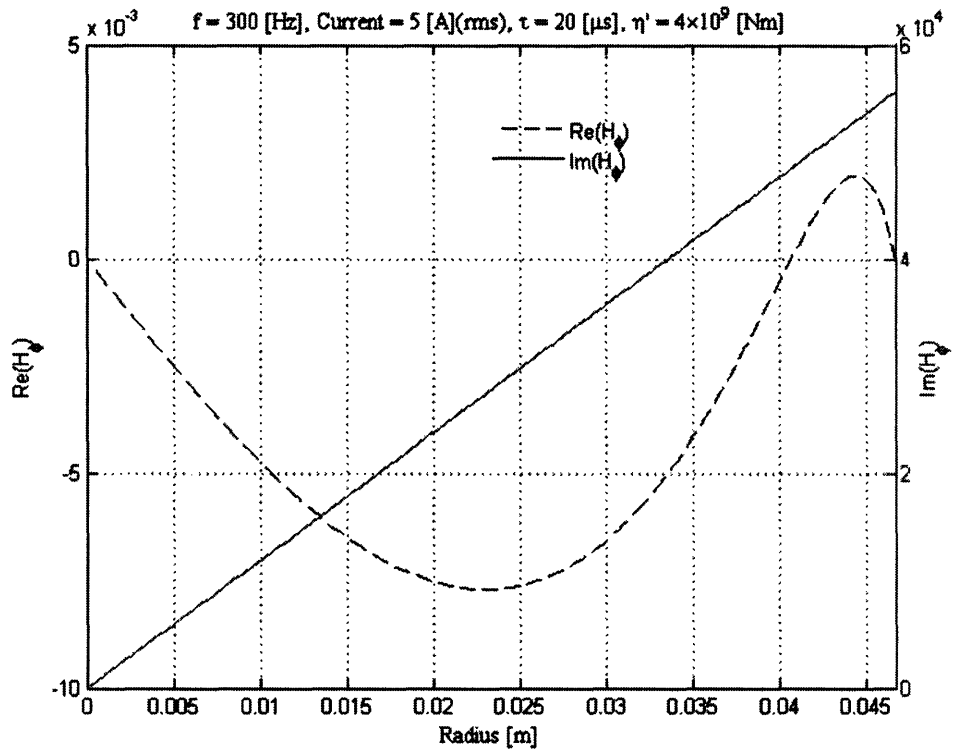


Figure 9-15 Simulated real and imaginary parts of ϕ component of the magnetic field \bar{H} of MSG W11 water-based ferrofluid in non-uniform rotating magnetic field with 300 Hz and 5 A rms input current to each winding of the 4 pole motor using $\tau = 20 \mu s$ and $\eta' = 4 \times 10^{-9} Nm$.

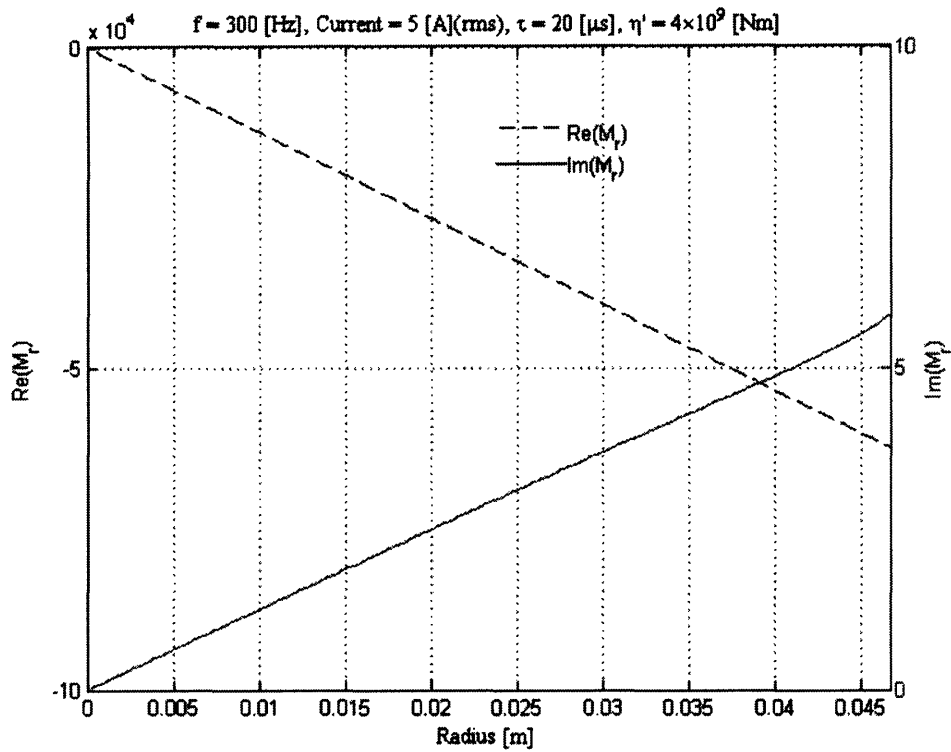


Figure 9-16 Simulated real and imaginary parts of r component of the magnetization \bar{M} of MSG W11 water-based ferrofluid in non-uniform rotating magnetic field with 300 Hz and 5 A rms input current to each winding of the 4 pole motor using $\tau = 20 \mu\text{s}$ and $\eta' = 4 \times 10^{-9} \text{ Nm}$.

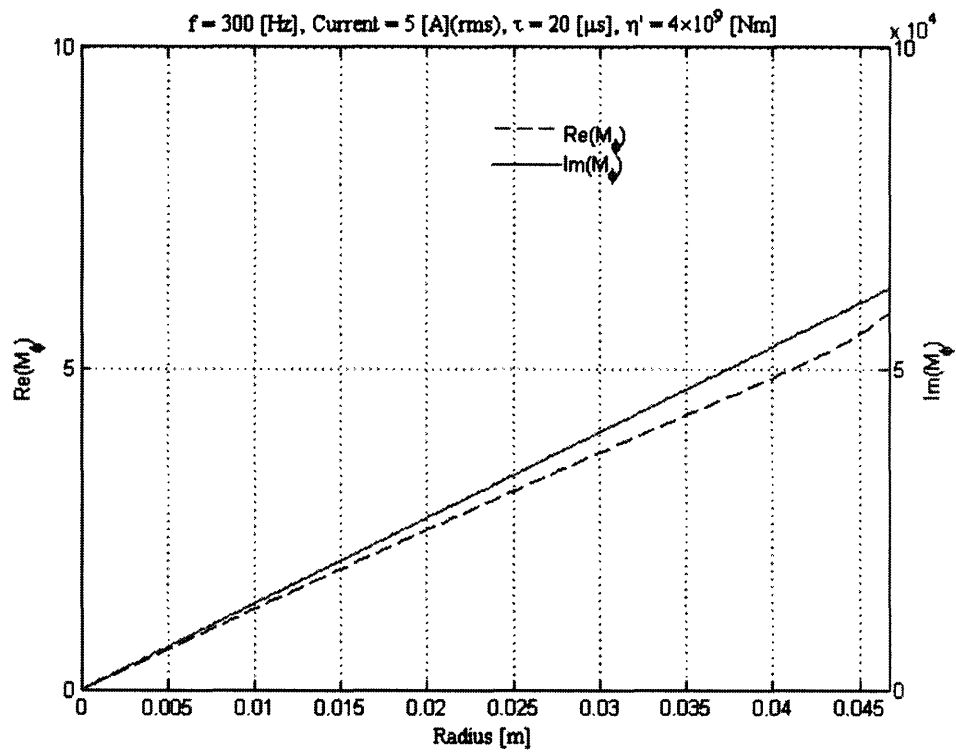


Figure 9-17 Simulated real and imaginary parts of ϕ component of the magnetization \bar{M} of MSG W11 water-based ferrofluid in non-uniform rotating magnetic field with 300 Hz and 5 A rms input current to each winding of the 4 pole motor using $\tau = 20\mu s$ and $\eta' = 4 \times 10^{-9} Nm$.

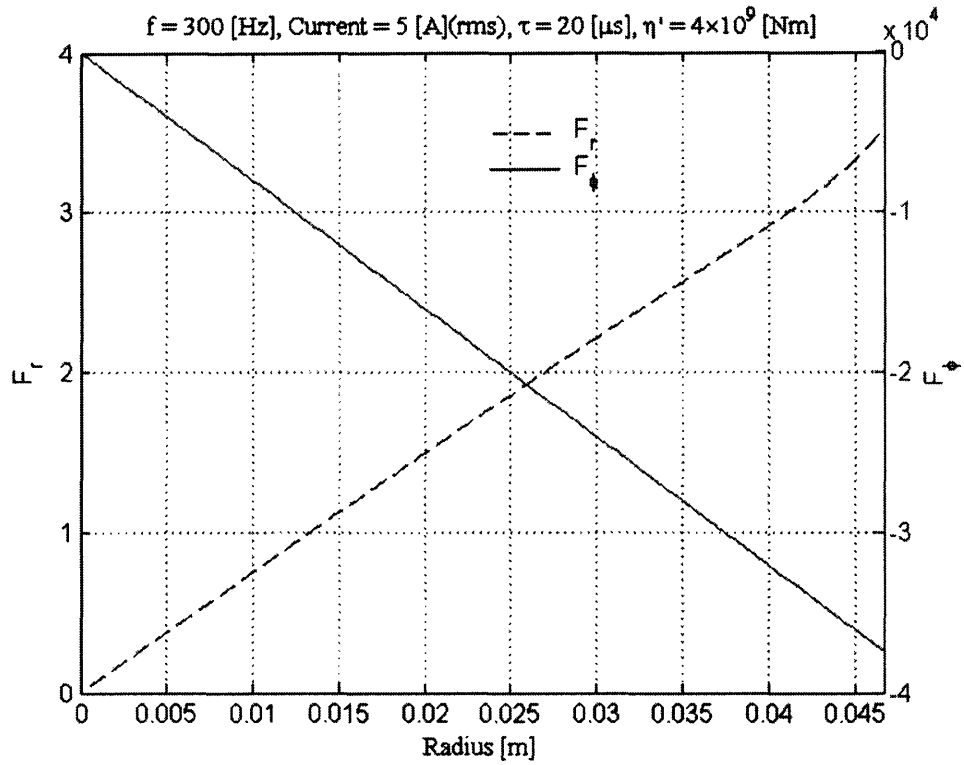


Figure 9-18 Simulated r and ϕ components of the body force density \bar{F} of MSG W11 water-based ferrofluid in non-uniform rotating magnetic field with 300 Hz and 5 A rms input current to each winding of the 4 pole motor using $\tau = 20 \mu s$ and $\eta' = 4 \times 10^{-9} Nm$.

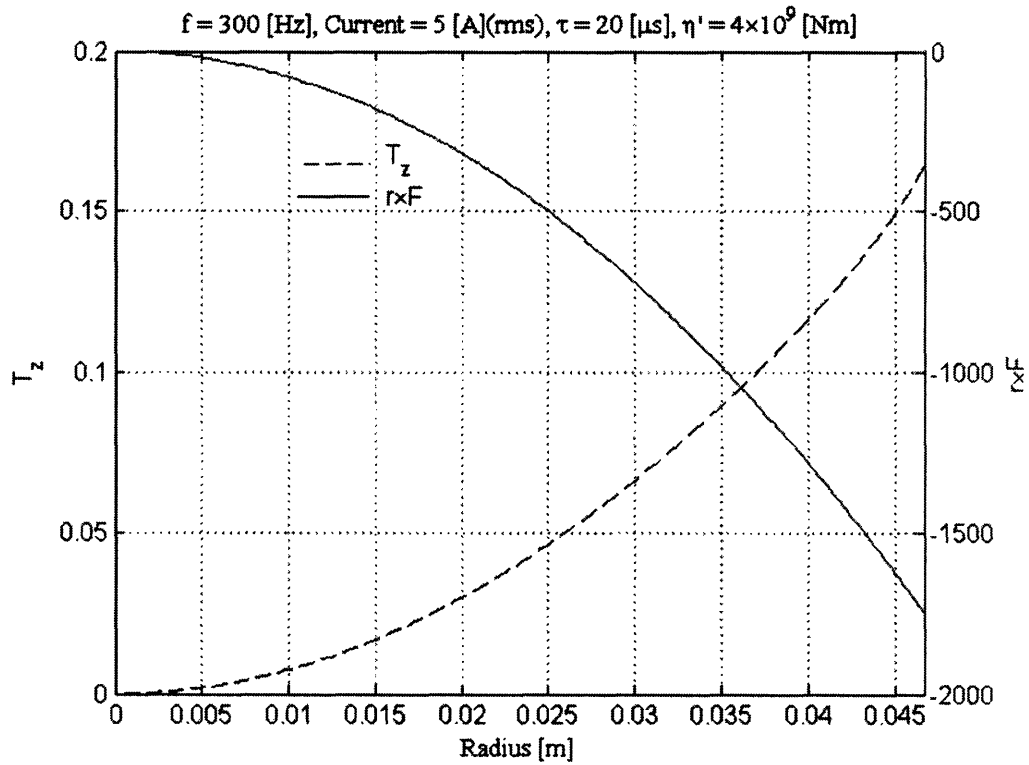


Figure 9-19 Simulated z component of the volume torque density \bar{T} and the body force density contribution $\bar{r} \times \bar{F}$ of MSG W11 water-based ferrofluid in non-uniform rotating magnetic field with 300 Hz and 5 A rms input current to each winding of the 4 pole motor using $\tau = 20 \mu s$ and $\eta' = 4 \times 10^{-9} Nm$.

9.5.1.3 Torque Simulation for Ferrofluid inside the Spindle in a Uniform Rotating Magnetic field

The torque simulation for the ferrofluid inside the spindle in a uniform rotating magnetic field uses the mean value of $\eta' = 1.66 \times 10^{-9} \text{ [N}\cdot\text{s]}$ from the spin-up velocity profile simulation and estimates the value of τ for MSG W11 water-based ferrofluid by fitting the experimental data with the simulation data. The estimated best fit value of relaxation time τ for MSG W11 water-based ferrofluid is $\tau = 3 \times 10^{-5} \text{ [s]}$.

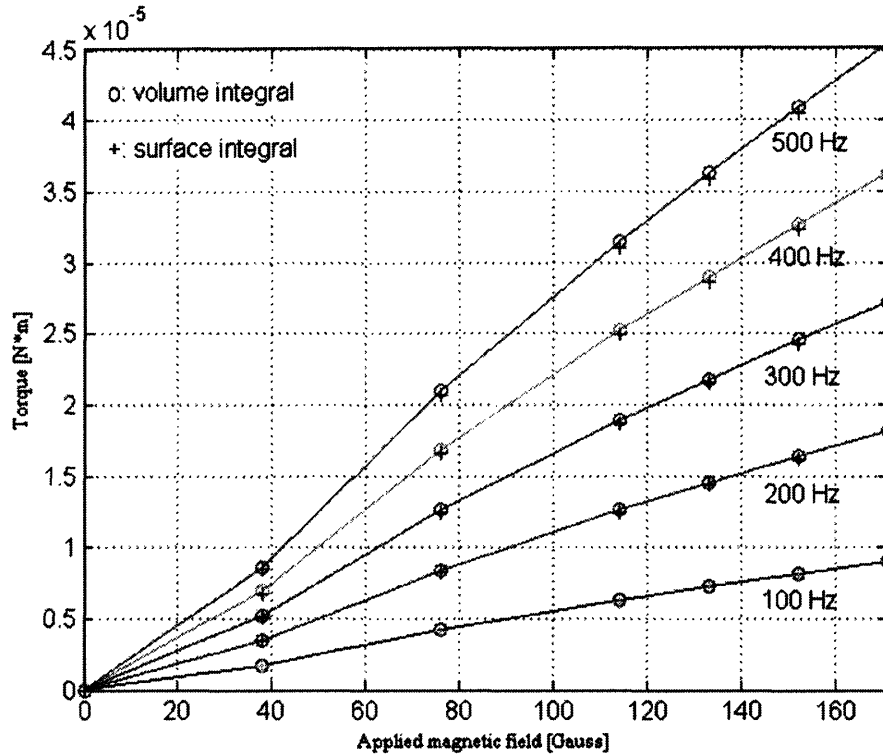


Figure 9-20 Torque simulations with MSG W11 ferrofluid just inside the spindle in a uniform rotating magnetic field at 100, 200, 300, 400 and 500 Hz with $\eta' = 1.66 \times 10^{-9}$ [N*s] and $\tau = 3 \times 10^{-5}$ [s] by the surface integral and volume integral methods of section 9.1.

Figure 9-20 shows the torque simulations with MSG W11 ferrofluid just inside the spindle in a uniform rotating magnetic field at 100, 200, 300, 400 and 500 Hz. The torque values increase with increasing applied magnetic field frequency. The plus sign data in Figure 9-20 is the total surface torque calculated by (9.31), using the no-slip boundary condition, which has $\gamma = 0$. The circle data in Figure 9-20 is the total torque integrated throughout the ferrofluid volume as given by (9.32). Here the total volume torque was calculated by (9.32) without the force density term, because the force density is zero in a uniform rotating magnetic field. Both methods give the same volume torque data, which verifies the statement that in a uniform rotating magnetic field the force density is zero. Figure 9-20 also shows that in the case of torque measurement with ferrofluid just inside the spindle, the total volume

torque is balanced by the surface torque at the boundary. Choosing the no-slip spin velocity boundary condition, $\gamma = 0$, or the slip boundary condition, $\gamma = 1$, makes a very small difference for the torque simulation with the ferrofluid inside the spindle, because the difference of the surface torques for the 2 different boundary conditions is just $2\pi R^2 D\zeta \frac{\partial v_\phi}{\partial r} \Big|_{r=R}$ from (9.11), which has the ratio of $\frac{\zeta}{\zeta + \eta} \approx \frac{\zeta}{\eta} \approx 1.5\phi$ from the total surface torque. Using MSG W11 water-based ferrofluid as an example $\phi = 2.75\%$, $\zeta = 1.5\phi\eta = 0.041\eta$, the difference of the total surface torque in the simulation between the two different boundary conditions is $\sim 4\%$.

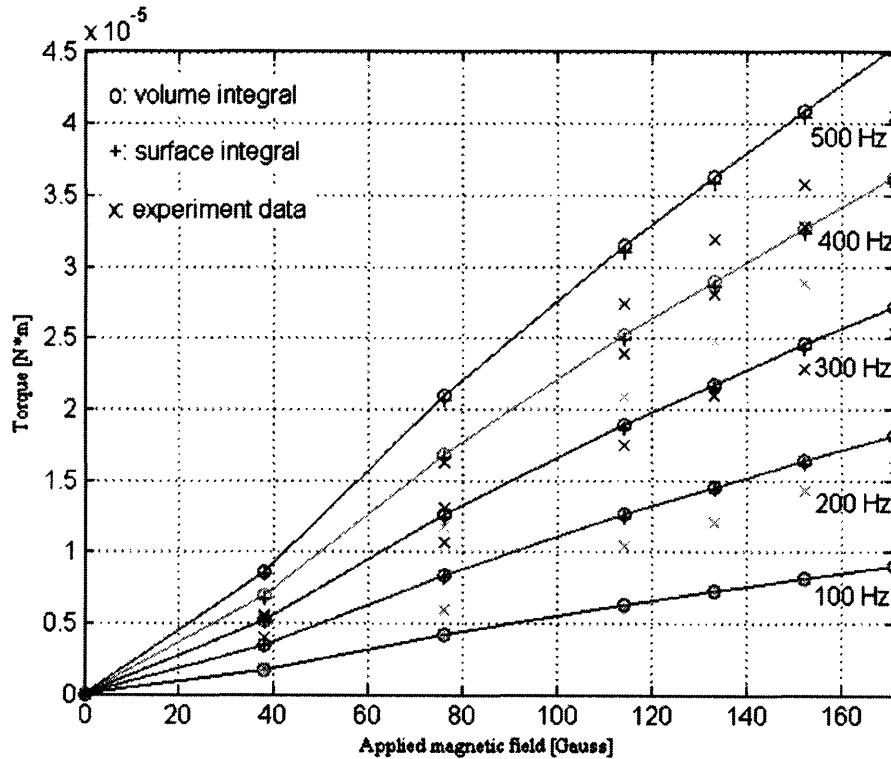


Figure 9-21 Comparison of experimentally measured (cross mark) and numerically calculated (circle and plus marks) torque with MSG W11 ferrofluid just inside the spindle in a uniform rotating magnetic field at 100, 200, 300, 400 and 500 Hz. Simulation uses the value of $\eta' = 1.66 \times 10^{-9}$ [N*s] and $\tau = 3 \times 10^{-5}$ [s].

Figure 9-21 shows the comparison of experimentally measured and numerically calculated torques with MSG W11 ferrofluid just inside the spindle in a uniform rotating magnetic field at 100, 200, 300, 400 and 500 Hz. The torque values increase with increasing applied magnetic field frequency. The plus sign data is the total surface torque calculated by (9.31), using the no-slip spin velocity boundary condition, which has $\gamma = 0$. The circle data is the total volume torque integrated throughout the ferrofluid volume as given by (9.32). The cross sign data is the experimental data. The simulation data and the experimental data show reasonable agreement in Figure 9-21. While Figure 9-8 - Figure 9-10 used different optimum values of η' and τ for each fitted curve, the comparison fitted figures of the ferrofluid torque measurement in Figure 9-21 used a single global best fit value of η' and τ for all the torque measurement data. In this way, the values of η' and τ represent a best global fit of the torque measurement data.

9.5.1.4 Torque Simulation for Ferrofluid inside the Spindle in a Non-uniform Rotating Magnetic field

As for the torque simulation in a uniform rotating magnetic field of section 9.5.1.2, the torque simulation for the ferrofluid inside the spindle in a non-uniform rotating magnetic field uses the same mean value of $\eta' = 1.66 \times 10^{-9}$ [N•s] from the spin-up velocity profile simulation and estimates the value of τ for MSG W11 water-based ferrofluid by fitting the experimental data with the simulation data. The estimated best fit value of relaxation time τ for MSG W11 water-based ferrofluid is $\tau \approx 8 \times 10^{-6}$ [s] in a non-uniform rotating magnetic field. The relaxation time estimated from the torque simulation of a non-uniform rotating magnetic field with the ferrofluid inside the spindle is different from the torque simulation in a uniform rotating magnetic field,

because although those two sets of experiments use the same type of MSG W11 water-based ferrofluid, measurements were performed about one year apart. Aging ferrofluid may suffer from agglomeration of magnetic nanoparticles as discussed in section 9.5.1.1.

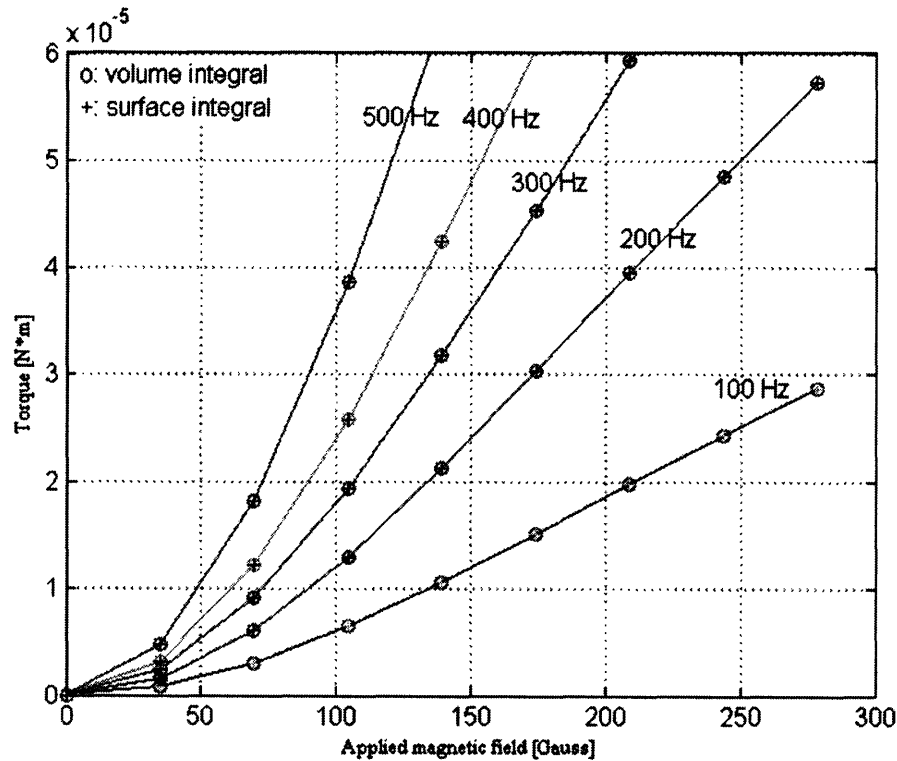


Figure 9-22 Torque simulations with MSG W11 ferrofluid just inside the spindle in a non-uniform rotating magnetic field at 100, 200, 300, 400 and 500 Hz with $\eta' = 1.66 \times 10^{-9}$ [N·s] and $\tau = 8 \times 10^{-6}$ [s] by the surface integral and volume integral methods of section 9.1.

Figure 9-22 shows the torque simulations with MSG W11 ferrofluid just inside the spindle in a non-uniform rotating magnetic field from the 4 pole stator winding described in section 8.1 at 100, 200, 300, 400 and 500 Hz. The torque values increase with increasing applied magnetic field frequency. The plus sign data in Figure 9-22 is the surface torque on the spindle inner wall calculated by (9.31) with the no-slip boundary condition, $\gamma = 0$. The difference

of choosing different boundary conditions is small as discussed in section 9.5.1.2. The circle data in Figure 9-22 is the total torque integrated through the ferrofluid volume given by (9.32), which includes the torque density term and force density terms, because the force density is no longer zero in a non-uniform rotating magnetic field. Calculation of the volume torque separately through torque density and force density and showing that the sum of those two terms balances the surface torque, verifies that in a non-uniform rotating magnetic field the force density in the ferrofluid is not zero. Figure 9-22 also shows that in the case of torque measurements with ferrofluid just inside the spindle, the total volume torque is balanced by the total surface torque at the boundary.

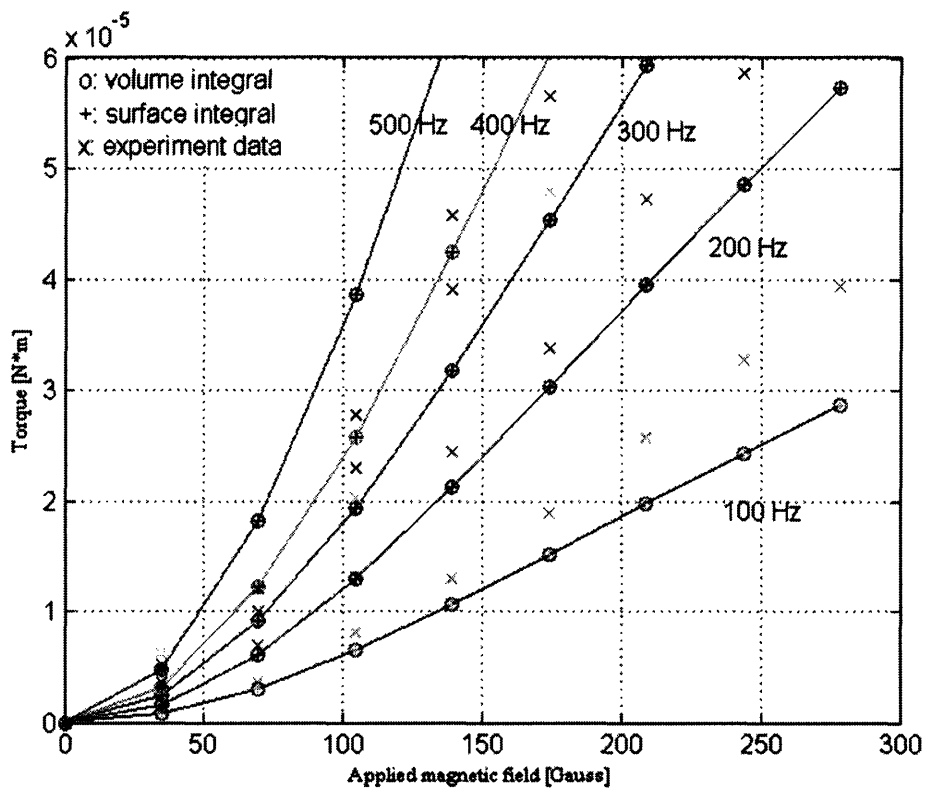


Figure 9-23 Comparison of experimentally measured (cross mark) and numerically calculated (circle and plus marks) torques with MSG W11 ferrofluid just inside the spindle in a non-uniform rotating magnetic field at 100, 200, 300, 400 and 500 Hz. Simulations use the values of $\eta' = 1.66 \times 10^{-9}$ [N*s] and $\tau = 8 \times 10^{-6}$ [s].

Figure 9-23 shows the comparison of experimentally measured and numerically calculated torques with MSG W11 ferrofluid just inside the spindle in a non-uniform rotating magnetic field at 100, 200, 300, 400 and 500 Hz. The torque values increase with increasing applied magnetic field amplitude and frequency. The plus sign data is the total surface torque calculated by (9.31) with a no-slip boundary condition. The circle data is the total volume torque integrated throughout the ferrofluid volume as given by (9.32). The cross sign data is the experimental data. The simulations agree well with the experimental data as shown in Figure 9-23.

9.5.2 Two Region Simulations

Two region simulations include torque simulations for the ferrofluid outside the spindle in uniform and non-uniform rotating magnetic fields. Two region simulations use the spin viscosity value, η' , estimated from the spin –up velocity simulation for the ferrofluid in a non-uniform rotating magnetic field and estimate the magnetization relaxation time constant, τ , for each case by fitting the measurement data with the simulation results.

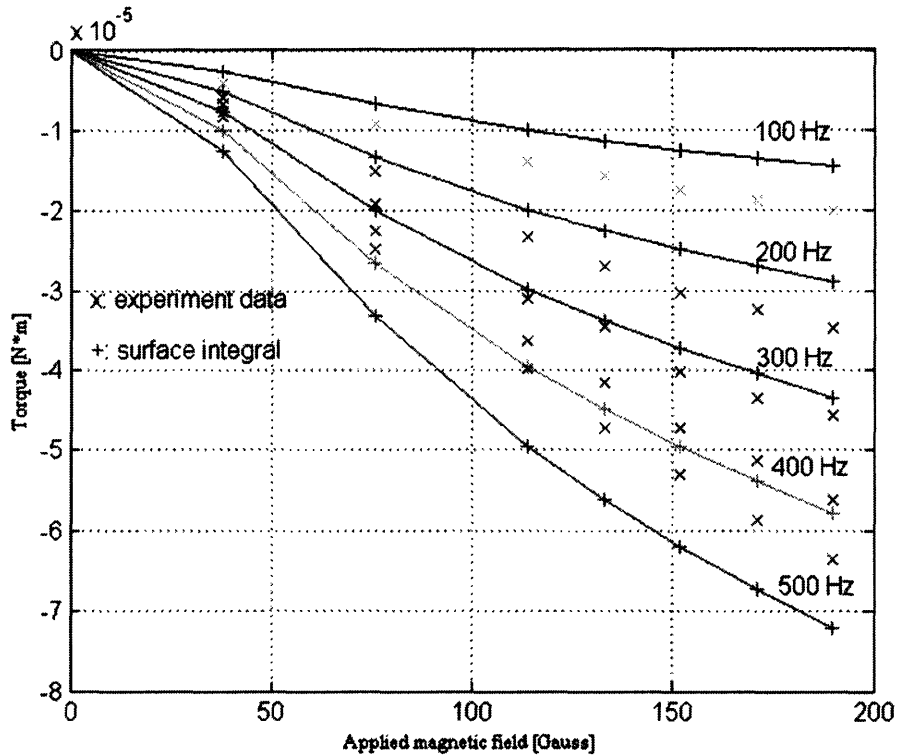


Figure 9-24 Comparison of experimentally measured (cross marks) and numerically calculated (plus marks) torque with MSG W11 ferrofluid outside the spindle in a uniform rotating magnetic field at 100, 200, 300, 400 and 500 Hz. Simulations use the value of $\eta' = 1.66 \times 10^{-9}$ [N*s] and $\tau = 2.5 \times 10^{-5}$ [s].

Figure 9-24 shows the comparison of experimentally measured and numerically calculated torques with MSG W11 ferrofluid outside the spindle in a uniform rotating magnetic field at 100, 200, 300, 400 and 500 Hz. The amplitude of torque values increase with increasing applied magnetic field amplitude and frequency. The plus sign data is the total surface torque calculated by (9.31) with a no-slip boundary condition. Here the total volume torques are not shown in Figure 9-24, because in this case of the ferrofluid outside the spindle there are two boundaries at the inner and outer surfaces of the ferrofluid annulus so that the volume torque calculated by the volume integration of the torque density equals the sum of surface torques on the inner and outer surfaces of the ferrofluid annulus. The torque experiment data was

taken only at the inner surface of the ferrofluid annulus. The cross sign data in Figure 9-24 is the experimental data. The simulation data and the experimental data show reasonable agreement in Figure 9-24 using the value of the spin viscosity $\eta' = 1.66 \times 10^{-9}$ [N•s], from the spin-up velocity profile simulation, and the magnetization relaxation time $\tau = 2.5 \times 10^{-5}$ [s].

Figure 9-25 shows the comparison of experimentally measured and numerically calculated torques with MSG W11 ferrofluid outside the spindle in a non-uniform rotating magnetic field at 100, 200, 300, 400 and 500 Hz. The torque values increase with increasing applied magnetic field amplitude and frequency. The plus sign data is the total surface torque calculated by (9.31) with a no-slip boundary condition. The cross sign data is the experimental data. The simulation data and the experimental data show reasonable agreement in Figure 9-25 using the value of the spin viscosity $\eta' = 1.66 \times 10^{-9}$ [N•s] from the spin-up velocity profile simulation and the magnetization relaxation time $\tau = 1.6 \times 10^{-5}$ [s] from a best fit.

Numerical simulation of the spin-up flow velocity profile in a non-uniform rotating magnetic field shows that the spin viscosity η' has a non-zero value. Numerical simulations of the torque measurements in uniform and non-uniform rotating magnetic fields were verified by calculating the torque with a surface integration and volume integration. It is also proved in the simulation for torque measurements that the body force density $\mu_0 (\vec{M} \cdot \nabla) \vec{H}$ is not zero in a non-uniform rotating magnetic field and the torque in a non-uniform rotating magnetic field is stronger than in a uniform rotating magnetic field with the contribution from the body force density $\mu_0 (\vec{M} \cdot \nabla) \vec{H}$. Numerical simulation also estimates the values of relaxation time $\tau \approx 1.3 - 30$ μ s and spin viscosity $\eta' \approx (1 - 11.8) \times 10^{-9}$ N•s by fitting the experimental data.

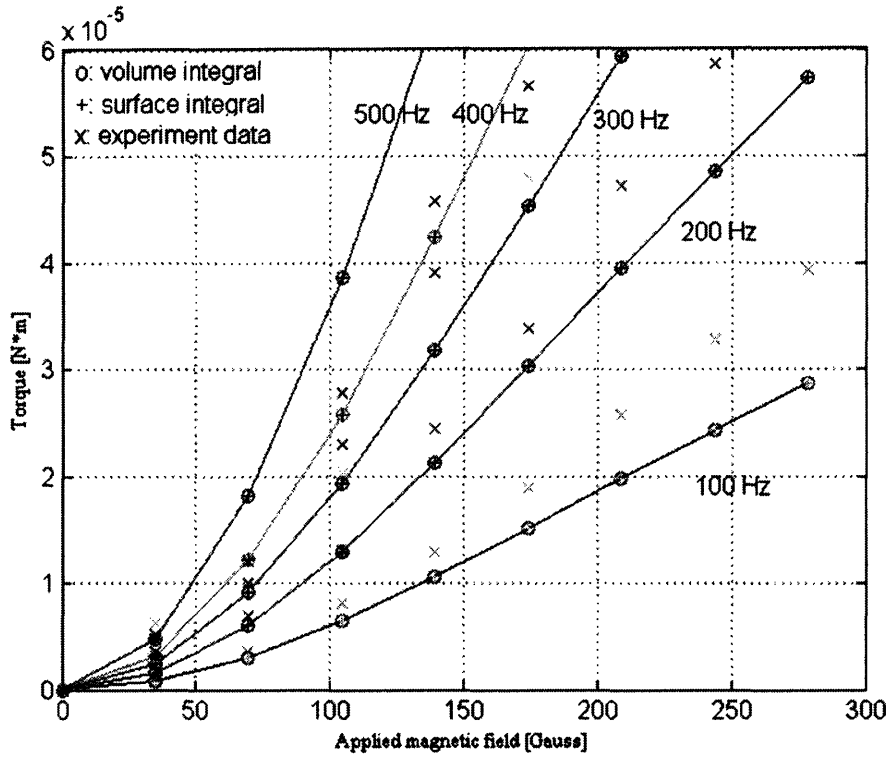


Figure 9-25 Comparison of experimentally measured (cross mark) and numerically calculated (plus mark) torque with MSG W11 ferrofluid outside the spindle in a non-uniform rotating magnetic field at 100, 200, 300, 400 and 500 Hz. Simulations use the value of $\eta' = 1.66 \times 10^{-9}$ [N·s] and $\tau = 1.6 \times 10^{-5}$ [s].

Chapter 10. Thesis Summary and Suggestions for Continuing Work

10.1 Key Contributions

Ferrofluid torques and spin-up flow profiles in uniform and non-uniform rotating magnetic fields are studied in order to develop analytical and numerical first principle models. The following points summarize the key contributions to ferrohydrodynamic research made in this thesis:

1. Ferrofluid negative viscosity as a function of magnetic field amplitude and frequency is measured in uniform and non-uniform rotating magnetic fields using a Couette viscometer as a torque meter. Torque measurements and spin-up velocity profiles in uniform and non-uniform rotating magnetic fields prove the volume torque density effect in uniform rotating magnetic fields and the body force density effect with the volume torque density effect in non-uniform rotating magnetic fields.

2. Numerical simulations of torque and spin-up flow in uniform and non-uniform rotating magnetic fields, including contributions from the flow and spin viscosity terms in the conservation of momentum equations, determine estimates of the range of magnetization relaxation time constant ($\tau \approx 1.3 - 30 \mu s$) and the value of spin viscosity ($\eta' \approx (1 - 11.8) \times 10^{-9}$) from fits to the experimental data.

Simulations that assume zero spin viscosity ($\eta' = 0$) do not fit the flow profile measurements of 1.

3. The magnetization relaxation equation is used to derive the complex magnetic susceptibility tensor, which includes the spin velocity effect of ferrofluid in a rotating magnetic field. The analysis derives the additional power dissipation in ferrofluid from the spin velocity effect and conditions for pumping

of the fluid. Impedance measurements demonstrate the change of complex magnetic susceptibility tensor elements of ferrofluid in a uniform rotating magnetic field as a function of impedance frequency.

4. Ferrofluid effective magnetoviscosity expressions are derived for planar Couette and Poiseuille flows assuming zero spin viscosity. The obtained multiple values of magnetoviscosity, magnetic field, and spin velocity at high values of applied magnetic field and flow velocity indicate that the zero spin viscosity limit may be non-physical.

10.2 Suggested Future Work

In closing, the following directions for future work are suggested to extend and build upon the results presented in this thesis:

1. Experimentally and theoretically investigate radial and axial recirculation velocity profiles in EMG705, MSG W11, and EFH1 ferrofluids. Examine the effects of reversing the direction of rotation of the magnetic field on the direction symmetry and shape of recirculation flow.
2. Extend the Femlab finite element analysis model to handle two dimensional (r, z) axisymmetric solutions to numerically investigate the effects of the top boundary condition and of recirculating flows in spin-up flows at high Reynolds number.
3. Analyze Couette, Poiseuille and other flows for effective magnetoviscosity as a function of magnetic field frequency and amplitude; in particular to determine conditions for negative viscosity. Include non-zero viscosity to determine if non-physical multiple value solutions are eliminated.
4. Examine effects of the nonlinear equilibrium Langevin magnetization on ferrofluid magnetoviscosity, the flow and spin velocity distributions, the

dissipated power as a function of magnetic field frequency and amplitude, and on measured impedance of inductors filled with ferrofluid.

5. Perform independent measurements of magnetic relaxation time constant τ and spin viscosity η' and compare to fitted values from numerical simulations.

6. Develop sensitive experiments of measurement of magnetic fields inside and outside ferrofluids stressed by magnetic field to detect perturbation components due to flow and spin velocities.

7. Develop measurement methods to determine every element of the complex magnetic susceptibility tensor and explore possible applications.

8. Repeat torque and flow profile measurements in more non-uniform rotating and oscillating magnetic fields using 6, 8, 10, and higher multipole motor stator windings.

Bibliography

- [1] R. E. Rosensweig, *Ferrohydrodynamics*. Mineola, NY: Dover Publications, 1997.
- [2] L. F. Shen, P. E. Laibinis, and T. A. Hatton, "Aqueous magnetic fluids stabilized by surfactant bilayers," *Journal of Magnetism and Magnetic Materials*, vol. 194, pp. 37-44, 1999.
- [3] L. F. Shen, P. E. Laibinis, and T. A. Hatton, "Bilayer surfactant stabilized magnetic fluids: Synthesis and interactions at interfaces," *Langmuir*, vol. 15, pp. 447-453, 1999.
- [4] L. F. Shen, A. Stachowiak, S. E. K. Fateen, P. E. Laibinis, and T. A. Hatton, "Structure of alkanolic acid stabilized magnetic fluids. A small-angle neutron and light scattering analysis," *Langmuir*, vol. 17, pp. 288-299, 2001.
- [5] R. Perez-Castillejos, J. A. Plaza, J. Esteve, P. Losantos, M. C. Acero, C. Cane, and F. Serra-Mestres, "The use of ferrofluids in micromechanics," *Sensors and Actuators A - Physical*, vol. 84, pp. 176-180, 2000.
- [6] A. Menz, W. Benecke, R. Perez-Castillejos, J. A. Plaza, J. Esteve, N. Garcia, J. Higuero, and T. Diez-Caballero, "Fluidic components based on ferrofluids," presented at 1st Annual International IEEE-EMBS Special Topic Conference on Microtechnologies in Medicine and Biology, Lyon, France, 2000.
- [7] A. Hatch, A. E. Kamholz, G. Holman, P. Yager, and K. F. Bohringer, "A ferrofluidic magnetic micropump," *Journal of Microelectromechanical Systems*, vol. 10, pp. 215-221, 2001.
- [8] M. Berger, J. Castelino, R. Huang, M. Shah, and R. H. Austin, "Design of a microfabricated magnetic cell separator," *Electrophoresis*, vol. 22, pp. 3883-3892, 2001.
- [9] M. Zahn, "Magnetic fluid and nanoparticle applications to nanotechnology," *Journal of Nanoparticle Research*, vol. 3, pp. 73-78, 2001.
- [10] J. Roger, J. N. Pons, R. Massart, A. Halbreich, and J. C. Bacri, "Some biomedical applications of ferrofluids," *European Physical Journal - Applied Physics*, vol. 5, pp. 321-325, 1999.

- [11]C. N. Ramchand, P. Pande, P. Kopcansky, and R. V. Mehta, "Application of magnetic fluids in medicine and biotechnology," *Indian Journal of Pure & Applied Physics*, vol. 39, pp. 683-686, 2001.
- [12]R. Moskowitz and R. E. Rosensweig, "Nonmechanical Torque Driven Flow in Magnetic Suspensions," *Applied Physics Letters*, vol. 11, pp. 1967, 1967.
- [13]R. Brown and T. S. Horsnell, "The wrong way round," *Electrical Review*, vol. 183, pp. 235, 1969.
- [14]I. Y. Kagan, V. G. Rykov, and E. I. Yantovskii, "Flow of a dielectric ferromagnetic suspension in a rotating magnetic field," *Magnitnaya Gidrodynamika*, vol. 9, pp. 135-137, 1973.
- [15]G. H. Calugaru, C. Cotae, R. Badescu, V. Badescu, and E. Luca, "A new aspect of the movement of ferrofluids in a rotating magnetic field," *Reviews in Roumanian Physics*, vol. 21, pp. 439-440, 1976.
- [16]R. E. Rosensweig and R. J. Johnston, "Aspects of magnetic fluid flow with nonequilibrium magnetization," in *Continuum Mechanics and its Applications*, C. A. C. Graham and S. K. Malik, Eds.: Hemisphere Publishing Company, 1989, pp. 707-729.
- [17]R. E. Rosensweig, J. Popplewell, and R. J. Johnston, "Magnetic fluid motion in rotating field," *Journal of Magnetism and Magnetic Materials*, vol. 85, pp. 171-180, 1990.
- [18]V. M. Zaitsev and M. I. Shliomis, "Entrainment of ferromagnetic suspension by a rotating field," *Journal of Applied Mechanics and Technical Physics*, vol. 10, pp. 696-700, 1969.
- [19]O. A. Glazov, "Motion of a ferrosuspension in rotating magnetic fields," *Magnitnaya Gidrodynamika*, vol. 11, pp. 16-22, 1975.
- [20]O. A. Glazov, "Role of higher harmonics in ferrosuspension motion in a rotating magnetic field," *Magnitnaya Gidrodynamika*, vol. 11, pp. 31, 1975.
- [21]O. A. Glazov, "Velocity profiles for magnetic fluids in rotating magnetic fields," *Magnitnaya Gidrodynamika*, vol. 18, pp. 27, 1982.

- [22]O. A. Glazov, "Dynamics of magnetic fluids in rotating magnetic fields," *Magnitnaya Gidrodynamika*, vol. 26, pp. 83-88, 1990.
- [23]A.F. Lehlooh, S.H. Mahmood, J.M. Williams, "On the particle size dependence of the magnetic anisotropy energy," *Physica B* 321(2002) 159-162.
- [24]M. I. Shliomis, "Magnetic fluids," *Sov. Phys.-Usp.*, vol. 17, pp. 156, 1974.
- [25]M. I. Shliomis, "Effective viscosity of magnetic suspensions," *Soviet Physics JETP*, vol. 34, pp. 1291-1294, 1972.
- [26]B. U. Felderhof, "Magnetoviscosity and relaxation in ferrofluids," *Physical Review E*, vol. 62, pp. 3848-3854, 2000.
- [27]M. I. Shliomis, "Comment on " Magnetoviscosity and relaxation in ferrofluids "," *Physical Review E*, vol. 6406, 2001.
- [28]B. U. Felderhof, "Reply to "Comment on 'Magnetoviscosity and relaxation in ferrofluids'"," *Physical Review E*, vol. 6406, 2001.
- [29]J. R. Melcher, *Continuum Electromechanics*. Cambridge, MA: MIT Press, 1981.
- [30]J. S. Dahler and L. E. Scriven, "Theory of structured continua I. General consideration of angular momentum and polarization," *Proceedings of the Royal Society of London Series A*, vol. 276, pp. 504-527, 1963.
- [31]C. Rinaldi, "Continuum Modeling of Polarizable Systems," PhD Thesis, Massachusetts Institute of Technology, Cambridge, MA, 2002, pp. 228.
- [32]H. Brenner, "Rheology of two-phase systems," *Annual Review of Fluid Mechanics*, vol. 2, pp. 137-176, 1970.
- [33]C. Rinaldi and M. Zahn, "Effects of spin viscosity on ferrofluid flow profiles in alternating and rotating magnetic fields," *Physics of Fluids*, vol. 14, pp. 2847-2870, 2002.
- [34]A. Mironer, *Engineering Fluid Mechanics*, NY: McGraw-Hill Publications, 1979.
- [35]J. O. Hinze, *Turbulence*, NY: McGraw-Hill Publications, 1975.
- [36]A. S. Monin, A. M. Yaglom, *Statistical Fluid Mechanics*, Cambridge, MA: The MIT Press, 1987.

- [37] N. Bilaniuk, S. George, and J. Wong. "Speed of sound in water as a function of temperature," *Acoust. Soc. Am.*, 93:1609 - 1612, 1993.
- [38] S. Odenbach, "Ferrofluids - magnetically controlled suspensions," *Colloids and Surfaces A: Physicochem. Eng. Aspects*, 217:171 - 178, 2003..
- [39] J.C. Bacri, R. Perzynski, D. Salin, and A. Cebres, *Mat. Res. Soc. Symp. Proc.*, 248:241, 1992.
- [40] Xiaowei He and Markus Zahn, "Effective Magnetoviscosity for Ferrofluid Planar Couette Flow," 21st International Congress of Theoretical and Applied Mechanics (ICTAM), Warsaw, Poland, 2004
- [41] X. He, S. Elborai, D. Kim, S. Lee and M. Zahn, "Effective Magnetoviscosity of Planar-Couette Magnetic Flow," 49th Conference on Magnetism and Magnetic Material (MMM), Jacksonville, Florida, 2004.
- [42] C. Rinaldi, F. Gutman, X. He, A. D. Rosenthal, M. Zahn, "Magnetoviscosity and torque measurements on ferrofluid cylinders in rotating magnetic fields," ICMF10, Brazil, 2004.
- [43] J. Connolly, St. Pierre, T.G., "Proposed biosensors based on time-dependent properties of magnetic fluids," *J. Magn. Magn. Mater.* 2001, 225 (1 - 2), 156-160.
- [44] C. Wilhelm, F. Gazeau, J. Roger, J.N. Pons, M.F. Salis, R. Perzynski, J.C. Bacri, "Binding of biological effectors on magnetic nanoparticles measured by a magnetically induced transient birefringence experiment," *Phys. Rev.*, E 2002, 65 (3), 031404.
- [45] Dias, A.F.; Dernick, G.; Valero, V.; Yong, M.G.; James, C.D.; Craighead, H.G.; Lindau, M. "An electrochemical detector array to study cell biology on the nanoscale," *Nanotechnology* 2002, 13 (3), 285-289.
- [46] Perez, J.M.; O'Loughin, T.; Simeone, F.J.; Weissleder, R.; Josephson, L. "DNA-based magnetic nanoparticle assembly acts as a magnetic relaxation nanoswitch allowing screening of DNA cleaving agents," *J. Am. Chem. Soc.* 2002, 124 (12), 2856-2857.

- [47] Ruuge, E.K.; Rusetski, A.N. "Magnetic fluids as drug carriers: Targeted transport of drugs by a magnetic field," *J. Magn. Magn. Mater.* 1993, 122, 335–339.
- [48] Chan, D.C.F.; Kirpotin, D.B.; Bunn, P.A., Jr. "Synthesis and evaluation of colloidal magnetic iron oxides for the site-specific radiofrequency induced hyperthermia of cancer." *J. Magn. Magn. Mater.* 1993, 122, 374–378.
- [49] Jordan, A.; Scholz, R.; Wust, P.; Fahling, H.; Felix, R. "Magnetic fluid hyperthermia (MFH): Cancer treatment with AC magnetic field induced excitation of biocompatible superparamagnetic nanoparticles." *J. Magn. Magn. Mater.* 1999, 201, 413–419.
- [50] Hiergeist, R.; Andra, W.; Buske, N.; Hergt, R.; Hilger, I.; Richter, U.; Kaiser, W. "Application of magnetite ferrofluids for hyperthermia." *J. Magn. Magn. Mater.* 1999, 201, 420–422.
- [51] Lange, J.; Kötz, R.; Haller, A.; Trahms, L.; Semmler, W.; Weitschies, W. "Magnetorelaxometry: A new binding specific detection method based on magnetic nanoparticles." *J. Magn. Magn. Mater.* 2002, 252, 381–383.
- [52] Fannin, P.C.; Scaife, B.K.P.; Giannitsis, A.T.; Charles, S.W. "Determination of the radius of nano-particles in a magnetic fluid by means of a constant frequency measurement technique." *J. Phys., D, Appl. Phys.* 2002, 35 (12), 1305–1310.
- [53] Kötz, R.; Weitschies, W.; Trahms, L.; Semmler, W. "Investigation of Brownian and Néel relaxation in magnetic fluids." *J. Magn. Magn. Mater.* 1999, 201, 102–104.
- [54] Ramchand, C.N.; Pande, P.; Kopcansky, P.; Mehta, R.V. "Application of magnetic fluids in medicine and biotechnology." *Indian J. Pure Appl. Phys.* 2001, 39 (10), 683–686.
- [55] Hergt, R.; Andra, W.; d'Ambly, C.G.; Hilger, I.; Kaiser, W.A.; Richter, U.; Schmidt, H.-G. "Physical limits of hyperthermia using magnetite fine particles." *IEEE Trans. Magn.* 1998, 34 (5), 3745–3754.
- [56] Jordan, A.; Wust, P.; Scholz, R.; Tesche, B.; Fahling, H.; Mitrovics, T.; Vogl, T.; Cervos-Navarro, J.; Felix, R. "Cellular uptake of magnetic fluid particles and their

- effects on human adenocarcinoma cells exposed to AC magnetic fields in vitro." *Int. J. Hypertherm.* 1996, 12 (6), 705–722.
- [57] Autenshlyus, A.I.; Brusentsov, N.A.; Lockshin, A. "Magnetic-sensitive dextran-ferrite immunosorbents (for diagnostic and therapy)." *J. Magn. Magn. Mater.* 1993, 122, 360–363.
- [58] Roath, S. "Biological and biomedical aspects of magnetic fluid technology." *J. Magn. Magn. Mater.* 1993, 122, 329–334.
- [59] Jordan, A.; Scholz, R.; Wust, P.; Fahling, H.; Krause, J.; Wlodarczyk, W.; Sander, B.; Vogl, T.; Felix, R. "Effects of magnetic fluid hyperthermia (MFH) on C3H mammary carcinoma in vivo." *Int. J. Hypertherm.* 1997, 13 (6), 587–605.
- [60] Roger, J.; Pons, J.N.; Massart, R.; Halbreich, A.; Bacri, J.C. "Some biomedical applications of ferrofluids." *Eur. Phys. J., Appl. Phys.* 1999, 5 (3), 321–325.
- [61] Hilger, I.; Andra, W.; Hergt, R.; Hiergeist, R.; Kaiser, W.A. "Treatment of breast cancers by magnetic thermoablation: In vivo experiments in mice." *Magnetohydrodynamics* 2001, 37 (3), 323–327.
- [62] Brusentsov, N.A.; Nikitin, L.V.; Brusentsova, T.N.; Kuznetsov, A.A.; Bayburtskiy, F.S.; Shumakov, L.I.; Jurchenko, N.Y. "Magnetic fluid hyperthermia of the mouse experimental tumor." *J. Magn. Magn. Mater.* 2002, 252, 378–380.
- [63] Lubbe, A.S.; Alexiou, C.; Bergemann, C. "Clinical applications of magnetic drug targeting." *J. Surg. Res.* 2001, 95 (2), 200–206.
- [64] Voltairas, P.A.; Fotiadis, D.I.; Michalis, L.K. "Hydrodynamics of magnetic drug targeting." *J. Biomech.* 2002, 35 (6), 813–821.
- [65] Browning, V.M. "Potential Department of Defense (DOD) applications of magnetic carriers." *Eur. Cells Mater.* 2002, 3 (2), 5–6.
- [66] Alexiou, C.P.; Arnold, W.; Hulin, P.; Klein, R.; Schmidt, A.; Bergemann, C.; Parak, F.G. "Therapeutic efficacy of ferrofluid bound anticancer agent." *Magnetohydrodynamics* 2001, 37 (3), 318–322.
- [67] Alexiou, C.; Schmidt, A.; Klein, R.; Hulin, P.; Bergemann, C.; Arnold, W. "Magnetic drug targeting: Biodistribution and dependency on magnetic field strength." *J. Magn. Magn. Mater.* 2002, 252, 363–366.

- [68] Lubbe, A.S.; Bergemann, C.; Riess, H.; Schriever, F.; Reichardt, P.; Possinger, K.; Matthias, M.; Dorken, B.; Herrmann, F.; Gurtler, R.; Hohenberger, P.; Haas, N.; Sohr, R.; Sander, B.; Lemke, A.J.; Ohlendorf, D.; Huhnt, W.; Huhn, D. "Clinical experiences with magnetic drug targeting: A phase I study with 4'-epidoxorubicin in 14 patients with advanced solid tumors." *Cancer Res.* 1996, 56 (20), 4686–4693.
- [69] Zhang, Y.; Kohler, N.; Zhang, M. "Surface modification of superparamagnetic magnetite nanoparticles and their intracellular uptake." *Biomaterials* 2002, 23, 1553–1561.
- [70] Doyle, P.S.; Bibette, J.; Bancaud, A.; Viovy, J.-L. "Self-assembled magnetic matrices for DNA separation chips." *Science* 2002, 295, 2237.
- [71] Moeser, G.D.; Roach, K.A.; Green, W.H.; Laibinis, P.E.; Hatton, T.A. "Water-based magnetic fluids as extractants for synthetic organic compounds." *Ind. Eng. Chem. Res.* 2002, 41, 4739–4749.
- [72] Sun, L.P.; Zborowski, M.; Moore, L.R.; Chalmers, J.J. "Continuous, flow-through immunomagnetic cell sorting in a quadrupole field." *Cytometry* 1998, 33 (4), 469–475.
- [73] Berger, M.; Castelino, J.; Huang, R.; Shah, M.; Austin, R.H. "Design of a microfabricated magnetic cell separator." *Electrophoresis* 2001, 22, 3883–3892.
- [74] Sestier, C.; Sabolovic, D.; Geldwerth, D.; Moumaris, M.; Roger, J.; Pons, J.N.; Halbreich, A. "Use of annexin V-ferrofluid to enumerate erythrocytes damaged in various pathologies or during storage in vitro. C. R. Acad. Sci., Ser. 3 Sci. Vie 1995, 318 (11), 1141–1146.
- [75] Halbreich, A.; Sabolovic, D.; Sestier, C.; Amri, A.; Pons, J.N.; Roger, J.; Geldwerth, D. Annexin V binding to mouse erythrocytes following infection with Plasmodium parasites." *Parasitol. Today* 1996, 12 (7), 292–293.
- [76] Sabolovic, D.; Roudier, M.; Boynard, M.; Pautou, C.; Sestier, C.; Fertil, B.; Geldwerth, D.; Roger, J.; Pons, J.N.; Amri, A.; Halbreich, A. "Membrane modifications of red blood cells in Alzheimer's disease." *J. Gerontol., Ser. A, Biol. Sci. Med. Sci.* 1997, 52 (4), B217–B220.

- [77] Kötitz, R.; Matz, H.; Trahms, L.; Koch, H.; Weitschies, W.; Rheinländer, T.; Semmler, W.; Bunte, T. "SQUID based remanence measurements for immunoassays." *IEEE Trans. Appl. Supercond.* 1997, 7 (2), 3678–3681.
- [78] Koneracká, M.; Kopcansky, P.; Antalík, M.; Timko, M.; Ramchand, C.N.; Lobo, D.; Mehta, R.V.; Upadhyay, R.V. "Immobilization of proteins and enzymes to fine magnetic particles." *J. Magn. Magn. Mater.* 1999, 201, 427–430.
- [79] Depeyrot, J.; Sousa, E.C.; Aquino, R.; Tourinho, F.A.; Dubois, E.; Bacri, J.-C.; Perzynski, R. "Rare earth doped maghemite EDL-MF: A perspective for nanoradiotherapy." *J. Magn. Magn. Mater.* 2002, 252, 375–377.
- [80] Kim, D.K.; Viot, W.; Zapka, W.; Bjelke, B.; Muhammed, M.; Rao, K.V. "Biomedical applications of ferrofluids containing magnetite nanoparticles". *Mater. Res. Soc. Symp. Proc.* 2001, 676, Y8.32.1–Y8.32.6.
- [81] Smith, C.J.; Field, M.; Coakley, C.J.; Awschalom, D.D.; Mendelson, N.H.; Mayes, E.L.; Davis, S.A.; Mann, S. "Organizing nanometer-scale magnets with bacterial threads." *IEEE Trans. Magn.* 1998, 34 (4), 988–990.
- [82] S. Elborai, "Ferrofluid Surface and Volume Flows in Uniform Rotating Magnetic Fields," PhD Thesis, Massachusetts Institute of Technology, Cambridge, MA, 2006, pp. 163.
- [83] M. Zahn and E. Adalsteinsson, MIT Research Proposal "Biomedical Applications of Magnetic Nanoparticle Suspensions: Applications to Enhanced MRI Imaging of Targeted Magnetic Nanoparticle Delivery for Hyperthermia" to the National Academies Keck Futures Initiative: Designing Nanostructures at the Interface between Biomedical and Physical Systems, Feb. 2005 (not funded).
- [84] R.B. Bird, W.E. Stewart and E.N. Lightfoot, *Transport Phenomena (2nd edition)*, John Wiley & Sons Inc. New York, Jan. 2002.
- [85] M. Zahn and D.R. Greer, "Ferrohydrodynamic Pumping in Spatially Uniform Sinusoidally Time-varying Magnetic Fields," *J. Magn. Magn. Mater.* 1995, 149, pp. 165–173.

[86]A. Chaves, C. Rinaldi, S. Elborai, X. He, and M. Zahn. "Bulk flow in ferrofluids in a uniform magnetic field," *Physical Review Letters*, Issue 19, Article 194501, 15 May, 2006

[87]R.M. Bozorth, 1951. *Ferromagnetism*, IEEE Press, New York, p849.

Appendix A. Oscillating and Rotating Magnetic Field Setup and Measurement

In this thesis, uniform and non-uniform magnetic fields are generated by a three phase motor stator winding. The uniform magnetic field is created by a 2 pole motor stator winding and the non-uniform magnetic field is from a 4 pole motor stator winding. Applying AC currents in phase at each winding, creates an oscillating magnetic field. A rotating magnetic is made by applying three 120° out of phase balanced AC currents through the three windings. The magnetic field pattern for oscillating or rotating magnetic fields can be easily measured by applying DC current through each of the three phase stator windings, where the DC current in each phase equals the instantaneous AC currents for oscillating or rotating magnetic fields. By measuring the magnetic field strength and direction in such a DC magnetic field, the relationship between applied current and magnetic field strength as a function of position within the stator winding region was determined for oscillating and rotating magnetic fields.

A.1 DC, Oscillating and Rotating Magnetic Fields

The 2 pole and 4 pole 3 phase motor stator have 3 identical windings spatially shifted from each other by 120 degrees in azimuthal angles. The three windings were connected in a Y configuration in this thesis as shown in Figure A-1 for the 2 pole winding simplified by assuming each of the 3 windings are concentrated. By applying current I_A through winding A, a magnetic field was created in space as

$$\vec{B}_A = K_w I_A (\cos 0 \vec{i}_x + \sin 0 \vec{i}_y) = K_w I_A \vec{i}_x \quad (\text{A.1})$$

where \vec{B}_A is the magnetic flux density created by winding A, K_w is the winding factor, representing the relation between the applied current and the

magnetic field, and I_A is the applied current in winding A. A current I_B through winding B creates a magnetic field in space as

$$\bar{B}_B = K_w I_B (\cos 120^\circ \bar{i}_x + \sin 120^\circ \bar{i}_y) = \frac{K_w I_B}{2} (-\bar{i}_x + \sqrt{3} \bar{i}_y) \quad (\text{A.2})$$

where \bar{B}_B is the magnetic flux density created by winding B, and I_B is the applied current in winding B. Similarly a current I_C through winding C creates a magnetic field in space as

$$\bar{B}_C = K_w I_C (\cos(-120^\circ) \bar{i}_x + \sin(-120^\circ) \bar{i}_y) = -\frac{K_w I_C}{2} (\bar{i}_x + \sqrt{3} \bar{i}_y) \quad (\text{A.3})$$

where \bar{B}_C is the magnetic flux density created by winding C, and I_C is the applied current in winding C. The total magnetic field in the interior region of the motor stator winding is the sum of the magnetic fields created by each winding

$$\bar{B} = \bar{B}_A + \bar{B}_B + \bar{B}_C \quad (\text{A.4})$$

A.1.1 DC Magnetic Field

A DC magnetic field was generated by activating winding A with a DC current I and grounding windings B and C as shown in Figure A-2. In this configuration, the current through each winding is

$$I_A = I, \quad I_B = I_C = -\frac{I}{2} \quad (\text{A.5})$$

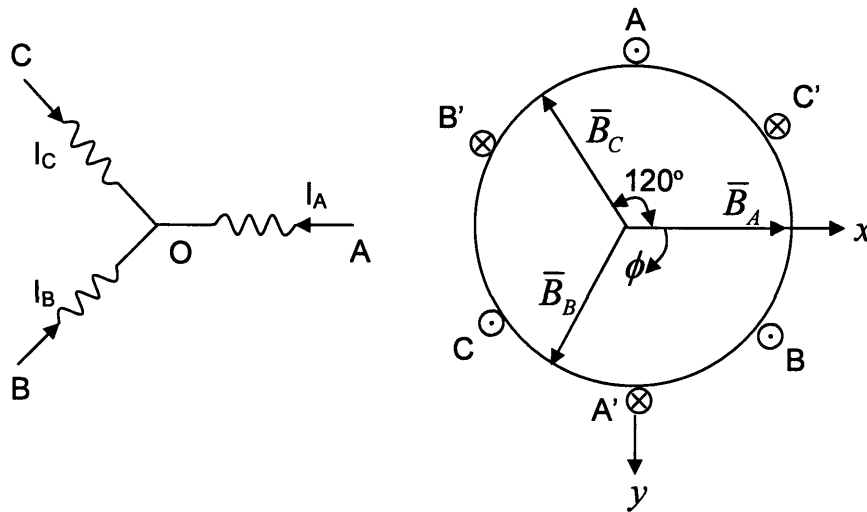


Figure A-1 The 2 pole motor stator windings are connected in a Y configuration with the neutral point O floating. In cylindrical coordinates, the magnetic field generated by each of the three windings has a 120° angle difference.

The total magnetic field flux density is then

$$\bar{B} = \bar{B}_A + \bar{B}_B + \bar{B}_C = K_w I \left[\bar{i}_x - \frac{1}{4}(-\bar{i}_x + \sqrt{3}\bar{i}_y) + \frac{1}{4}(\bar{i}_x + \sqrt{3}\bar{i}_y) \right] = \frac{3}{2} K_w I \bar{i}_x \quad (\text{A.6})$$

The total DC magnetic field from the three windings is purely in the x direction.

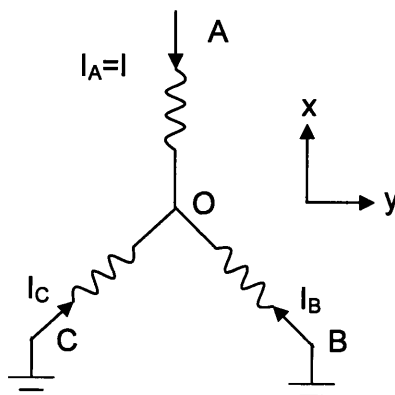


Figure A-2 The 2 pole DC magnetic field current configuration. Winding A was activated with a DC current I with windings B and C grounded.

A.1.2 Oscillating Magnetic Field

An oscillating magnetic field in this thesis research was generated by activating winding A with an AC current $I_A = I \cos \omega t$ and grounded windings B and C as shown in Figure A-3. By the configuration shown in Figure A-3, the current through each winding is

$$I_A = I \cos \omega t, \quad I_B = I_C = -\frac{1}{2} I \cos \omega t \quad (\text{A.7})$$

The total magnetic flux density equals the sum of the magnetic flux densities from the three windings as

$$\begin{aligned} \bar{B} &= \bar{B}_A + \bar{B}_B + \bar{B}_C = K_w I \cos \omega t \left[\bar{i}_x - \frac{1}{4}(-\bar{i}_x + \sqrt{3}\bar{i}_y) + \frac{1}{4}(\bar{i}_x + \sqrt{3}\bar{i}_y) \right] \\ &= \frac{3}{2} K_w I \cos \omega t \bar{i}_x \end{aligned} \quad (\text{A.8})$$

which is an oscillating magnetic field in the x direction.

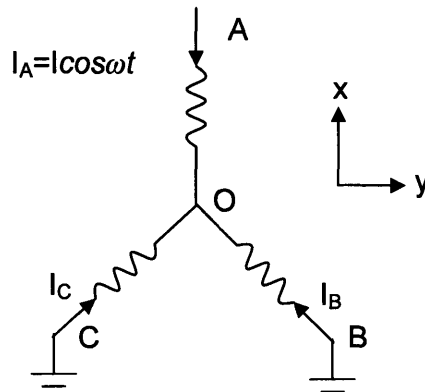


Figure A-3 The current configuration for an oscillating magnetic field in a 2 pole stator winding. Winding A was activated with an oscillating current with windings B and C grounded.

A.1.3 Rotating Magnetic Field

A.1.3.1 Counter Clockwise Rotation

A rotating magnetic field is generated by activating windings A, B and C with balanced 120° out of phase AC currents. A clockwise rotating magnetic field is generated with AC currents shown in Figure A-4 is

$$I_A = I \cos \omega t, \quad I_B = I \cos(\omega t + 120^\circ), \quad I_C = I \cos(\omega t - 120^\circ) \quad (\text{A.9})$$

The current into the neutral point O equals the sum of the currents from each winding

$$I_O = I_A + I_B + I_C = I(\cos \omega t + \cos(\omega t + 120^\circ) + \cos(\omega t - 120^\circ)) = 0 \quad (\text{A.10})$$

which is zero.

The total magnetic flux density of the rotating magnetic field is the sum of the magnetic flux densities from the three windings as

$$\begin{aligned} \bar{B} &= \bar{B}_A + \bar{B}_B + \bar{B}_C \\ &= K_w I \left[\cos \omega t \bar{i}_x + \cos(\omega t + 120^\circ) \left(-\frac{1}{2} \bar{i}_x + \frac{\sqrt{3}}{2} \bar{i}_y \right) - \cos(\omega t - 120^\circ) \left(\frac{1}{2} \bar{i}_x + \frac{\sqrt{3}}{2} \bar{i}_y \right) \right] \\ &= \frac{3}{2} K_w I (\cos \omega t \bar{i}_x + \sin \omega t \bar{i}_y) = \frac{3}{2} K_w I \bar{i}_r |_{\phi=\omega t} \end{aligned} \quad (\text{A.11})$$

where the total magnetic field is radial and rotating counter-clockwise at a radian frequency ω .

A.1.3.2 Clockwise Rotation

A clockwise rotating magnetic field is created by applying the same balanced 120° out of phase AC currents but with opposite phases on the B and C winding

$$I_A = I \cos \omega t, \quad I_B = I \cos(\omega t - 120^\circ), \quad I_C = I \cos(\omega t + 120^\circ) \quad (\text{A.12})$$

which has a total magnetic flux density as

$$\begin{aligned} \bar{B} &= \bar{B}_A + \bar{B}_B + \bar{B}_C \\ &= K_w I \left[\cos \omega t \bar{i} + \cos(\omega t - 120^\circ) \left(-\frac{1}{2} \bar{i}_x + \frac{\sqrt{3}}{2} \bar{i}_y \right) - \cos(\omega t + 120^\circ) \left(\frac{1}{2} \bar{i}_x + \frac{\sqrt{3}}{2} \bar{i}_y \right) \right] \\ &= \frac{3}{2} K_w I (\cos \omega t \bar{i}_x - \sin \omega t \bar{i}_y) = \frac{3}{2} K_w I \bar{i}_r |_{\phi = -\omega t} \end{aligned} \quad (\text{A.13})$$

where the total magnetic field is rotating clockwise at a radian frequency ω .

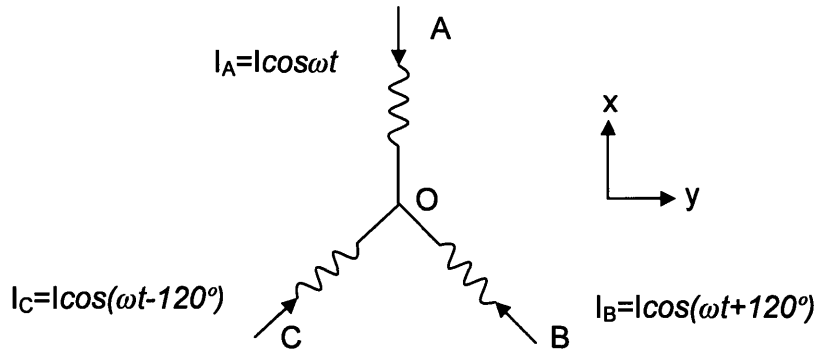


Figure A-4 Counter clockwise rotating magnetic field current configuration for a 2 pole motor stator winding activated with balanced 120° out of phase AC currents. The clockwise rotating magnetic field has the same configuration but with

$$I_B = I \cos(\omega t - 120^\circ) \quad \text{and} \quad I_C = I \cos(\omega t + 120^\circ).$$

A.2 DC, Oscillating and Rotating Magnetic Field Apparatus

The experimental setup for DC, oscillating and rotating magnetic fields is shown in Figure A-5. A Wavetek Datron 40MS/s Model 195 Universal Waveform Generator was used to generate two channel DC or sinusoidal waveforms. The waveform signals were amplified by an AE Techron 5050 Linear Amplifier and output to the 2 pole motor stator winding through a terminal box, from which 3 Fluke 45 Dual Display multimeters were connected to measure DC or AC (rms) currents to guarantee that the currents had the correct amplitudes. In addition, a Tektronix Model 2230 100 MHz Digital Storage Oscilloscope was used to guarantee that the current waveforms in each winding had the correct phase.

The waveform generator just generated 2 channel synchronized waveforms. A DC or oscillating magnetic field just needs one channel DC or AC waveform to drive the motor stator winding, but a rotating magnetic field needs 3 balanced 120° out of phase AC currents, which was created by 2 AC voltages with 60° phase difference from the waveform generator as shown in Figure A-6.

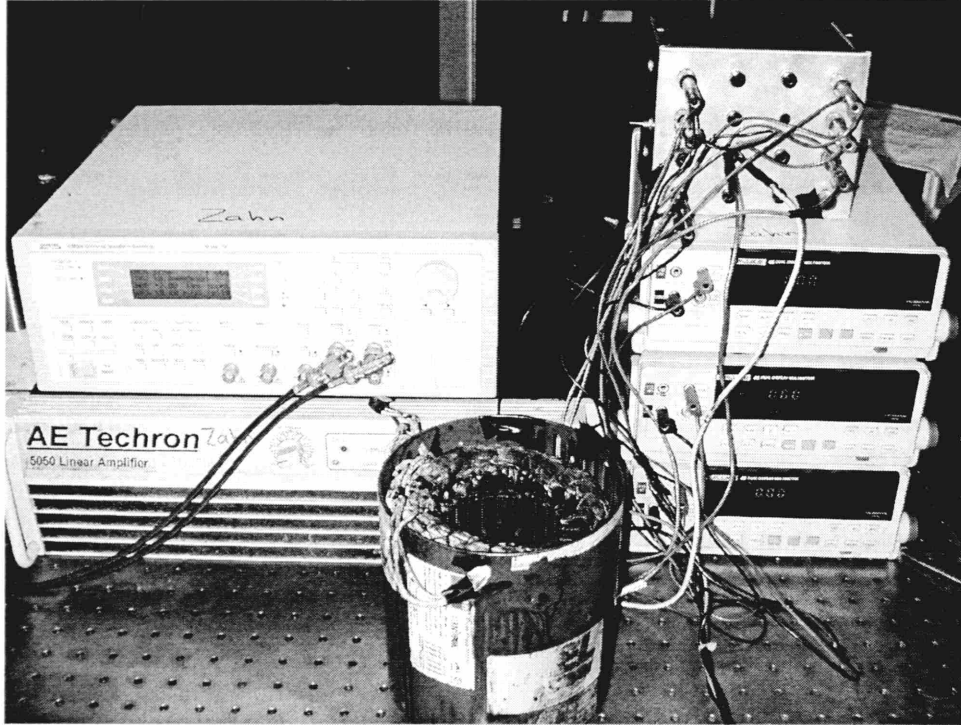


Figure A-5 Photograph of the experimental setup for DC, oscillating and rotating magnetic fields. A 2 pole motor stator winding for a uniform magnetic field or a 4 pole motor stator winding for non-uniform magnetic field was driven by the AE Techron 5050 Linear Amplifier and the Model 195 Wavetek Datron 40MS/s universal waveform generator. Three Fluke 45 Dual Display multimeters are connected in DC or AC (rms) current modes to guarantee that balanced DC or three phase AC currents were applied to the motor stator windings.

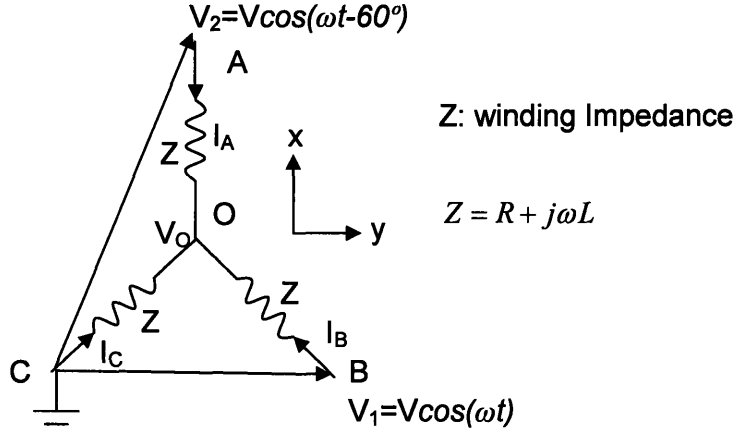


Figure A-6 Counter-clockwise rotating magnetic field voltage configuration. Windings A and B were activated with balanced 60° out of phase AC voltages. Winding C was grounded. Each winding has a winding impedance Z. Three balanced 120° out of phase AC currents were generated by the two applied voltages.

To generate a counter-clockwise rotating magnetic field, the 2 channel balanced 60° out of phase AC voltages were given as

$$V_1 = V \cos \omega t, \quad V_2 = V \cos(\omega t - 60^\circ) \quad (\text{A.14})$$

The total current at the neutral point O is

$$I_O = I_A + I_B + I_C = \frac{V_2 - V_O}{Z} + \frac{V_1 - V_O}{Z} + \frac{0 - V_O}{Z} = 0 \quad (\text{A.15})$$

Applying (A.14) into (A.15), the neutral point voltage is

$$\begin{aligned} V_O &= \frac{V_1 + V_2}{3} = \frac{V}{3} (\cos \omega t + \cos(\omega t - 60^\circ)) \\ &= \frac{V}{6} (3 \cos \omega t + \sqrt{3} \sin \omega t) = \frac{\sqrt{3}}{3} V \cos(\omega t - 30^\circ) \end{aligned} \quad (\text{A.16})$$

Using the solution of (A.16), currents through each winding are

$$\begin{aligned}
I_A &= \frac{V_2 - V_O}{Z} = \frac{V}{Z} \left[\cos(\omega t - 60^\circ) - \frac{\sqrt{3}}{3} \cos(\omega t - 30^\circ) \right] = \frac{\sqrt{3}}{3Z} V \cos(\omega t - 90^\circ) \\
I_B &= \frac{V_1 - V_O}{Z} = \frac{V}{Z} \left[\cos(\omega t) - \frac{\sqrt{3}}{3} \cos(\omega t - 30^\circ) \right] = \frac{\sqrt{3}}{3Z} V \cos(\omega t + 30^\circ) \quad (\text{A.17}) \\
I_C &= \frac{0 - V_O}{Z} = -\frac{\sqrt{3}}{3Z} V \cos(\omega t - 30^\circ) = \frac{\sqrt{3}}{3Z} V \cos(\omega t + 150^\circ)
\end{aligned}$$

where the currents through each winding are equal amplitude (balanced) 120° out of phase AC currents, which generate a counter-clockwise rotating magnetic field.

A clockwise rotating magnetic field is generated by reversing the phase with the same balanced 60° out of phase AC voltages as

$$V_1 = V \cos \omega t, \quad V_2 = V \cos(\omega t + 60^\circ) \quad (\text{A.18})$$

The voltage at the neutral point changes to

$$V_O = \frac{\sqrt{3}}{3} V \cos(\omega t + 30^\circ) \quad (\text{A.19})$$

and the currents change to

$$\begin{aligned}
I_A &= \frac{\sqrt{3}}{3Z} V \cos(\omega t + 90^\circ) \\
I_B &= \frac{\sqrt{3}}{3Z} V \cos(\omega t - 30^\circ) \\
I_C &= \frac{\sqrt{3}}{3Z} V \cos(\omega t - 150^\circ)
\end{aligned} \quad (\text{A.20})$$

which are balanced 120° out of phase AC currents but with reverse phase delay from those in (A.17).

During our experiments, the 3 phase currents were monitored by 3 Fluke multimeters to guarantee balanced three phase amplitude AC currents were applied through the motor stator winding. A Tektronix Model 2230 100 MHz Digital Storage Oscilloscope was used to guarantee that the current waveforms in each winding had the correct phase. The direction of the rotating

magnetic field was verified at low frequency using a compass needle which responds in the direction of rotating magnetic field.

A.3 Magnetic Field Measurement

The magnetic flux density strength was measured by a F. W. Bell Model 7030 Gauss/Tesla meter with a DC magnetic field configuration shown in Figure A-2. By measuring the magnetic field flux density strength with a DC magnetic field configuration, the winding factor K_w was calculated. Thus the relationship between current (rms) and magnetic flux density (rms) was determined.

In the uniform rotating magnetic field generated by the 2 pole motor stator winding used in our experiments, each Ampere rms current in each of the 3 windings create a uniform rotating magnetic field of 38 Gauss rms in the absence of ferrofluid.

In the non-uniform rotating magnetic field generated by the 4 pole motor stator winding used in our experiments, each Ampere rms current in each of the 3 windings create a cylindrically symmetric non-uniform rotating magnetic field with a slope of 821.6 Gauss/m (rms) linearly along the radius of the stator winding. With a diameter of 116 mm, each Ampere rms current excites a non-uniform rotating magnetic field maximum amplitude of 47.65 Gauss (rms) at the inner wall (radius = 58 mm) of the 4 pole motor stator winding.

A.4 Motor Parameters

The resistance and inductance of the 2 pole and 4 pole motor stator windings were measured as given in Table A-1.

Table A-1 Measured winding resistance R and inductance L at 1 kHz of a single winding.

| Motor | Winding Resistance, R [Ohm] | Winding Inductance, L [mH] |
|--------------|-----------------------------|----------------------------|
| 2 pole motor | 3.1 | 8.0 |
| 4 pole motor | 1.8 | 4.43 |

A.5 High Frequency Operation

In our experiments, the waveform generator and the linear amplifier worked together as a voltage source, which delivers adjustable fixed values of voltage to the motor stator winding. Under an AC voltage the actual current through each winding is determined by the total impedance of the winding. At higher frequencies, the impedance from the inductance of the windings becomes larger as $Z_L = j\omega L$, where ω is the radian frequency of the applied voltage, thus limiting the current delivered to the windings or requiring a higher voltage to deliver the same current for the same magnetic field. As an example for the 2 pole motor stator winding, the inductive reactance at 1 kHz is 52.3 ohms so that the impedance magnitude of the winding is 52.4 ohms. For a 5 Ampere rms current to create a 190 gauss rms magnetic field, the voltage across each winding rises to 262 Volt rms (449 Volt rms for each channel from the amplifier). Such a high voltage is a potential danger to the winding and people operating the experiment. To reduce the required voltage, a capacitor was connected in series to each winding of the motor stator so that the negative reactance of the capacitor cancelled the positive reactance of the inductance at the frequency of operation. With the series capacitance the total impedance was

$$Z = R + j\omega L - j\frac{1}{\omega C} \quad (\text{A.21})$$

where C is the capacitance serially connected to the motor stator winding. At resonance, $Z = R$ and $\omega L = \frac{1}{\omega C} \rightarrow \omega^2 = \frac{1}{LC}$. Thus for a given operating frequency $f = \frac{\omega}{2\pi}$ a resonance capacitance was calculated as

$$C = \frac{1}{L\omega^2} = \frac{1}{L(2\pi f)^2} \quad (\text{A.22})$$

Table A-2 lists the capacitance required for generating a rotating magnetic field at high frequencies with a lower voltage required from the power amplifier. However, even though the voltage required from the power amplifier has decreased, the actual voltage across the winding, equal to that across the capacitor, is much larger than the voltage from the power amplifier and can still exceed their voltage rating which can cause sparking, overheating, shock hazards and other damage to the winding, capacitor, and user.

Table A-2 Calculated capacitor values for the 2 pole and 4 pole stator windings necessary to achieve resonance at various frequencies.

| Frequency, f [Hz] | 500 | 1000 | 2000 | 3000 |
|-------------------|--------------------|-------------------|-------------------|--------|
| 2 pole motor | 13.0 μF | 3.1 μF | 800 nF | 130 nF |
| 4 pole motor | 22.9 μF | 5.7 μF | 1.4 μF | 229 nF |

Appendix B. Additional Flow Profile Data In Non-uniform Rotating Magnetic Fields

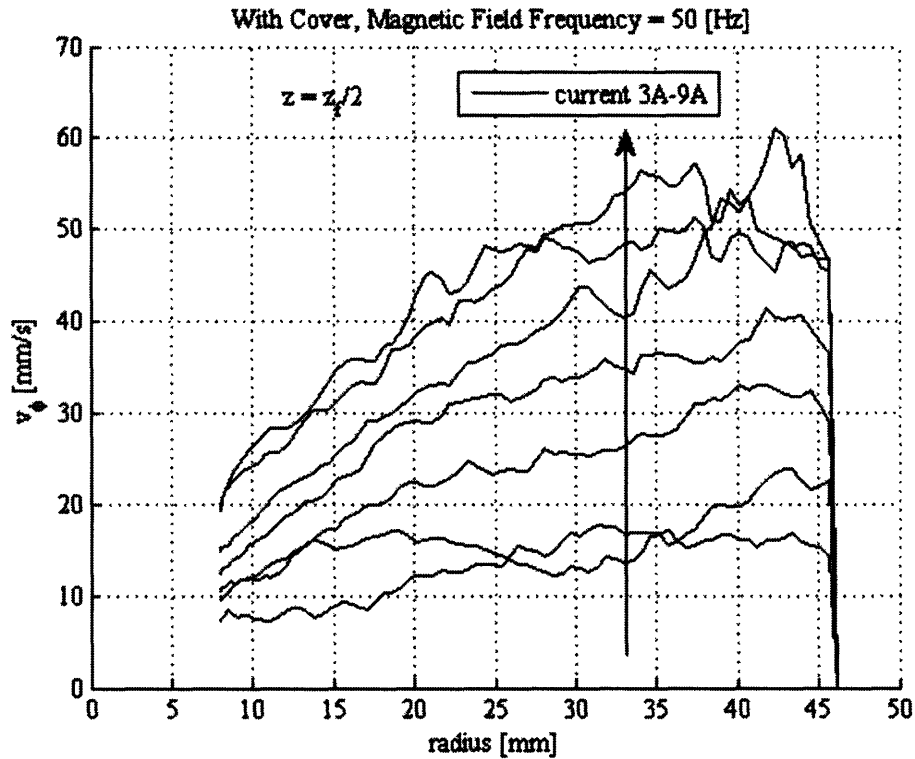


Figure B-1 The measured azimuthal component of spin-up flow profiles at $z = z_f/2$ for MSG W11 water-based ferrofluid excited by a non-uniform magnetic field rotating counter-clockwise at 50 Hz. Velocities increase with increasing applied magnetic field (increasing current in A rms). The cylindrical container was covered so that there were no free ferrofluid surfaces.

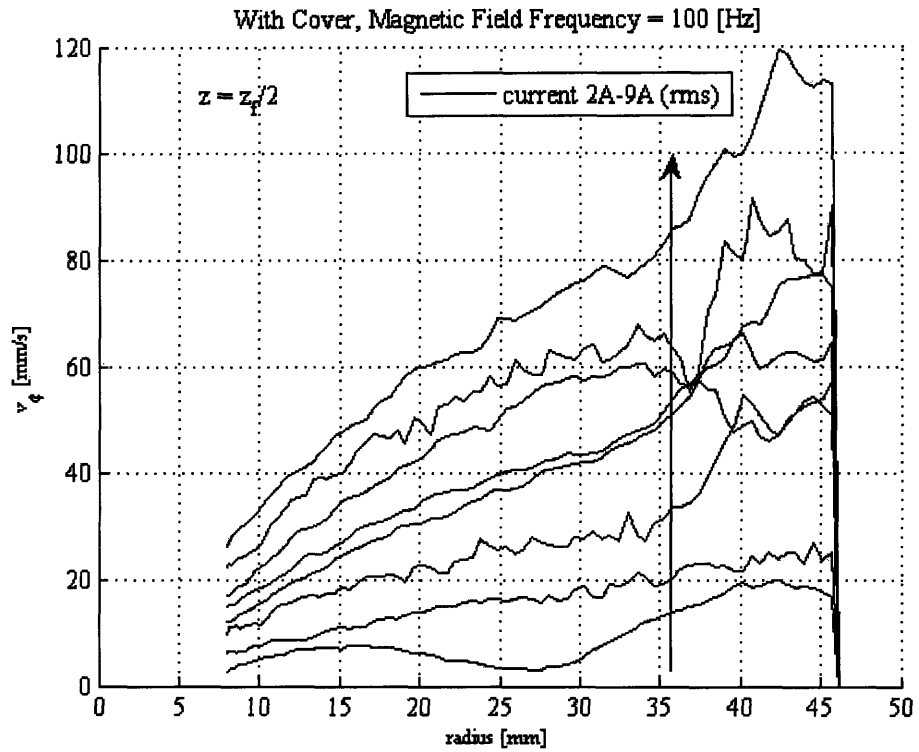


Figure B-2 The measured azimuthal component of spin-up flow profiles at $z = z_f/2$ for MSG W11 water-based ferrofluid excited by a non-uniform magnetic field rotating counter-clockwise at 100 Hz. Velocities increase with increasing applied magnetic field (increasing current in A rms). The cylindrical container was covered so that there were no free ferrofluid surfaces.

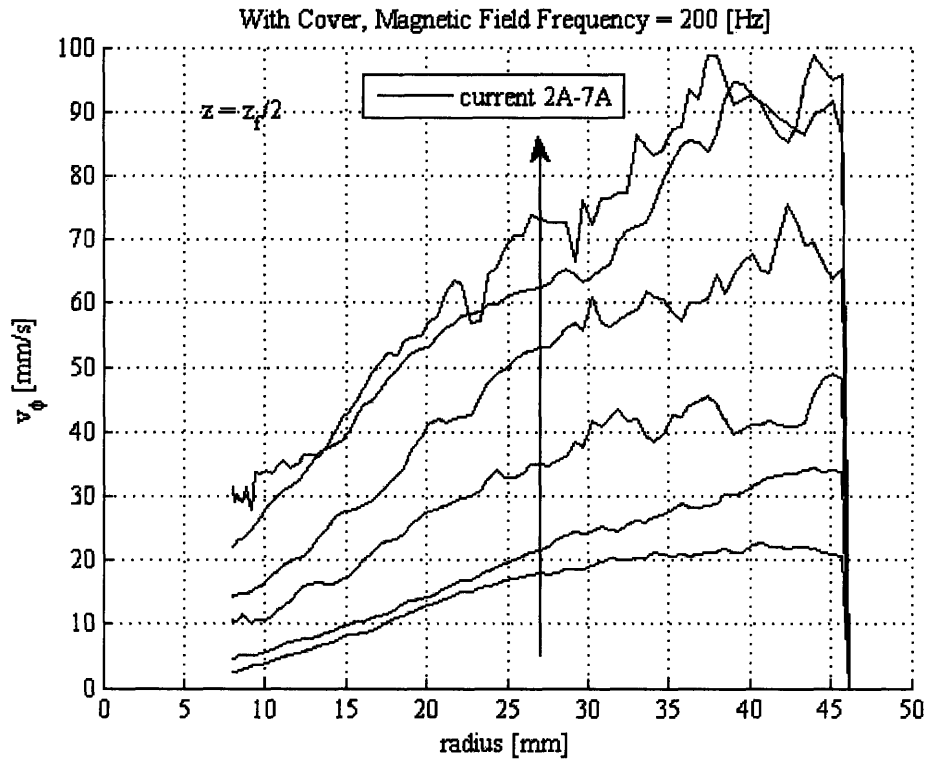


Figure B-3 The measured azimuthal component of spin-up flow profiles at $z = z_f/2$ for MSG W11 water-based ferrofluid excited by a non-uniform magnetic field rotating counter-clockwise at 200 Hz. Velocities increase with increasing applied magnetic field (increasing current in A rms). The cylindrical container was covered so that there were no free ferrofluid surfaces.

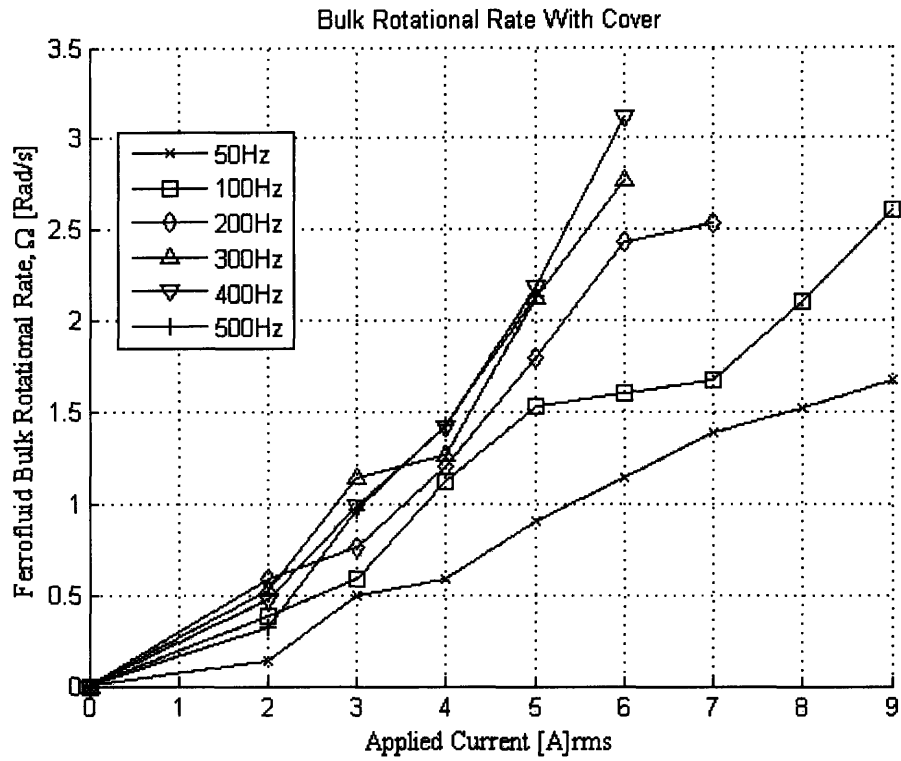


Figure B-4 Relation between the measured bulk rotational rate in the central region of the MSG W11 ferrofluid, $\Omega = v_{\phi}/r$, and the applied current for various magnetic field frequencies. The ultrasound probe was placed at height $z = z/2$ in the outside wall of the cylindrical container with a top cover. The rate of rotation increases monotonically with applied field strength for the investigated range of magnetic field strength.

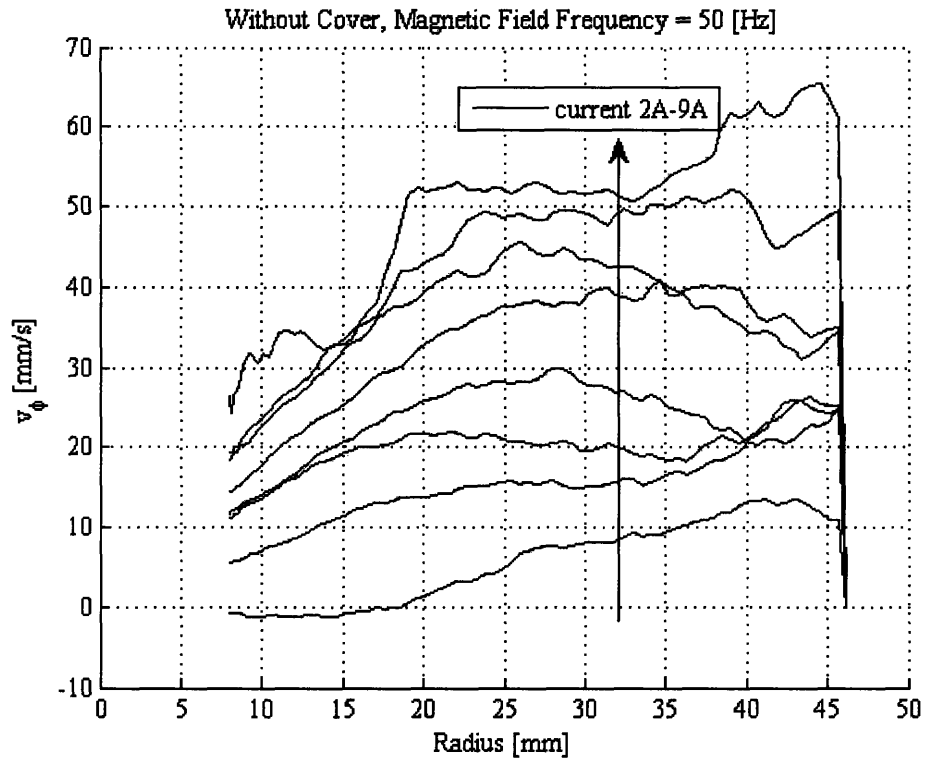


Figure B-5 The measured azimuthal component of spin-up flow profiles at $z = z_i/2$ for MSG W11 water-based ferrofluid excited by a non-uniform magnetic field rotating counter-clockwise at 50 Hz. Velocities increase with increasing applied magnetic field (increasing current in A rms). The cylindrical container was uncovered so that there was a free ferrofluid surface.

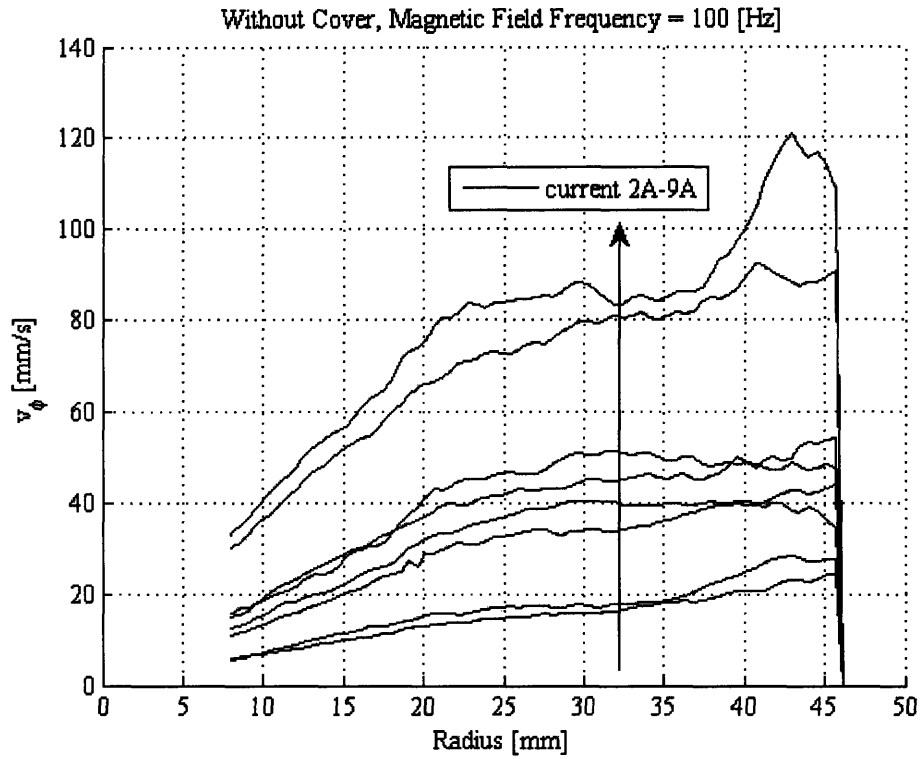


Figure B-6 The measured azimuthal component of spin-up flow profiles at $z = z_r/2$ for MSG W11 water-based ferrofluid excited by a non-uniform magnetic field rotating counter-clockwise at 100 Hz. Velocities increase with increasing applied magnetic field (increasing current in A rms). The cylindrical container was uncovered so that there was a free ferrofluid surface.

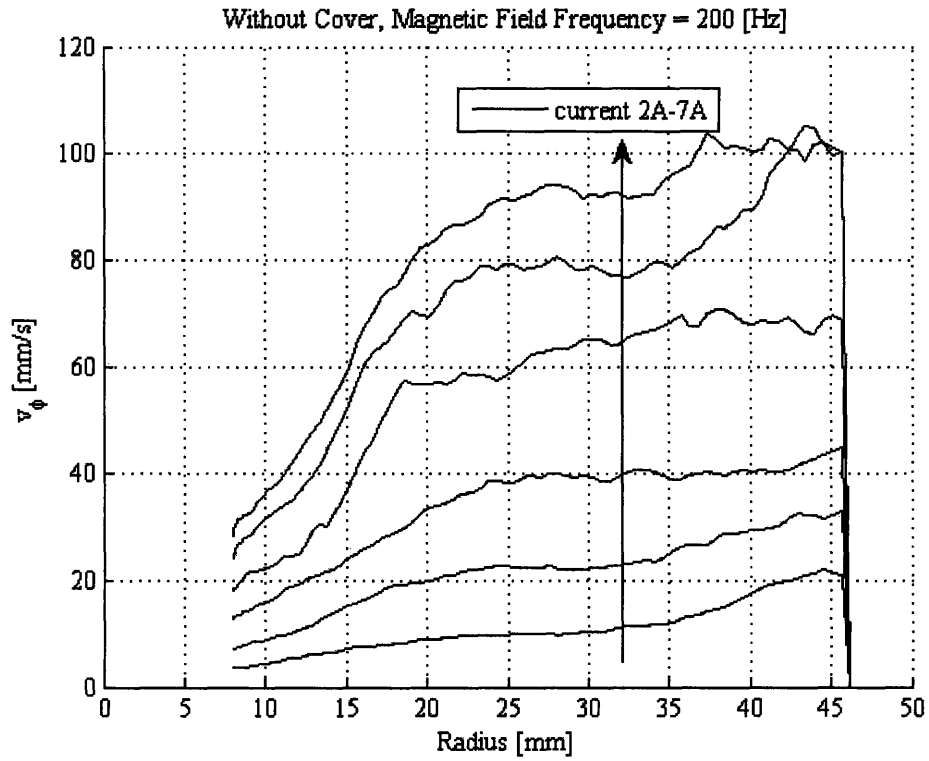


Figure B-7 The measured azimuthal component of spin-up flow profiles at $z = z_c/2$ for MSG W11 water-based ferrofluid excited by a non-uniform magnetic field rotating counter-clockwise at 200 Hz. Velocities increase with increasing applied magnetic field (increasing current in A rms). The cylindrical container was uncovered so that there was a free ferrofluid surface.

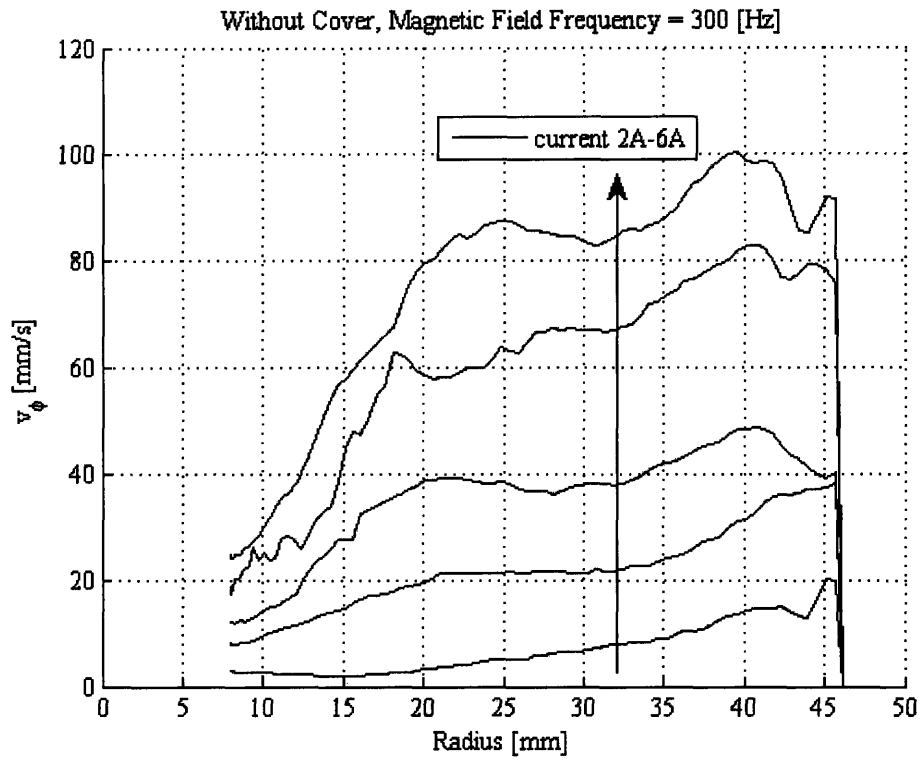


Figure B-8 The measured azimuthal component of spin-up flow profiles at $z = z_i/2$ for MSG W11 water-based ferrofluid excited by a non-uniform magnetic field rotating counter-clockwise at 300 Hz. Velocities increase with increasing applied magnetic field (increasing current in A rms). The cylindrical container was uncovered so that there was a free ferrofluid surface.

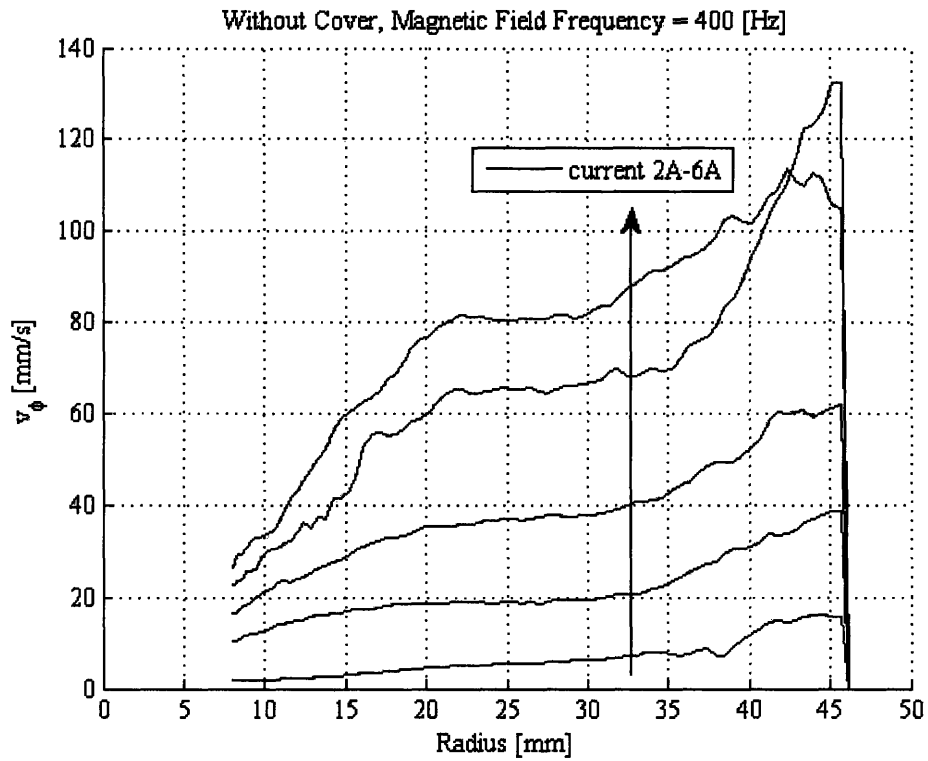


Figure B-9 The measured azimuthal component of spin-up flow profiles at $z = z_i/2$ for MSG W11 water-based ferrofluid excited by a non-uniform magnetic field rotating counter-clockwise at 400 Hz. Velocities increase with increasing applied magnetic field (increasing current in A rms). The cylindrical container was uncovered so that there was a free ferrofluid surface.

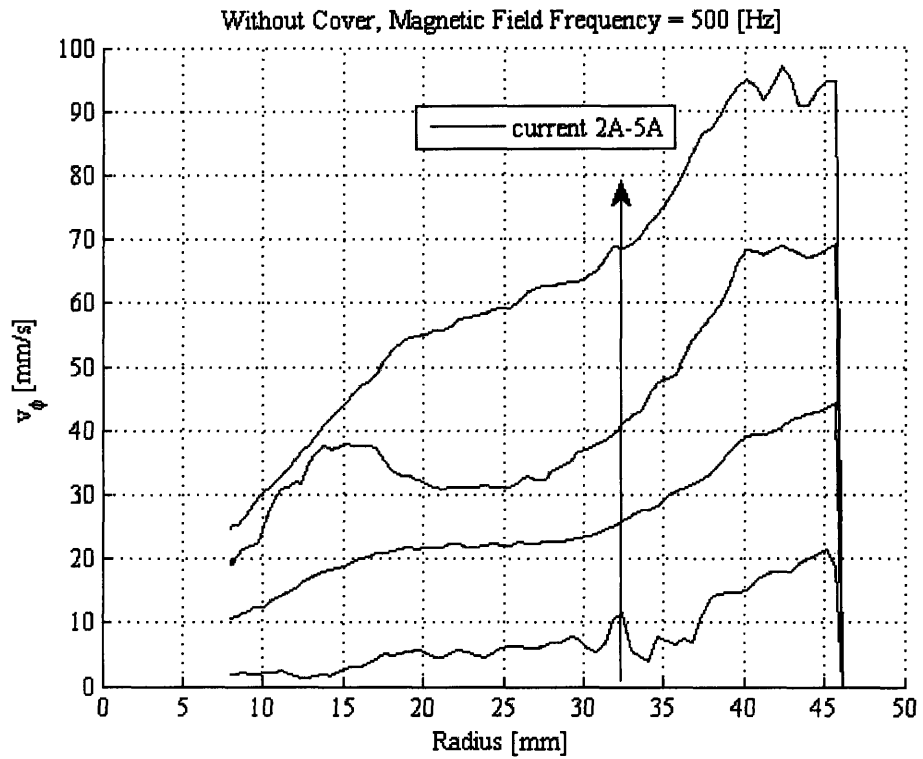


Figure B-10 The measured azimuthal component of spin-up flow profiles at $z = z/2$ for MSG W11 water-based ferrofluid excited by a non-uniform magnetic field rotating counter-clockwise at 500 Hz. Velocities increase with increasing applied magnetic field (increasing current in A rms). The cylindrical container was uncovered so that there was a free ferrofluid surface.

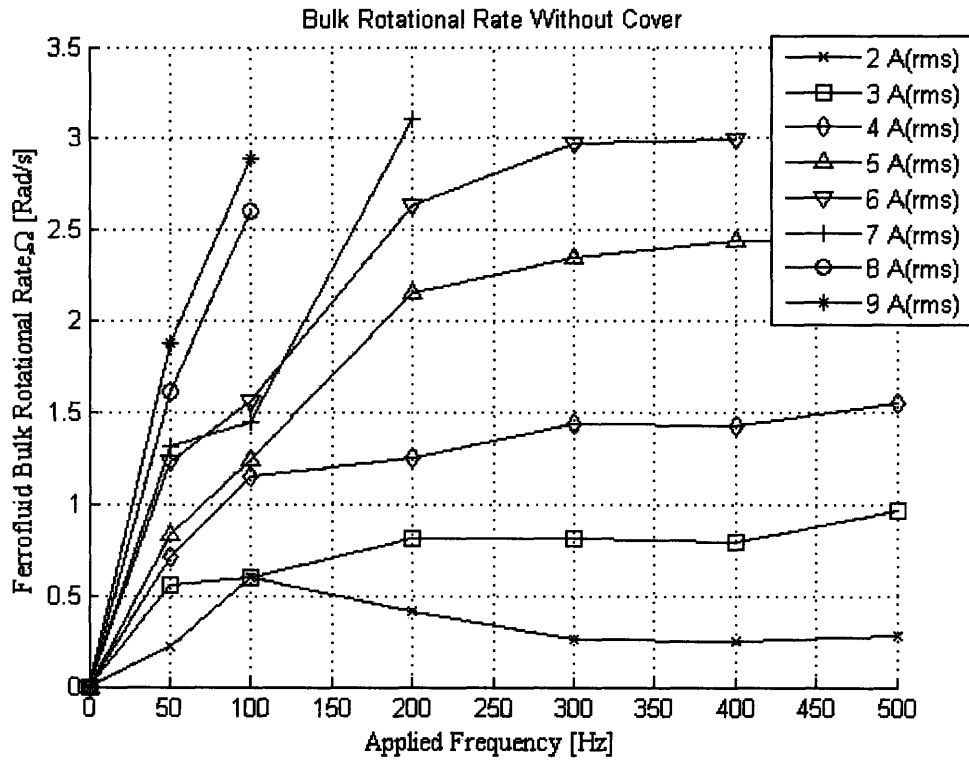


Figure B-11 Measured relationships between the bulk rotational rate in the central region of the MSG W11 ferrofluid, $\Omega = v/r$, and the frequency of the applied rotating magnetic field for various applied current. The ultrasound probe was placed at height $z = z/2$ in the outside wall of a cylindrical container without a top cover.

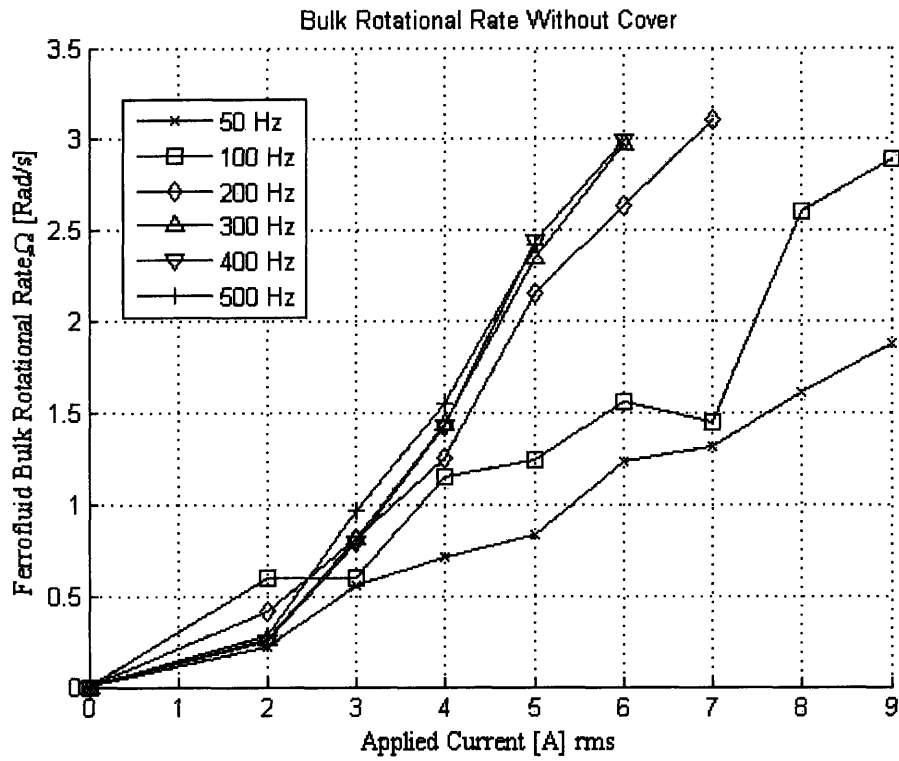


Figure B-12 Measured relationships between the bulk rotational rate in the central region of the MSG W11 ferrofluid, $\Omega = v_{\theta}/r$, and the currents for various magnetic field frequencies. The ultrasound probe was placed at height $z = z/2$ in the outside wall of a cylindrical container without a top cover. The rate of rotation increases monotonically with applied current for the investigated range of magnetic field frequencies.